UNIVERSITY OF
BIRMINGHAM

Electro-Mechanical Behaviour of Indium Tin Oxide Coated Polymer Substrates for Flexible Electronics

by

Grzegorz A. Potoczny

A thesis submitted to the
University of Birmingham
for the degree of
DOCTOR OF PHILOSOPHY

School of Metallurgy and Materials
University of Birmingham
January 2012

Abstract

Highly conductive and transparent ITO thin films were successfully fabricated on both glass and polymer substrates (PET, PEN and PC) by pulsed laser deposition at low temperatures (24 – 150 ^{o}C). The influence of oxygen pressure, target-to-substrate distance, number of pulses and deposition temperature on the structural and physical properties of ITO-coated glass substrates was studied. The samples were investigated using Scanning Electron Microscopy (SEM), Atomic Force Microscopy (AFM), X-Ray Diffraction (XRD), the four-point probe and a spectrophotometer. Uncoated polymers were also characterised. Amorphous 100 nm thick ITO films with low resistivity, of 3.0 x 10^{-4} Ω cm, and high transparency, of 85%, were obtained on glass substrates at a temperature of 150 ^{o}C. A low resistivity, of ~ 5.0 x 10^{-4} Ω cm, and high transparency, of 80%, was achieved for ITO-coated polymer substrates at room temperature. For the ITO thickness range 50 – 250 nm a stable resistivity between ~ 5.0 and 6.0 x 10^{-4} Ω cm was achieved. This result is important for flexible display designers, where low thickness of the film is necessary to increase flexibility whilst simultaneously maintaining a low resistivity and a high transparency for high device efficiency. Sol-gel derived ITO films dip-coated on glass substrates were also studied. The optimum film obtained at a firing temperature of 600 ^{o}C had a resistivity of 1.8 x 10^{-2} Ω cm, and optical transmittance of ~ 80%.

The electro-mechanical behaviour of ITO/polymer systems, used for touch and flexible displays, was investigated under uniaxial tension and controlled buckling in both tension and compression. The resistance changes were monitored *in situ*. Mechanically-tested samples were characterised *ex situ* by SEM and AFM techniques. Cracking and buckling delamination failure modes were observed for all samples investigated under uniaxial tensile strain at

critical strains raging from 2.8 to 3.5%, and from 7.0 to 8.0%, respectively. The results showed that the dominant critical failure mode depends on the applied deformation conditions. The ITO/PEN samples showed high flexibility; the samples were bent in tension down to a 2.6 mm radius of curvature before cracks start to occur. The major conclusion is that the electro-mechanical properties of ITO-coated polymer substrates can be improved by a careful control of the thickness of ITO film during its growth by pulsed laser deposition and a proper selection of the polymer substrate.

“Imagination is more important than knowledge. For knowledge is limited to all we now know and understand, while imagination embraces the entire world, and all there ever will be to know and understand”

A. Einstein

Acknowledgments

I would like to acknowledge sincerely to my supervisors Dr Stephen Kukureka and Professor Stuart Abell for their kindness, fruitful suggestions and constant encouragement throughout my project.

I am deeply indebted to Mr Frank Biddlestone and Mr Andy Bradshaw for their outstanding technical support and ideas during my experiments.

I am also grateful to all my colleagues and staff in the School of Metallurgy and Materials for their help and support.

In addition, I would like to acknowledge financial support from the Technology Strategy Board sponsored research grant SOLFLEX and the School of Metallurgy and Materials at the University of Birmingham.

Special thanks to my parents and brothers for their enormous support and encouragement.

Finally, special thanks to Agnieszka for her love and reminding me that life exists too beyond the laboratory.

Contents

CHAPTER 1

1. INTRODUCTION

1.1 Flexible displays and related issues

As display devices used for presentation of information in visual form are present in all aspects of our daily life, e.g. they permeate our homes, our work places or our vehicles, designers are hungry for greater freedom (Cairns and Crawford, 2005b). It is believed that in the near future many electronic assemblies on rigid substrates will be replaced by mechanically flexible or stretchable alternatives (Morent et al., 2007). Polymer substrates used for flexible displays instead of brittle glass substrates can lead to devices that are robust, light-weight, portable, and hence satisfy consumer demands (Choi et al., 2008). Polymer substrates also provide great design freedom and allow displays to be rolled-up when not used (Han et al., 2005). These features make flexible displays a new generation of display devices and are very attractive for a variety of electronic products ranging from cell phones and smartphones to computers, television, toys, electronic books and wearables (Laser_Focus_World, 2004). Figure 1.1 shows examples of flexible plastic electronics. The market opportunities for flexible displays are so broad that many electronic, plastics and printing companies are investing in the development of new polymer substrates and low or room-temperature manufacturing processes toward the mass production of flexible liquid crystal displays (LCDs) and flexible organic light emitting diodes (FOLEDs) (Laser_Focus_World, 2004). Low-temperature, novel, wet-deposition methods for functional

layers, such as UV-curable sol-gel derived conductive indium tin oxide thin films (Al-Dahoudi and Aegerter, 2003; Asakuma et al., 2003) can significantly reduce production costs and allow the material to be printed on the substrate via roll-to-roll processes (see Figure 1.2) under atmospheric pressure (Koniger and Munstedt, 2008a). Figure 1.3 shows market prospects for flexible display devices.

However, the performance, efficiency and lifetime of flexible displays strongly depends on the polymer properties, such as their optical, electrical and structural properties. In addition, polymer substrates considered for plastic electronics do not match all the reliability requirements for display processing, such as mechanical (e.g. scratch resistance), chemical (e.g. solvent resistance) or physical (e.g. low water and gas permeability) and the right choice of polymer substrates is essential (Burrows et al., 2001; Bouten et al., 2005; Logothetidis, 2008).

Another issue is indium tin oxide (ITO), the most commonly-used anode material coated on polymer substrates, which is found almost in all touch screen devices currently available on the market. There is a thermal and mechanical mismatch between the hard, brittle ITO and a viscoelastic substrate which may lead to cracking and delamination during the fabrication process and in operation (Han, 2005). Figure 1.4 shows how ITO/polymer systems are integrated into the structure of flexible displays. Conductive ITO layers deposited on polymer substrate significantly limit the flexibility of the devices (Chen et al., 2002). When this system is submitted to bending, tensile stresses appear and cracks form in the brittle layer. The scale of cracks and the strain at which they form depend on the ITO and polymer properties, the thickness of the conductive film and the interfacial strength (Cairns and Crawford, 2005b).

The cracking of brittle ITO layers decreases the electrical functionality of the flexible devices. Therefore, electro-mechanical tests of ITO/polymer systems are necessary to find their limits, such as the maximum strains that can be introduced to the brittle layer before cracking occurs and to provide this information for display designers.

Flexible displays have been one of the most important issues in the last 15 years due to their potential advantages (Han, 2005). Currently many electronic companies are researching flexible displays based on liquid crystal displays (LCDs), organic light-emitting diodes (OLEDs), electrophoretic displays (Cairns et al., 2003; Han, 2005; MacDonald et al., 2005; Cheol et al., 2012) and even plasma displays (Cairns, 2005; Cheol et al., 2012). Furthermore, flexible displays can be categorised as those that are curved but not flexed during use (e.g. displays for automotive and aerospace industries), displays that are mildly flexible but do not undergo severe treatment such as rolling (e.g. smart packaging, smart cards, labels or flexible lighting applications) and fully rollable or even crumplable displays (e.g. paper-like electronic newspaper, TVs that we could make disappear when not in use or a PDA that could roll up into a pen (Cairns et al., 2003), and wearable displays) (MacDonald et al., 2005). Though some flexible displays have been developed (Cheol et al., 2012), fully flexible displays remain very much a work in progress as manufacturers continue to address issues in fabrication and stability (Melnick, 2011). To date, there are no flexible displays available on the market. However, SAMSUNG presented a prototype of a cell phone employing a flexible active-matrix OLED display at the Consumer Electronics Show (CES) in 2011 and 2012, (see Figure 1.1 (d)) and is hoping to launch it in 2012[*]. Recently, Nokia demonstrated an

[*] For mor information visit http://www.linkedin.com/news?viewArticle=&articleID=892773002&gid=3244188&type=member&item=8245 7172&articleURL=http%3A%2F%2Fwww.tomsguide.com%2Fus%2FSamsung-AMOLED-Flexible-bendy-display-screen%2Cnews-13047.html&urlhash=GdlZ&trk=group_most_popular-0-b-shrttl

interesting device with a flexible display that is controlled by bending and twisting at Nokia World in London. Currently, there is much interest in the development of educational devices, such as e-textbooks (Melnick, 2011). All the above-mentioned applications require high robustness and performance during operation, especially when used by school children. Therefore, their components, such as conductive anodes (e.g. ITO coated polymers) should be able to withstand repeated flexing without losing opto-electrical characteristics in order to develop next-generation flexible displays. Despite high electrical stability during flexing, low resistivity is required to provide faster display refresh rates while maintain high optical transmission (Paine et al., 2005). High clarity is important, e.g. for bottom-emissive displays a transparency of > 85% in the visible range for conductive films, barrier layers and polymer substrates is required (MacDonald et al., 2005). In addition, conductive transparent anodes can be used for flexible thin film solar cells (Guillen and Herrero, 2011) where bendability will improve assembling process, e.g. on curved building structures. Therefore, the major aim of this work is to fabricate conductive ITO film on polymer substrates that exhibits high optical and electrical characteristics coupled with the reliability demanded by mildly and fully rollable opto-electronic devices.

In this work two deposition methods for conductive ITO are used: pulsed laser deposition (PLD) and a wet-deposition route (sol-gel derived ITO films). ITO films are usually deposited on substrates by classical physical vapour deposition (PVD) methods (e.g. magnetron sputtering) which yield high-quality films. However, these methods are costly due to high wastage of the expensive ITO and the necessity to use vacuum systems. The deposition costs can be significantly reduced by novel, wet sol-gel deposition methods. These methods are more economical and allow the production of films with excellent homogeneity, easily-

controlled thickness and doping levels, and the fabrication of thin films on large and complex shapes via roll-to-roll processes (Park and Mackenzie, 1995; Kim et al., 1999c; Alam and Cameron, 2000). Thus, as a part of this work, sol-gel derived ITO was developed during the SOLFLEX project (see appendix A for more detail). However, the resistivity of SOLFLEX sol-gel ITO is found to be very high and the process requires high annealing temperatures, which limits its use to glass substrates. Therefore, pulsed laser deposition is also used in this work (outside SOLFLEX) to allow deposition of ITO films on polymer substrates at low temperatures. The advantage of using the PLD technique is that it allows stoichiometric transfer of a material from a target (Kim et al., 1999a; Kim et al., 2006; Norton, 2007) and minimises film contamination since the laser beam is focused only on the source material (Yong et al., 2005). In comparison with other deposition techniques, PLD will always produce better-quality thin films, especially at room temperature (Zheng and Kwok, 1993). Moreover, PLD is ideal for investigating the behaviour of thin films and the results may be applicable to other PVD techniques (Sierros et al., 2010a).

The PLD process to grow ITO on polymers is optimised in this work in order to achieve the highest possible optical, electrical, and mechanical performance. There are two ways to increase the flexibility of electronic devices based on brittle thin films: i) by reducing the thickness of the thin layer and ii) by placing the brittle coatings near the neutral axis (Chen et al., 2001b). Therefore, in this work the deposition process is optimized in such way as to achieve the thinnest possible ITO films with low resistivity and high transparency. It is not a trivial task, since it is well known that with decreasing layer thickness the resistivity increases. Another issue is the trade-off between low resistivity and high transparency. Therefore, careful control of the ITO growth conditions is very important. The deposition parameters such as oxygen partial pressure, target-to-substrate distance, number of pulses and

temperature are varied systematically. Also ITO/polymer systems are tested under a variety of applied stress conditions possibly present during device fabrication and service, in order to understand the factors affecting their electro-mechanical reliability. The influence of ITO thickness, type of polymer substrate and interfacial strength on crack-resistance of the ITO/polymer systems is investigated. This is of high importance, since ITO-coated polymer substrates are widely utilised in flexible electronic applications as an anode material. As stresses are also present for roll-to-roll processes, identifying and simulating different deformation modes and stress conditions are crucial before commercialisation of flexible electronic devices.

The hypothesis that a careful control of deposition conditions will improve electro-mechanical stability of ITO film by reducing its thickness with a negligible effect on electrical conductivity is suggested.

1.2 Aims of this work

i) To investigate pulsed laser deposition conditions on optical and electrical properties of ITO thin films. The pulsed laser deposition process will be optimise to achieve the thinnest possible ITO films with low resistivity and high transparency.

ii) To investigate and understand the factors affecting electro-mechanical reliability of functional pulsed-laser deposited ITO thin films on different polymer substrates used as anode materials for plastic electronics. The electro-mechanical behaviour of the ITO/polymer

systems will also be studied to provide representative results as a foundation for scientific and technological interest.

1.3 Scope of this work

In order to understand the factors affecting opto-electrical and mechanical performance of ITO films, and also to provide a solid foundation for future projects, the following topics are covered in this thesis:

1. A review of the relevant work previously reported in the literature.
2. Characterisation of bare polymer substrates as a candidates for plastic electronics in terms of structural, mechanical and morphological properties.
3. Fabrication and characterisation of pulsed-laser deposited transparent, conductive indium tin oxide (ITO) thin films on glass and polymer substrates at low temperatures.
4. Characterisation of ITO films coated glass substrates by novel, wet sol-gel method.
5. Investigation of electro-mechanical reliability of ITO/polymer systems under variety of deformation modes and stress conditions.

1.4 Organisation of the thesis

Chapter 2 provides a detailed description of the substrates, samples, and the deposition and characterisation techniques used in this study. The mathematical formulae used in this study are also given. A developed buckling device is described in detail.

Chapter 3 gives a literature review of polymer substrates used as candidates for plastic electronics. The results of substrate characterisation are also provided. The degree of crystallinity, transparency, surface morphology and influence of polymer chain orientation on mechanical properties of poly(ethylene terephthalate) PET, poly(ethylene naphthalate) and polycarbonate (PC) are investigated and discussed.

Chapter 4 gives the detailed background theory and a literature review of ITO films deposited on glass and polymer substrates by pulsed laser deposition (PLD) and other techniques. The chapter contains detailed results of the PLD optimisation process for ITO film on glass substrates. The effect of oxygen pressure, target-to-substrate distance, number of pulses and temperature on optical, electrical, structural and morphological properties is investigated. ITO films are also deposited on polymer substrates and the influence of polymer substrate on morphology and opto-electrical properties of ITO is also discussed.

Chapter 5 provides background theory and a literature review of sol-gel derived ITO films coated both glass and polymer substrates by dip and spin-coating techniques. The ITO/glass systems are characterised and the influence of film thickness and of the kind of indium precursors on optical and electrical properties is discussed.

Chapter 6 deals with electro-mechanical properties of thin-film coated polymer substrates. Essential theory and a literature review of failure modes in thin films/polymer systems and their mechanisms are given. The influence of polymer substrates (PET, PEN and PC) and the thickness of the ITO layer on residual stress and electro-mechanical properties is investigated. The results of ITO/polymer systems subjected to uniaxial tensile electro-fragmentation with *in*

situ observation of crack evolution, monotonic and cycling buckling in tension and compression tests are described and discussed. A new failure mechanism is proposed for ITO-coated PC substrates. *Ex situ* surface observations of ITO layers after the mechanical tests are conducted by scanning electron microscopy (SEM) and atomic force microscopy (AFM).

Chapter 7 concludes the thesis. The overall conclusions and the main findings are given. Future work related to PLD of functional thin films on polymer substrates and electro-mechanical tests is also suggested. Different deposition techniques are also discussed.

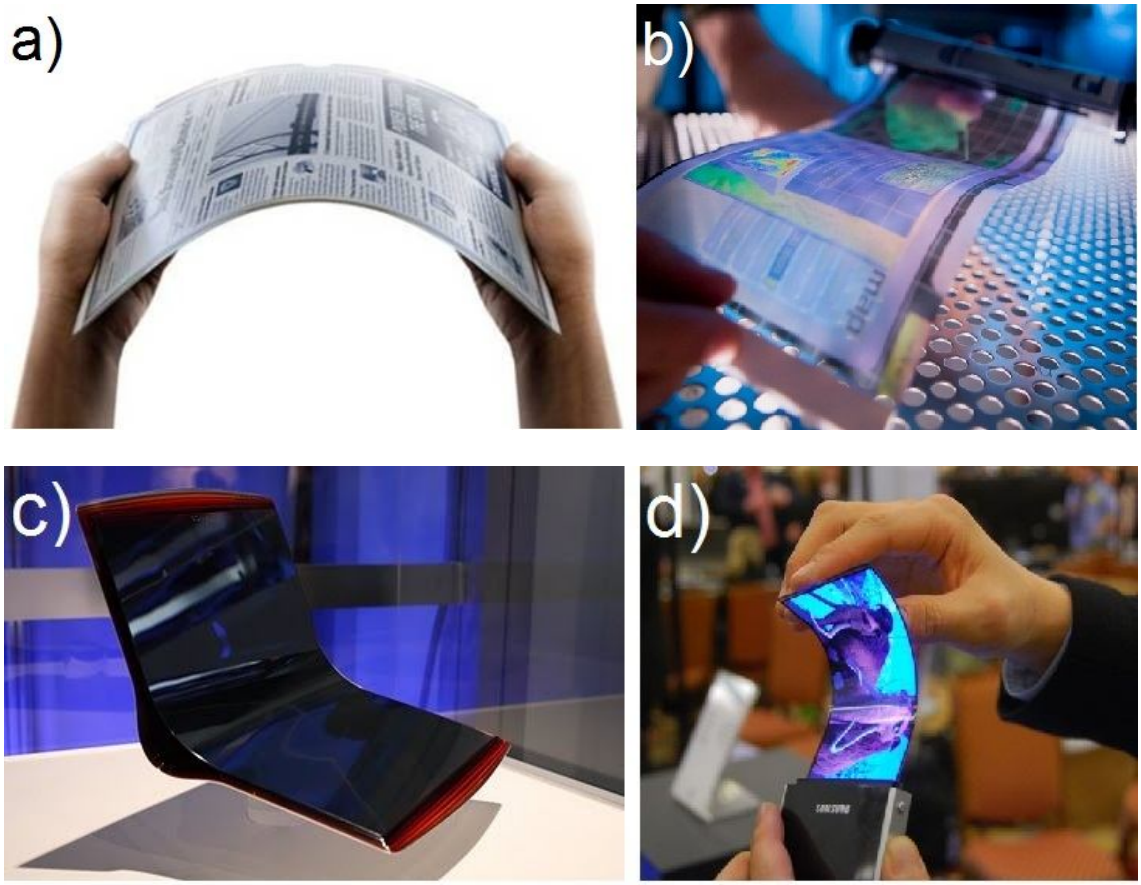

Figure 1.1 Examples of flexible electronics. Adapted from a) www.impactlab.net, b) www.asunews.asu.edu, c) www.arbertechno.blogspot.com and d) www.itechfuture.com.

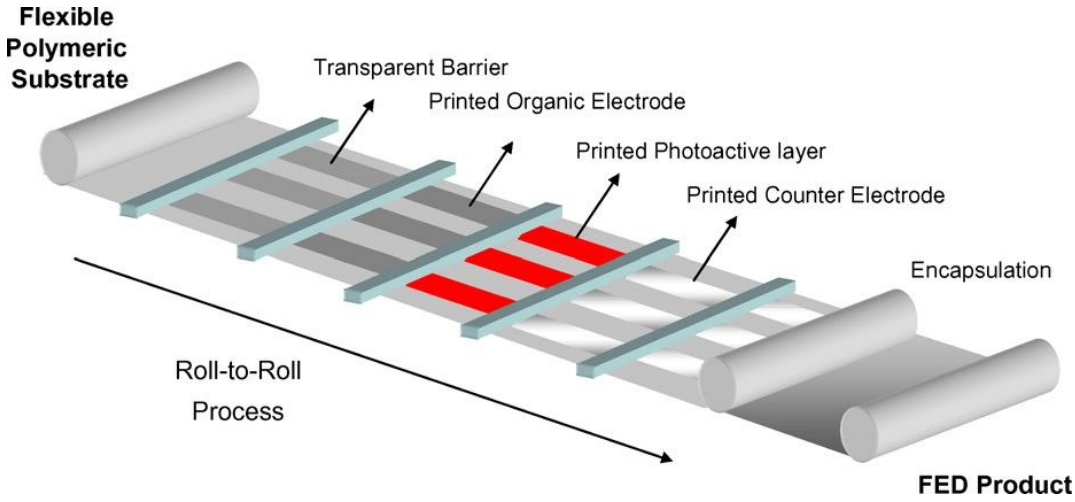

Figure 1.2 Schematic representation of the future roll-to-roll process for flexible electronic devices (FEDs). Adapted from (Logothetidis, 2008).

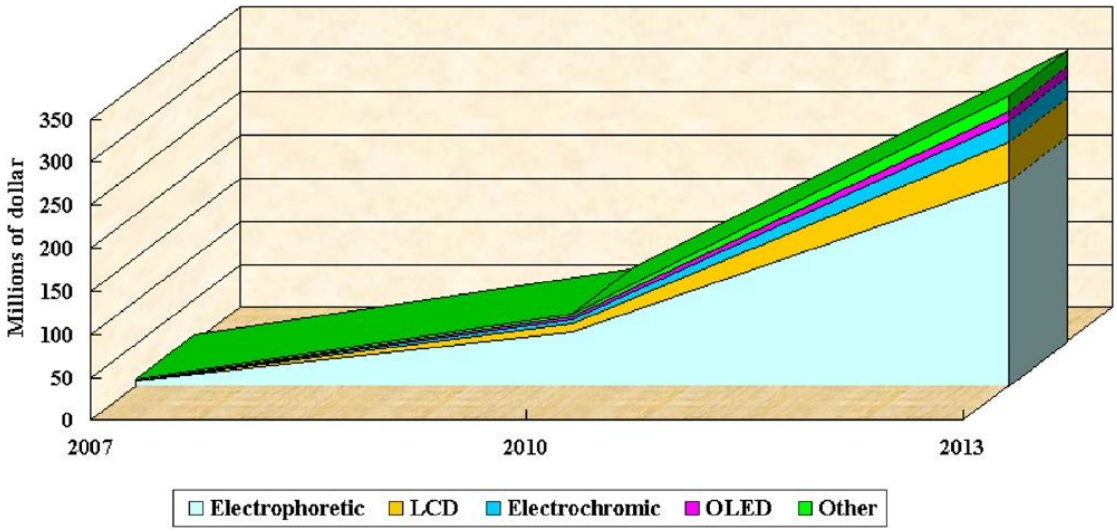

Figure 1.3 Market prospects for flexible displays. Adapted from (Choi et al., 2008).

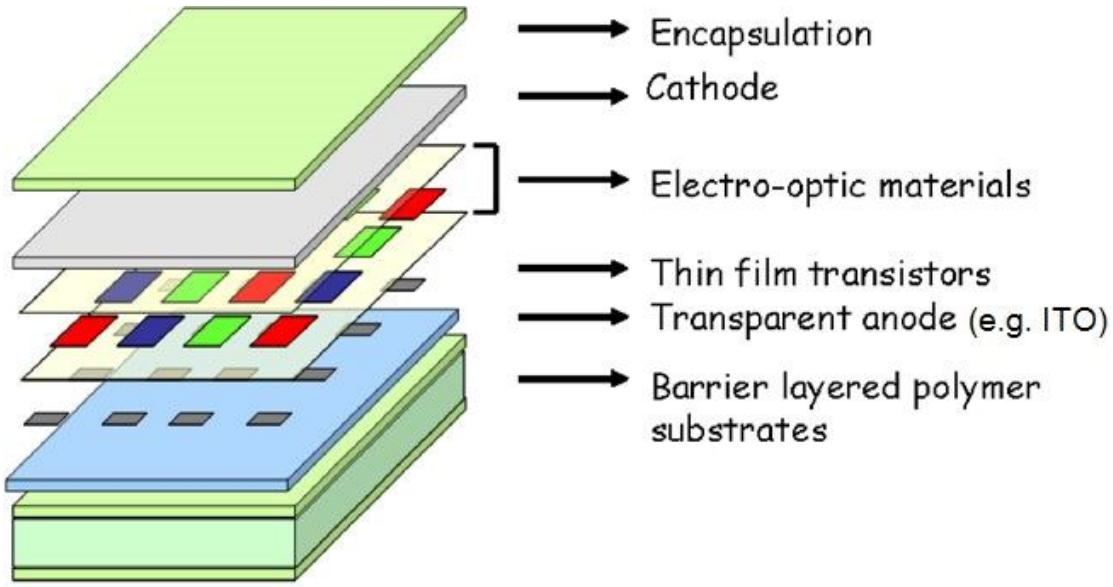

Figure 1.4 Cross-sectional structure of a typical plastic electronics device. Adapted from (Choi et al., 2008).

CHAPTER 2

2. MATERIALS AND EXPERIMENTAL METHODS

2.1 Substrates and samples

2.1.1 Polymer substrates

The polymer substrates to be tested are two semi-crystalline polyesters, polyethylene naphthalate (PEN Teonex Q65 FA) and polyethylene terephthalate (PET Melinex ST 505), and amorphous polycarbonate (PC Lexan 8010 MC). All polymer substrates were supplied through Cadillac Plastic Limited[1] in A4 format. The polymer sheets were separated from each other by thin paper to avoid surface damage. In addition, PC films were coated by removable plastic foil on both sides to protect the surface against undesirable scratches. PEN and PET films were biaxially-oriented, heat-stabilised and their surfaces were pre-treated on one side by an unknown adhesion-promotion coating (MacDonald et al., 2008) during manufacturing processes (see section 3.2.1 for more detail). The thickness of polymer substrates was measured by micrometer and Table 2.1 shows characteristic features of the films used in this study.

[1] All substrates and samples suppliers are listed in appendix B.

2.1.2 Glass substrates and ITO target

The glass substrates used for the PLD process are borosilicate Corning 1737 with dimensions of 50 x 75 x 1.1 mm supplied through Delta Technologies Limited. No passivation layer is required, as the content of alkali oxides is very low, and ITO thin films can be directly deposited on the glass. The Corning glass substrates exhibit a transparency of ~ 92% in the visible range and are commonly used for active-matrix liquid-crystal displays. The glass substrates were cut into small pieces (15 x 10 mm) with a diamond pen for deposition on them by PLD.

The ITO-sintered ceramic target is 90 wt.% In_2O_3 doped by 10 wt.% SnO_2. It is 5 mm high and has a diameter of 25 mm. The target density is 7.1 g/cm^3 and it was supplied through PI-KEM Limited.

2.1.3 ITO coated on glass (SOLFLEX project)

The development process of sol-gel derived ITO films can be divided into three stages: preparation of ITO ink precursors via chemical processes, ITO ink rheology modification and printing of ITO ink on both glass and polymer substrates. The stages of ITO ink development are presented schematically in Figure 2.1. The samples for characterisation were provided through SOLFLEX partners and only the best results are presented in this work.

ITO ink precursors were developed starting from indium acetate [$In(C_2H_3O_2)_3$] and tin acetate [$Sn(C_2H_3O_2)_4$] as source materials and modified via chemical reactions with neodecanoate

(ND) ($C_{10}H_{20}O_2$) in xylene. The mixtures of indium neodecanoate $In(ND)_3$ [see Figure 2.2 (a)] and tin neodecanoate $Sn(ND)_4$ [see Figure 2.2 (b)] dissolved in alcoholic solutions were hydrolysed in a further process to form the continuous liquid phase – gel. Two batches (batch 1 and 2) were prepared using different content of $In(ND)_3$. Then the glass substrates were dip-coated with hydrolysed In/Sn(ND) with two different speeds per batch by one of our co-workers and sent for characterisation.

- Batch 1. The dip-coating rates are 5 and 10 mm/min and hence the sample names are 0309 5 and 0309 10 mm/min, respectively.

- Batch 2. The dip-coating rates are 10 and 20 mm/min and hence the sample names are 0509 10 and 0509 20 mm/min, respectively.

2.2 Experimental techniques

2.2.1 Pulsed laser deposition of ITO thin films

ITO films were deposited on both glass and polymer substrates using a 248 nm KrF excimer laser (Lambda Physics LPX300). A vacuum chamber was evacuated to a base pressure of ~10^{-6} Torr. The laser beam was focused on to the target at a 45^o angle of incidence with an output of 24 ns pulse and 10 Hz repetition rate. The sintered ITO ceramic target was mounted onto the target carrousel and rotated at 10 rpm during deposition. Prior to the actual deposition the target surface was ablated with an unfocused laser beam of 500 pulses in order

to remove contamination and create proper conditions in the deposition chamber. After each 10 depositions the target was polished by wet and dry slide discs with grit designation P400, P800 and P1200 for a better target utilization and in order to avoid particulate formation during the deposition process. It is important to note that the particles of nano- or micron-sizes ablated from the craters' edges left on the target by the penetrated laser beam, have an influence on thin film growth (Eason, 2007). In addition, they can creates centres of stress in the thin layers and hence have an influence on their mechanical reliability.

The standard dumb-bell polymer samples were cut before deposition from A4 sheets using a Moore Hydraulic Press (see also section 2.2.5). Prior to the deposition process the glass and polyester (PEN and PET) samples were cleaned using ultrasonic methods in acetone, ethanol and water for 15 min total time (5 min/solvent). PC substrates are non acetone-resistant and for that reason they were cleaned by ethanol and water only. After cleaning the substrates were dried by blowing air for around 2 min. For the sample preparation process laboratory gloves were worn to avoid any surface contamination. Then the clean samples were held on a heater in the deposition chamber by a metal mask ready for the deposition process. The metal mask was used in order to produce a step in the ITO film during deposition and hence enabling further thickness measurements.

Different deposition conditions were chosen for ITO films deposited on glass substrates to produce high quality ITO films with low resistivity and high transparency in the visible range. The target-to-substrate distance was set up in the range of 55 - 85 mm. The number of pulses and the temperature was set up in the range of 1000 – 8000 pls and 24 – 150 ^{o}C, respectively. The oxygen partial pressure (P_{O_2}) was set up in the range of 2.5 – 20 mTorr. When elevated

temperatures were used the samples were cooled to room temperature in the deposition chamber under background pressure (~ 10^{-6} Torr).

In the case of polymer substrates ITO films were deposited under the following conditions: 55 mm target-to-substrate distance, 7.5 mTorr P_{O_2} at room temperature. A different number of pulses was used depending on the ITO film thickness requirements (500, 1000 and 1200 pulses for 50, 100 and 150 nm, respectively). No annealing treatment was performed for any samples investigated in this study.

2.2.2 Morphological properties

A few experimental techniques were involved in this study to analyse the surface physical and chemical state:

- **Scanning Electron Microscopy (SEM)** is a very common technique in modern laboratories due to high lateral resolution and great depth of focus. It enables also microstructure analysis by X-ray, which was highly adapted by a large number of researchers and used particularly in materials science (Godehardt, 2008). Conventional JEOL 6060 and JEOL JSM – 7000F FE – SEM microscopes were used. Two different experimental methods were used for microanalysis: energy dispersive X-ray (EDX) and wavelength dispersive X-ray (WDX). This means, that the emitted X-ray can be analysed as a function of the energy or its wavelength (Godehardt, 2008). The samples (10 x 5 mm or 10 x 15 mm) were attached to the cylinder-type SEM specimen mounts

by a copper conductive tape. Prior to SEM characterisation the samples were coated by a thin gold layer using a sputter coater in order to reduce charging effects of non conductive glass and polymer substrates. The SEM was operating using the working distance (WD) of 10 mm and the energy of 20 keV.

- **Atomic Force Microscopy (AFM)** is an effective instrument for characterisation of nanostructures due to sub-nanometer precision of the tip movement (Tseng, 2010) and ease of samples preparation. The roughness of ITO films was investigated using Dimention™ 3100 AFM operating in contact-mode. Silicon nitride cantilevers with spring constant of 0.58 N/m and spherical tips were used. For bare polymer substrates tapping-mode was used with a silicon cantilever with an operating frequency of 330 Hz. In tapping-mode the tip oscillates at its resonance frequency, having only intermittent contact with the soft polymer surface, and hence reduces the lateral drag forces and surface damage compared to contact-mode AFM (Sauer et al., 2000). The samples were scanning with a speed of 1 Hz at room temperature. The roughness measurements were taken from five different places and an average value of root mean square (RMS) roughness was calculated.

- **Profilometer Dektak 3** operating in clean room was used in order to evaluate the thickness of ITO films. In this method a small feeler–needle stylus comes in contact with the sample, and moves up and down giving the surface topography. The scan speed was set at 20 seconds/μm and 10 measurements were taken from different places of the sample in order to calculate an average and standard deviation. A white

line on Figure 2.3 shows a typical profile of ITO film thickness measurement. It is important to note that no specimen preparation is required for this technique.

- **Microscopy: a camera PixeLINK** was used to collect images of the ITO cracks evolution during uniaxial tensile loading, and ITO/polymer sample profiles after PLD deposition process and during buckling tests. More details are provided in section 2.2.5.

2.2.3 Structural and physical properties

- **X-ray diffraction** (XRD) is a technique used to determine the crystalline structure of the materials. The crystalline structure of the materials can be derived by measuring Bragg reflections, i.e. their position, shape, intensity etc. (Birkholz, 2006), which satisfy Bragg's law (Cullity, 1978)

$$n\lambda = 2d\sin\theta \tag{2.1}$$

where n is the order of diffraction peak, λ is the wavelength of the x-ray beam, d is lattice inter-planar spacing and θ is the angle of diffraction.

The θ/2θ diffractometer is commonly used to measure the Bragg reflection. The incoming X-ray beam is directed to the sample surface at an angle θ_{in} and the exiting scattered radiation is also detected at the same angle ($\theta_{in} = \theta_{out}$). The 2θ means that the exiting beam is determined with respect to the extended incoming beam (Birkholz,

2006). Figure 2.4 shows a schematic of a θ/2θ scan. A Siemens X-ray diffractometer with a Cu K-alpha radiation (0.154 nm) was used in this study to determine the diffraction pattern for ITO thin films deposited on both glass and polymer substrates by PLD. The scan angle was set from 15^o to 70^o with step size of 0.05 and counting time of 3 seconds. The average grain size of crystalline ITO films was calculated using Scherrer's formula (Khodorov et al., 2007; Hao et al., 2008)

$$D = \frac{K\lambda}{B\cos(\theta)} \tag{2.2}$$

where $K = 0.9$ is a crystal shape constant, λ is the X-ray wavelength, B is the broadening of diffraction line measured at half of its maximum intensity (FWHM) in radians and θ is the Bragg diffraction angle.

- **Differential Scanning Calorimetry** (DSC) is a widely used technique to study thermal properties of polymer materials, i.e. glass transition temperature (T_g), melting temperature (T_m), crystallization temperature (T_c) or changes in enthalpy (ΔH) (Cheremisinoff, 1996). It measures the heat capacity (C_p) of the sample under atmospheric pressure as a function of increasing temperature at a constant rate.

The aluminium pan filled with a few mg of polymer is placed in the sample holder. An empty pan is used as a reference and placed in the reference holder. The chambers are heated to the desired temperature or cooled at a constant rate. The system monitors the temperature changes between two chambers and programmed temperature. If the

temperature difference occurs, heat or coolant are provided to one chamber in order to equalize it with programmed temperature. The energy supplied to that chamber is proportional to the heat capacity of the sample, which is monitored and presented graphically (Brown, 1998; Bower, 2002).

A DSC Perkin Elmer 7 differential scanning calorimeter was used in this study. The polymer samples were held at a temperature of 20 ^{o}C for 1 minute and then heated to 290 ^{o}C at a rate of 20 ^{o}C/minute. Changes in the heat of fusion were calculated from the area under the melting point (Figure 2.5) by DSC software for all semi-crystalline polymer samples. Errors in calculating the degree of crystallinity exist due to an arbitrary drawn baseline. The average value and standard deviation were calculated from several measurements of the heat of fusion in order to decrease the error of the method. Changes in heat of fusion for 100% crystalline PET and PEN polymers equal to 103.4 (Schoukens et al., 2003) and 140 J/g (Zumailan et al., 2002), respectively, were used to calculate the degree of crystallinity following equation (3.1).

2.2.4 Electrical and optical properties

- **A four-point probe** Keithley 580 Micro-Ohmmeter was used to measure the resistance of ITO films. It consists of four tungsten probes, which are aligned linearly and separated from each other by a distance of 1 mm. Figure 2.6 shows a schematic of the four-point probe. A high current is applied to the two outer probes and the two inner probes measure a voltage potential of the sample (Schroder, 1990). Hence, the

sheet resistivity or resistance, R_s (Ω/□) is calculated using equation (Runyan and Shaffner, 1997)

$$R_s = R \times \frac{\pi}{\ln 2} = R \times 4.532 \tag{2.3}$$

where R is a measured resistance. Multiplying the sheet resistance of the film by its thickness h, the bulk resistivity ρ (Ω cm) is calculated

$$\rho = R_s \times h \tag{2.4}$$

A minimum of ten measurements of the resistance were performed on different places of the sample at room temperature and the average and standard deviation were calculated. The bulk resistivity is used in this study in order to characterise electrical properties of ITO films.

- **Optical transparency measurements** were conducted using a Jenway 6310 spectrophotometer. A spectrum scan from 250 nm to 1000 nm is obtained using monochromatic light (8 nm bandwidth) passing through the measured sample and detected by the detector. Figure 2.7 shows schematic of optical system used in this study.

Prior to each measurement the system was calibrated. The samples were scanned between 250 nm and 1000 nm. The absorbance spectrum was recorded by the

spectrophotometer and then converted manually to transmittance using the well-known Lambert-Beer's equation (Owen, 2000)

$$A = -\log T \tag{2.5}$$

where A is absorbance and T is transmittance. The transparency values of the samples were determined as an average in the visible range from 400 to 800 nm.

Since it is not possible to achieve simultaneously the maximum transparency and electrical conductivity, as these properties are inversely related, a figure of merit was introduced to determine the utility of TCO thin films for optoelectronic applications (Kim et al., 1999a). The formula considers the ratio of optical transmittance at 550 nm of the film to its sheet resistance (Deokate et al., 2010)

$$\phi = \frac{T^{10}}{R_s} \tag{2.6}$$

2.2.5 Mechanical and electro-mechanical properties

- **Residual (intrinsic) stress determination**. The residual compressive stress (negative by convention) is calculated from the radius of curvature *r*, of the bent sample after PLD deposition, using an extended Stoney's formula (1909), which considers also the Young's modulus of the coating (Leterrier et al., 2004)

$$\sigma_i = -\frac{E_s h_s^2}{6(1-\upsilon_s)h_f}\left(1+\frac{h_f}{h_s}\left(4\frac{E_f}{E_s}-1\right)\right)*\left(\frac{1}{R_2}-\frac{1}{R_1}\right) \quad (2.7)$$

where E_s, and E_f, are the Young's modulus of the substrate and the thin film, respectively, h_s and h_f are the thicknesses of the substrate and the film, respectively and υ_s is the substrate Poisson's ratio. Internal strain is calculated using equation (Leterrier et al., 2004)

$$\varepsilon_i = \frac{\sigma_i(1-\nu_f)}{E_f} \quad (2.8)$$

where σ_i is intrinsic stress, ν_f and E_f are Poisson's ratio and Young's modulus of the thin film, respectively.

The Young's modulus values were evaluated in this work by means of tensile testing and equal to 3.20, 3.40 and 1.20 GPa for PET Melinex ST 505, PEN Teonex Q65 FA and PC Lexan 8010 MC, respectively. The Poisson's ratios for PET and PEN listed in Table 3.2 and for PC, Table 3.3, were also used. The Young's modulus and the Poisson's ratio of indium tin oxide (ITO) thin film equal to 100 GPa (Leterrier et al., 2004) and 0.2 (Izumi et al., 2002a; Leterrier et al., 2003), respectively were used for calculations.

In order to evaluate the radius of curvature of the bent samples after deposition, PixeLINK microscopy camera and the image processing and analysis software – ImageJ are used. The sample is placed on two vertical razor blades separated from

each other and the profile image is captured by the camera. The ruler is placed below the sample to set the scale for further measurements. The length of the sample and the angle with respect to the x axis are measured, as Figure 2.8 shows. The radius of curvature is calculated using a following relationship (Chen et al., 2001a; Chen et al., 2002)

$$\lambda = 2\left[1 - \frac{E(k)}{K(k)}\right], \qquad \frac{l}{r} = 4K(k)k \tag{2.9}$$

where $K(k)$ and $E(k)$ are complete elliptic integrals of the first and second, $k = \sin(\theta/2)$, l the original length of the beam, r the radius of curvature, and λ the contraction ratio.

- **Instron model 5566 tensile machine** was used to conduct mechanical and electro-mechanical tests of bare polymer substrates and ITO-coated samples by PLD. Standard dumb-bell samples (Figure 2.9) of 50 mm length, 4 mm gauge width with gauge length of 18 mm were prepared before tensile tests using a Moore Hydraulic Press. Bare polymer substrates were strained with crosshead speed set at 0.5 mm/min and 1 mm/min at a temperature of 24 ^{o}C. Young's modulus was calculated from the slope of the initial straight line of the stress-strain curve (Hooke's Law), as Figure 2.10 indicates. It is defined as (Nielsen, 1974b)

$$E = \frac{d\sigma}{d\varepsilon} \tag{2.10}$$

where $d\sigma$ and $d\varepsilon$ are the stress and the strain, respectively. For tensile test the stress is defined as

$$\sigma = \frac{F}{A} \tag{2.11}$$

where F is the force or load and A is the cross sectional area of the sample. For engineering, the strain is defined as

$$\varepsilon = \frac{L - L_0}{L_0} = \frac{\Delta L}{L_0} \tag{2.12}$$

where L_0 is the original length of the sample and L is the stretched length.

Stiffness parameter such as Young's modulus is thickness independent, thus it does not indicate how rigidity will change with thickness (MacDonald et al., 2007). Therefore, the bending stiffness of a film can be defined by its rigidity (MacDonald et al., 2007)

$$D = \frac{Eh^3}{12(1-\nu)} \tag{2.13}$$

where E is the Young's modulus, h is the polymer thickness and ν is the Poisson's ratio.

- **Electro-mechanical tensile tests** of ITO coated polymer samples were conducted using a slightly modified Instron tensile machine, developed in a previous project (Sierros, 2006). Two copper wires are attached to the Instron's grips and connected to the multi-meter. One wire is connected to the upper grip and another to the lower grip.

A polytetrafluoroethylene (PTFE) foil is placed between the lower grip and the base of the machine in order to close the electrical circuit. (This is necessary, in order to monitor resistance changes during the tensile test.) In addition, PTFE screws are used to attach the lower grip to the base of the Instron machine in the same purpose. The multi-meter FLUKE 45 is connected to the computer and the data is monitored and recorded using National Instruments LabVIEW software. NI – LabVIEW software is also capable of monitoring extension and load signals, which come from Instron tensile machine. Therefore, the extension-load-resistance data are monitored at the same time and storied by the program, which is very convenient for further data analysis. Figure 2.11 shows a schematic of the operated electro-mechanical tensile testing system, described above. The conductive failure of the ITO films at a certain strain was characterised by means of 10% increment in resistance with respect to the resistance of unloaded sample. Five samples were used to determine the average and standard deviation of the critical onset strain (COS) at which 10% increment in resistance occurred. Intrinsic crack onset strain (COS*) of ITO film is calculated using equation (Leterrier et al., 2004)

$$COS = COS^{*} - \varepsilon_i \tag{2.14}$$

where ε_i is the internal compressive strain [calculated from equation (2.8)].

The analysed samples were strained at room temperature with a constant crosshead speed of 0.05 and 0.5 mm/min.

- **Electro-mechanical buckling test.** A simply device designed in this project was used to investigate flexibility of ITO/polymer systems, by means of a controlled buckling

test. Special grips were prepared and attached to the Instron machine. They consist of small metal clamps, which are attached to PTFE rods by pins. The clamps are attached loosely enough to allow rotation around the pins. The copper wires are attached to the clamps and connected to the multi-meter FLUKE 45. The resistance changes are monitored by National Instruments LabVIEW software, as was used for electro-mechanical tensile test, described previously. The samples (4 x 25 mm) are placed between two clamps. The camera (PixeLINK microscopy camera) is placed in front of the device in order to record a buckling profile of the samples during the test. When the test runs the upper grip travels down and causes buckling of the sample in a direction perpendicular to the loaded axis. The samples can collapse to a radius of curvature below 1 mm. The advantage of our device over those described previously (Gorkhali et al., 2004; Koniger and Munstedt, 2008b) is that it allows bending without physical contact with the active ITO surface subjected to stresses. The developed device provides simple support for the sample's ends. Figure 2.12 shows the device with the buckled sample. From the recorded images the geometry of the samples is measured and the radius of bending curvature is calculated using equation (2.9). The critical onset radius (COr) is determined as 10% increment in resistance. The corresponding strain of ITO film is equal to (Gere and Timoshenko, 1999; Chen et al., 2001a)

$$\varepsilon = \frac{y}{r} \tag{2.15}$$

where y is the distance between the neutral axis of the composite and the top layer, and r is the radius of curvature.

It is assumed, that the neutral axis lies in the centre of the composite due to the far lower thickness of the films compared with the polymer substrates. Hence, the critical onset strain is calculated from the following equation (Chen et al., 2002)

$$\varepsilon_{\cos} = \frac{h_s + h_f}{2r} \tag{2.16}$$

where h_s and h_f are the thickness of the substrate and the film, respectively.

In the monotonic buckling test the samples were flexed in tension and compression side with the crosshead speed set at 2 mm/min. The samples were also loaded repeatedly in tension and compression at the fixed radius of curvature, 4 mm with the speed of 30 and 60 second/cycle. After buckling tests the surface of ITO films was observed using SEM and AFM microscopes.

- **Fragmentation test of ITO films** was conducted with a Miniature Materials Tester - Minimat (PL Thermal Sciences) attached to the table of the optical microscope Leitz Wetzlar model Epivert (10x magnification). A microscopy camera (PixeLINK) is also attached to the optical microscope in order to observe and record cracking of the thin films, *in situ*. The evolution of cracks of ITO films on polymer substrates is monitored as a function of applied uniaxial tensile strain. The resistance changes are monitored during the test using National Instruments LabVIEW software. The device is shown in Figure 2.13. The samples were strained with speed set at 0.1 mm/min. Crack density (CD) of ITO films, defined as the inverse of the average ITO fragment length $\langle l \rangle$ (Cairns et al., 2000a; Leterrier et al., 2004), is used to analyse cracked ITO films. The

average and standard deviation of crack density was calculated from five CD values obtained from different positions on the micrograph. In total, one hundred measurements of the ITO fragment lengths were performed using one micrograph linked to a certain strain level. Five samples were used to determine the average and standard deviation of the critical onset strain (COS) at which 10% increment in resistance occurred. The intrinsic crack onset strain (COS*) was calculated from equation (2.14).

Table 2.1 Polymer substrates investigated in the present study

Name of specimen	Measured thickness h (mm)	Structural data	Additional information
PEN Teonex Q65 FA	0.145	Semi-crystalline	Biaxially-oriented, heat-stabilised and pre-treated on one side to enhance adhesion
PET Melinex ST 505	0.137	Semi-crystalline	Biaxially-oriented, heat stabilised and pre-treated on both sides to enhance adhesion
PC Lexan 8010 MC	0.185	amorphous	----------

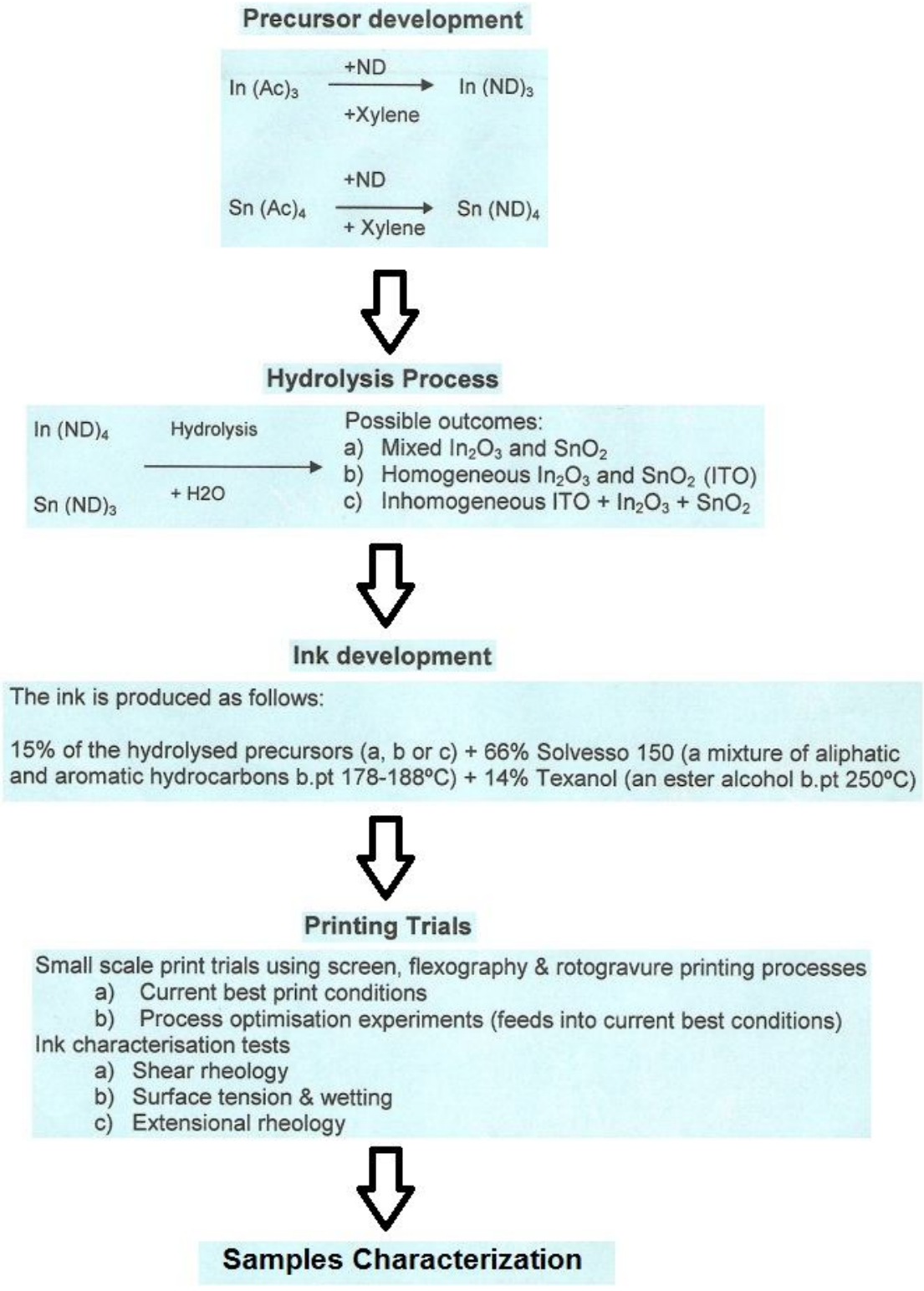

Figure 2.1 Flowchart showing ITO ink development in the SOLFLEX project.

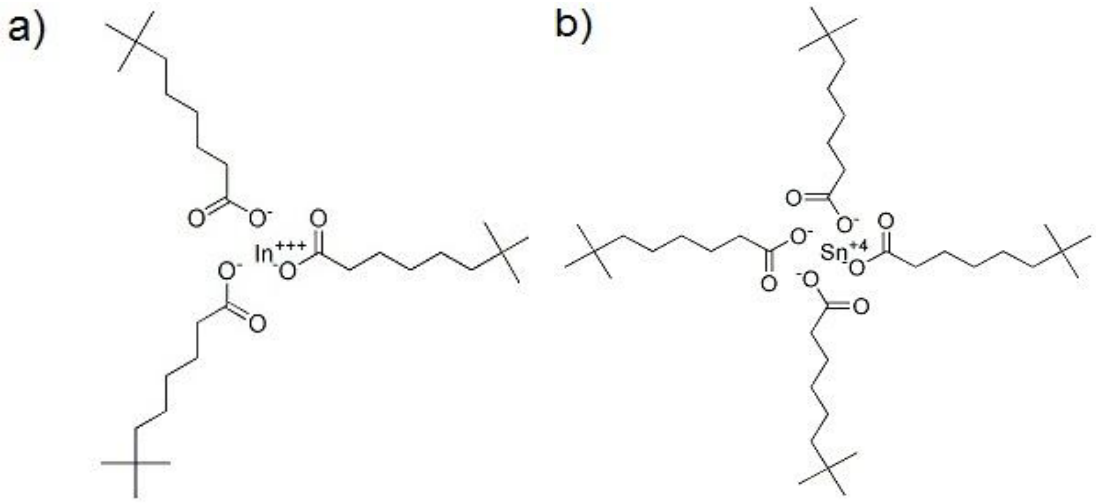

Figure 2.2 Chemical structure of a) indium neodecanoate $In(ND)_3$ ($C_{30}H_{57}O_6In$) and b) tin neodecanoate $Sn(ND)_4$ ($C_{40}H_{76}O_8Sn$). Adapted from **www.chemicalbook.com** .

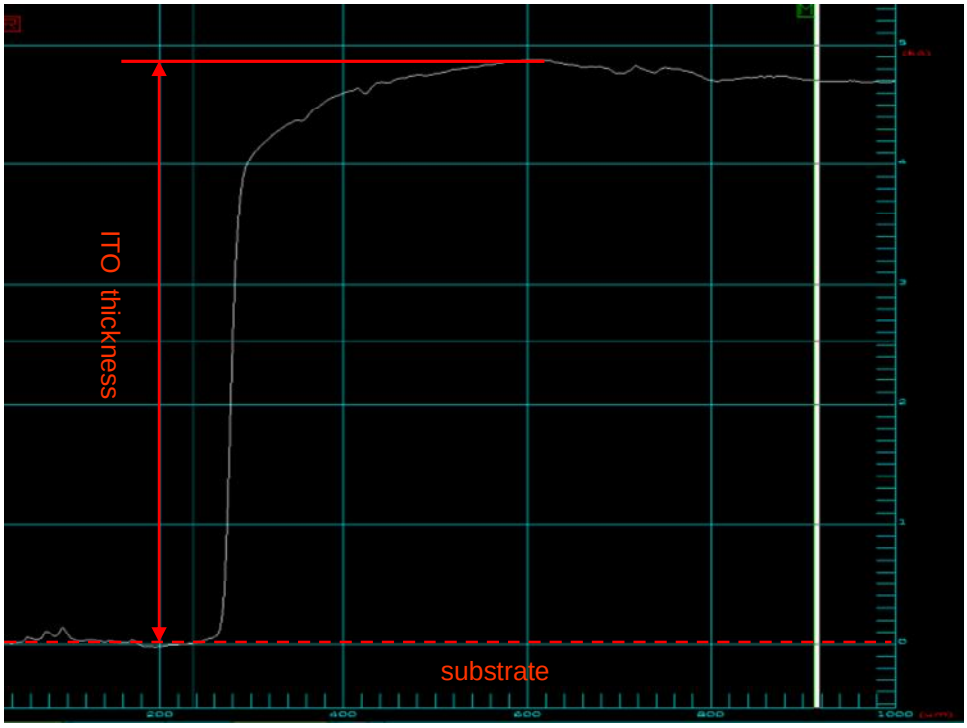

Figure 2.3 Thickness measurement by profilometer Dektak 3; ITO film on glass substrate deposited by PLD.

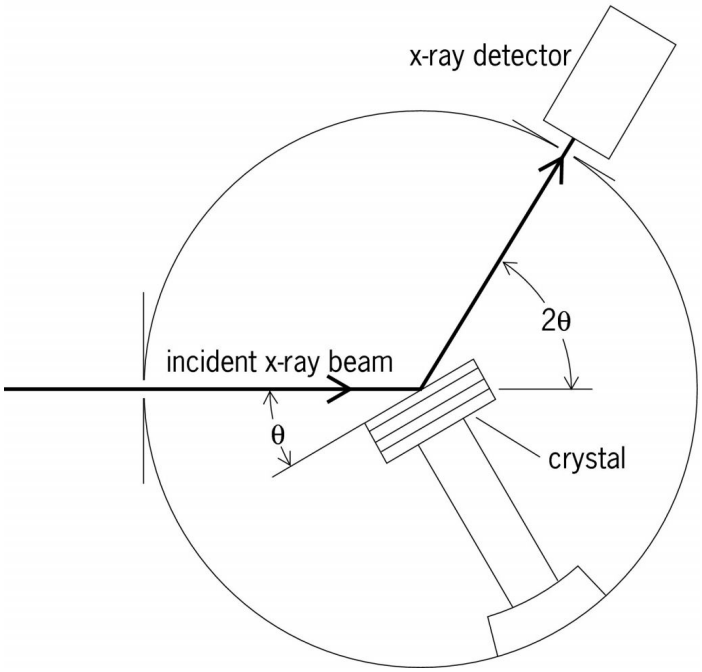

Figure 2.4 Schematic of a θ/2θ scan. Adapted from (McGraw-Hill_Concise_Encyclopedia_of_Physics, 2004).

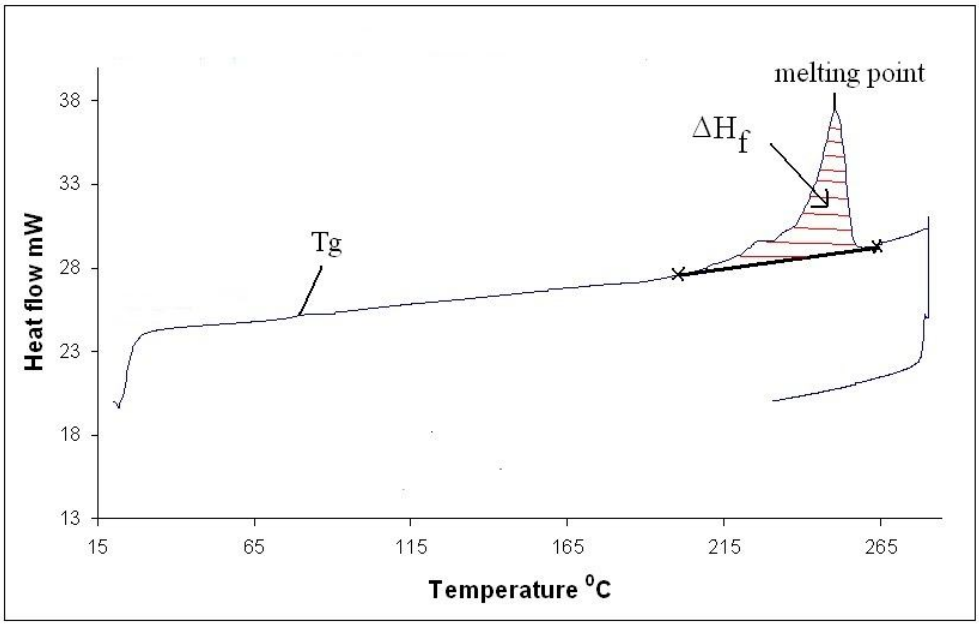

Figure 2.5 A typical DSC curve of semi-crystalline PET polymer.

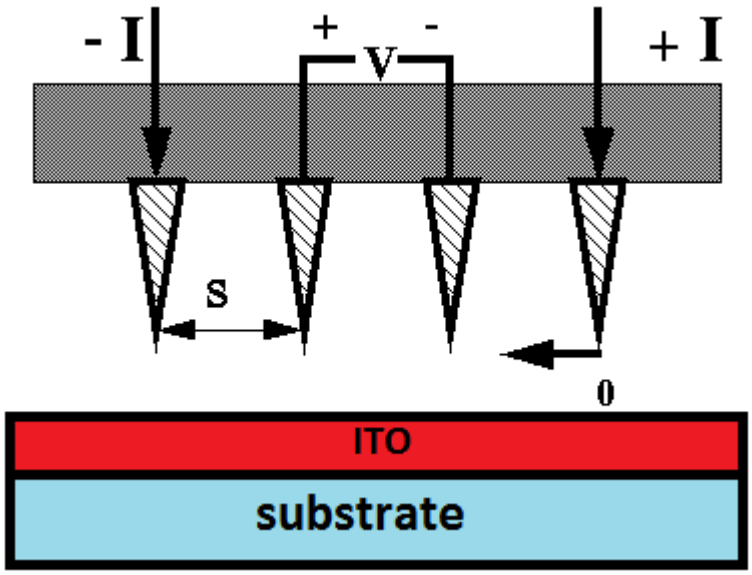

Figure 2.6 Schematic of four-point probe. Adapted from (Chan, 1994).

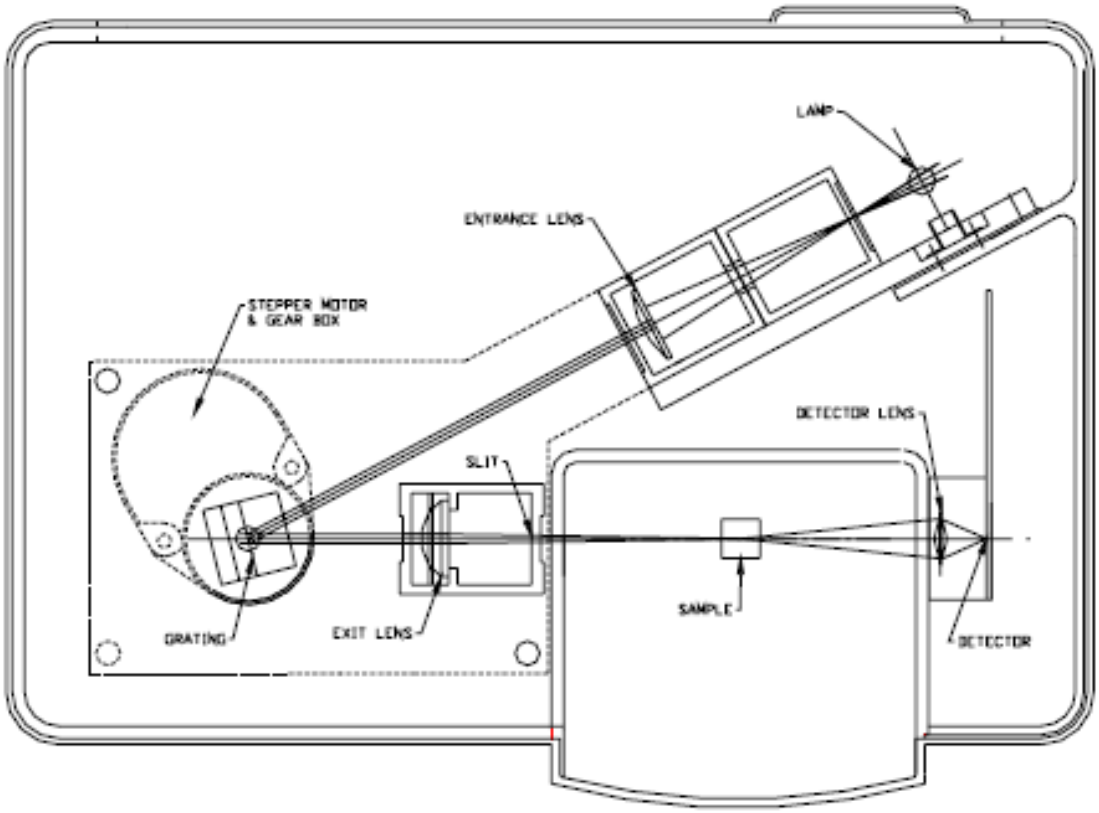

Figure 2.7 Schematic of optical system. Adapted from www.jenway.com.

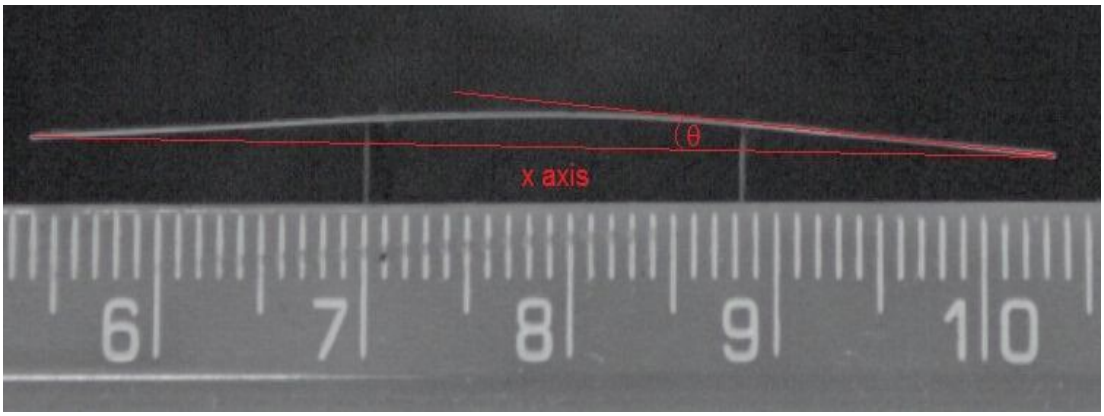

Figure 2.8 Bent sample after PLD deposition, ITO (100 nm) on PEN deposited at 150 ^{o}C.

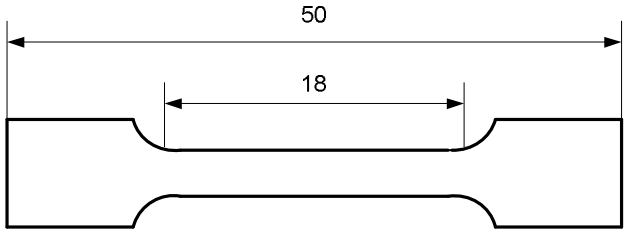

Figure 2.9 Standard dumb-bell sample.

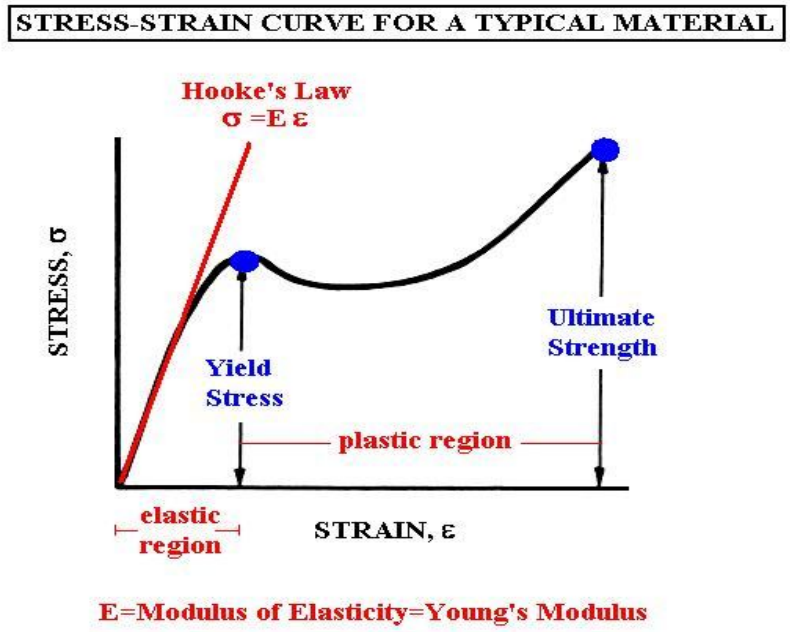

Figure 2.10 A typical stress-strain curve. Adapted from (http://www.mae.ufl.edu/~uhk/STRENGTH.html).

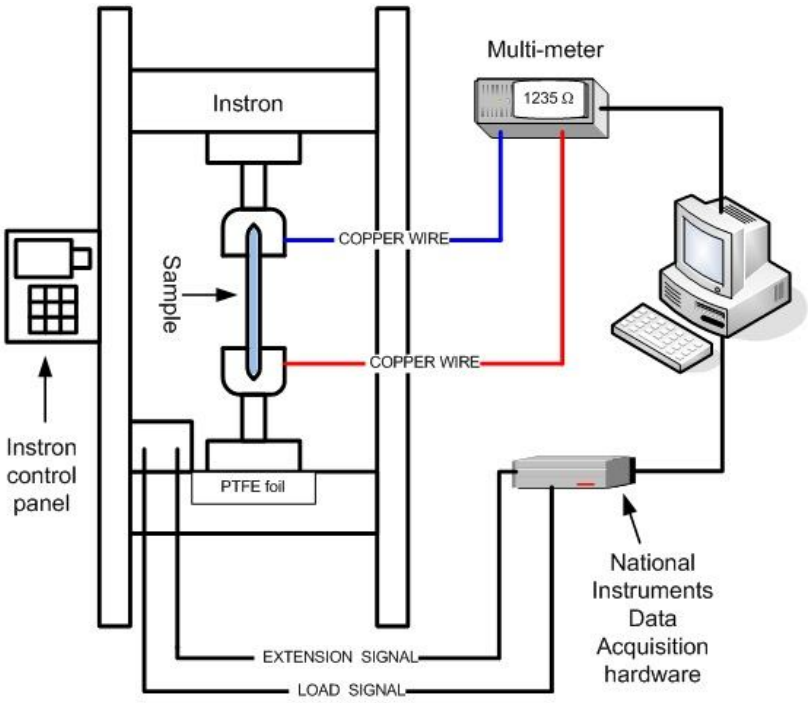

Figure 2.11 Schematic of electro-mechanical tensile testing system.

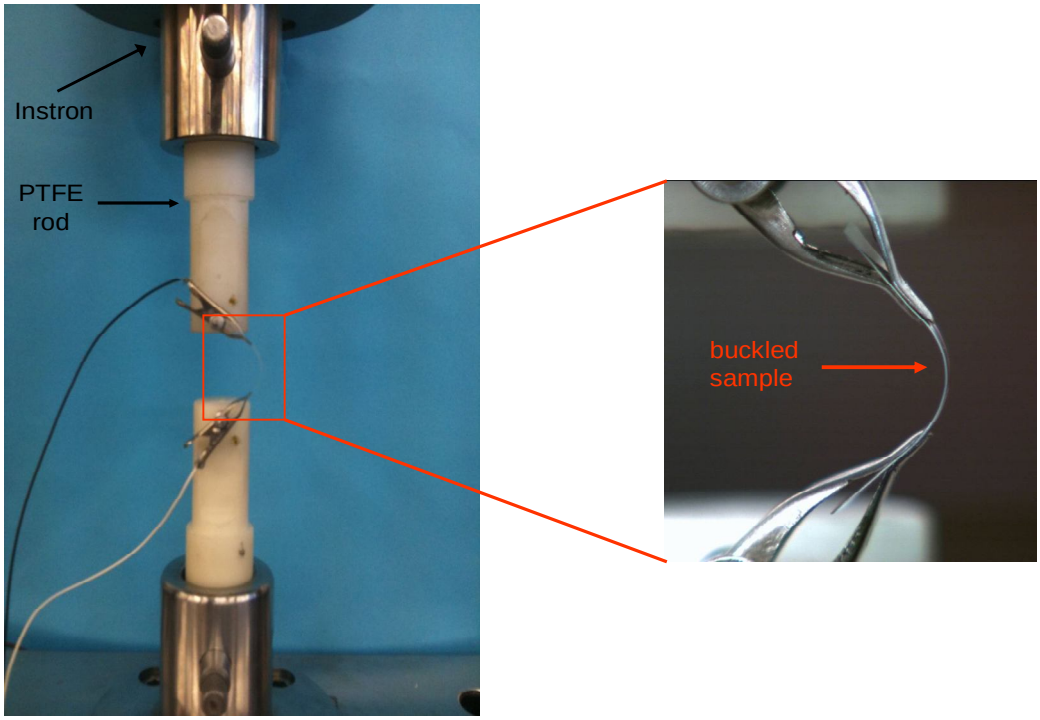

Figure 2.12 Bending equipment with buckled ITO/polymer sample.

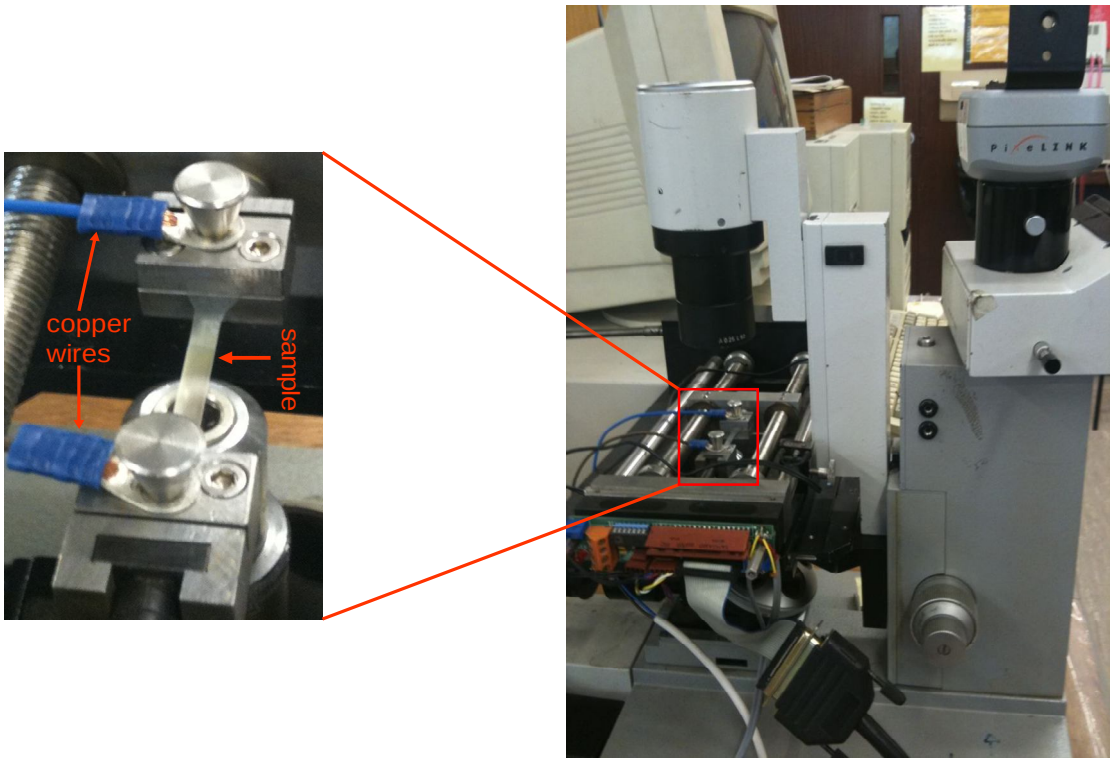

Figure 2.13 Miniature Materials Tester (Minimat) with loaded sample attached to optical microscope.

CHAPTER 3

3. POLYMER SUBSTRATES FOR TOUCH SCREENS AND FLEXIBLE DISPLAYS

3.1 Introduction

Thin flexible films can be produced from glass substrates but they are still brittle and cannot be used for flexible displays. Polymer substrates introduced to flexible displays instead of brittle glass substrates can make the devices robust, light-weight and potable, and hence satisfy consumer demand (Choi et al., 2008). To completely replace glass substrates, polymer films should offer their properties, such as optical transparency, mechanical and dimensional stability, a low coefficient of thermal expansion, barrier properties solvent and gas resistance and a smooth surface (Logothetidis, 2008; MacDonald et al., 2008). Flexible organic light emitting diodes (FOLEDs) have special requirements in the case of oxygen and water permeability due to the high susceptibility of their components to chemical reactions and degradation (Lewis, 2006). To increase the life-time of these devices, barrier solvent and gas resistance should be significantly improved (Lewis and Weaver, 2004b). No known polymers meet all these requirements, so displays have to consist of a multilayer composite structure (Lewis and Weaver, 2004b; MacDonald et al., 2005; Lewis, 2006). Polymer substrates are good materials for flexible displays as they possess good mechanical, optical and chemical properties (Choi et al., 2008). In addition, they are not expensive materials, and exhibit the ability for in-line mass production via roll-to-roll processing (R2R, Figure 1.2) (MacDonald et

al., 2005; Choi et al., 2008; Logothetidis, 2008; MacDonald et al., 2008). There are several polymer materials which can be considered in terms of glass transition temperature (T_g) and can be categorised into films that are semi-crystalline (e.g. PET and PEN), amorphous (e.g. PC) and solution-cast amorphous (Choi et al., 2008; MacDonald et al., 2008).

3.2 Polyesters – an introduction to PET and PEN

Polyesters are commonly used materials in a wide range of applications. They can exist in a few important forms such as laminating resins (as unsaturated thermosets), moulding compositions (thermoplastics), surface coating resins, fibres, films, rubbers and plasticisers (Brydson, 1999).

These polymers can be synthesised by polycondensation reactions of bifunctional or polyfunctional components with elimination of small molecules such as water, alcohol or hydrogen from the reaction environment (Brydson, 1999; Harper, 2002; Puszynski and Pielichowski, 2003; Braun et al., 2005)

$$nOH-R-OH+nHOOC-R-COOH \rightarrow H[O-R-O-CO-R'-CO]nOH+(2n-1)H_2O$$

Figure 3.1 Polycondensation reaction of polyesters (diols with dicarboxylic acids).

Polyesters can be recognised by a very characteristic for their family *ester* linkage (Harper, 2002; Braun et al., 2005)

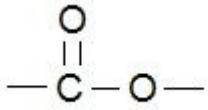

Figure 3.2 Characteristic *ester* linkage.

Polyethylene terephthalate (PET) was discovered by J. R. Whinfield and J. R. Dickson in 1941 (Brydson, 1999; MacDonald et al., 2002) and due to its rapid development through the last decades became a material in common usage. PET is produced in a large scale, e.g. in 2004 the production was 37 million tons in the global market (McClure, 2007). In comparison, the global market in 2008 for the most widely used plastic – polyethylene (all forms) was estimated to be 77 million tons (Malpass, 2010). The highest fraction of PET production belongs to fibres and the second to bottles for carbonated drinks. The remaining fraction is used for films and other special materials (MacDonald et al., 2002; McClure, 2007). Biaxially-oriented PET films were developed by both DuPont and ICI in the 1950's but the first commercially available films were introduced by DuPont in the late 1950's (MacDonald et al., 2003a)

Due to their great physical, chemical, thermal and electrical properties, PET films occupy a significant place in the current market including computer production, automotive industry, capacitors, flexible circuitry, photographic applications, labels and packaging (MacDonald et al., 2007; McClure, 2007).

Polyethylene nphthalate (PEN) was first patented by J. G. Cook, H. P. W. Huggill and A. R. Lowe in 1948 and the first PEN films were produced in the early 1970's (MacDonald et al., 2002). However, the production costs were much higher in comparison with PET films and

PEN films were found to be beneficial for high-value speciality applications (MacDonald et al., 2003b). Further development of PEN raw material was mainly focused on reduction of costs of production. As the result, in the early 1990's PEN films were fully commercialised (MacDonald et al., 2002; MacDonald et al., 2003a).

The differences in the chemical, physical, mechanical, and thermal properties between PET and PEN origin from their chemical structure, Figure 3.3. The phenyl group of PET is substituted by the naphthalene group of PEN (Douillard et al., 2003; MacDonald et al., 2003a). Introduction of the naphthalene group into the main chain of the polymer reduces its mobility, which has a significant effect on T_g (Brydson, 1999). It results in an increase of the T_g from 78 ^{o}C for PET to 120 ^{o}C for PEN (MacDonald et al., 2002). For amorphous solid polymers the glass transition temperature is the temperature at which a polymer softens and the motion of the segments of a polymer chains increases. Above the transition temperature the physical properties of an amorphous polymer are rubber-like (Birley et al., 1991; Brydson, 1999). For semi-crystalline polymers (e.g. PET and PEN) the T_g only applies to the amorphous regions which lie between the crystalline regions. There is also a crystalline melting point for the crystallites which corresponds to the 'ultimate' melting or softening point. The amorphous and semi-crystalline states of polymers are discussed in section 3.2.2.

The good properties of polyester films are the results of the manufacturing processes coupled with the properties of a base polymer. Biaxially-oriented and heat-stabilised PET and PEN polyester films exhibit high mechanical strength, good gas and solvent resistance, excellent dielectric properties and good dimensional stability (due to low shrinkage) (MacDonald et al., 2002; McClure, 2007; Logothetidis, 2008).

Biaxially-oriented PET films, e.g. DuPont Teijin Films™ Melinex® and PEN films, e.g. DuPont Teijin Films™ Teonex® are widely used as a substrates for vacuum coating techniques (MacDonald et al., 2002) and they became the main candidates for flexible displays applications (Choi et al., 2008; Logothetidis, 2008). Polycarbonate (PC) films, e.g. Lexan® developed by General Electric are also widely used as substrates for vacuum deposition techniques and will be described separately in section 3.3 due to their different properties compared with semi-crystalline PET and PEN films.

3.2.1 Biaxial orientation of PET and PEN films and dimensional stability

Polymer chains have the ability to become aligned during processing by *molecular orientation*. The polymer chains can be aligned in one or two directions (uniaxial or biaxial orientation, respectively) (Birley et al., 1991). During stretching of a polymer, the molecular chains are oriented or aligned parallel to the applied tensile force (Lukkassen and Meidell, 2007). The molecular orientation procedure makes the polymers anisotropic, which means that many properties are dependent on direction (Birley et al., 1991).

Orientation during processing has strong influence on both crystallite morphology and rates of crystallisation, and is so called *strain-induced crystallization*. It was first reported in 1930's for natural rubber, which was crystallising at room temperature during uniaxial orientation. Further studies revealed that nucleation process is induced by orientation and the nuclei are formed along the lines of flow (row nucleation) (Birley et al., 1991).

PET and PEN films are produced by extrusion of dried polyester resins achieved from a polycondensation reaction. Figure 3.4 shows processing of the polyester films. In the first stage the melted resin is extruded as a sheet and rapidly quenched to the amorphous state. To ensure good quality of the films, the resins prior to extrusion were filtered in order to remove impurities such as polymer gels and particulates, catalyst residues or pipe deposits (McClure, 2007).

Next the film is heated to 85 - 90 ^{o}C (McClure, 2007) and stretched in the machine direction (MD) by a factor of 3 - 4 (Brydson, 1999; McClure, 2007). The film becomes oriented and crystalline by 10 - 20%. The orientation process gives higher strength and modulus to the film. Then the film is clamped on its edges, heated above 100 ^{o}C and aligned in the transverse direction (TD) also by a factor of 3 - 4. After the biaxial orientation the film is 25 - 40% crystalline (McClure, 2007). Further detailed information about processing of polyester films can be found in *Encyclopedia of Polymer Science and Engineering* (Janocha et al., 1988).

After biaxial orientation the film can be heat stabilised at high temperature to improve dimensional stability. By this process the induced internal strain in the film is relaxed and the shrinkage of the film is minimised (MacDonald et al., 2002; McClure, 2007).

The heat-stabilization process increases the upper operating temperature of the polymer films, by means of reduced a coefficient of thermal expansion (CTE) above the glass transition temperature. The low CTE of polymer films is crucial to match the CTE of inorganic coatings, and hence reduce a thermal mismatch (MacDonald et al., 2004). It is of significant importance for vacuum-deposited thin films, such as indium tin oxide (ITO) or barrier

coatings, at elevated temperatures (MacDonald et al., 2002). A difference in the CTE between bonded elements induces a stress in a deposited thin layers (Freund and Suresh, 2003), which leads to cracking under thermal cycling during device fabrication (Choi et al., 2008) and has an influence on a final performance of flexible displays. More details about the origins of stresses in the thin film can be found in section 6.2 of chapter 6.

Bauer (1997) investigated the effect of degree of stretching (2.5 x 2.5, 3.0 x 3.0 and 3.5 x 3.5) and heat-setting temperatures (120, 150 and 180 ^{o}C) on density, shrinkage and oxygen permeability of biaxially-oriented PET films modified with naphthalate as copolymers and blends. He observed that with increasing degree of stretching and heat-set temperature the density of all investigated films increased, and hence crystallinity also increased. At high heat-set temperature the density was observed to be the same for all samples, independent of the degree of stretching. He also showed that with increasing degree of stretching the shrinkage increases. The low shrinkage (< 2%) was observed for all samples at the temperature of 85 ^{o}C. The naphthalate content in PET films reduced significantly the shrinkage and oxygen permeability with respect to unmodified PET films. In addition, the oxygen barrier increased on increasing the degree of stretching and heat-set temperature.

Schoukens *et al.* (2003) investigated shrinkage behaviour and structural changes in biaxially-oriented PEN films and bottles as a function of temperature and time of heat-setting. They reported that the start temperature of shrinkage is directly proportional to the heat-set temperature. This was contrary to the case for PET, for which the start temperature of shrinkage was around the glass transition temperature in all cases. They found, that above the heat setting temperature of 220 ^{o}C and with the time of heat-treatment between 30 - 60 s, the

shrinkage of 500 μm thick film is less than 1% due to variations of structural changes in the polymer. During the drawing process two types of rigid amorphous phases are induced. The one rigid amorphous phase is more temperature-stable than the other one and the heat-setting at high temperatures transforms the low temperature stable fase into the high temperature stable phase. They finally concluded, that despite many similarities between PEN and PET, the shrinkage behaviour is completely different and the presence of naphthalene rings in PEN plays a crucial role in this behaviour.

McClure (2007) described in his review how the manufacturing process influences many important properties of PET films subjected to vacuum deposition, such as thermal properties, chemical and mechanical properties. He also pointed, like other authors (Bauer, 1997; Schoukens et al., 2003), that the shrinkage depends on temperature and treatment time, and that the heat-setting process has strong influence on the amount of shrinkage. The shrinkage in the machine direction (MD) is higher than the shrinkage in the transverse direction (TD) and the heat-stabilised PET films exhibit lower shrinkage compared with untreated films, as it is shown in Figure 3.5.

Kim *et al.* (1998) investigated the effect of composition on orientation, optical and mechanical properties of biaxially-stretched PEN films and their blends. They observed, that optical anisotropy occurs when the film is biaxially-stretched. The refractive index in the normal direction decreases with increasing areal expansion ratio (the product of stretch ratios in both directions, MD x TD). They pointed out that it is due to conformational changes in the naphthalene rings, which become aligned parallel to the sample surface. They also found, that Young's modulus depends on the measured directions with respect to the film plane. They concluded that the modulus increases in all directions as the stretching ratio in TD increases.

3.2.2 Crystallinity of PET and PEN

In the solid state the morphology of a polymer depends on its chemical structure and manufacturing processes. If the molecular chains are unordered and exhibit entangled conformation (Figure 3.6), the polymer is amorphous. When some regions of the molecular chains exhibit regularity and orientation, they can be packed tightly into a crystalline structure and the polymer becomes semi-crystalline (Harper, 2002). The semi-crystalline structure consists of both ordered crystals (lamellar crystallites and/or spherulites, Figures 3.7 and 3.8, respectively) and amorphous regions (Martinez-Vega et al., 2001). The morphology of the semi-crystalline polymers can be controlled by the cooling rate from the liquid state, annealing and orientation (Hardy et al., 2001; , 2003; Strobl, 2007), as discussed in the previous section.

PET crystallizes in triclinic form (one chain per unit cell) (Bower, 2002) and the crystallographic data can be found in the literature (Lawton and Ringwald, 1989; Bower, 2002). PEN crystallizes in two triclinic forms: α and β. The β form can be only achieved in special conditions involving rapid quenching and annealing. Therefore, the α form, which consists of one molecular chain per unit cell is commonly observed to occur (Hardy et al., 2001; , 2003). The crystallographic data of the PEN unit cell can be found elsewhere (Buchner et al., 1989; Douillard et al., 2003; Krutphun and Supaphol, 2005).

Many of the physical properties of semi-crystalline polymers are determined by the degree of crystallinity and orientation of chain crystals (Harper, 2002). The degree of crystallinity can be evaluated by commonly-used methods, such as density measurements, differential scanning calorimetry (DSC) and X-ray diffraction measurements (Bower, 2002). DSC is the

most utilised method for determination of fractional crystallinity of polymers and it allows to measurement of the change in enthalpy (heat of fusion) ΔH_f due to melting and crystallisation of the sample (Bower, 2002). For this method the heat of fusion of the fully crystalline polymer must be known. Since the polymer cannot fully crystallize it can be found by using an extrapolation method. If the heat of fusion of 100% crystalline polymer is known, the degree of crystallinity follows (Martinez-Vega et al., 2001; Harper, 2002; Hu et al., 2002; Strobl, 2007)

$$X_c = \frac{\Delta H_f - \Delta H_c}{\Delta H_f^0} \tag{3.1}$$

where ΔH_f is the heat of fusion of the semi-crystalline sample, ΔH_c is the enthalpy of cold crystallization and ΔH_f^o is the heat of fusion of 100% crystalline polymer. ΔH_f for PET and PEN and other important parameters, such as glass transition temperature, melting temperature and coefficient of thermal expansion are presented in Table 3.1.

The orientation of chain crystals enhances the elastic moduli and strength of polymers, and hence is highly desirable (Fischer, 2009). The Young's modulus of the sample is strongly related to the conformation of the polymer chains and the semi-crystalline nature of the polymer sample. Nakamae *et al.* (1993; , 1995) investigated the elastic modulus of the crystalline phase of PEN films in a direction parallel to the polymer chains. They show that the elastic modulus of the crystalline regions of biaxially-stretched PEN films is temperature independent in the range from 22 to 228 ^oC, hence mechanical deformation of the polymer chains did not occur. However, the Young's modulus of the sample decreased linearly with

increasing temperature suggesting that it is may be due to decrease of the elastic modulus in the amorphous region. They concluded that the elastic modulus of the crystalline phase defines the maximum value of the Young's modulus of the polymer sample and is strongly related to its mechanical properties.

3.2.3 Optical properties of PET and PEN

Optical clarity requirements of base substrates are dependent on the type of electronic devices. For bottom-emissive displays polymer films should possess high clarity of > 85% in the visible range with a low haze of < 0.7%. PET and PEN films meet these requirements and can be successfully utilised for these kinds of displays. In the case of top-emissive displays, the clarity is not required, which gives freedom in selection of the base substrates. Hence, both metal and plastic films can be used (MacDonald et al., 2005).

Biaxially-oriented PET and PEN films exhibit optical anisotropy (Kim et al., 1998) and cannot be used for liquid crystal displays (LCDs) due to changes in polarisation state in these devices (MacDonald et al., 2005). Optical properties of the polymer are strongly related to its morphology and structural arrangement of the molecular chains (Logothetidis, 2008) and these were studied extensively for PET and PEN films by Laskarakis and Logothetidis (2006).

3.2.4 Barrier properties and chemical resistance of PET and PEN

Polymer substrates are porous and exhibit high water permeability > 1 $g/m^2/day$ (Greener et al., 2007). The commonly used PET and PEN polyester films exhibit the highest oxygen transmission rate (OTR) 10^{-1}–10^{2} $cm^3/m^2/day$ and water vapour transmission rate (WVTR) $g/m^2/day$ (Logothetidis, 2008), e.g. 0.1 mm-thick PEN film exhibits a WVTR of 2 $g/m^2/day$ (Heya et al., 2008), which is not sufficient for flexible OLED or LCD electronic devices. To ensure long-lived OLED devices the polymers must poses barrier properties, that reduce diffusion rate to less than 10^{-6} $g/m^2/day$ and 10^{-5} $cm^3/m^2/day$ for moisture and oxygen, respectively (Lewis and Weaver, 2004b; Yan et al., 2005).

In order to meet permeability requirements of OLED devices, polymer films need to be coated by inorganic or hybrid inorganic/organic ultra-high barrier (UHB) layers (Chwang et al., 2005; Lewis, 2006). Hybrid Al_2O_3/polyacrylate multi stack barrier layers (Barix™ system) were prepared in a vacuum system via roll-to-roll process (Burrows et al., 2001) showing promising results in barrier coating technology for moisture sensitive devices. The Barix™ substrate from Vitex company claimed low WVTR of ~10^{-6} $g/m^2/day$ measured using the calcium test (Nisato et al., 2003).

Polymer substrates must also possess high resistance to solvents and chemicals that are used in organic electronic device fabrication steps (e.g. OLEDs). A typical list of aggressive media which the polymer must withstand includes methanol, isopropanol, acetone, tetrahydrofuran, n-methylpyrrolidone, ethylacetate, sulphuric acid, glacial acetic acid, hydrogen peroxide, sodium hydroxide (Yan et al., 2005) and acrylic acid present in pressure-sensitive adhesives used in device stacks (Sierros et al., 2009). The engineered PEN films (e.g. Teonex® brand)

have excellent resistance to many acids and organic solvents, which makes them a great candidate to withstand the production processes of flexible OLED (FOLED) devices.

3.2.5 Surface quality of PET and PEN films

Good surface properties of polymer substrates, such as smoothness and cleanliness are of high importance for display applications to ensure integrity with subsequent barrier and conductive layers (MacDonald et al., 2003b; Choi et al., 2008). A smooth surface of the polyester film can be achieved by controlling the recipe and production (MacDonald et al., 2003b) and also by using planarization coatings, which provide both surface smoothness and hardness to increase scratch resistance (MacDonald et al., 2008). The surface roughness of the polymer film, which yields dark spots after the OLED fabrication process can be modified by the application of a multilayer structure (Lee et al., 2008). Burrows *et al.* (2001) deposited a polyacrylate layer on the PET film and reported that non-uniformity of the film surface can be significantly reduced. The high of spikes was reduced from 150 $\overset{0}{A}$ to a value below 10 $\overset{0}{A}$, as Figure 3.9 shows. In addition, the fact that deposition of barrier films is a vacuum-based process, ensures that the product exhibits the highest level of cleanliness.

3.2.6 Mechanical properties of PET and PEN films

Once again, the mechanical properties of PET and PEN polyester films depend on chemical structure, degree of crystallinity and the orientation process, as described in the previous sections.

For roll-to-roll (R2R) processing the mechanical properties of the film should be carefully considered (Choi et al., 2008). During R2R processing a winding tension is present and a film with low modulus will deform, especially at elevated temperatures (MacDonald et al., 2008).

At room temperature PEN is slightly stronger and 25% stiffer than PET, however at elevated temperatures, e.g. in the region between 120 – 160 ^{o}C, PEN exhibits 3 – 4 times higher stiffness and almost twice as high Young's modulus than that of PET (MacDonald et al., 2002; , 2008). Mechanical properties of PET and PEN polymer substrates are presented in Table 3.2.

3.2.7 Comparison of key properties of PET and PEN films

Key properties of engineered polyester substrates for flexible electronics are highlighted on the star diagram, as Figure 3.10 shows. PEN exhibits greater thermal and mechanical properties than that of PET and can be chosen for applications where high demands of substrates are required.

3.3 Polycarbonate (PC) films for flexible displays

PC was discovered by Einhorn in 1898 and it was a cross-linked insoluble polymer (Brydson, 1999). The first linear thermoplastic PC was made in 1953 and its commercial production started in 1960 (Bower, 2002). On an industrial scale, the aromatic polycarbonates are achieved by a polycondensation reaction between bisphenol A (BPA) and phosgene (Puszynski and Pielichowski, 2003; Braun et al., 2005). Figure 3.11 shows the chemical structure of PC polymer. Due to its angled chain structure and limited rotation of aromatic rings, PC exhibits a high glass transition temperature and is often in an amorphous state. Moreover, polycarbonates exhibit high transparency between 85 – 90% (Lukkassen and Meidell, 2007), good mechanical properties (Braun et al., 2005), heat resistance, self-extinguishing and good electrical insulation characteristics (Brydson, 1999).

In the market PC is known as Lexan and Makrolon, which are the products of General Electric and Bayer, respectively (Brydson, 1999).

Amorphous PCs find use in nonbreakable windshields, housings for electric and electronic, and as substrate in optical storage devices, e.g. CD and DVD (Braun et al., 2005). Crystalline form of PC can be achieved, but due to its reluctance to crystallize, the process requires annealing at 180 ^{o}C for several days (Harper, 2002). Hence, thermally crystallized PC is not observed in practice (Rudder et al., 2006).

Polycarbonates exhibit excellent dimensional stability at elevated temperatures (Rudder et al., 2006). PCs can withstand high operating temperatures holding their rigidity and toughness up to 140 ^{o}C. However, they possess poor resistance to UV light and solvents (e.g. aromatic

solvents: benzene, toluene and xylene (Harper, 2002)), limited scratch resistance, and are susceptible to crazing under strain (Brydson, 1999). Table 3.3 shows thermal and mechanical properties of PC. PC is ideal replacement for glass (Rudder et al., 2006) and it finds use as a substrate for flexible displays (Choi et al., 2008).

A new polycarbonate substrate – high-temperature PC – for flexible and flat-panel displays was recently developed using the solvent casting method from dichloromethane solution (Hanada et al., 2010). The high-temperature PC exhibits lower birefringence than the conventional PC film based on bisphenol, and hence can be used in LCDs. Moreover, it possess high light transmittance, over 90% in the visible spectrum. High-temperature PC shows great dimensional stability at elevated temperatures. Low shrinkage of 0.01% at 180 ^{o}C has been reported. In addition, at the same temperature the sample exhibited a Young's modulus of 2.8 GPa (Hanada et al., 2010). Great mechanical properties at elevated temperatures are due to an extended glass transition temperature from 145 (Brydson, 1999) for the conventional PC to 215 ^{o}C (Hanada et al., 2010) for the high-temperature PC.

Furthermore, the high-temperature PC film exhibits a water vapour permeation rate of 0.05 g/m^2/day and high surface smoothness with the root mean square roughness equal to 0.5 nm (Hanada et al., 2010).

3.4 Other polymer candidates for flexible displays

Besides the commonly-used PET, PEN and PC films other polymers, such as polyether-ether-ketone (PEEK), polyethersulphone (PES), polyarylate (PAR), polycyclic olefin (PCO), polynorbonene (PNB), polyimide (PI) (MacDonald et al., 2005; Choi et al., 2008) or paper (Logothetidis, 2008) are also considered as candidates for flexible electronic devices. Detailed description of these polymers is not within the scope of this work.

3.5 Results and discussion

3.5.1 T_g, T_m and degree of crystallinity

Figure 3.12 shows DSC thermogram of PET film. The glass transition temperature and melting temperature occur at a temperature of 78 and 251 ^oC, respectively. These results are in good agreement with the data reported elsewhere (Lawton and Ringwald, 1989; MacDonald et al., 2003b). Before final melting, pre melting point is observed at the temperature of 225 ^oC. It is due to small or imperfect crystallites (Nielsen, 1974b) created during orientation process and/or heat-setting.

PEN, Figure 3.13, exhibits T_g and T_m at the temperature of 121 and 259 ^oC, respectively. The results published previously by McDonald et al. for T_g (2003b) and T_m (2008) values are comparable with the results in this work. Similarly to the PET sample, PEN also exhibits pre melting point, which takes place at the temperature of 231 ^oC. PEN film shows higher T_g and

T_m than PET due to substitution of the phenyl ring of PET by the naphthalene ring of PEN (Brydson, 1999; MacDonald et al., 2002).

In addition, the area under the melting peak represents heat of fusion, ΔH_f, which is equal to 40.1 and 35.5 J/g and gives a degree of crystallinity of 28.6 and 34.4% for PET and PEN, respectively. Table 3.6 shows the degree of crystallinity for PET and PEN films, and summarises their thermal properties. It is clear to see that the degree of crystallinity of PEN film is almost 6% higher than that of PET. It affects mechanical properties according to the rule, that the higher the degree of crystallinity the higher the elastic modulus (Bower, 2002), which will be discussed in the next section.

In case of PC Lexan 8010 MC film, the T_g equal to 153 ^oC was observed, which is in good agreement with the commonly cited value (Brydson, 1999; Arrese-Igor et al., 2006). A melting point was not observed, clearly indicating that the polymer is amorphous.

3.5.2 Mechanical properties – tensile test

To compare mechanical properties of polymer samples the elastic modulus was extracted from the initial slope of stress-strain curves. For the tensile test the dumb–bell polymer samples were cut from an A4 sheet at the different angles 0, 45 and 90 ^{o} with respect to x–axis, as Figure 3.14 shows. The test was performed at a constant strain rate of 0.5 and 1 mm/min at a temperature of 24 ^oC.

Figure 3.15 shows the stress-strain behaviour of a bare polymer substrates. It is clear to see, that the PEN exhibits the highest resistance to deformation with yield strength equal to ~ 112 MPa. The PET shows the second highest yield strength of ~ 85.0 MPa. The lowest tensile strength belongs to the PC, that exhibits the yield strength equal to ~ 58.0 MPa. The stress-strain behaviour of the polymer substrates is typical for hard ductile materials. However, the curves of PEN and PET substrates represent materials with uniform extension. In case of the PC film, the curve has a clear yield point and is typical of the material which cold-draws with necking formation within a limited area of the specimen.

Figure 3.16 shows the Young's modulus for polymer samples as a function of angle with respect to A4 sheet x-axis and Table 3.4 summarises the results. The Young's modulus for PEN equal to ~ 3.30 and ~ 3.40 GPa at the angles of 0 and 90^{o}, respectively, is almost the same. A slightly lower modulus, ~ 2.70 GPa, is observed at the angle of 45^{o}.

PET exhibits the highest modulus of ~ 3.20 GPa at an angle of 90^{o}. Significantly lower elastic modulus values are observed at the angles of 0 and 45^{o} and equal to ~ 2.40 and ~ 2.40 GPa, respectively.

PC does not show any anisotropy in mechanical properties. The same elastic modulus equal to ~ 1.2 GPa, is observed at all angles investigated.

The highest mean Young's modulus value shows PEN equal to 3.12 ± 0.35 GPa. PET shows the second highest modulus value of 2.65 ± 0.48 GPa and the lowest modulus value of 1.25 ± 0.034 belongs to PC. The result obtained in this work for PC polymer film is

comparable to that reported previously (Kong, 2002). In addition, the lower and constant elastic modulus of PC film compared with PET and PEN films is related to its amorphous nature and a lack of orientation (isotropic properties).

The differences in Young's modulus of PET and PEN samples, which were cut at different angles with respect to A4 sheet x-axis, are due to anisotropic properties introduced during biaxial orientation of the molecular chains (Birley et al., 1991). Moreover, crystallinity induced during orientation process defines the highest value of the Young's modulus of the polymer samples (Nakamae et al., 1995). Elastic modulus increases with an increase in the degree of crystallinity, because the crystalline regions act as cross-links between molecular chains and hence limit deformation of amorphous regions. The lower elastic modulus observed for intermediate angle of 45^{o} of PEN film, might be related to the bimodal orientation of the polymer chains (Kim et al., 1998). The lowest elastic modulus was also reported for the low-density polyethylene sheets cut at 45^{o} to the stretch direction by Raumann and Saunders (1961). An AFM image obtained in this work for biaxially-oriented PET film, Figure 3.21, supports the above observations and explains the lower Young's modulus at 45^{o} to stretch directions (MD and TD), which will be discussed in section 3.5.4.

Samples tested at a crosshead speed of 0.5 mm/min have shown almost the same results to those tested at 1 mm/min and for that reason are not presented in this work. The PET and PEN polyester films shown the highest Young's modulus at the angle of 90^{o}, which means that the polymer chains at that angle are aligned parallel to the applied tensile force (Bower, 2002). That angle was chosen to cut the substrates for further experiments to maximise

mechanical compatibility between the flexible polymer substrates and the brittle ITO films. (Electro-mechanical properties of the ITO/polymer systems will be described in chapter 6.)

Table 3.5 shows rigidity of the polymer films. In contrast to the Young's modulus, the bending stiffness of the sample defined by its rigidity is thickness dependent and gives additional information about how the stiffness changes with the thickness (MacDonald et al., 2004). It is clear to see, that the PEN substrates shows the highest rigidity equal to 13.3 x 10^{-4} Nm. The rigidity of the PC substrate, equal to 11.0 x 10^{-4} Nm, is similar to that of the PET substrate, 11.5 x 10^{-4} Nm. The Young's modulus of the semi-crystalline PET film is almost three times higher (Table 3.5) than that of the amorphous PC film, hence a higher rigidity should be expected. However, a higher thickness of the PC film increases its rigidity. As a result, it is resistant to distortion at similar level to the PET film.

3.5.3 Optical properties

Figure 3.17 shows transparency spectra of semi-crystalline PET, PEN and amorphous PC in the range from 350 to 1000 nm. All polymer films show high and almost the same transparency $\geq$ 88% in the visible range (400 - 800 nm). The observed ripples in transmission spectra of PEN substrate may arise from the planerize layer (usually formed by an acrylate polymer) (Sim et al., 2009). The results, summarised in Table 3.7, meet the requirements of polymer substrates for bottom-emissive displays (MacDonald et al., 2005). High transparency may indicate that the density fluctuations in polymer matrix are minimised, even for semi-crystalline PET and PET films, and hence the light scattering is low (Birley et al., 1991).

3.5.4 SEM and AFM surface investigation

The surface quality of polymer films was investigated by SEM and tapping-mode AFM techniques to understand the role it plays in terms of adhesion and crack initiation during mechanical tests of ITO/polymer systems. The size of the investigated area by AFM technique is 2.5 x 2.5 μm. Two sides of polymer films were examined. Both sides (side A and side B) of PET were pre-treated by adhesion promotion coating during manufacturing. PEN was one side coated - side A. Side B was uncoated. In case of PC both sides were uncoated.

Figure 3.18 presents SEM images of the surface morphology of PET (coated side A). It shows a smooth surface of the polymer film. However, impurities are also clear to see on image (a). Random-like white features are dispersed on the polymer surface. The size of the impurities is around 1 μm or below, as image (b) clearly shows. They may come from the production processes and/or subsequent handling.

PEN and PC show almost identical dispersed features on the surface to that of the PET substrate, as Figure 3.19 (a) and (b), and Figure 3.20 (a) and (b) show, respectively. However, the cleanest surface is observed for the PC film, which exhibits the lowest concentration of impurities. It may be due to the additional plastic-foil cover used on both sides of the PC films to protect them from scratches and impurities.

Figure 3.21 shows the surface topography of coated side A of the PET film. The mean roughness of the film is relatively small and equal to 2.72 ± 0.25 nm. Side B, as Figure 3.22 shows, exhibits similar mean roughness (3.10 ± 1.04 nm) to that of side A, which is a result of planarization processing on both sides of the polymer film. Elongated columnar features are

observed on both sides of the film. In addition, their characteristic alignment in x and y direction forming the angle of 90^{o}, as white arrows indicate in Figure 3.21, is clear to see, which may indicate oriented crystallites in the drawing directions. The lamella-like features are also noticeable, as a red circle indicates (Figure 3.21), suggest that the crystallites protrude above the surface. Elongated features were previously observed for biaxially-oriented PET Melinex 506 (Sierros and Kukureka, 2007) and PET Mylar D and PET Melinex (Beake et al., 2001). Moreover, Beake *at al*. (2001) concluded, based on their observations, that they may represent oriented crystallites. However, they did not observe such a pronounced orientation in transverse and longitudinal directions compared with the results obtained in this work.

Figure 3.23 presents coated side A of the PEN. Small grains, thought to be crystallites, tightly packed to each other are observed and the mean roughness of the film is equal to 1.43 ± 0.20 nm. Two times lower root mean square (RMS) roughness was reported for the PEN Teonex Q65 using white light interferometry technique (MacDonald et al., 2004). Uncoated side B exhibits different topography and much higher roughness, of 10.7 ± 4.6 nm than coated side A, as Figure 3.24 shows. Islands of biaxially-oriented crystallites can be also seen.

Table 3.8 summarises the roughness of the polymer films. In comparison with PET and PEN films, PC exhibits the lowest surface roughness of 0.77 ± 0.11 nm on both sides, as Figure 3.25 shows. It is an artefact of having an amorphous nature, which makes the surface very smooth. In other words, in the semi-crystalline state (e.g. semi-crystalline PET or PEN films) the crystallites protrude above the surface and hence make it rougher than that in an amorphous state (Dinelli et al., 2000). Very small lumps on the PC film's surface are clear to

see, though. They might be additives (e.g. fillers or lubricants) used during the polymer processing. Slightly lower surface roughness, 0.5 nm, measured by tapping-mode AFM was observed for the high-temperature PC film (Hanada et al., 2010). However, in their report, the small lumps were not observed, which may be related to a different production method of the high-temperature PC films.

3.6 Conclusions

The results show that the Young's modulus is sensitive to the orientation distribution in the plane of biaxially-oriented PET and PEN films. PEN Teonex Q65 FA exhibited the highest Young' modulus from all the samples investigated.

All samples investigated shown high transparency in the visible range and very low surface roughness, which makes them very good candidates for flexible flat–panel displays.

The degree of crystallinity up to ~ 40% of PET Melinex ST 505 and PEN Teonex Q65 FA did not influence the transparency, however, the protruded crystallites over the surface are shown to have an influence on the surface roughness.

Table 3.1 Thermal properties of PET and PEN substrates

Thermal properties	PET	PEN
Glass transition temperature, Tg (^{o}C)	67-81[a], 78[b]	120[b], 124[c]
Melting temperature, Tm (^{o}C)	250-265[a], 255[d]	263[d], 270-273[c]
Heat of fusion, ΔH_f^0 (J/g)	96[e],140[f]	103.4[g, h], 190[h]
Coefficient of thermal expansion (up to 150 ^{o}C), CTE (ppm/^{o}C)	20-25[i]	18-20 [i], 23[j]

a: (Lawton and Ringwald, 1989), b: (MacDonald et al., 2003b), c: (Brydson, 1999), d: (MacDonald et al., 2008), e: (Kong and Hay, 2002), f: (Zumailan et al., 2002), g: (Schoukens et al., 2003), h: (Douillard et al., 2003), i: (MacDonald et al., 2008) and j: (MacDonald et al., 2005).

Table 3.2 Mechanical properties of PET and PEN polymers.

Property	PET[a,b]	PEN[c,d]
Young's modulus, E (GPa)	4.5, 4.9 at 25 ^{o}C 1.4 at 120 ^{o}C	5.0 at 20 ^{o}C 3.0 at 150 ^{o}C
Poisson's ratio, ν	0.37 in TD 0.44 in MD	0.35 in TD

a: (McClure, 2007), b: (Lawton and Ringwald, 1989), c: (MacDonald, 2006) and d: (Ma and Bhushan, 2003)

Table 3.3 Thermal and mechanical properties of PC

Property	PC[a, b]
Glass transition temperature, Tg (^{o}C)	145
Coefficient of thermal expansion, CTE (ppm/^{o}C)	70
Elongation at yield, (%)	6-7
Young's modulus, E (GPa)	2.4
Poisson's ratio, ν	0.4

a: (Brydson, 1999), b: (Siviour et al., 2005)

Table 3.4 Young's modulus related to different angle with respect to x-axis of polymer sheet.

Substrate	Young's modulus, E (GPa), related to different angle		
	0^{o}	45^{o}	90^{o}
PET Melinex ST 505	2.38 ± 0.324	2.36 ± 0.155	3.21 ± 0.0848
PEN Teonex Q65 FA	3.26 ± 0.0956	2.72 ± 0.151	3.37 ± 0.0378
PC Lexan 8010 MC	1.29 ± 0.0530	1.26 ± 0.0562	1.22 ± 0.0737

Table 3.5 Rigidity of the polymer films.

Substrate	Young's modulus, E (GPa)	Thickness, h (μm)	Rigidity, D ($Nmx10^{-4}$)
PET Melinex ST 505	3.21	137	11.5
PEN Teonex Q65 FA	3.4	145	13.3
PC Lexan 8010 MC	1.25	185	11

Table 3.6 Degree of crystallinity and thermal properties of PET Melinex ST 505, PEN Teonex Q65 FA and PC Lexan 8010 MC polymer films.

Polymer film	Glass transition temperature, Tg (^oC)	Melting point, Tm (^oC)	ΔHf (J/g)	Degree of crystallinity, Xc (%)
PET Melinex ST 505	78	251	40.1	28.6
PEN Teonex Q65FA	121	259	35.5	34.4
PC Lexan 8010 MC	153	-	-	-

Table 3.7 Transparency of PET, PEN and PC in the visible range (400 - 800 nm)

Polymer sample	Transparency (%)
PET Melinex ST 505	88 ± 0.723
PEN Teonex Q65 FA	88.2 ± 3.12
PC Lexan 8010 MC	89.2 ± 0.577

Table 3.8 Results for surface roughness of PET Melinex ST 505, PEN Teonex Q65 FA and PC Lexan 8010 MC polymer films.

Polymer film		Roughness, Rms (nm)
PET Melinex ST 505	Side A	2.72 ± 0.256
	Side B	3.1 ± 1.04
PEN Teonex Q65 FA	Side A	1.43 ± 0.202
	Side B	10.7 ± 4.63
PC Lexan 8010 MC	Both sides	0.77 ± 0.116

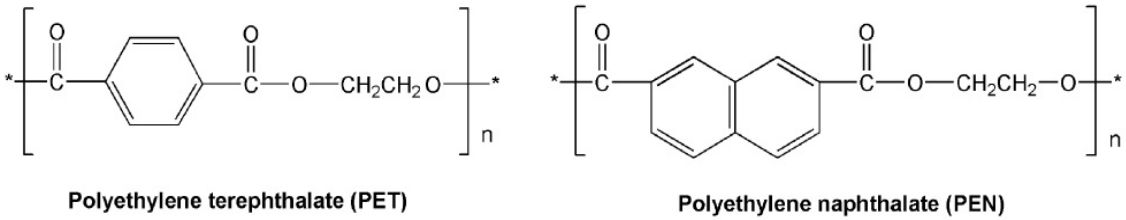

Figure 3.3 Chemical structure of PET and PEN polymer substrates, adapted from (Choi et al., 2008).

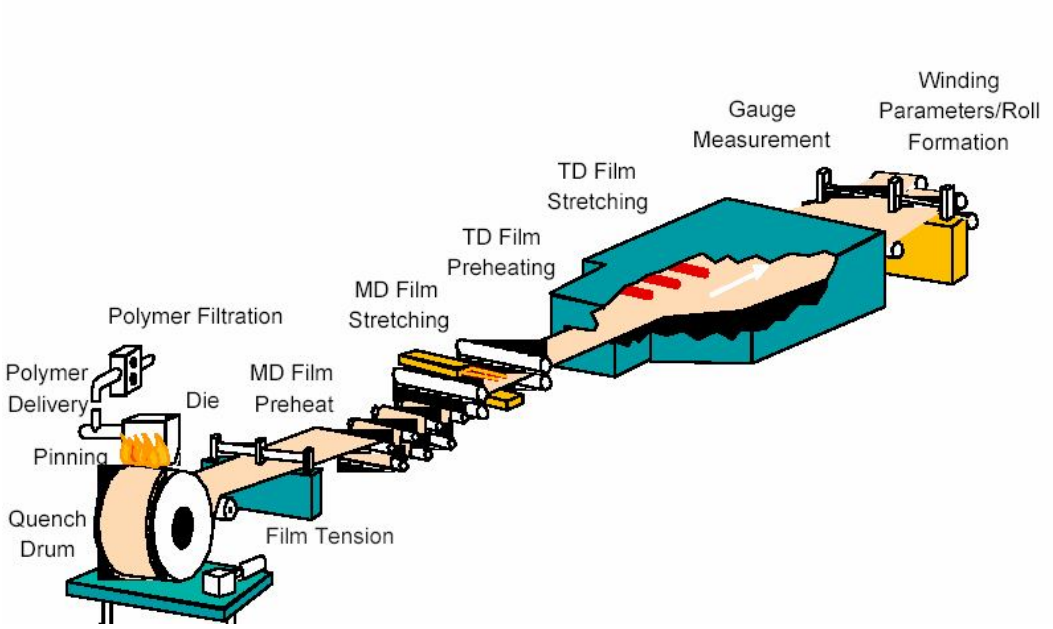

Figure 3.4 Biaxial orientation process of polyester films, adapted from (Sierros, 2006).

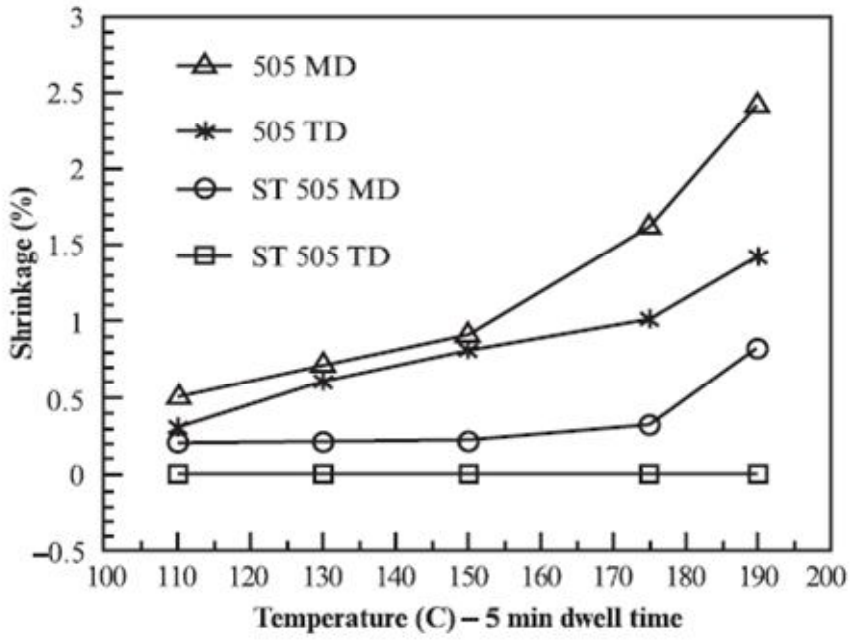

Figure 3.5 Shrinkage behaviour of standard PET 505 film and heat stabilized PET ST 505 film as a function of temperature in machine direction (MD) and transverse direction (TD). Adapted from (McClure, 2007).

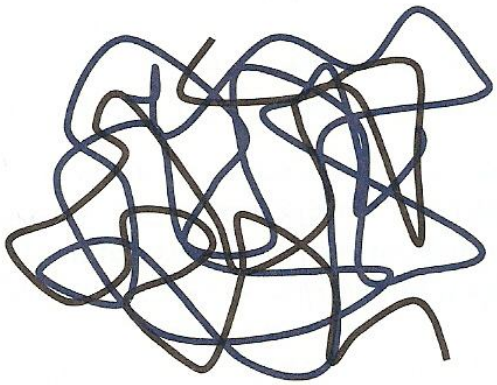

Figure 3.6 Entangled polymer chains, adapted from (Fischer, 2009).

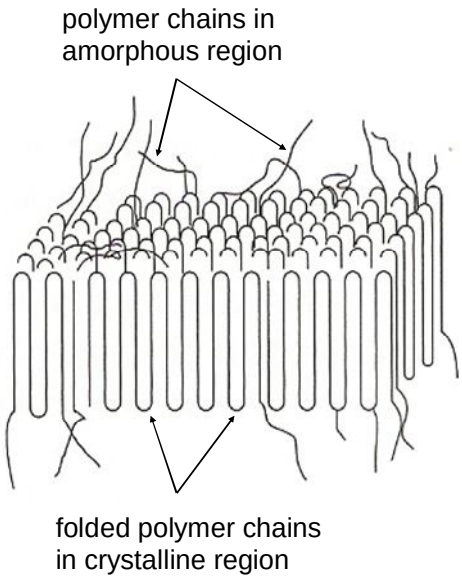

Figure 3.7 Crystalline lamellae, adapted from (Fischer, 2009).

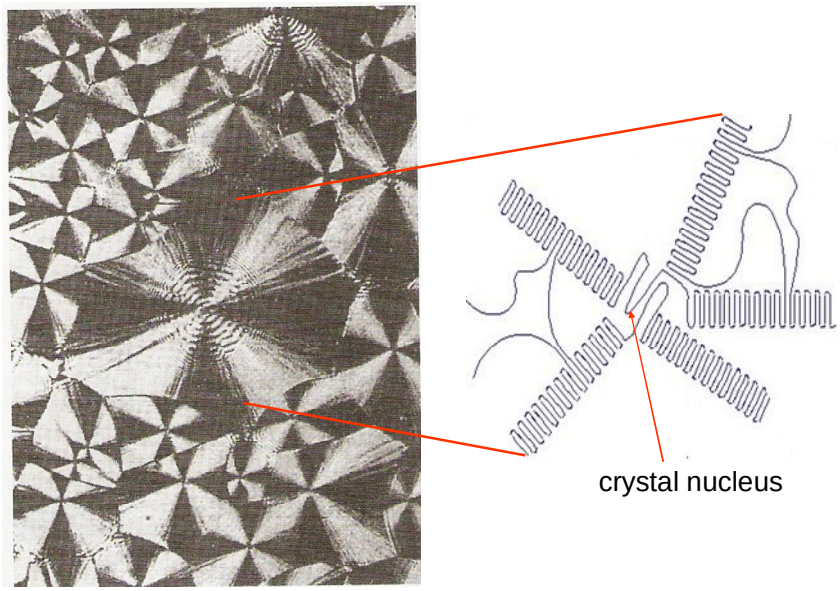

Figure 3.8 Spherulite structure of polyethylene, adapted from (Fischer, 2009) and www.pslc.ws.

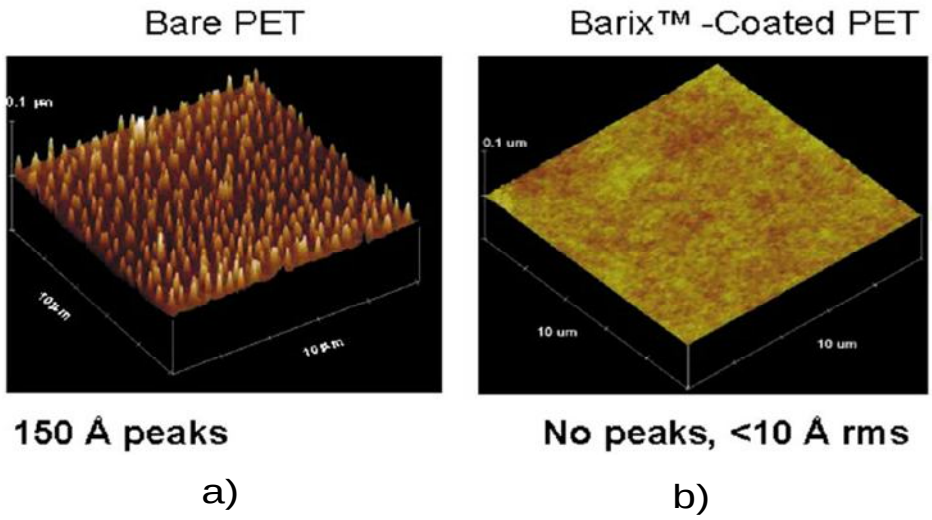

Figure 3.9 AFM images of a) bare PET film and b) coated by planarizing layer, adapted from (Burrows et al., 2001).

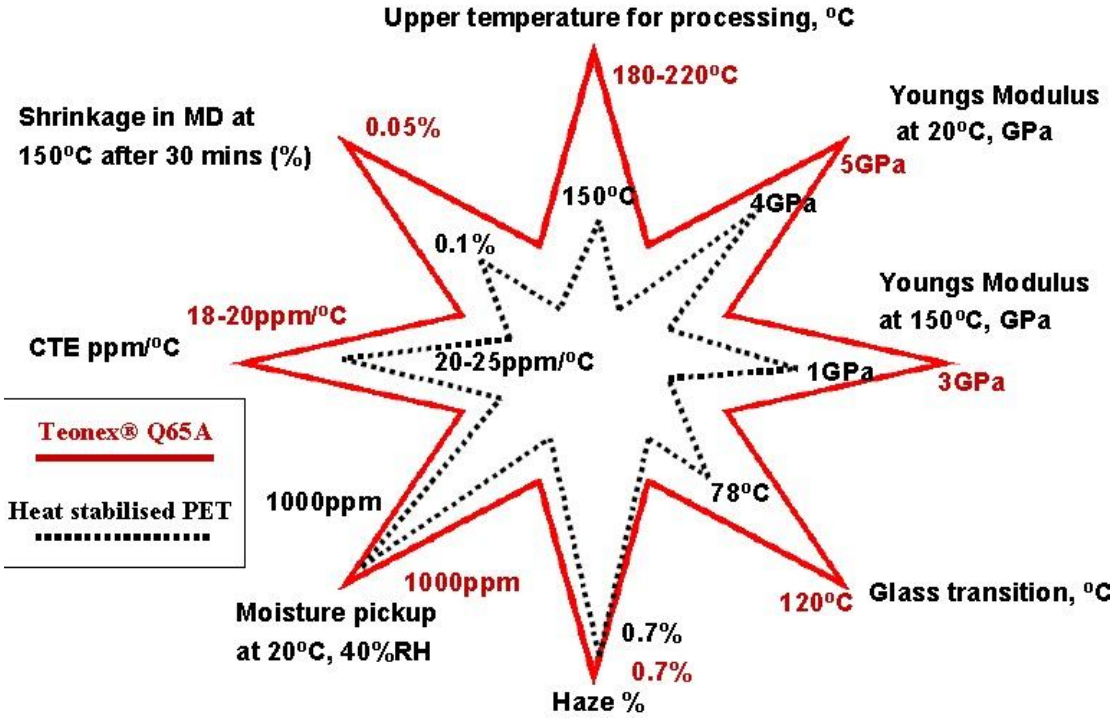

Figure 3.10 Comparison key properties of PEN Teonex® Q65 films with heat stabilised PET films, adapted from (DuPont Teijin Films www.dupontteijinfilms.com).

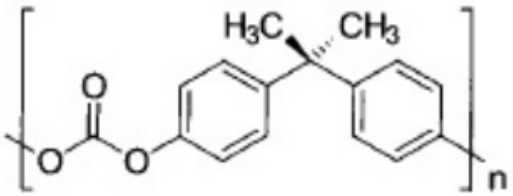

Figure 3.11 Chemical structure of polycarbonate (PC), adapted from (Braun et al., 2005).

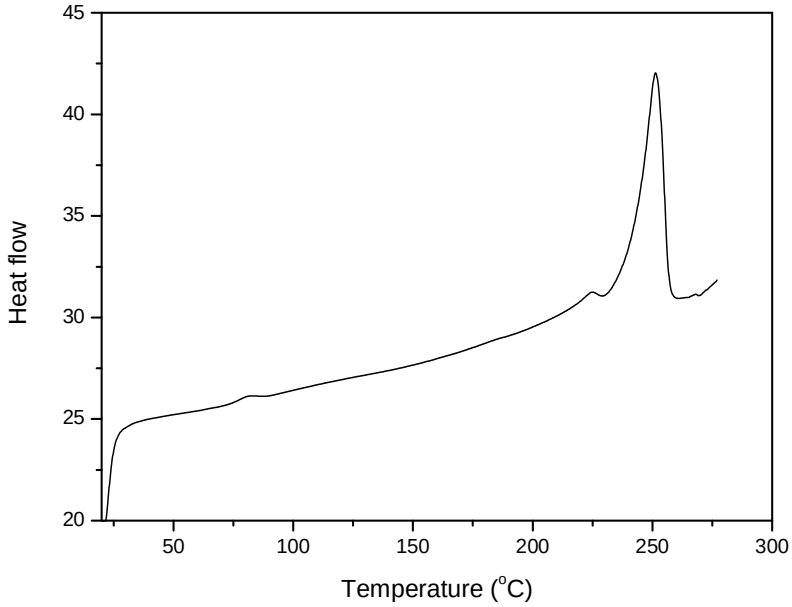

Figure 3.12 DSC thermogram of semicrystalline PET Melinex ST 505.

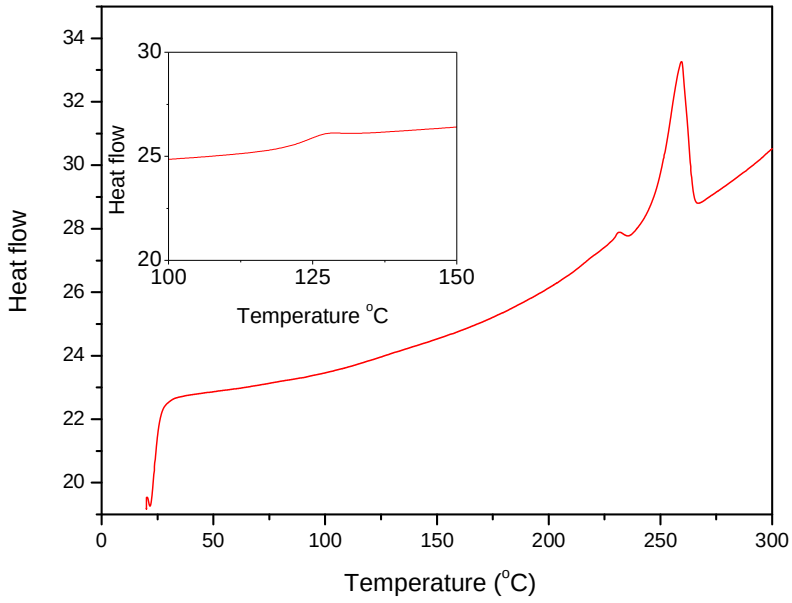

Figure 3.13 DSC thermograms of semicrystalline PEN Teonex Q65 FA.

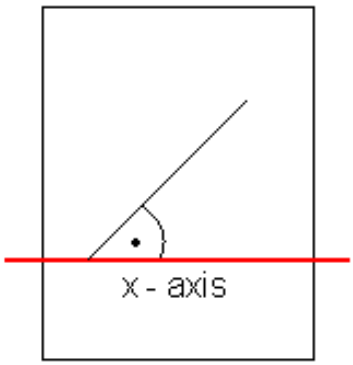

Figure 3.14 A4 polymer sheet and angle with respect to x-axis.

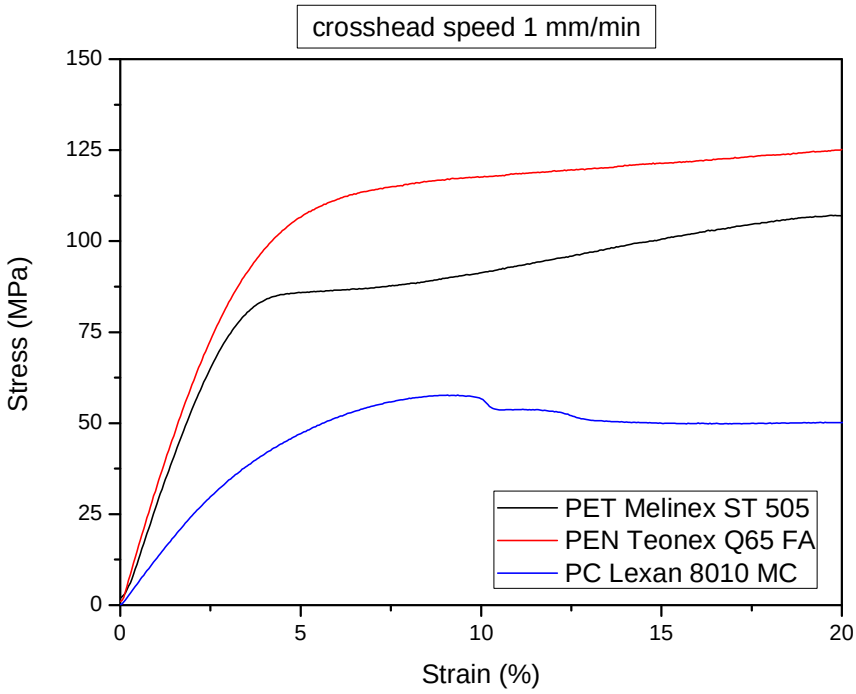

Figure 3.15 Stress-strain behaviour of bare PET, PEN and PC polymer substrates.

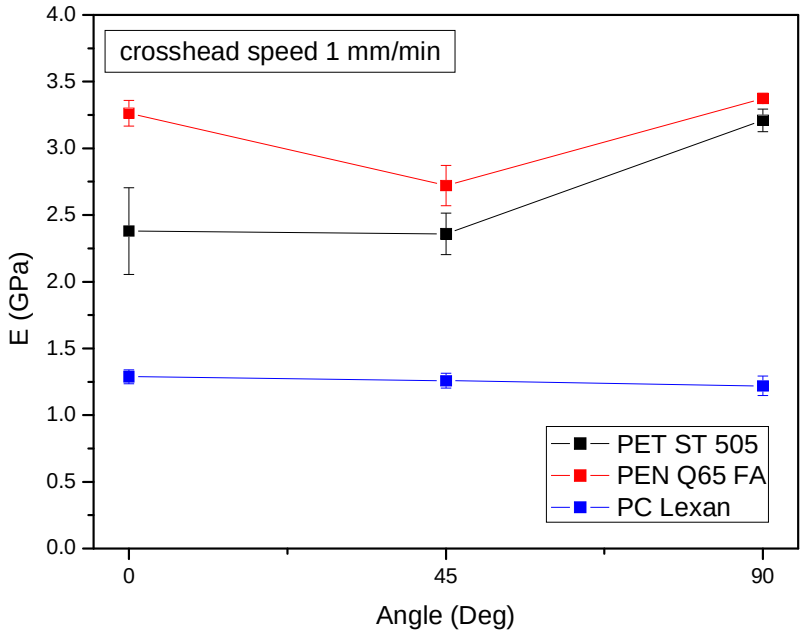

Figure 3.16 Young's modulus of bare PET, PEN and PC polymers as a function of angle with respect to x-axis.

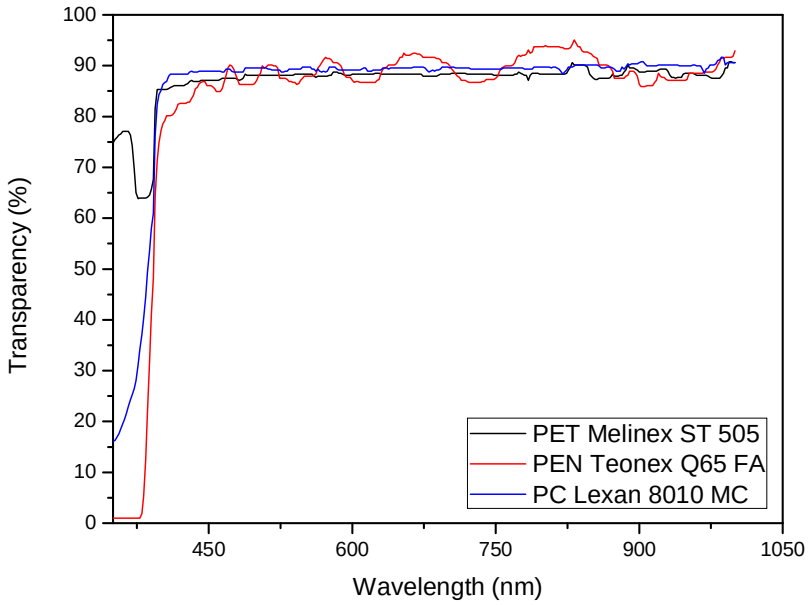

Figure 3.17 Transparency of PET, PEN and PC films in the visible range.

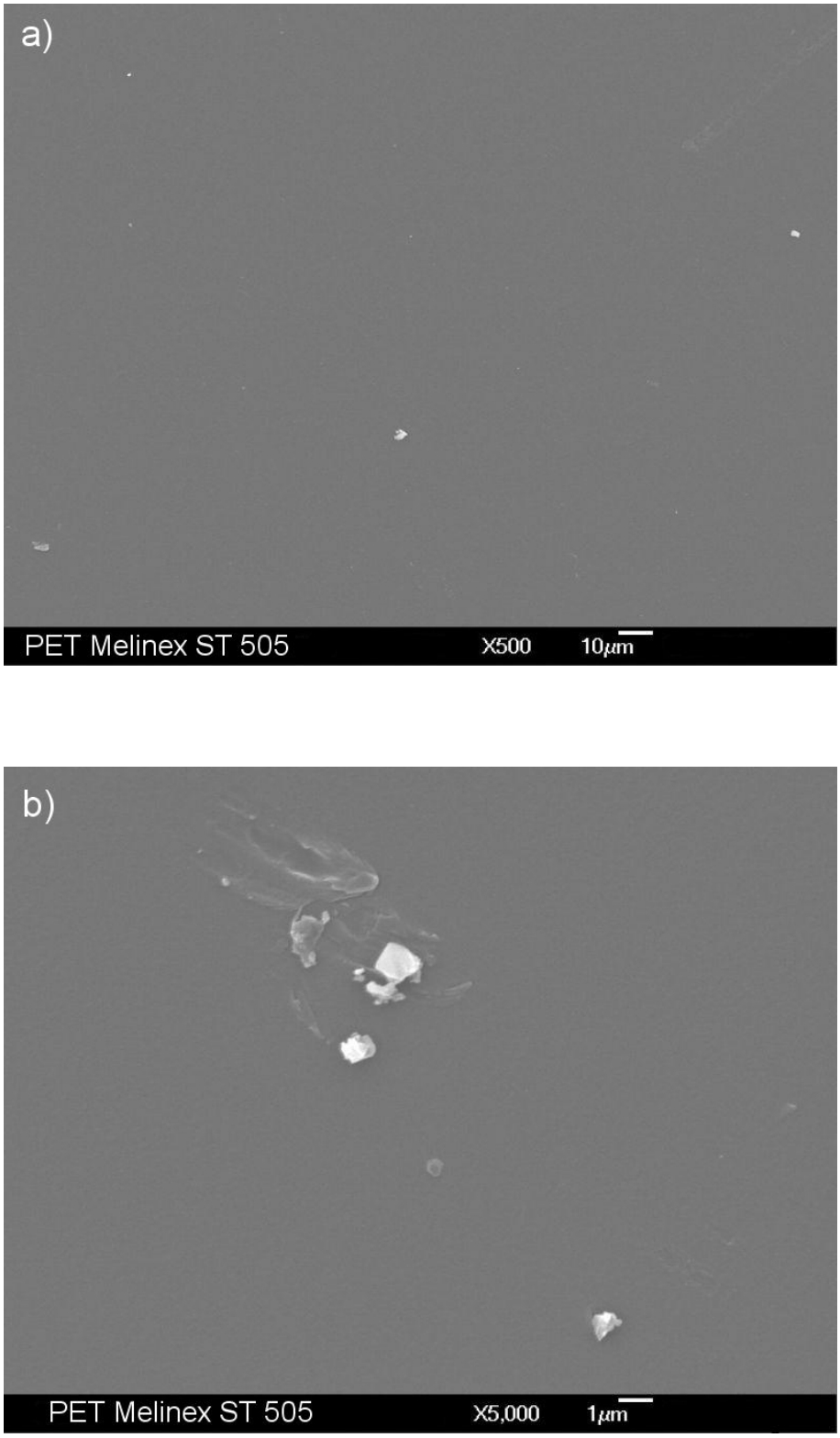

Figure 3.18 SEM images of a surface morphology of PET Melinex ST 505 polymer substrate. Note a difference in magnification between image (a) and (b).

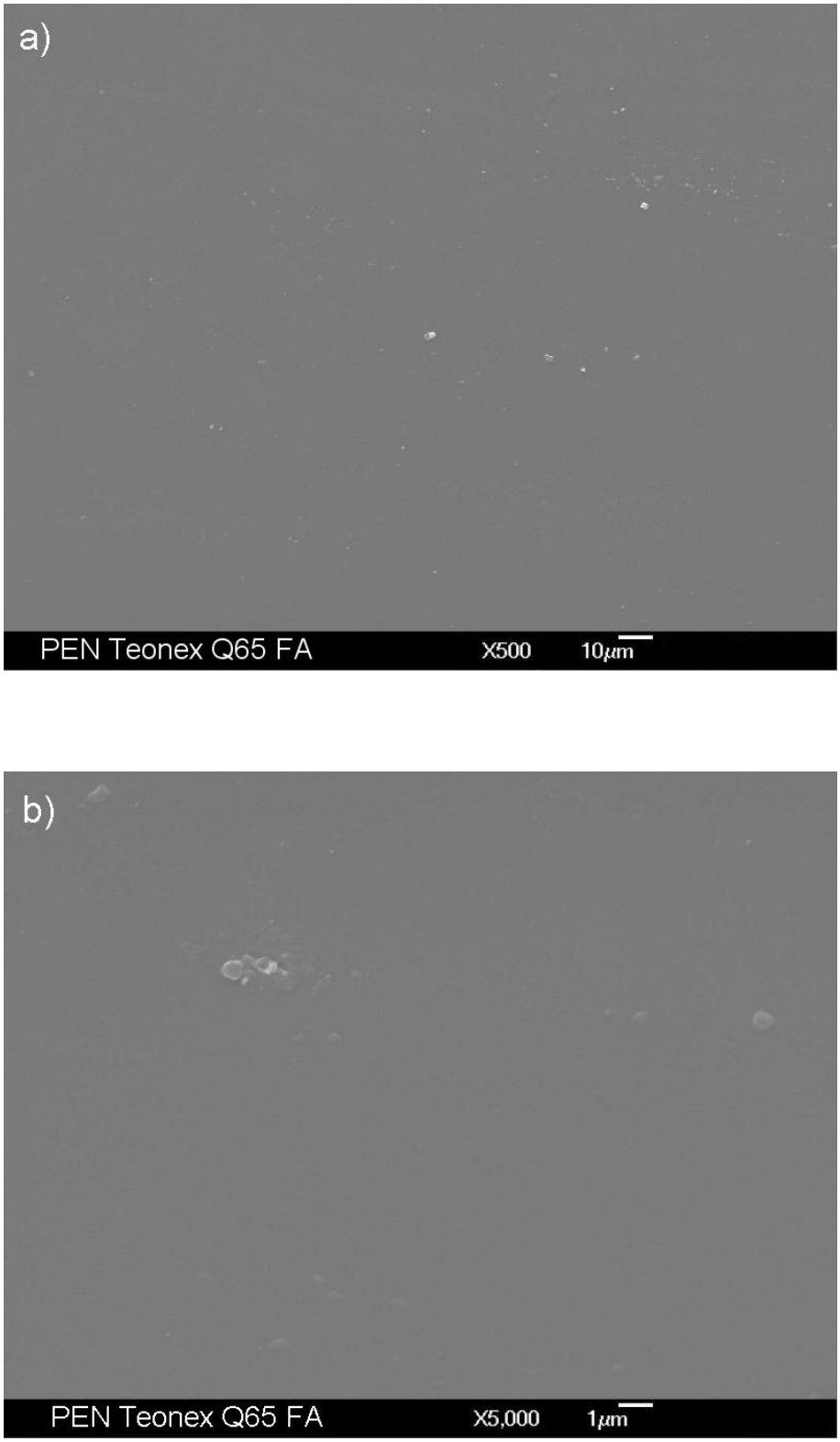

Figure 3.19 SEM images of a surface morphology of PEN Teonex Q65 FA polymer substrate. Note a difference in magnification between image (a) and (b).

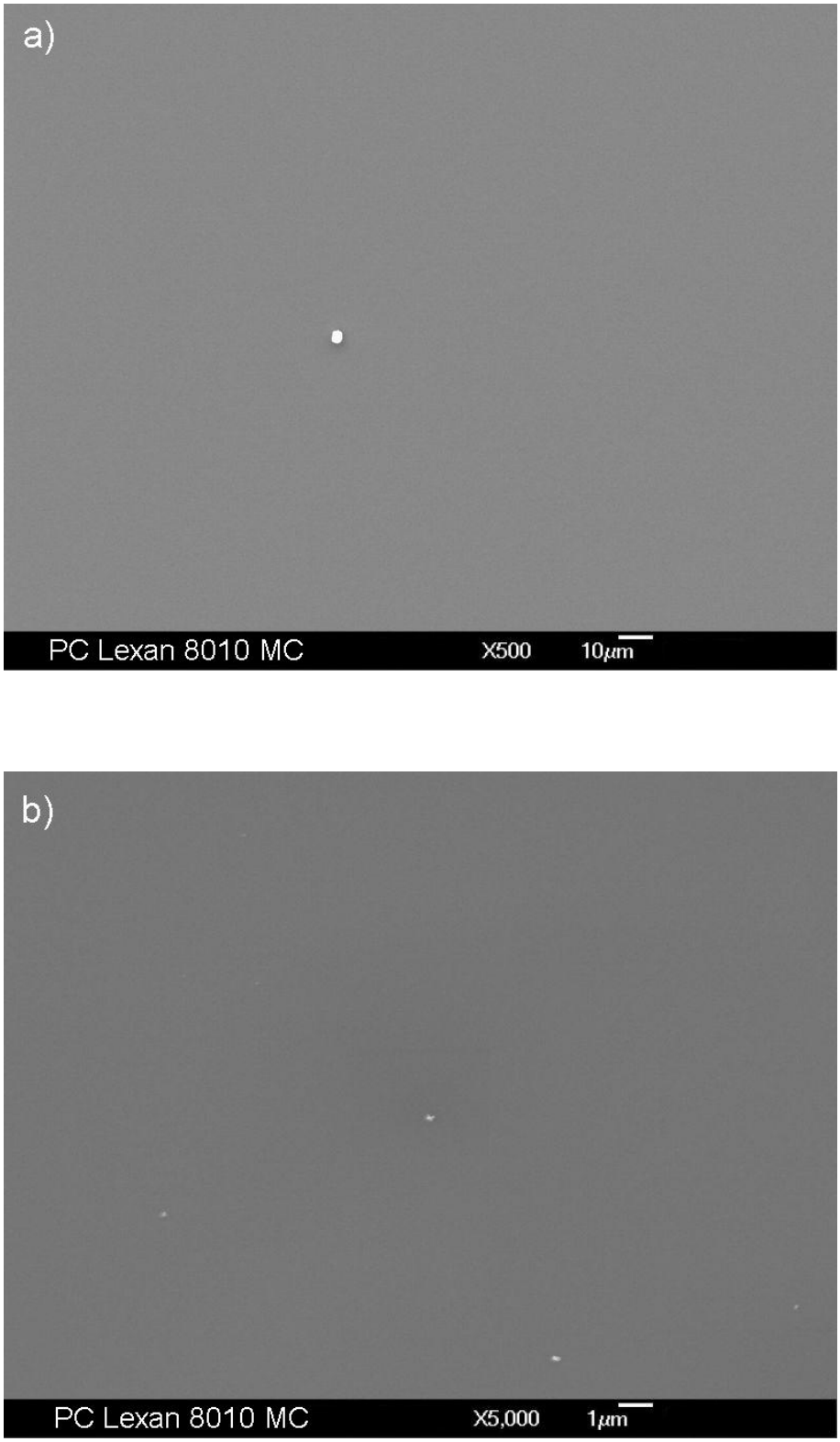

Figure 3.20 SEM images of a surface morphology of PC Lexan 8010 MC polymer substrate. Note a difference in magnification between image (a) and (b).

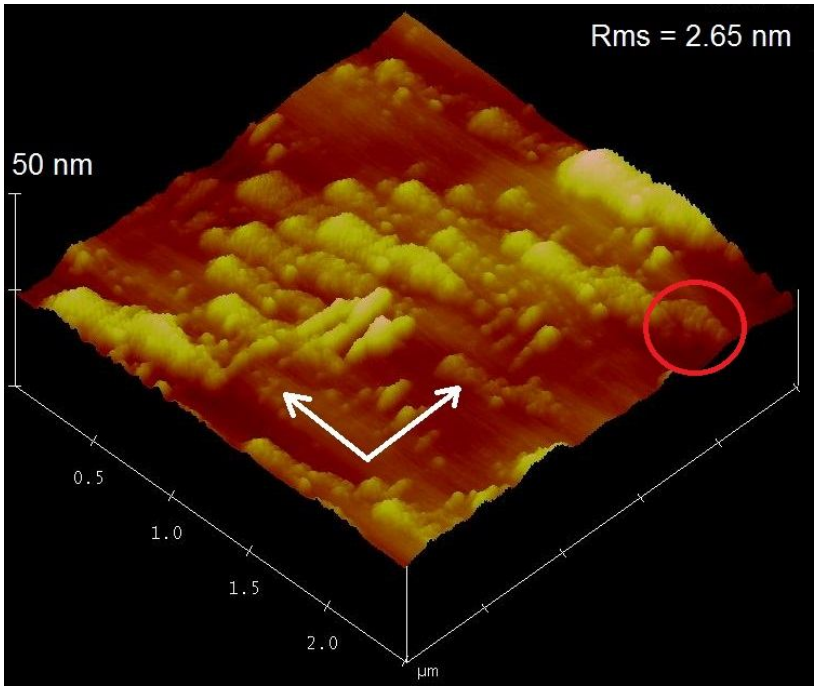

Figure 3.21 AFM micrograph of a surface of PET Melinex ST 505, side A – coated.

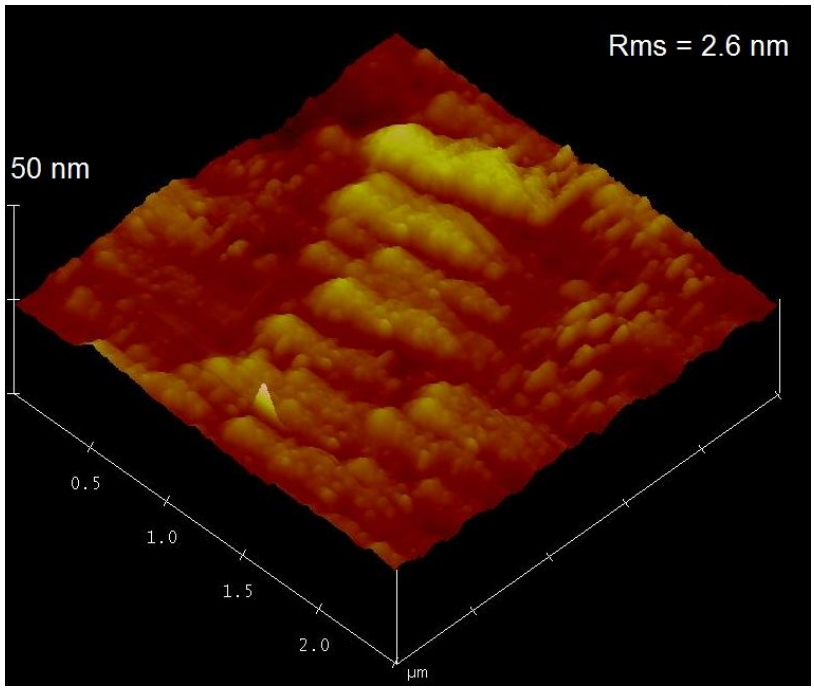

Figure 3.22 AFM micrograph of a surface of PET Melinex ST 505, side B – coated.

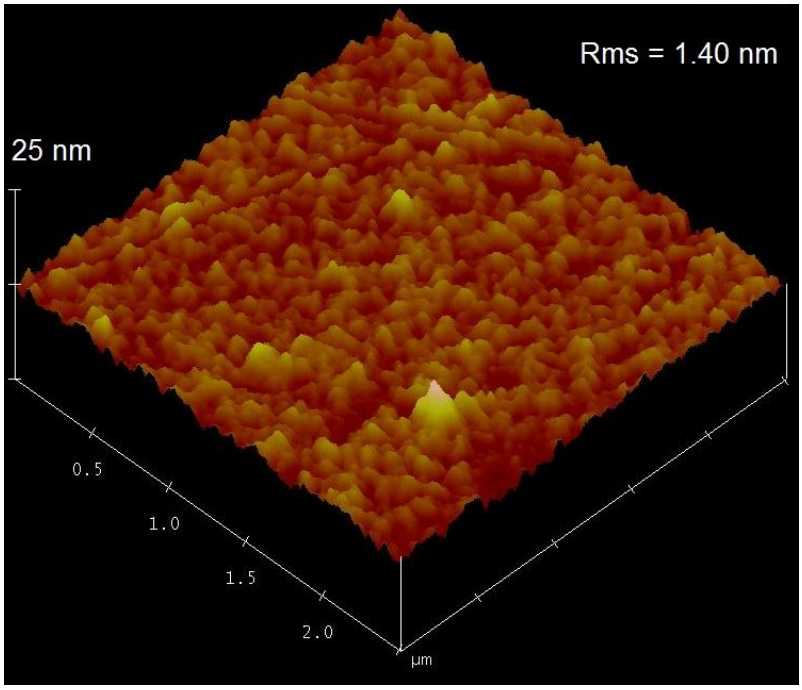

Figure 3.23 AFM micrograph of a surface of PEN Q65 FA, side A – coated.

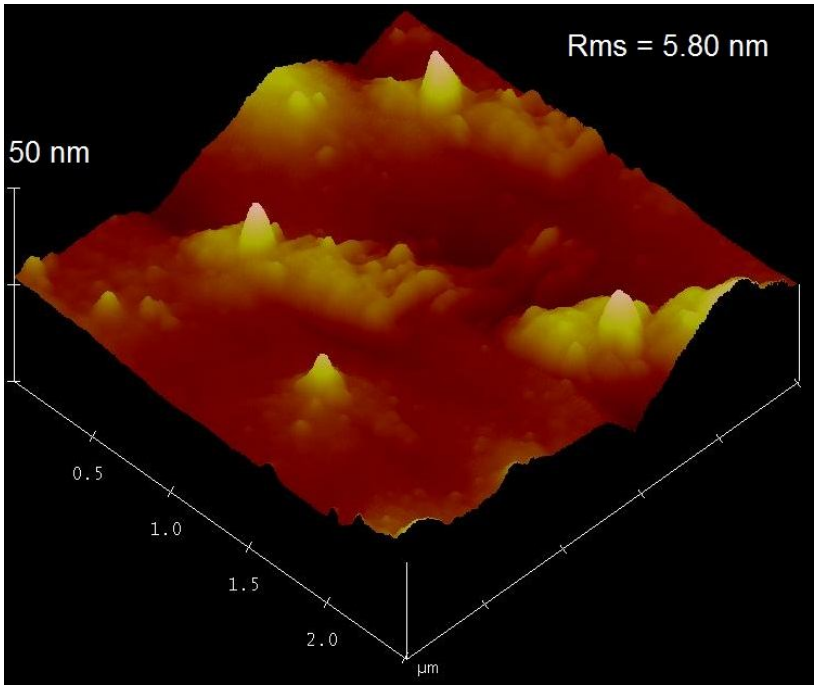

Figure 3.24 AFM micrograph of a surface of PEN Teonex Q65 FA, side B – uncoated.

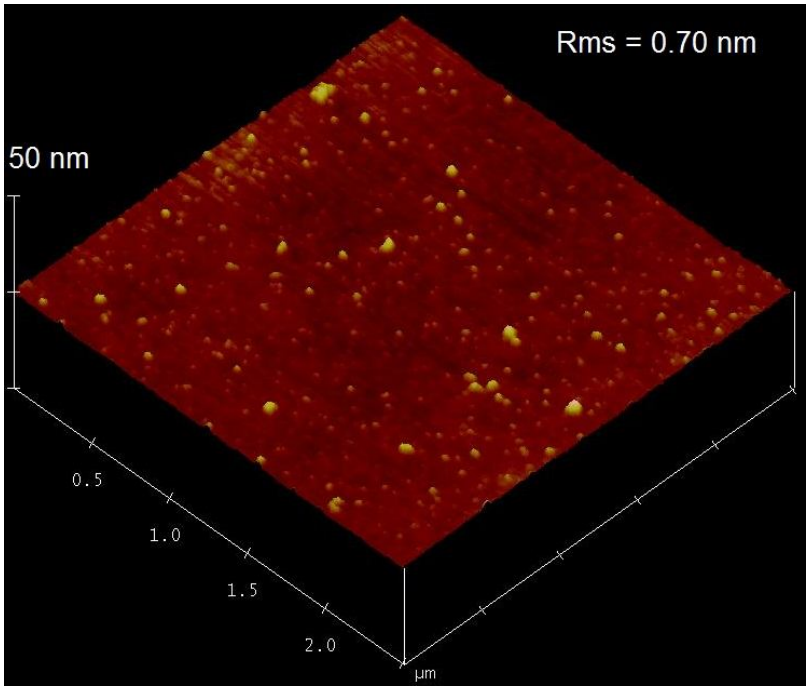

Figure 3.25 AFM micrograph of a surface of PC Lexan 8010 MC.

CHAPTER 4

4. PULSED LASER DEPOSITION OF ITO THIN FILMS

4.1 Transparent conductive oxides (TCOs) and indium tin oxide (ITO)

Transparent electrodes play a significant role in modern display technology for applications in many devices such as touch pads, organic light-emitting diodes (OLEDs), electroluminescence lamps, and so on. For these electrodes high transparency and conductivity is essential (Koniger and Munstedt, 2008a). High transparency requires band gaps larger than 3.3 eV and it makes carrier doping very difficult. Hence, there is inverse relationship between high transparency and high electric conductivity. However, transparent conducting oxides (TCOs) are exceptional because of their unique transparent and conducting properties (Hosono, 2007). The first TCO CdO film was prepared by Bädeker in 1907 and since then there have been remarkable developments in optoelectronic technology (Tahar et al., 1998). The first investigation on an In_2O_3 was carried out by Rupprecht in 1954 (Hosono, 2007). Transparent conductive oxides have found vast use in the area of flat-panel displays such as televisions, computers, electrochromic windows, photovoltaics and hand-held devices (Choi et al., 2008).

Indium tin oxide (In_2O_3:SnO_2) is the most commonly used TCO due to its excellent transmittance in the visible region, high conductivity and environmental stability (Wong et

al., 2004; Paine et al., 2005; Nam et al., 2010; Diniz, 2011). Another material exhibiting good electrical and optical properties is ZnO which attracts many researchers around the world as an alternative, nontoxic, cheap TCO to scarce and expensive ITO (Norton, 2007; Sittinger et al., 2008). The derivatives of transparent conductive oxides of ZnO, In_2O_3 and SnO_2, such as aluminium zinc oxide (AZO) (Thestrup and Schou, 1999), fluorine-doped tin oxide (FTO) (Ouerfelli et al., 2008), Ti doped ITO (Ti:ITO) (Paeng et al., 2010), In-Zn-Sn-O (IZSO) (Kim et al., 2010a) and many others have been, and continue to be, investigated. The above-mentioned oxides are n-type semiconductors and the list of TCOs can be finished by p-type semiconductors [quoted as transparent oxide semiconductors (TOSs)], which were extensively reviewed by Hosono (2007).

Tin-doped indium oxide (ITO) is a degenerate n-type semiconductor with a band gap energy between 3.5 and 4.3 eV (Kim et al., 1999b; Alam and Cameron, 2000; Zhang et al., 2008). Due to its low electrical resistivity of from 1 to 3 x 10^{-4} (Ω cm), high transparency of 90% in the visible spectrum (Kim et al., 1999b; , 2001; Paine et al., 2005) and excellent substrate adherence and hardness (Manavizadeh et al., 2009) ITO films are extensively studied and find use as an anode material for gas sensors, solar cells, flat-panel displays and other optoelectronic devices (Kim et al., 1999b; George and Menon, 2000).

4.1.1 Optical and electrical properties of ITO

The optical and electrical properties of ITO films are strongly dependent on oxygen vacancies and tin substitution for the matrix cations (Moriga et al., 2000; Baía et al., 2001). Other

parameters such as thin-film composition, deposition temperature and thickness of the film strongly affect the optical and electrical properties of ITO (Kim et al., 1999a). High conductivity in ITO film is proportional to the mobility and concentration of carrier electrons (Kim et al., 1999a; Yoshioka et al., 2000; Kim, 2007). Substitution of Sn^{4+} for In^{3+} provides one electron to the conduction band and this process is thermally activated (Dekkers et al., 2006). Thus Sn atoms in the ITO film acts as donors (Kim et al., 1999a). Oxygen vacancies, dependent on oxygen partial pressure during deposition, supply two free electrons each and hence dominates the conduction mechanism of ITO (Manavizadeh et al., 2009). However, a high deficiency of oxygen atoms lowers the band gap and reduces transparency, decreases the Sn doping efficiency and carrier mobility. Hence, there is a trade-off between carrier density and carrier mobility for achieving low-resistivity ITO films (Kim, 2007). In addition, optical and electrical properties are related to structural characteristics (Terzini et al., 2000).

4.1.2 Amorphous and crystalline ITO (a-, c-ITO) – properties

Indium tin oxide may exist in amorphous or crystalline forms (a-ITO and c-ITO, respectively. In order to achieve a crystalline structure a heated substrate or an annealing treatment are necessary (Paine et al., 2005). C-ITO has better opto-electrical properties than a-ITO and its structure depends on deposition conditions such as substrate temperature, oxygen pressure and deposition rate. ITO films deposited at a temperature below 200 ^{o}C exhibit electrical resistivity above 5 x 10^{-4} Ω cm due to their amorphous state (Izumi et al., 2002b). The relevance of amorphous ITO film in the commercial production of transparent anodes for opto-electronic applications is still not clear. However, an amorphous nature for ITO films

makes patterning and the wet-etching process easier at low substrate temperatures compared with those needed for crystalline films (Adurodija et al., 2002; Paine et al., 2005). With increasing temperature during thin-film deposition, the proportion of crystalline phase increases and a temperature ranging from 150 to 165 ^{o}C is commonly cited as the crystallization temperature of ITO film (Adurodija et al., 2006). The growth of the crystalline phase with increasing annealing time is well presented in Figure 4.1. ITO exhibits a complex cubic bixbyite structure (also called c-type rare earth oxide structure) of In_2O_3 originating from vacant tetrahedral oxygen anion sites (Adurodija et al., 2006), as Figure 4.2 shows. It has in total 80 atoms per unit cell with a lattice constant α = 10.117 Å (Janowitz and et al., 2011).

The microstructure and morphology of polymer substrates used for flexible flat-panel displays, play an important role in growing ITO films. Due to the low density and surface energy of polymer substrates, mostly a-ITO is grown without a large amount of thermal activation energy for phase transformations (Yang and Park, 2010). When residual or external stresses act on the film, amorphous a-ITO shows lower cracking-resistance than that of crystalline c-ITO due to its larger free volume (Yang and Park, 2010). Plasma treatment of polymer surfaces, that changes the chemical states, and post-thermal annealing may increase the crystallinity of ITO films (Yang and Park, 2010).

4.2 Deposition methods for conductive thin films

Typical deposition processes can be categorised as (Exarhos and Zhou, 2007):

- Physical Vapour Deposition (PVD), which can be further categorised into sputtering and thermal evaporation (Wasa et al., 2004). Sputtering includes dc sputtering, radio frequency (rf) sputtering or reactive sputtering. Sputtering is the most commonly used deposition method of thin films due to low costs and the possibilities to growth thin films on large-area substrates (Exarhos and Zhou, 2007). In this process atoms are dislodged from the material source (target) surfaces through the impact of gaseous ions (Ohring, 1992). Pulsed laser deposition (PLD) is a thermal evaporation technique and is described in detail in the next subsection.
- Chemical Vapour Deposition (CVD), where a few CVD methods can be distinguished: atmospheric pressure CVD (APCVD), low pressure CVD (LPCVD), plasma enhanced CVD (PECVD) and metallo-organic CVD (MOCVD).
- Solution deposition, which includes sol-gel and nanoparticles dispersion. Sol-gel deposition is within the scope of this project and is described separately in a next chapter.
- Spray pyrolysis.

Fan (1979) investigated the optical and electrical properties of ITO films deposited at low temperature on glass and polymer substrates by ion-beam sputtering. They showed that oxygen pressure strongly influences the opto-electrical properties of ITO films. High-quality layers with low resistivity and high transparency can be achieved by careful control of the oxygen pressure during deposition. They achieved a resistivity of ~ 5.5×10^{-4} Ω cm, and transparency > 80%, for both ITO/glass and ITO/polymer systems over a very narrow range of oxygen pressure ($2 – 3 \times 10^{-5}$ Torr).

Furthermore, Han *et al*. (2005) investigated the influence of oxygen content and surface morphology on opto-electrical properties of ITO film coated on PEN substrates by radio-frequency (rf) magnetron sputtering at room temperature. They observed that with increasing oxygen content the resistivity increases due to a drop of oxygen vacancies; hence leading to a lower carrier concentration. The surface roughness of 400 nm thick ITO film on 125 μm thick PEN was higher than that of ITO on 200 μm thick PEN (~ 8 and ~ 4 nm, respectively), which was attributed to the roughness of the polymer itself. The resistivity of ITO/PEN (125 μm) was also higher compared with ITO/PEN (200 μm), (19 and 3.5 x 10^{-3} Ω cm, respectively). They concluded that despite the influence of oxygen content, the surface roughness of ITO film also influences its electrical properties. The resistivity increases with surface roughness due to electron scattering. With increasing ITO thickness a similar drop of transmittance was observed for both PEN substrates.

In addition, Meng and Dos Santos (1997) showed that with increasing total deposition pressure (argon + oxygen) for rf reactive magnetron sputtering, the roughness of the ITO film increases, as the grain size along the sample surface increases. They achieved the lowest resistivity, of 2.0 x 10^{-3} Ω cm, of ITO-coated glass substrates for low deposition pressures. Similar observations were reported in (Guillen and Herrero, 2005).

Kumar and Mansingh (1989) were the first who investigated an effect of target to substrate distance on the growth and properties of ITO films. The ITO was deposited on glass at room temperature by rf sputtering. They observed that structural, optical and electrical properties are affected by the energy distribution of the sputtered atoms reaching the substrate. The ejected atoms from the target lose a part of their energy due to collisions with the ambient gas.

Thus, the ITO properties depend on the energy of the sputtered particles. They observed that for particles with higher energy the intensity of (400) reflection increases. In contrary, the atoms with lower energy prefer to orient in the (222) direction. Hence, the change in orientation may be due to the change of atom mobility, which decreases with increasing background or active gas pressure and target to substrate distance. The results showed that a shorter distance between the material source and the substrate results in better electrical conductivity of the ITO films. In addition, a study of crystallization kinetics of ITO film (Adurodija et al., 2006) showed that highly energetic particles impinging on the substrate surface reduce the crystallization temperature. Furthermore, Antony *et al*. (2004) also observed a strong dependence of target-substrate distance on structural and opto-electrical properties of ITO film deposited on glass by rf magnetron sputtering. They also observed that a shorter target-to-substrate distance results in higher conductivity of the ITO film and increased intensity of the (400) orientation.

Guillen and Herrero (2008b) deposited polycrystalline ITO films with thickness range between 200 and 700 nm on glass and PET substrates at room temperature by sputtering. They observed that transparency and sheet resistance decrease with increasing ITO thickness due to an increase in carrier concentration. The ITO-coated PET showed comparable transparency and slightly lower resistivity to ITO-coated glass substrates for all ranges of the layer thickness. The XRD results showed (222) diffraction as a favourite orientation for the film thickness up to 500 nm and (400) orientation for the thicker ITO films. Other authors (Hao et al., 2008) also investigated properties of ITO-sputtered PET as a function of the layer thickness. They have found that pre-deposition plasma cleaning of the PET surface with

multi-arc ion plating results in a crystalline structure, which increases with ITO thickness. The decrease of resistivity and transparency with thickness was also reported.

Shin *et al*. (2001) investigated opto-electrical and mechanical properties of ITO films deposited by dc magnetron sputtering on glass, acrylic (AC), PC and PET polymer substrates as a function of dc power, working pressure and oxygen content. They noticed that for 1 mTorr working pressure the lowest resistivity (9.3×10^{-4} Ω cm) of ITO-coated glass, AC, PC and PET can be obtained in the vicinity of 13% oxygen content. In addition, with an increase in working pressure from 1 to 5 mTorr, the oxygen content for minimum resistivity is reduced from 13 to 10%. The lowest resistivity, of 6.0×10^{-4} Ω cm was achieved for ITO-coated PET under 3 mTorr working pressure and 12% of oxygen content. The highest transparency of 85% (at 550 nm wavelength) was also found for the ITO/PET sample. The scratch adhesion test showed that ITO-coated polymer substrates exhibit higher adhesion levels compared with ITO/glass samples. It was pointed out that there is relationship between mechanical properties and opto-electrical properties of ITO films, where oxygen content may act as a link.

Finally, Guillen and Herrero (2005) deposited ITO films on glass and PET substrates at room temperature by rf magnetron sputtering for a comparison study. They observed that at a certain oxygen pressure ITO-coated PET exhibit lower sheet resistance compared to the ITO/glass system (7 and 9 Ω/□, respectively), although the transparency is similar for both samples (~ 85%). They pointed out that the lower resistivity of ITO/PET may be due to a larger grain size; hence lower grain-boundary scattering of carriers.

4.2.1 Pulsed laser deposition of ITO

Pulsed laser deposition is a physical vapour deposition carried out in a vacuum system, where ablation of the material from the material source is achieved by selecting an ultraviolet laser wavelength and nanosecond pulse width (Norton, 2007). Detailed information about physical vapour deposition and the PLD process can be found in (Leonid et al., 2002; Charsha, 2006; Norton, 2007). Figures 4.3 and 4.4 show a schematic of the pulsed laser deposition system and the laser plume respectively during the deposition process. In the PLD system a high-power pulsed laser is focused through a quartz lens on to the target of the material to be deposited. Each laser pulse vaporizes a small amount of the material creating a plasma plume. The ablated material is ejected from the source in a highly-directed plume and is deposited on the substrate forming a thin film (Norton, 2007).

For the pulsed laser deposition (PLD) process substrate temperature and energy of ejected particles from the ITO target play important roles for the thin film growth (Adurodija et al., 2006). The advantage of using the PLD technique is that it allows one to achieve crystalline thin films at low deposition temperatures due to highly energetic species (Adurodija et al., 1999). PLD also allows stoichiometric transfer of a material from a target (Kim et al., 1999a; Kim et al., 2006; Norton, 2007) and minimises film contamination since the laser beam is focused only on the source material (Yong et al., 2005). The PLD technique has been successfully applied to deposit a variety of materials such as insulators, semiconductors, superconductors, dielectric materials, metals (Zheng and Kwok, 1993), polymers and even biological materials (Norton, 2007). To improve conductivity of TCOs, thin-film UV irradiation, oxygen radical-assisted deposition, or magnetic field-promoted deposition can be coupled with the PLD technique (Exarhos and Zhou, 2007). In comparison with other

deposition techniques, PLD will always produce better quality thin films, especially at room temperature (Zheng and Kwok, 1993).

Zheng and Kwok (1993) used PLD to deposit high-quality ITO films on glass substrates for optoelectronic devices. They found that resistivity of the film is weakly dependent on oxygen pressure at elevated temperatures. In contrast, at room deposition temperature, resistivity and transparency were strongly dependent on oxygen pressure. It was possible to obtain the lowest resistivity and highest ITO transparency, of 5.6×10^{-4} Ω cm and 90%, respectively over a very narrow range of oxygen pressure (in the vicinity of 15 mTorr) at room temperature. They pointed out that the strong dependence of oxygen pressure on resistivity at low temperatures is due to the nature of the PLD technique. In the PLD process, the ejected species from the target travel to the substrate with different speeds. If the oxygen pressure is too low the density of the various species will not be uniform at the substrate surface, as the indium atoms arrive first followed by tin and oxygen atoms. In this case the film is not uniform. Therefore optimum oxygen pressure is necessary to uniform energetic atoms, through the collisions between oxygen atoms and atoms ejected from the target, in order to produce high-quality uniform films.

Kim *et al*. (1999b) also observed that the resistivity of ITO is strongly dependent on oxygen pressure at low deposition temperatures. Low resistivity values were obtained between 10 – 15 mTorr of oxygen pressure. They concluded that the oxygen pressure dependence of resistivity is due to the oxygen vacancies in the film. Oxygen vacancies provide free carriers; hence the lower the oxygen pressure, the higher the conductivity. However, severe reduction

of oxygen pressure may lead to structural lattice disorder, which in turn reduces the mobility of free carriers.

Suzuki et al. (2002) investigated influence of target-to-substrate distance on opto-electrical properties of indium tin oxide films deposited by pulsed laser deposition at 400 ^{o}C. They achieved the lowest resistivity, of 1.15 x 10^{-4} Ω cm, for the lowest target to substrate distance, of 10 mm. However, low transparency was measured, of ~ 74% for 300 nm thick film, due to scattering caused by high surface roughness. They found that by optimising oxygen pressure it is possible to reduce roughness from 11.5 to 1.26 nm, which in turn increased transparency up to 80% and further decreased resistivity to 8 – 9 x 10^{-5} Ω cm. They finally concluded that highly conductive and transparent ITO films are obtained with high plasma density for a 10 mm target-to-substrate distance resulting from sufficient oxygen pressure and high pulsed-laser energy.

Kim *et al*. (1999a) studied the influence of film composition, thickness and temperature on opto-electrical and structural properties of ITO films deposited on glass by PLD. They showed that 5 wt % content of SnO_2 in a ITO target gives the lowest resistivity of the film deposited at 250 ^{o}C under 10 mTorr of oxygen pressure. Furthermore, the resistivity of the ITO film decreased from 3.8 to 1.9 x 10^{-4} Ω cm with an increase of temperature from 25 to 300 ^{o}C. They pointed out that this is due to an increase of carrier concentration caused by diffusion of Sn atoms from interstitial locations and grain boundaries into In cation sites. They also observed that the crystallinity increases with thickness. It was also found that the transparency is strongly related to the SnO_2 content in the ITO target, deposition temperature, oxygen pressure and the thickness of ITO film. With increasing oxygen pressure the

transparency increases, which may be related to the increase of crystallinity. They also observed that with increasing oxygen pressure the (222) diffraction peak increases, indicating an increase of crystallinity.

Viespe *et al*. (2007) studied the influence of oxygen pressure, substrate temperature and laser fluence on opto-electrical properties of ITO films deposited on glass substrates by advanced pulsed laser deposition. They observed that oxygen pressure and laser fluence strongly influence the thickness and opto-electrical properties of the film. By increasing the substrate temperature from room temperature to 180 ^{o}C, the resistivity decreased from ~ 8 to ~ 5 x 10^{-4} Ω cm. The transparency increased up to 89% in the visible range.

Yong *et al*. (2005) deposited ITO films on polycarbonate substrates at room temperature by pulsed laser deposition. The results showed that the resistivity increases with increasing target-to-substrate distance. However, the transparency decreases as the space between target and substrate reduces. They fabricated ITO films on PC substrates that exhibit resistivity, of 1.5 x 10^{-3} Ω cm and transparency, of 94%. They concluded that the relatively high resistivity is due to the type of laser source (Nd:YAG) that produces higher wavelengths (355 and 532 nm) than the more commonly-used KrF excimer laser (248 nm). They pointed out that the lower laser wavelength, of 248 nm, is strongly absorbed by the ITO target, resulting in a highly efficient ablation, which allows the formation of high-quality ITO films.

Furthermore, Izumi *et al*. (2002b) investigated PLD deposition conditions in order to achieve crystalline ITO films on PC substrates at room temperature. They used *in situ* UV laser irradiation during the PLD process. They observed that resistivity of ITO/PC with irradiation

is higher than without. Moreover the transparency decreased due to degradation of UV-sensitive PC substrates. They coated PC substrates with CeO_2 film in order to absorb UV light and protect PC substrates. However, the resistivity of ITO/CeO_2/PC sample was still high, despite the irradiation process. This means that the underlayer influences the ITO properties. Finally, they used another layer (Al_2O_3) to form an ITO/Al_2O_3/CeO_2/PC sample. The irradiation process helped to achieve crystalline 100-nm thick ITO films at room temperature with low resistivity, of 1.3 x 10^{-4} Ω cm, due to densification of the ITO particles (grains with sizes of ~ 30 nm).

Adurodija et al. (2002) investigated opto-electrical properties as a function of Sn content (0, 5 and 10 wt %) in indium oxide films deposited on glass substrates at room temperature by PLD. The properties of the films were similarly sensitive to the changes of oxygen pressure. In addition, they observed that at optimum oxygen pressure, conductivity decreases with increasing Sn content, which may result from scattering effects from the Sn atoms. They pointed out that better conductive films at room temperature can be achieved without Sn doping. This means that in the amorphous state the presence of Sn atoms in the ITO films does not contribute free electrons to the conduction band. High optical transmittance (> 90%) was observed for all the samples, irrespective of Sn content.

In addition, Dekkers et al. (2006) also investigated the effects of Sn doping in In_2O_3 films on opto-electrical and structural properties. They deposited thin films on PET substrates at room temperature by PLD. They found that the number of Sn atoms decreases the electrical conductivity of ITO films. They pointed out that at room temperature resistivity depends only on oxygen vacancies, as Sn atoms are activated only at high temperatures. Therefore at room

temperature Sn atoms can form neutral complexes with oxygen anions and act as scattering centres for free electrons. It was also observed that with increasing Sn doping, the crystallinity of the ITO film decreases. As a result carrier mobility decreases due to grain boundary scattering. They finally concluded that at room temperature crystalline, highly conductive (4.1×10^{-4} Ω cm) and transparent (> 85%) films coated PET substrates can be obtained for undoped In_2O_3 films.

Kim *et al*. (2005a) investigated opto-electrical and morphological properties of ITO films as a function of oxygen and deposition temperature. 180 nm thick ITO films were deposited on polyethersulphone (PES) polymer substrates at a temperature of 25 and 130 ^oC by PLD for use in organic light emitting diodes. At 25 ^oC, they achieved a low resistivity, of 2.9×10^{-4} Ω cm and high transparency, of 84%. Higher deposition temperature (130 ^oC) slightly decreased the resistivity down to 2.7×10^{-4} Ω cm. They observed that the surface roughness increases with increasing oxygen pressure (in the range between 15 and 75 mTorr). However, the surface roughness of ITO/PES was found to be lower compared with sputtering methods. Furthermore, they concluded that smooth ITO films can be obtained at high temperatures and low oxygen pressure during the deposition process.

Sierros *et al*. (2010a) deposited high quality 240 nm thick ITO films on PEN polymer substrates at room temperature using the pulsed laser technique. They showed that low resistivity, of 1.0×10^{-4} Ω cm and high transparency, of 90% can be achieved in the narrow range of 1 - 1.33 Pa of oxygen pressure. Furthermore, they observed that the studied range of oxygen pressure does not influence electro-mechanical properties of ITO/PEN systems

subjected to tensile stresses. However, the adhesion between ITO and PEN may be influenced by oxygen background pressure.

4.3 Results and discussion

There are two ways to increase the flexibility of electronic devices based on brittle thin films: i) by reducing the thickness of the thin layer and ii) by placing the brittle coatings near the neutral axis (Chen et al., 2001b). As mechanical properties of the two-layer components are within the scope of this work the emphasis is to optimize the deposition process in such way as to achieve the thinnest possible ITO films with low resistivity and high transparency. Therefore, the deposition parameters such as oxygen partial pressure, target-to-substrate distance and number of pulses were varied systematically. For the optimization process glass substrates were used. The deposition temperature of 150 ^{o}C, was chosen as the highest operational temperature that can be applied for polymer substrates. After the optimization process ITO films were deposited on PET, PEN and PC polymer substrates. All transparency values in this work represent the transparency of the samples (ITO/glass and ITO/polymers).

4.3.1 Influence of oxygen pressure on ITO film properties

To investigate the influence of oxygen pressure on ITO film properties the following deposition conditions were applied: 55 mm target to substrate distance, temperature set at 150 ^{o}C and 5000 the number of pulses.

4.3.1.1 Influence of oxygen pressure on opto-electrical properties

Figure 4.5 shows resistivity and transparency as a function of oxygen pressure. With decreasing oxygen pressure, the resistivity decreases due to an increase of the number of oxygen vacancies, which generate free electrons (carriers) for the conduction band (Fan, 1979; Kim et al., 1999b; Adurodija et al., 2006). Similar trends of ITO resistivity as a function of oxygen pressure were reported previously (Kim et al., 1999b; Adurodija et al., 2006). It is clear that the low resistivity films can be achieved within a narrow range of oxygen pressure between 5 to 8 mTorr. Fan (1979) and others (Zheng and Kwok, 1993; Kim et al., 1999b) also observed that low resistivity and high transparency can be achieved in a very narrow range of oxygen pressure. In addition, in this work the oxygen pressure in the vicinity of 7.5 mTorr yields sufficient oxygen vacancies for the production of low resistivity ITO films. When the oxygen pressure is below 5 mTorr, resistivity increases in a reverse fashion. It can be explained that if many free electrons exist in ITO films the mobility is rapidly decreased by scattering with carriers or with structural defects (Kim et al., 1999a; , 2005a). A drop of conductivity is also related to a change in chemical composition and micro-crystalline structure of the ITO film (Kim et al., 2005a). Also optical transmittance is closely related to oxygen vacancies which is clearly seen in Figure 4.5. The transparency, e.g. below 7.5 mTorr, is reduced. The yellowish or brownish of ITO film at low oxygen pressure is related to carrier concentration (Dekkers et al., 2006). The transparency drops because of many electrons, delivered by the oxygen vacancies, or disordered lattice structures scatter the incident light (Kim et al., 2005a). It can be seen (see Figure 4.5) that with increasing oxygen pressure the transparency of the samples increases, reaching the highest value, of ~ 80%, at ~ 12 mTorr of oxygen pressure. With a further increase of oxygen pressure the transparency is less dependent on the oxygen pressure. The increase of transparency with increasing oxygen

pressure may be related to the improvement of the crystallinity of ITO film (Kim et al., 1999a). (This is discussed in section 4.3.1.3). At higher oxygen pressures the transmittance decreases due to narrowing band gap (Dekkers et al., 2006).

4.3.1.2 Influence of oxygen pressure on thickness and morphology of ITO films

Figure 4.6 shows thickness of ITO film deposited on glass substrates as a function of oxygen pressure. It is clear to see that the thickness decreases linearly, from 600 to 500 nm, with increasing oxygen pressure. This is consistent with the results reported previously (Adurodija et al., 1999; Yong et al., 2005). The decrease of film thickness is a result of increasing numbers of collision of oxygen particles with ejected species in the plasma, which in turn reduces the deposition rate (Zheng and Kwok, 1993; Kim et al., 1999b; Yong et al., 2005; Eason, 2007). Due to this, some particles ejected from the ITO target may not reach the substrate at all (Tian, 2009).

Figure 4.7 shows an SEM cross-sectional view of ITO films deposited on glass substrates under varying oxygen pressure. The decrease of ITO thickness with increasing oxygen pressure is evident. In addition, Figure 4.8 shows comparison of the ITO thickness measured by the two techniques; an SEM cross-sectional view and profilometer. The results of both techniques are comparable and for further thickness measurements a profilometer was chosen as a faster technique in comparison with SEM.

Furthermore, Figure 4.9 shows morphology of ITO films, investigated by atomic force microscopy (AFM), and deposited under varying oxygen pressure. For all cases ITO islands are clearly visible. The samples show very low roughness, RMS 〈 1nm. In addition the results show that the roughness is not dependent on the oxygen pressure in the range from 7.5 to 17.5 mTorr. The previous investigation (Kim et al., 2005a) showed that the roughness is dependent on oxygen pressure, and increases with oxygen pressure. However, the results were reported for higher range of oxygen pressure (15 – 75 mTorr) than that of this work.

4.3.1.3 Influence of oxygen pressure on structural properties

Figure 4.10 shows XRD patterns of ITO films deposited at different oxygen pressure. In all cases the ITO film exhibits a polycrystalline structure. ITO films deposited below 10 mTorr of oxygen pressure exhibit (222) and (400) orientation. However, the intensity of the peaks is low. Above 10 mTorr, with further increase of oxygen pressure, the (400) orientation disappears. By contrast, the intensity of (211) and (222) orientations increases with increasing oxygen partial pressure. These results are consistent with the results previously reported (Kim et al., 1999a; Guillen and Herrero, 2005). The columnar structure of the ITO film is clearly visible, e.g. in Figure 4.7 (b). The orientation depends on the mobility of arriving atoms, which is proportional to their energy (Vasant Kumar and Mansingh, 1989; Yong et al., 2005). The energy decreases with increasing oxygen pressure due to collisions between oxygen particles and highly energetic particles ejected from the ITO target (Vasant Kumar and Mansingh, 1989; Yong et al., 2005). Therefore, Figure 4.10 also shows that at 17.5 mTorr oxygen pressure the mobility of atoms is optimal to produce an ordered crystalline structure

with (211) and (222) preferred orientation. In contrast, below 10 mTorr oxygen pressure the intensity of the (211) and (222) peaks is very low due to highly energetic particles bombarding the growing film introducing lattice structural disorder and stress in the film (Yong et al., 2005; Tian, 2009). It is evident though, that the structural properties are strongly influenced by the oxygen partial pressure. In addition, the highly energetic species (due to severe oxygen deficiency) favour the formation of ITO films with low resistivity, as shown in Figure 4.5. This is consistent with the previous results (Kumar and Mansingh, 1989; Antony et al., 2004).

Furthermore, Figure 4.11 shows variation of grain size of crystallites as a function of oxygen pressure for (211) and (222) orientations. In both cases the grain size increases with increasing oxygen pressure. Therefore it is evident, that lower mobility of ejected species from the ITO target enhances lattice order. As a result a greater grain size is observed. This result explains the increase of transparency as a function of oxygen presented in Figure 4.5. However, it was previously found that above 50 mTorr of oxygen pressure the intensity of (222) peak decreases due to the lower mobility of ejected species hence leading to a less crystalline state (Tian, 2009).

Table 4.1 shows a summary of the results of ITO films achieved by varying the oxygen pressure. The lowest resistivity, equal to 3.1×10^{-4} (Ω cm), with corresponding transparency, of 74%, is obtained at the oxygen pressure, of 7.5 mTorr. Therefore, 7.5 mTorr oxygen pressure was chosen for further optimization processes.

4.3.2 Influence of target-to-substrate distance on ITO film properties

To investigate the influence of target-to-substrate distance on ITO film properties the following deposition conditions were applied: temperature set at 150 ^{o}C, number of pulses 5000, and 7.5 mTorr oxygen pressure.

4.3.2.1 Influence of target-to-substrate distance on resistivity and thickness of the ITO film

Figure 4.12 shows the influence of target-to-substrate distance on resistivity and thickness of the ITO film. With an increase in target-to-substrate distance from 55 to 65 mm, the resistivity slightly increases from 3.1 to 3.4 x 10^{-4} (Ω cm). This is due to lowering carrier concentration with target-to-substrate distance (Suzuki et al., 2002). The increase of resistivity may be related to the smaller grain size with the greater target-to-substrate distance; hence resistivity increases as a result of increase of grain boundaries, which causes a trap for free electrons and reduces their mobility (Antony et al., 2004). As Figure 4.12 shows, further increase of target-to-substrate distance does not influence resistivity of ITO film and its value remains constant. However, a strong influence of target-to-substrate distance on the thickness of the ITO film is observed. With increasing target-to-substrate distance the thickness of the ITO film decreases linearly from ~ 600 to ~ 200 nm. The decrease of thickness with increasing target-to-substrate distance is due to lowering the deposition rate of the ITO film (Suzuki et al., 2002).

4.3.2.2 Influence of target-to-substrate distance on transparency of ITO film

A monotonic decrease of transparency is observed with a decreasing target-to-substrate distance from 85 to 55 mm, as Figure 4.13 shows. This may be due to scattering caused by the large grains on the ITO film surface (Suzuki et al., 2002).

An increase of resistivity and transparency with increasing target-to-substrate distance is observed due to reduced deposition rate (Vasant Kumar and Mansingh, 1989; Suzuki et al., 2002).

The lowest resistivity, of 3.1×10^{-4} (Ω cm), is observed for 55 mm target to substrate distance. Therefore, this distance was chosen for further investigation.

4.3.3 Influence of number of pulses on ITO properties

To investigate the influence of number of pulses on ITO film properties, the following deposition conditions were applied: temperature set at 150 ^{o}C, 55 mm target-to-substrate distance, and 7.5 mTorr oxygen pressure. The number of pulses was varied from 1000 to 8000.

4.3.3.1 Influence of number of pulses on opto-electrical properties of ITO film

Figure 4.14 shows the opto-electrical properties of ITO film-coated glass substrates as a function of the number of pulses. It is clear to see that with an increase in number of pulses, from 1000 to 4000, the ITO resistance decreases rapidly from 6.0 to 1.5 Ω and then remains less dependent on the number of pulses (hence the thickness). This means that the carrier concentration and carrier mobility reach their maximum values in the vicinity of 4000 number of pulses (for 470 nm thick ITO film). This is consistent with the carrier concentration and Hall mobility measurements conducted by Kim et al. (1999a). The transparency of ITO/glass decreases, from 85 to 72%, with increasing the number of pulses, from 1000 to 8000. The decrease of resistance and transparency is due to an increase of the thickness of ITO film as the number of pulses increases. It was previously (Kim et al., 1999a) pointed out that the grain boundary decreases with increasing film thickness due to increase of the grain size of crystallites. Hence an increase of transparency should be expected due to reduction of light scattering at the grain boundaries. The decrease of transparency with increasing ITO thickness means that the boundary scattering is not the dominant scattering mechanism affecting transparency of the film (Kim et al., 1999a). With increasing thickness the transparency decreases due to interference phenomena (Kim et al., 2000) and increase of carrier concentration (Guillen and Herrero, 2008a, 2008b). A linear increase of ITO thickness is observed, as Figure 4.15 shows.

Figure 4.16 shows that the resistivity increases linearly with increasing the number of pulses. According to equation (2.4), this means that a significant increase of the thickness overcomes the decrease of resistance and dictates a final resistivity values. The lowest resistivity, of

3.0×10^{-4} Ω cm, and the highest transparency, of 85%, of the ITO/glass systems is achieved for 1000 number of pulses, which gives an ITO thickness of ~ 100 nm.

4.3.3.2 Influence of number of pulses on structural properties of ITO film

Figure 4.17 shows XRD spectra of ITO film deposited under varying numbers of pulses. With increasing number of pulses an increase of peak intensity for the (400) orientation is observed. This indicates that crystallinity increases with increasing number of pulses. The (400) diffraction peak indicates preferred orientation along the [100] direction (Kim et al., 1999a). However, amorphous films are achieved for the number of pulses equal to 1000, despite the fact that the films were deposited at a crystallization temperature of ITO. This means that the crystalline structure is thickness-dependent and the transition from an amorphous to crystalline structure is observed above 100 nm ITO thickness (or above 1000 number of pulses). The increase of intensity for the (400) orientation with increasing thickness is due to the increase of grain size (Kim et al., 2000). It was previously observed that the thicker the film, the higher the crystallinity (Kim et al., 1999a; Hao et al., 2008). With increasing grain size the grain boundary scattering decreases, which in turn causes an increase of carrier concentration and carrier mobility (Kim et al., 1999a). This explains the decrease of resistance as a function of the number of pulses presented in Figure 4.14.

Figure 4.18 shows grain size as a function of the number of pulses. It is clear that the grain size of crystallites in ITO film increases, from ~ 12.8 to ~ 14.5 nm, with an increase in the number of pulses from 1000 to 5000. Above 5000 number of pulses the grain size decreases.

A similar grain size, up to 14 nm, was observed at the deposition temperature ranging from room temperature to 200 ^{o}C (Kim et al., 1999b).

4.3.3.3 Influence of thickness on ITO film morphology

Figure 4.19 shows 3D-AFM images of the ITO surface as a function of thickness. It is clear to see that the ITO islands grow with an increase of thickness, as Figure 4.19 (a), (b) and (c) shows. Above a thickness of 600 nm agglomerates of ITO islands are visible, as Figure 4.19 (d) shows. In addition, all the ITO films with different thickness show very low roughness, below 1 nm. Kim et al. (1999b) also measured the roughness below 0.5 nm of ITO films deposited at low oxygen pressure (10 mTorr) by pulsed laser deposition. However, it is evident that the surface roughness increases with increasing ITO thickness, (see Figure 4.20). This is consistent with previous work conducted in (Kim et al., 2000; Qiao et al., 2004; Guillen and Herrero, 2008a), where it was pointed out that the roughness of the film increases due to increase of crystallinity. However, in Figure 4.20, a characteristic transition point from low to higher roughness is observed at the ITO thickness of ~ 450 nm (equivalent to 5000 number of pulses), which may be somehow related to the drop in grain size of the ITO film observed above 5000 number of pulses (see Figure 4.18).

In addition, structure and surface morphology have an influence on transparency; as the surface roughness increases with thickness the surface scattering is slightly enhanced which results in a drop of transparency (Hao et al., 2008), as was shown in Figure 4.14.

4.3.4 Influence of temperature on opto-electrical properties of ITO film

Figure 4.21 shows resistivity and transparency as a function of deposition temperature. With increasing substrate temperature resistivity decreases linearly, from ~4.0 to ~3.0 x 10^{-4} Ω cm. This is due to an increase of crystalline size which causes a decrease of grain boundary scattering (Kim et al., 1999b). Hence an increase of carrier concentration (Kim et al., 2005b) and Hall mobility is observed (Shin et al., 1999). It is also evident that transparency increases with deposition temperature, which may be also related to larger grain size formation. It should be noted that the further decrease of resistivity with further increase of temperature should be expected due to thermal activation of Sn into Sn^{4+} in ITO film, where substitution of Sn^{4+} for In^{3+} provides one electron to the conduction band (Adurodija et al., 2006; Dekkers et al., 2006). Thermal activation processes require the temperature to be equal to or higher than 150 ^{o}C. Therefore a small decrease of resistivity is observed in the range of temperature from room temperature to 150 ^{o}C. This is consistent with previous studies (Adurodija et al., 2006).

4.3.5 Summary of optimisation of the deposition process

The optimisation deposition process showed that the lowest resistivity, of 3 x 10^{-4} Ω cm, and the highest transparency, of 85% in the visible spectrum, of ITO-coated glass substrates can be achieved under the following deposition conditions: 150 ^{o}C temperature, 7.5 mTorr oxygen pressure, 55 mm target-to-substrate distance and 1000 number of pulses. In addition, the above conditions allow to achieve amorphous ITO films with thickness equal to ~ 100 nm.

4.3.6 ITO deposited on polymer substrates

After optimising the deposition process the following deposition conditions were used to deposit ITO film on PEN, PET and PC polymer substrates: room temperature, 7.5 mTorr oxygen pressure, 55 mm target to substrate distance and 1000 number of pulses. Room temperature deposition was chosen to minimise residual stresses in the film, which arise during the deposition process due to thermal mismatch between the ITO film and the polymer substrates.

4.3.6.1 Opto-electrical properties of ITO-coated polymer substrates

Table 4.5 summarizes the results of ITO films-coated polymer substrates. Resistivity and transparency were similar for all samples investigated, 4.6 – 5.4 x 10^{-4} Ω cm and ~ 80%, respectively. Transparency spectra for all samples are presented in Figure 4.22. The differences in resistivity between the samples may be related to the surface roughness of ITO/polymer systems. It should be noted that the resistivity of ITO polymer systems is higher than that of ITO/glass for the same deposition conditions. These results are opposite to the previously achieved (Shin et al., 2001; Guillen and Herrero, 2005). This may be related to the fact that a different deposition chamber was used to deposit ITO films on polymer substrates. It may be also a result of low density and surface energy of polymer substrates, which influence mobility of arriving atoms during thin-film growth.

4.3.6.2 Influence of thickness on opto-electrical properties and morphology of ITO-coated polymer substrates

With increasing thickness from 50 to 150 nm the ITO sheet resistance decreases from 105 to 40 Ω/□, as Table 4.6 shows. However, Figure 4.23 shows that the resistivity of ITO film-coated PEN does not change significantly and remains in the range from 5.3 to 6.0 x 10^{-4} Ω cm for a film thickness range 50 – 250 nm. Figure 4.24 shows transparency as a function of ITO thickness. It is clear to see that the transparency decreases linearly with increasing ITO thickness. The roughness of the ITO film increases with thickness, as Table 4.6 show. This is consistent with the results for ITO/glass systems investigated in the previous sections (see sections 4.3.3.1 and 4.3.3.3).

4.4 Conclusions

Opto-electrical, structural and morphological properties of ITO films pulsed-laser deposited on glass substrates were investigated as a function of a variety of deposition conditions such as temperature, oxygen pressure, target to substrate distance and number of pulses. The influence of PET, PEN and PC polymer substrates on morphology and opto-electrical properties of ITO films was also studied. All deposition parameters were found to have a strong influence on ITO properties.

Opto-electrical and structural properties are strongly dependent on oxygen pressure. Low resistivity ITO films can be achieved by reducing oxygen pressure during the deposition

process. The lowest resistivity, of 3 x 10^{-4} Ω cm, can be achieved only at the very narrow range of oxygen pressure, from 5 to 7.5 mTorr.

The thickness and opto-electrical properties can also be controlled by positioning the substrate at different distances with respect to the ITO target and applying different number of pulses. The lowest resistivity equal to 3 x 10^{-4} Ω cm was found for a 55 mm target-to-substrate distance, whereas the highest transparency was found for 1000 number of pulses.

All deposition parameters show a strong influence on ITO properties. The structural properties can be controlled by both the oxygen pressure and the film thickness. The transition from amorphous to crystalline state can be achieved by increasing the film thickness. High-quality, amorphous 100 nm thick ITO films with low resistivity, of 3 x 10^{-4} Ω cm and high transparency, of 85% in the visible spectrum, were successfully deposited on glass substrates at a temperature of 150 ^{o}C.

The results showed that by optimisation deposition parameters it is possible to achieve conductive ITO films coated polymer substrates at room temperature with stable resistivity (5 – 6 x 10^{-4} Ω cm) for different film thicknesses. This result is important for flexible display designers where low thickness of the film is necessary to increase flexibility whilst simultaneously maintaining low resistivity and high transparency for a high device efficiency.

Table 4.1 Summary of ITO/glass deposition results by varying oxygen pressure.

Oxygen pressure, P (mTorr)	Resistance, R (Ω)	Thickness, h (nm)	Resistivity, ρ (Ωcm)	Transparency, T (%)
2.5	1.3	600	3.5×10^{-4}	66
5	1.2	570	3.1×10^{-4}	67
7.5	1.2	570	3.1×10^{-4}	74
10	1.4	550	3.5×10^{-4}	76
12.5	2.1	525	5.0×10^{-4}	79
15	2.6	515	6.0×10^{-4}	79
17.5	3.5	510	8.0×10^{-4}	77
20	4.0	500	9.0×10^{-4}	76

Table 4.2 Summary of ITO/glass deposition results by varying target to substrate distance.

Target to substrate distance, d (mm)	Resistance, R (Ω)	Thickness, h (nm)	Resistivity, ρ (Ωcm)	Transparency, T (%)
55	1.2	570	3.1×10^{-4}	74
65	1.7	450	3.4×10^{-4}	77
75	2.5	300	3.4×10^{-4}	81
85	3.8	200	3.4×10^{-4}	79

Table 4.3 Summary of ITO/glass deposition results by varying number of pulses.

Number of pulses	Resistance, R (Ω)	Thickness, h (nm)	Resistivity, ρ (Ωcm)	Transparency, T (%)
1000	6.0	110	3.0×10^{-4}	85
2000	3.3	220	3.3×10^{-4}	84
3000	2.2	327	3.3×10^{-4}	77
4000	1.5	481	3.4×10^{-4}	76
5000	1.4	569	3.5×10^{-4}	76
6000	1.4	619	4.0×10^{-4}	74
7000	1.2	752	4.2×10^{-4}	72
8000	1.0	858	4.0×10^{-4}	72

Table 4.4 Summary of ITO/glass deposition results by varying deposition temperature.

Deposition temperature, ^{o}C	Resistance, R (Ω)	Thickness, h (nm)	Resistivity, ρ (Ωcm)	Transparency, T (%)
25	8.2	106	3.9×10^{-4}	79
65	7.4	106	3.6×10^{-4}	86
100	6.8	112	3.5×10^{-4}	83
150	6.0	110	3.0×10^{-4}	85

Table 4.5 Results of pulsed laser deposited ITO films on polymer substrates at room temperature.

Sample	Sheet resistance, R (Ω/□)	ITO thickness, h (nm)	Resistivity, ρ (Ωcm)	Transparency T (%)	Roughness, Rms (nm)
ITO/PEN	54	100	5.4×10^{-4}	80 ± 4.0	8.4 ± 0.5
ITO/PET	46.5	100	4.6×10^{-4}	80 ± 1.0	5.8 ± 0.16
ITO/PC	48	100	4.8×10^{-4}	79 ± 1.2	1.1 ± 0.21

Table 4.6 Results of pulsed laser deposited ITO films with varying thickness on PEN substrates at room temperature.

Sample	Sheet resistance, R (Ω/□)	ITO thickness, h (nm)	Resistivity, ρ (Ωcm)	Transparency, T (%)	Roughness, Rms (nm)
ITO/PEN	105.3	50	5.3×10^{-4}	84 ± 6.3	2.2 ± 0.5
ITO/PEN	46.5	100	5.4×10^{-4}	80 ± 4.0	
ITO/PEN	39.6	150	5.9×10^{-4}	77 ± 4.2	3.2 ± 0.4

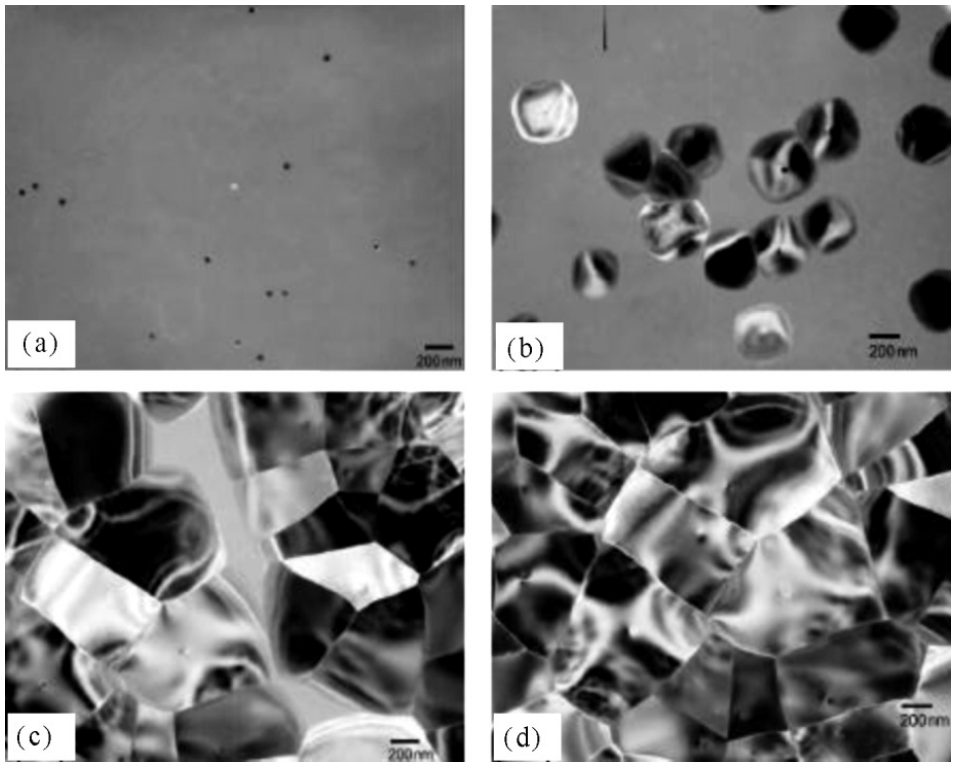

Figure 4.1 Crystallization of amorphous ITO film deposited by DC magnetron sputtering during annealing at 250 ^{o}C for a) 0, b) 0.5, c) 2.5 and d) 5 h. Adapted from (Yeom et al., 2002)

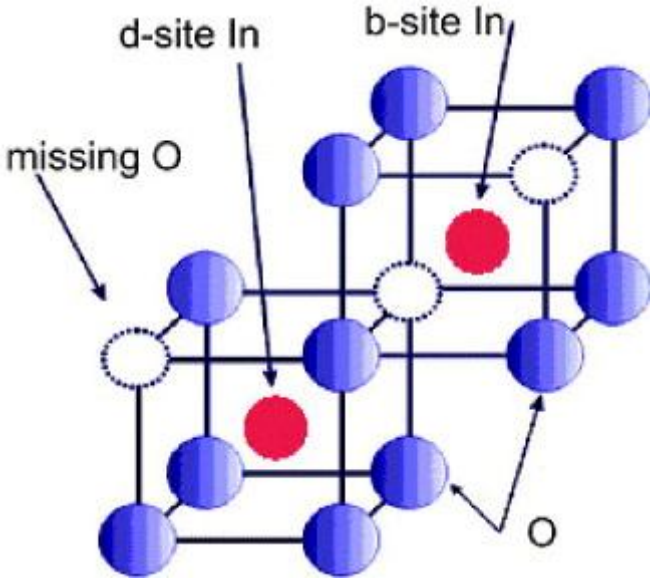

Figure 4.2 Cubic bixbyite structure of In_2O_3. Open circles denote oxygen vacancies, blue and red spheres indicate oxygen and indium atoms, respectively. A quarter of the oxygen anions are missing from the ideal structure. There are 48 anions in edge positions, 16 missing anions, 8 cations in b-positions and 24 cations in d-positions (80 atoms in total per unit cell). Adapted from (Janowitz and et al., 2011).

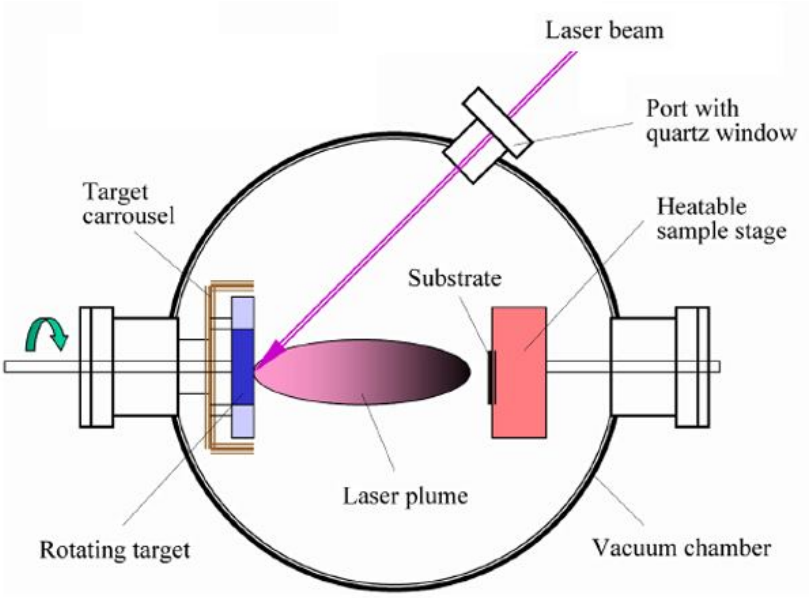

Figure 4.3 Schematic of pulsed laser deposition process. Adapted from www.pulsedlaser.net.

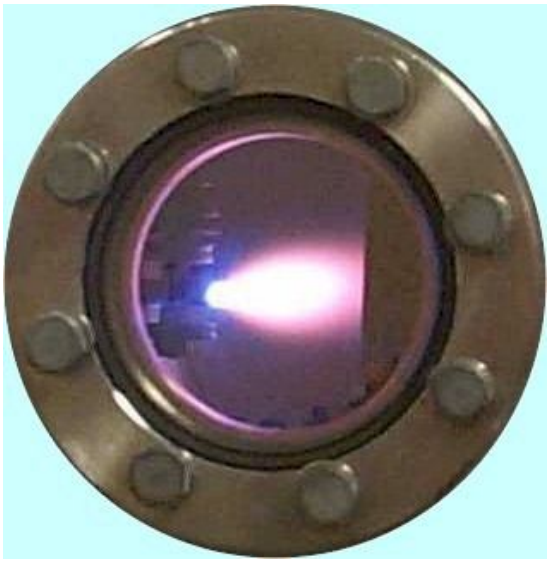

Figure 4.4 Ejected laser plume from material source during deposition process. Adapted from www.physics.unifr.ch.

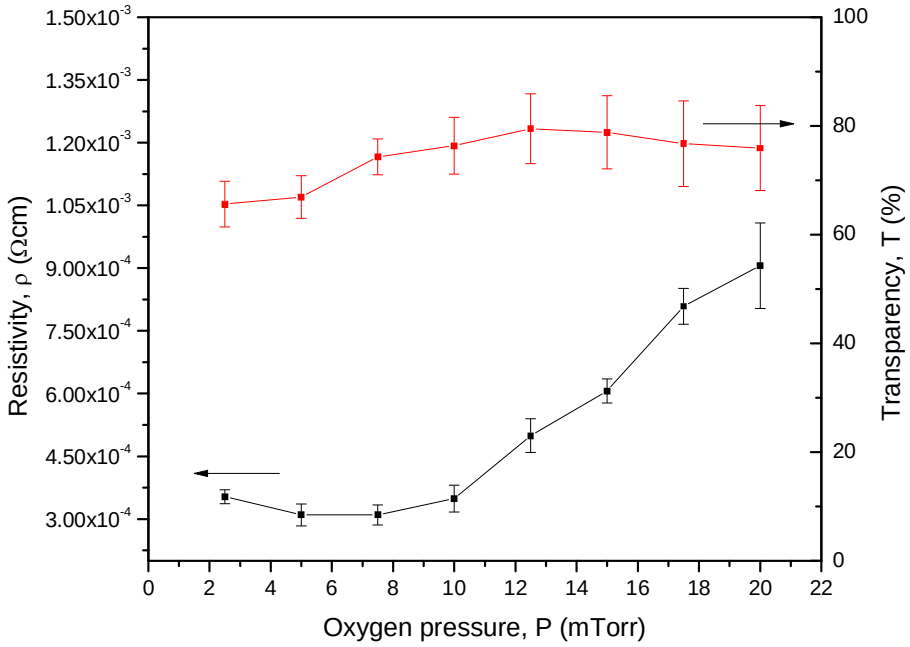

Figure 4.5 Resistivity and transparency as a function of oxygen pressure. Deposition parameters: 150 ^{o}C deposition temperature, 55 mm target-to-substrate distance and 5000 number of pulses.

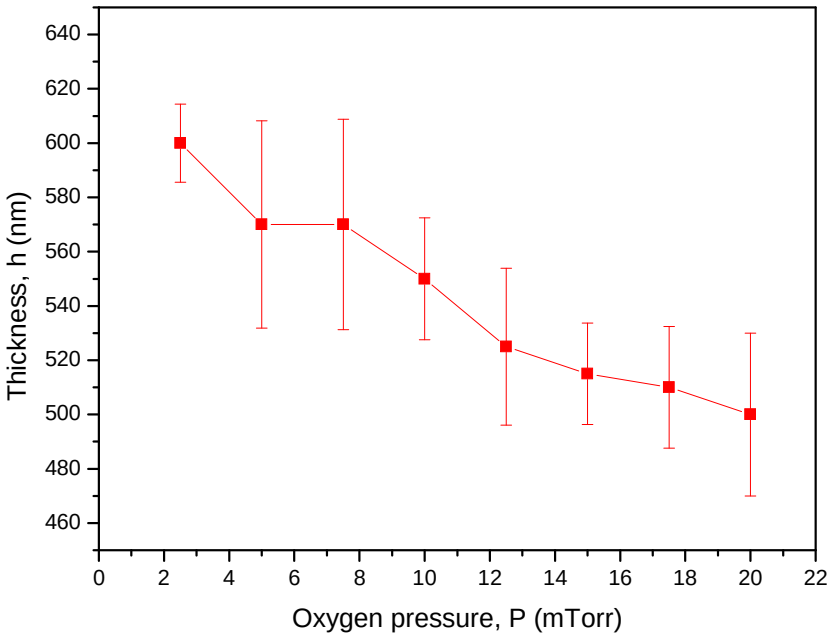

Figure 4.6 Influence of oxygen pressure on the thickness of ITO films. Deposition conditions: 150 ^{o}C deposition temperature, 55 mm target-to-substrate distance and 500 number of pulses.

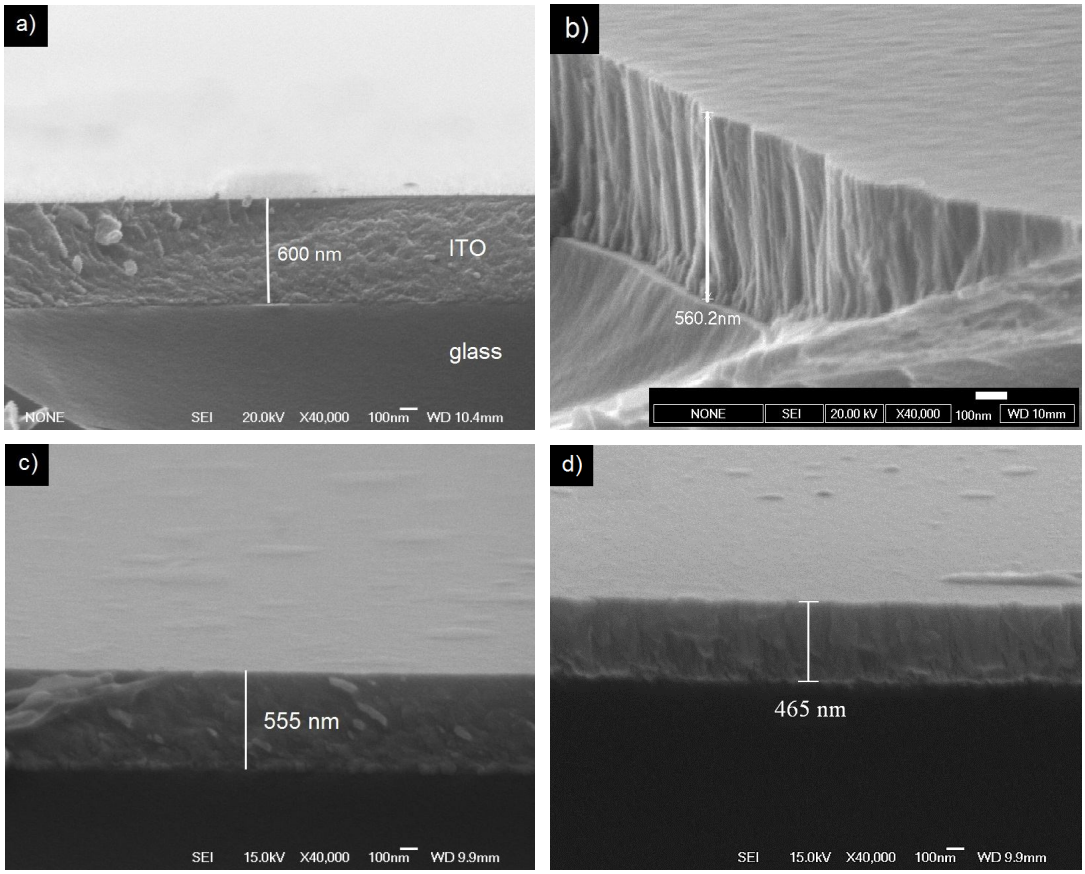

Figure 4.7 SEM cross sectional view of ITO films deposited on glass substrates at the different oxygen pressure: a) 7.5 mTorr, b) 10 mTorr, c) 15 mTorr and d) 17.5 mTorr.

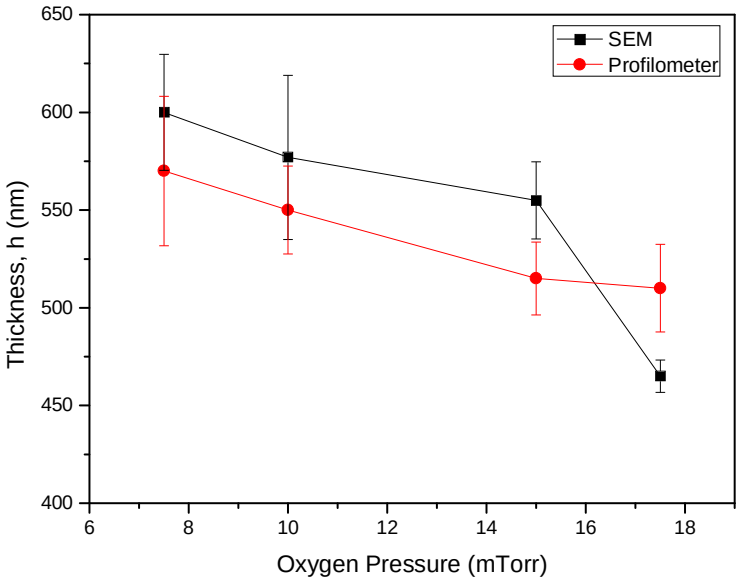

Figure 4.8 Comparison of thickness of ITO films conducted by profilometer and SEM (cross-section view).

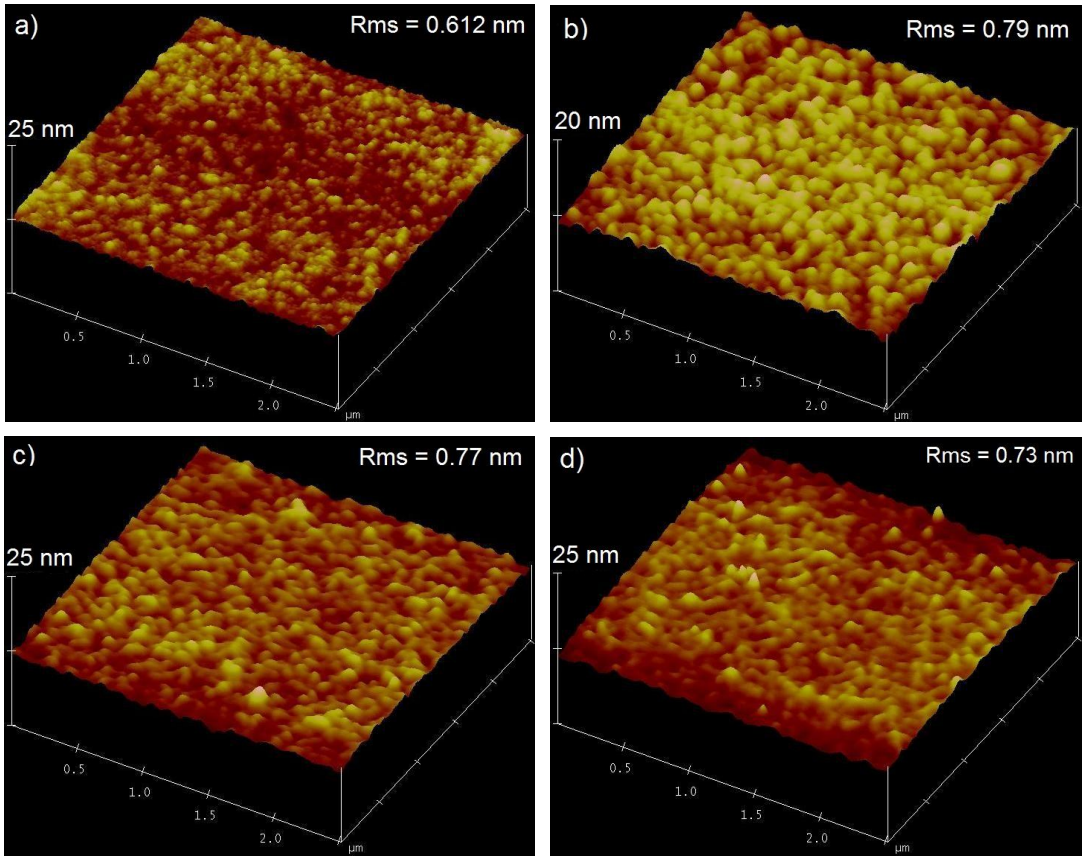

Figure 4.9 3D-AFM images showing surface morphology of ITO films deposited at different oxygen pressure: a) 7.5 mTorr, b) 10 mTorr, c) 15 mTorr and d) 17.5 mTorr.

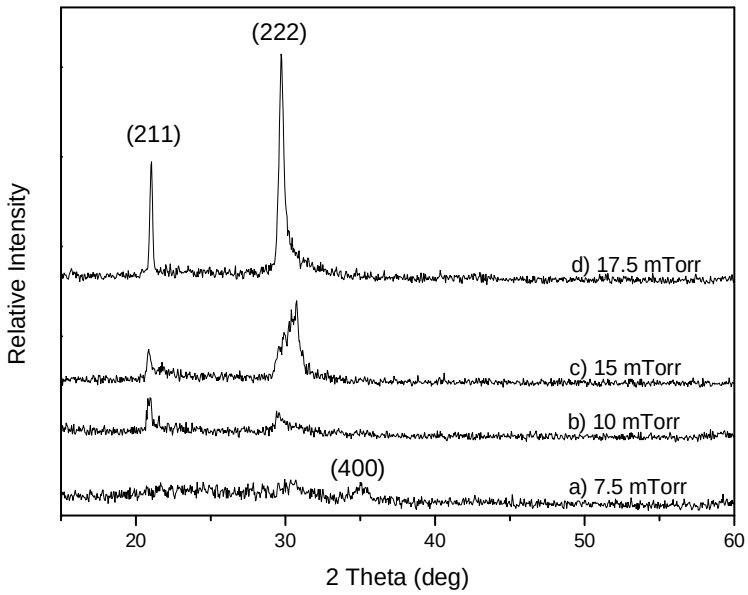

Figure 4.10 The XRD spectra of ITO films deposited on glass under varying oxygen pressure: a) 7.5 mTorr, b) 10 mTorr, c) 15 mTorr and d) 17.5 mTorr. Other deposition conditions used: 150 ^{o}C deposition temperature, 55 mm target-to-substrate distance and 5000 number of pulses.

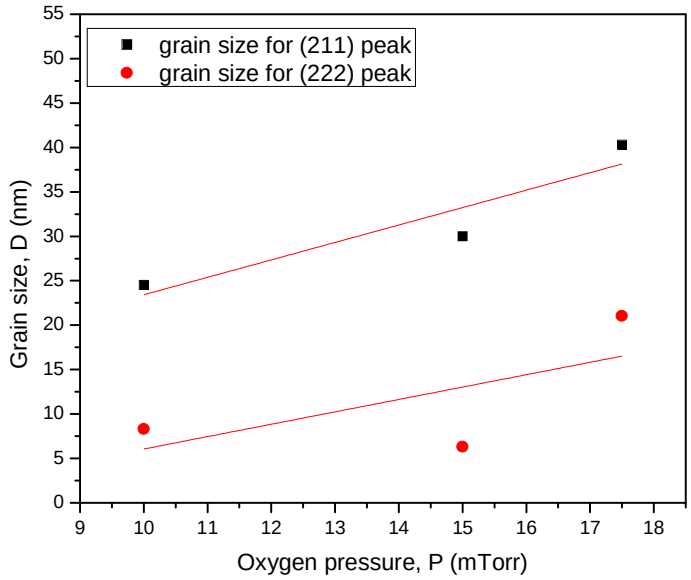

Figure 4.11 Variation of grain size as a function of oxygen pressure for (211) and (222) faze orientation. Other deposition conditions used: 150 ^{o}C deposition temperature, 55 mm target-to-substrate distance and 5000 number of pulses.

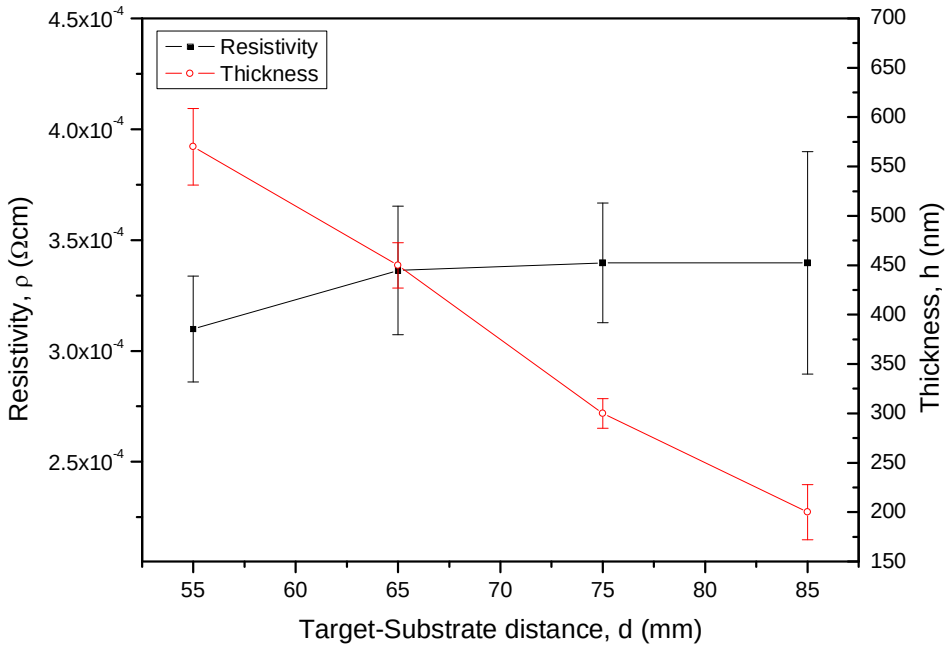

Figure 4.12 Resistivity and thickness of ITO film as a function of target-to-substrate distance. Other deposition conditions: 150 ^{o}C deposition temperature, 5000 number of pulses and 7.5 mTorr oxygen pressure.

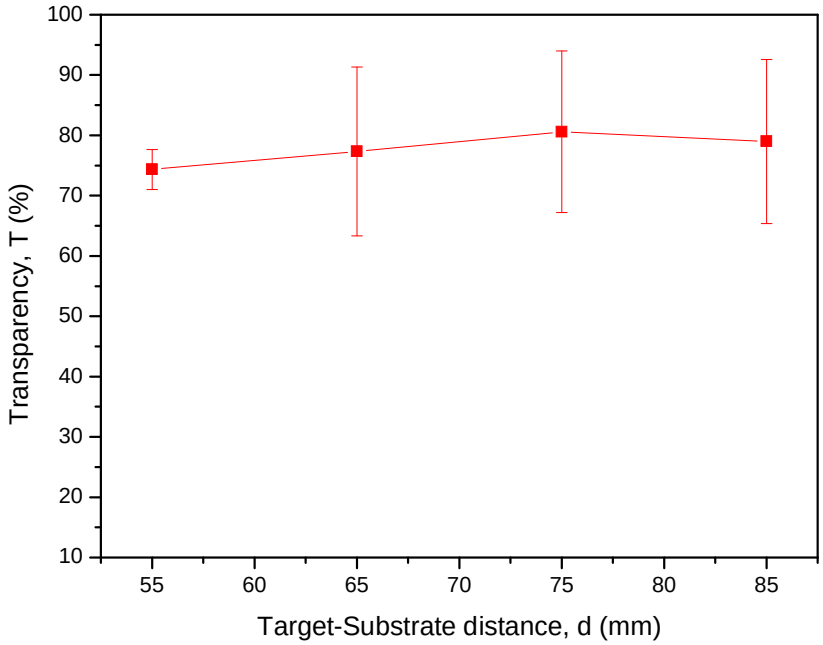

Figure 4.13 Transparency as a function of target-to-substrate distance. Other deposition conditions: 150 ^{o}C deposition temperature, 5000 number of pulses and 7.5 mTorr oxygen pressure.

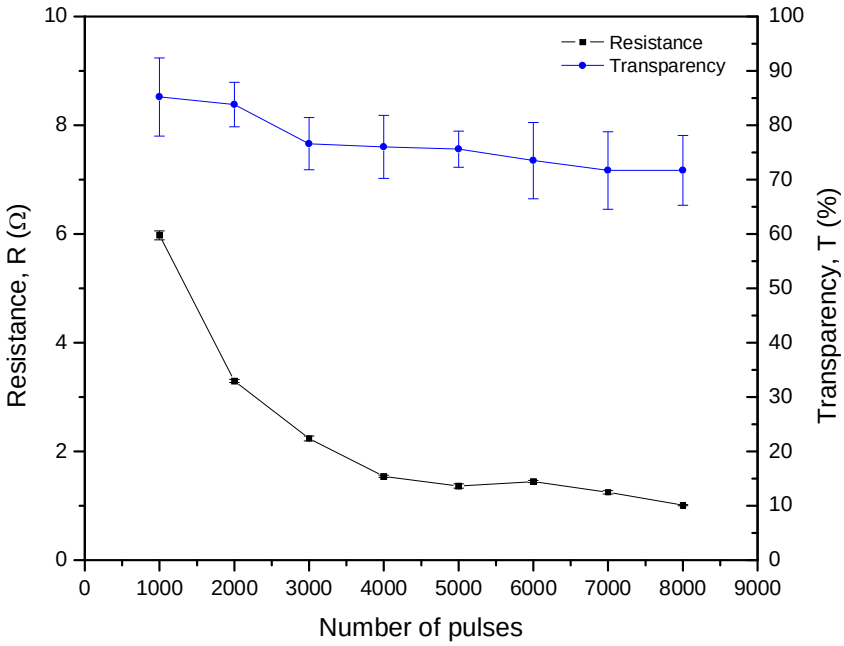

Figure 4.14 Resistance and transparency of ITO films coated glass substrates as a function of number of pulses. Other deposition parameters: temperature of 150 ^{o}C, 55 mm target-to-substrate distance and 7.5 mTorr oxygen pressure.

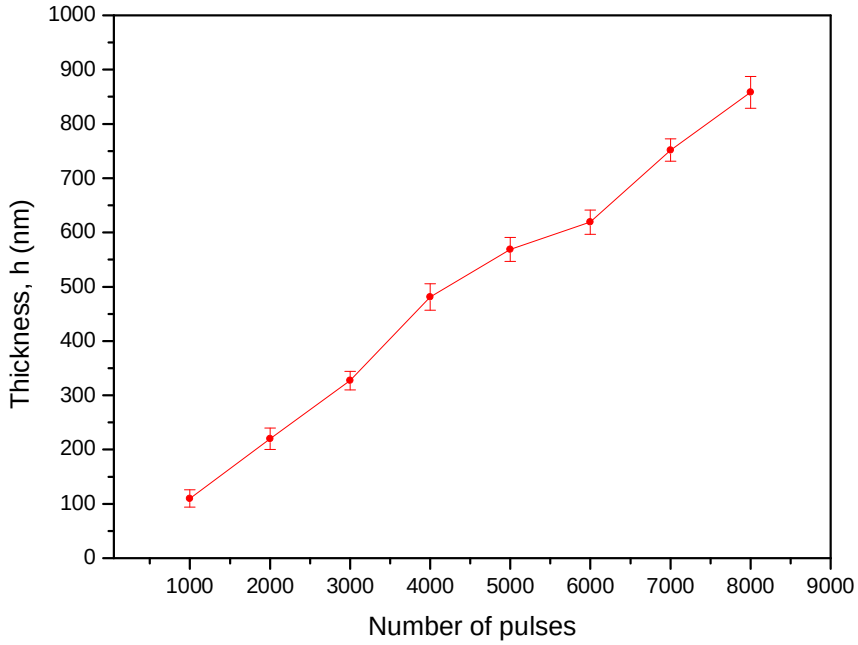

Figure 4.15 Thickness of ITO films coated glass substrates as a function of number of pulses. Other deposition parameters: temperature of 150 ^{o}C, 55 mm target-to-substrate distance and 7.5 mTorr oxygen pressure.

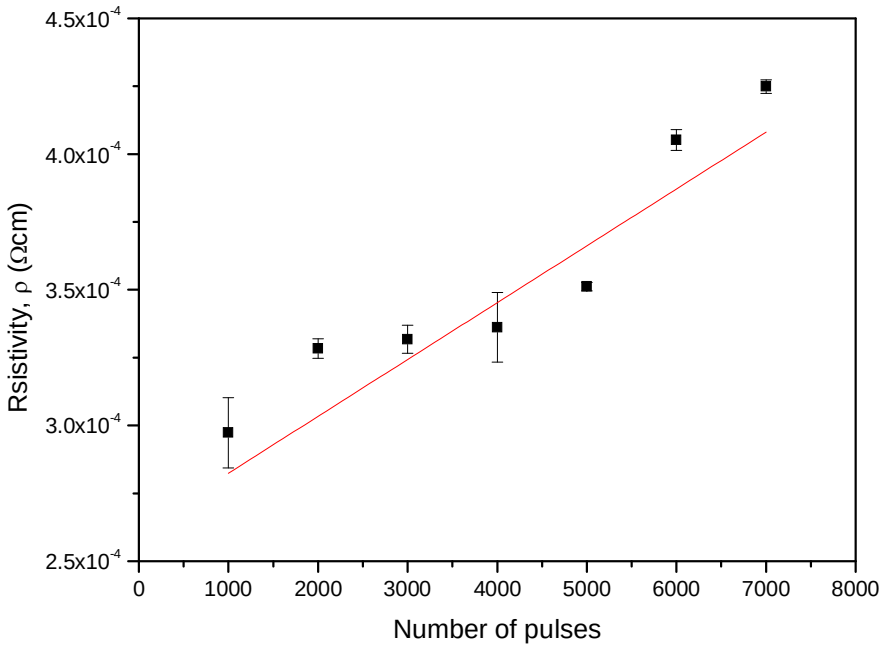

Figure 4.16 Resistivity of ITO film as a function of number of pulses. Other deposition conditions: 150 ^{o}C deposition temperature, 55 mm target-to-substrate distance and 7.5 mTorr oxygen pressure.

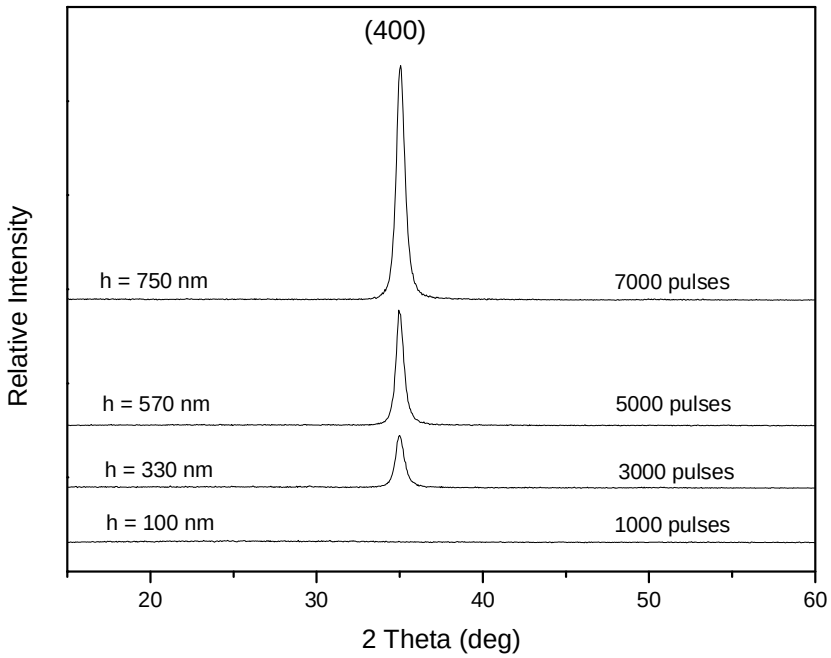

Figure 4.17 XRD pattern of ITO film coated glass substrates by varying number of pulses. Other deposition parameters: temperature of 150 ^{o}C, 55 mm target to substrate distance and 7.5 mTorr oxygen pressure.

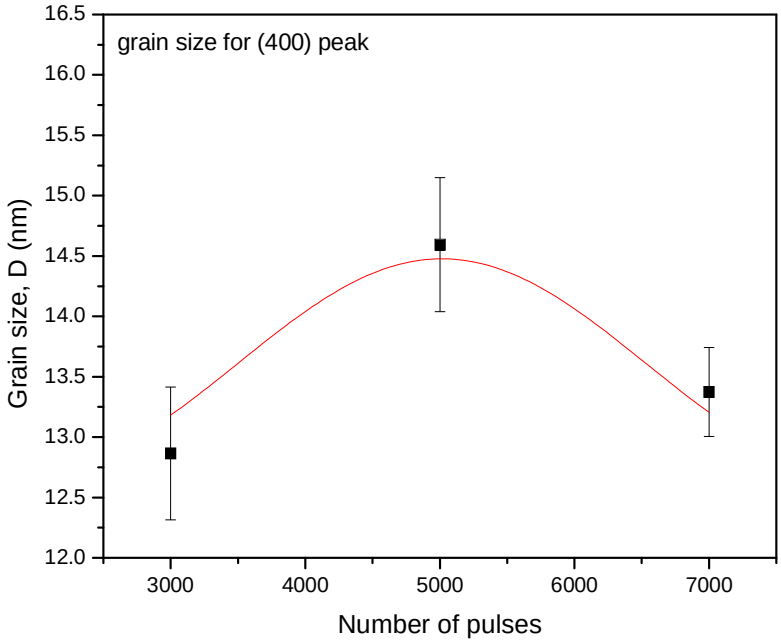

Figure 4.18 Variation of ITO grain size as a function of number of pulses. Other deposition parameters: temperature of 150 ^{o}C, 55 mm target-to-substrate distance and 7.5 mTorr oxygen pressure.

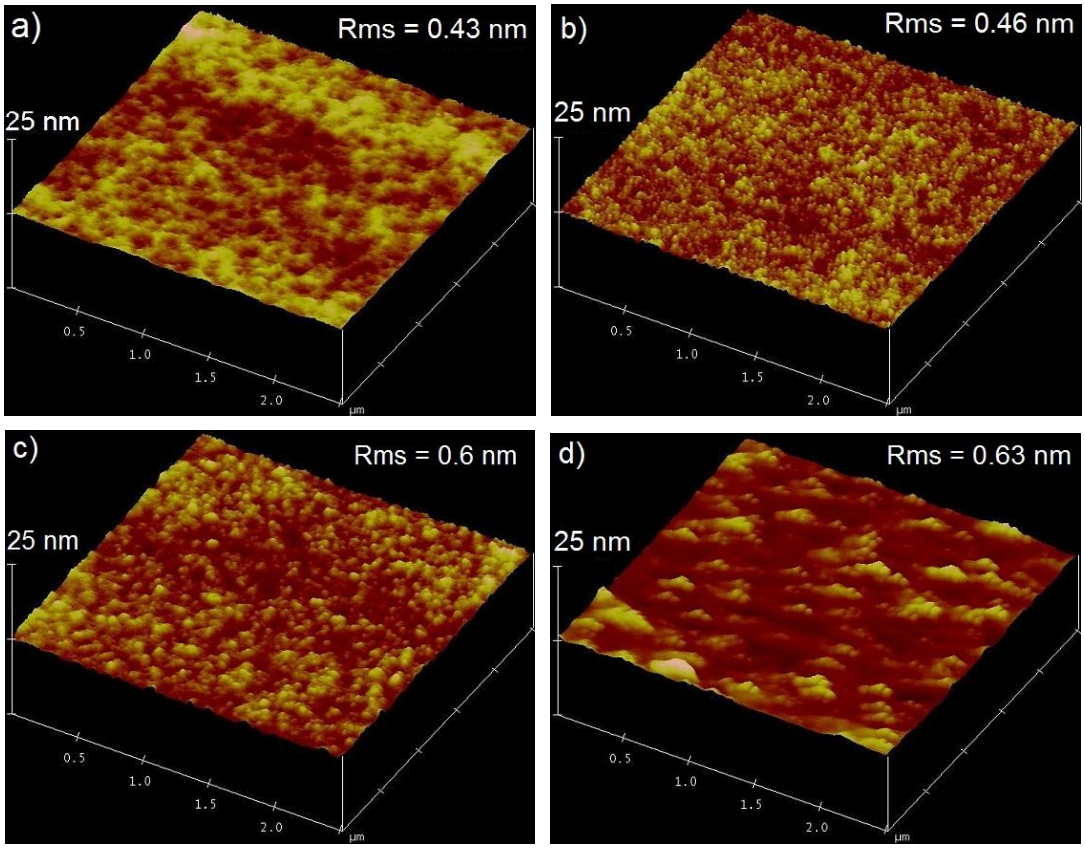

Figure 4.19 AFM images showing surface morphology of ITO films with different thickness: a) 100 nm, b) 330 nm, c) 570 nm and d) 750 nm. Other deposition conditions: 150 ^{o}C deposition temperature, 55 mm target-to-substrate distance and 7.5 mTorr oxygen pressure.

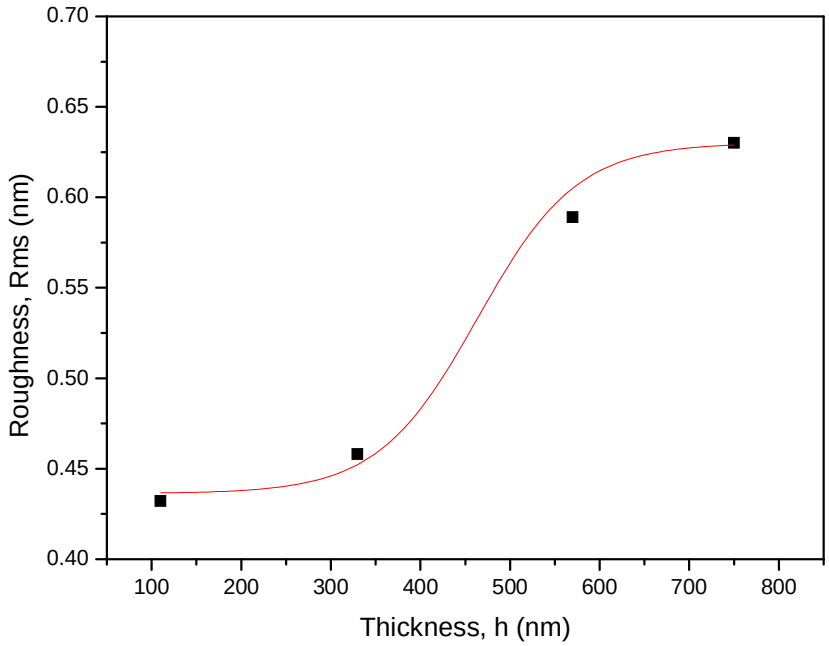

Figure 4.20 Roughness of ITO film as a function of thickness. Other deposition conditions: 150 ^{o}C deposition temperature, 55 mm target-to-substrate distance and 7.5 mTorr oxygen pressure.

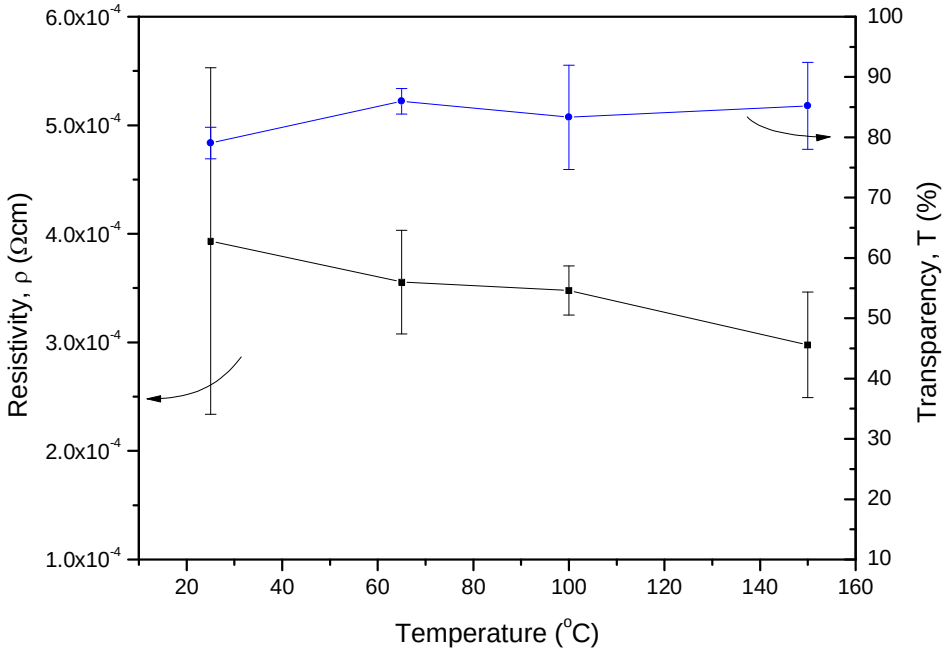

Figure 4.21 Resistivity and transparency of ITO film coated glass substrates as a function of deposition temperature. Other deposition conditions: 55 mm target-to-substrate distance, 7.5 mTorr oxygen pressure and 1000 number of pulses.

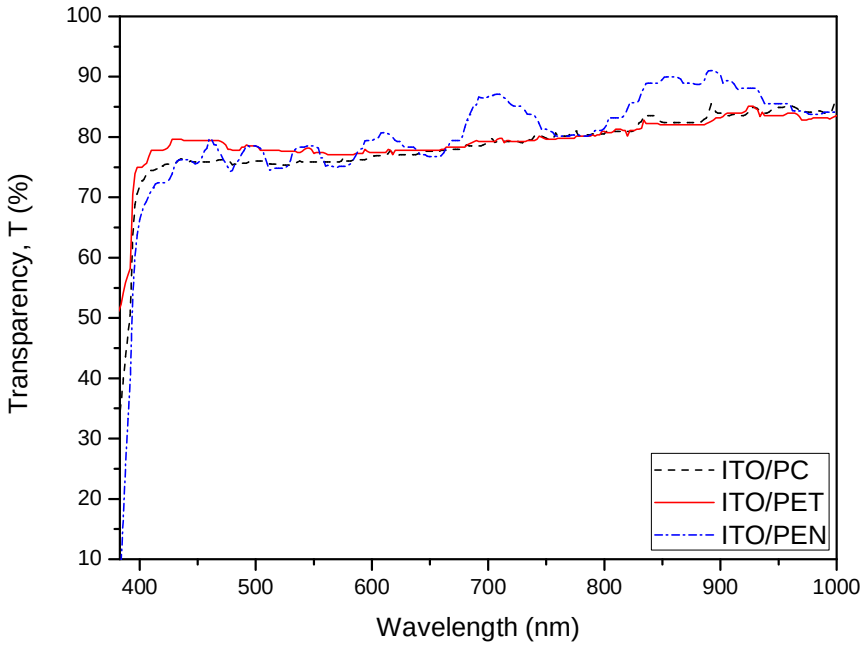

Figure 4.22 Transparency spectra of ITO-coated polymer substrates. Deposition conditions: room deposition temperature, 55 mm target-to-substrate distance, 7.5 mTorr oxygen pressure and 1000 number of pulses.

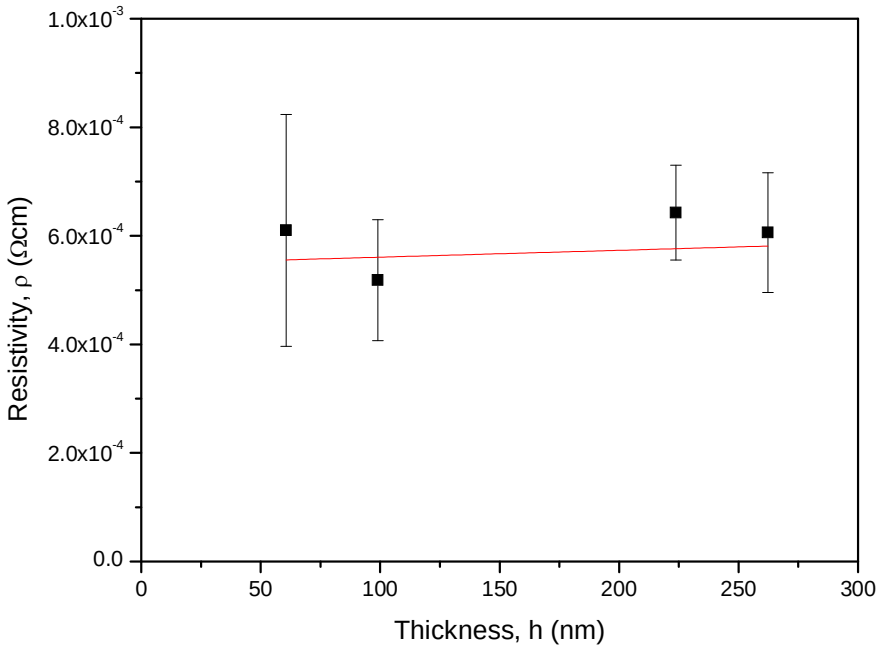

Figure 4.23 Resistivity as a function of thickness of ITO-coated PEN substrates. Deposition conditions: room deposition temperature, 55 mm target-to-substrate distance, 7.5 mTorr oxygen pressure and 1000 number of pulses.

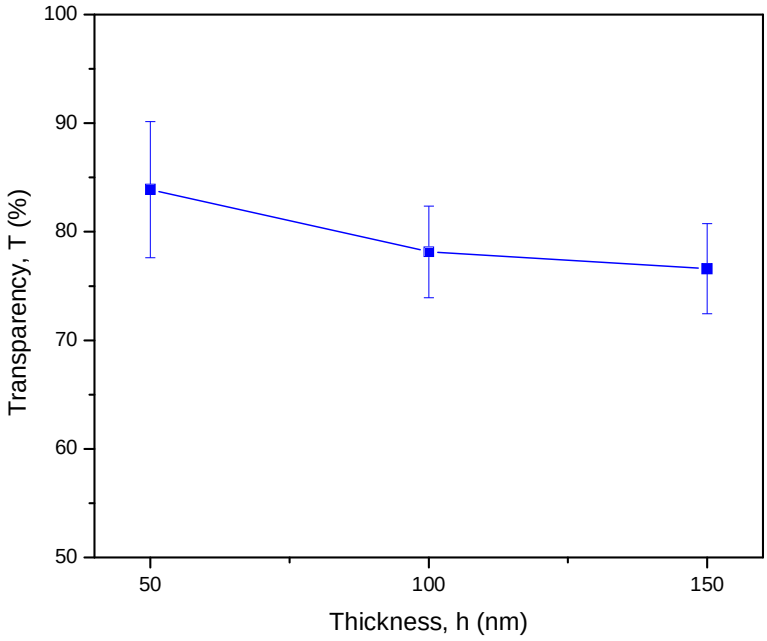

Figure 4.24 Transparency as a function of thickness of ITO-coated PEN substrates. Deposition conditions: room deposition temperature, 55 mm target-to-substrate distance, 7.5 mTorr oxygen pressure and 1000 number of pulses.

CHAPTER 5

5. CHARACTERISATION OF SOL-GEL DERIVED ITO FILMS

5.1 Sol-gel as a promising deposition method for transparent conductive thin films

ITO films are usually deposited on substrates by classical PVD methods (e.g. magnetron sputtering) which yield high-quality films, as discussed in the previous chapter. However, these methods are costly due to high wastage of the expensive ITO and the necessity to use vacuum systems. The deposition costs can be significantly reduced by novel wet deposition methods: the sol-gel and nanoparticle dispersion. These methods are more economical and allow the material to be printed on the substrate via roll-to-roll processes under atmospheric pressure (Koniger and Munstedt, 2008a). Moreover, the sol-gel technique allows to produce films with excellent homogeneity, easily-controlled thickness and doping level, and fabricate thin films on large and complex shapes (Park and Mackenzie, 1995; Kim et al., 1999c; Alam and Cameron, 2000). However, the resistivity of sol-gel thin films is found to be at least one order of magnitude higher than that obtained by other deposition methods, such as CVD, sputtering or spray pyrolysis (Goebbert et al., 2000). In addition, high annealing temperatures are necessary to remove organic residue; hence increase transparency and conductivity (Koniger and Munstedt, 2008a). In the case of flexible electronics, the challenge for sol-gel deposition is to reduce the curing temperature with limited effect on opto/electrical properties of the film to allow its deposition on temperature-sensitive polymer substrates. This can be

achieved by using post-deposition ultraviolet-irradiation treatment that has a strong impact on structural changes (densification and crystallisation) of the sol-gel derived films due to the thermal effects of powerful incident beams (Asakuma et al., 2003).

5.2 TCO deposition via sol-gel route

5.2.1 Sol-gel evolution mechanism of TCO thin films

Sol-gel is a chemical deposition process that can be used to form transparent oxide thin films. In this process the continuous liquid phase (gel) is achieved through the evolution of inorganic networks forming a colloidal suspension (sol) and then its gelation. Figure 5.2 shows this sol-gel chemical evolution process. In order to deposit TCOs, metal alkoxides and acetates (metal element surrounded by various reactive ligands) are commonly-used in the sol-gel process as precursors for synthesising colloids because they react readily with water to form the metal oxide (Klein, 1988; Exarhos and Zhou, 2007). Precursors usually are dissolved in alcoholic solutions with desired pH. The extended oxide network is produced through a slow hydrolysis process, which then can be transferred to the substrate by dipping or spin-coating techniques (Exarhos and Zhou, 2007). The presence of ROH groups (R represents alkyl group, e.g. $-CH_3$) in the hydrolysed precursors promotes bonding to the hydroxyl-covered glass surfaces while the oxide bonding reduces the reaction temperature required to densify the oxide (Douglas M, 1991). Following the coating process thermal treatment is necessary to remove the organic constituents (water and aliphatic alcohols) via volatilization and form the metal oxide (Klein, 1988; Exarhos and Zhou, 2007). Temperatures as low as

500 ^{o}C are usually used for the baking process leaving dense thin films (Douglas M, 1991). To form ITO films via sol-gel, indium and tin precursors are prepared separately and then mixed together. Figure 5.3 shows a flowchart of the sol-gel preparation procedure to achieve ITO films by the dip-coating technique. Due to the different solubilities and activities of the above-mentioned two precursors, segregation tendencies are observed. Recently, new precursor materials based on bimetallic In-Sn alkoxides as a single source have been developed to overcome this problem (Veith et al., 2011).

5.2.2 Sol-gel deposition of ITO films

Radhouane Bel Hadj *et al*. (1998) investigated the influence of tin concentration (0 – 20 at.%) in indium oxide films prepared via sol-gel, using indium acetate as precursor, on electrical conductivity. The 150 nm thick ITO films were dip-coated on glass substrates and baked at 650 ^{o}C. They observed that the carrier mobility of tin oxide films is higher than that of ITO film with Sn > 2 at.%. They obtained highly conductive ITO films with a resistivity of 3.2 x 10^{-4} Ω cm at a Sn doping range of 4 – 6 at.%. They concluded that above the Sn solubility limit in indium oxide (5 at.%) the ionised and neutral impurities (e.g. SnO and/or SnO_2) increased leading to decrease of carrier mobility; hence increase of resistivity. They also pointed out that the grain-boundary scattering plays a minor role in the scattering mechanism for their films.

Park and Mackenzie (1995) investigated the influence of dip-coating parameters, such as solution concentration, withdrawal speed and baking temperature on thickness and opto-

electrical properties of tin oxide films prepared from tin alkoxide. They pointed out that the thickness can be controlled only if the dip-coating parameters are known. They found good agreement between measured and theoretically-predicted film thickness with respect to the deposition speed. They observed that with increasing solution concentration the film thickness increases linearly. In addition, the thicker films showed better crystallinity and particle size. The resistivity decreased with increasing solution concentration, film thickness and baking temperature due to an increase of carrier concentration in the film. However, they observed that above 600 ^{o}C the resistivity increased as oxygen vacancies were compensated by oxygen from the atmosphere. This resulted in a drop of carrier concentration. They were able to achieve thin films with resistivity of 6 x 10^{-4} Ω cm, and high transparency of between 84 and 89% in the visible range.

Furthermore, structure, morphology and opto-electrical properties of sol-gel derived ITO films spin-coated glass substrates were studied by Kim et al. (1999c). Indium nitrate and tin acetate were used to form Sn-doped (10 wt.%) In_2O_3 films in different firing atmospheres (O_2, N_2 and air). It was found that polycrystalline ITO films were formed at 400 ^{o}C with no preferred orientation. In addition, the crystallinity and the size of crystallites were found to be not affected by post-annealing atmospheres. However, they observed that the firing atmosphere influences electrical properties. The lowest sheet resistance, of 0.7 x 10^{3} Ω/□ (for 350 nm thick films) was observed for ITO films annealed in a nitrogen atmosphere and the highest in oxygen. They postulated that the difference in sheet resistance between the atmospheres is due to different carrier concentrations. The spin-coated 150 nm thick films showed high transparency, > 80%, regardless of the fired atmosphere, high homogeneity and low surface roughness, < 2.5 nm.

Alam and Cameron (2000) prepared ITO films on glass substrates via a sol-gel route using non-alkoxide compounds and inorganic salts at temperature above 400 ^{o}C. They investigated the effects of Sn dopant concentration and annealing temperature on electrical and optical properties of ITO films. The samples were prepared by multiple dip-coating and a heat treatment procedure (after each dipping at 260 ^{o}C) to achieve the desired thickness of the film (~ 250 nm). They showed that with increasing annealing temperature (in air) the resistivity of ITO films significantly decreases and transparency increases due to enhancement of structural homogeneity and crystallinity. The lowest resistivity, of 1.5 x 10^{-3} Ω cm, and the highest transmittance, > 90%, was obtained at 600 ^{o}C for 10 wt.% Sn doping. With Sn content higher than 10 wt.% resistivity started to increase indicating that the best solubility of Sn atoms in In_2O_3 can be achieved for 10 wt.% doping with no evidence of Sn neutral complexes. In addition, they also prepared 10 wt.% Sn-doped tin oxide films on titanium dioxide films-coated glass substrates using the same sol-gel dip-coating procedure (Alam and Cameron, 2001) and achieved slightly lower resistivity, of 9.5 x 10^{-4} Ω cm and the same transparency at lower firing temperature equal to 500 ^{o}C. Moreover, Sutapa Roy (2001) also studied the influence of Sn content in tin oxide films prepared via sol-gel using metal salts and fired at 500 ^{o}C in air. He also found that the lowest sheet resistance, of 95 Ω/□, of ~ 500 nm thick ITO films can be achieved for In/Sn ratio equal to 90/10 with no presence of crystalline phases corresponding to oxides of tin. It was observed that with annealing treatment, conducted at 550 ^{o}C in N_2/H_2 atmosphere, sheet resistance significantly decreased down to 11 Ω/□, which gives the lowest final resistivity equal to 5.4 x 10^{-4} Ω cm. They pointed out that this decrease in resistivity may be due to an increase in oxygen vacancies resulting in the increase in carrier concentration.

Goebbert *et al*. (2000) investigated the influence of the single-layer thickness and three different dip-coating procedures on the morphology and electrical properties of sol-gel prepared antimony-doped tin oxide, aluminium-doped zinc oxide and tin-doped indium oxide (ATO, AZO and ITO, respectively) multilayer coatings. They observed that by changing the thickness of individual layers in multilayer coatings, the structural and morphological properties can be controlled. They found that thick single layers are made of small spherical crystallites and exhibit high surface porosity and high resistivity, of ~ 10^{-2} Ω cm, due to low density. Lower resistivity, of ~ 10^{-3} Ω cm, was found for the single layers with thickness below 20 nm due to dense columnar growth of the crystallites.

Su *et al*. (2005) investigated the influence of annealing temperature, annealing time, tin content and morphology on opto-electrical properties of dip-coated sol-gel derived ITO films on glass substrates using indium nitrate [$In(NO_3)_3 \bullet 4.5H_2O$] and anhydrous tin chloride ($SnCl_4$) as precursors. They found that the lowest resistivity, of ~ 7.7 x 10^{-2} Ω cm can be achieved for 8 wt.% Sn content, 550 ^oC annealing temperature and 30 minutes annealing time. They pointed out that this is due to crystallisation, grain size grow of crystallites and densification of ITO film. It was also observed that low resistivity is due to uniform morphology with no presence of cracks and voids, regardless of annealing time. However, high annealing time may create more defect sites and an increase in resistivity. It was found that with decreasing film thickness (from 530 to 200 nm) the resistivity increased due to an increase in surface roughness (from 1.2 to 2.7 nm) which is associated with aggregate formation of surface defects that hampered the electron transfer. Furthermore, Ting *et al*. (2011) prepared dip-coated sol-gel derived ITO films on glass substrates using anhydrous indium nitrate [$In(NO_3)_3$] and anhydrous tin chloride as starting materials. They claimed

resistivity of 4.3 x 10^{-3} Ω cm and visible transmittance, of ~ 90%. Other authors (Li et al., 2011) prepared so-gel ITO films using hydrous indium nitrate [$In(NO_3)_3 \bullet 4.5H_2O$] and hydrous tin chloride ($SnCl_4 \bullet 5H_2O$) as starting materials. They achieved slightly lower resistivity equal to 3.5 x 10^{-3} Ω cm and higher optical transmittance, 97%, for 175 nm thick ITO films.

Asakuma *et al*. (2003) prepared low-temperature sol-gel ITO films derived from alkoxide sources and spin coated on glass, PET, polyimide, PC and polyether-ether-ketone (PEEK) polymer substrates. After drying at 100 ^oC the samples were treated with a UV irradiation beam in order to improve structural and opto-electrical properties of the ITO films. They observed that for ITO-coated glass the crystallinity increases with increasing number of laser shots. The lowest resistivity, of 3.1 x 10^{-2} Ω cm, was achieved for the 20 mJ/cm^2 laser fluence with 100 shots. However, with increasing an number of laser shots, the transmittance decreased due to scattering at the rough film surface. They pointed out that the laser-treated film surface is porous due to removal of residual organic compounds. In the case of ITO-coated polymer substrates, the lowest resistivity, of ~ 6.2 x 10^{-2} Ω cm, was achieved for ITO-coated PET and polyimide under 20 mJ/cm^2 laser fluence with 10 shots. However, no conductive films prepared on PC and PEEK were observed. They observed that the high resistivity of ITO/PC and ITO/PEEK systems is due to the cracking of the ITO film which may be attributed to the damage of polymer substrates under UV irradiation. They concluded that proper control of the film thickness and the irradiation conditions are necessary to avoid damage to some polymer substrates and improve electrical conductivity.

Al-Dahoudi and Aegerter (2003) prepared ITO films on polymer substrates (PMMA and PC) at low temperature (130 ^{o}C) using already conductive, crystalline ITO nanoparticles dispersed in alcohol. ITO particles were modified by adding a binder (hydrolyzed 3-methacryloxypropyltrimethoxysilane) to favour coalescence of particles and to allow the deposition of thick single layers. Dip and spin-coating deposition techniques were employed. Before firing in air, UV irradiation curing was used to break C=C and C=O bonds and reduce resistivity by making conductive Si – O – Si networks in the film. They observed that the sheet resistance after UV curing and annealing is not stable in an air atmosphere and increases with time. The lowest stable resistivity equal to 9 x 10^{-2} Ω cm was achieved with transmittance, of ~ 87%, in the visible spectrum for 570 nm thick ITO film coated polycarbonate substrates.

Koniger and Munstedt (2008a) investigated the influence of polymer substrate (PET, PEN, PEEK and PI) with different thermal stabilities and surface roughness on opto-electrical properties of ITO films deposited by nanoparticle-dispersion method. They dispersed ITO nanoparticles in ethanol and applied an 3 – 4 μm thick ITO layer on the substrates. Then the samples were annealed at the maximum operating temperature with respect to the substrate. They observed that the greater roughness causes higher sheet resistance due to the formation of inhomogeneous films through which the electrons cannot pass easily. ITO-coated PET and PEN shown one order of magnitude lower resistivity (0.6 and 0.9 Ω cm, respectively) than ITO-coated PEEK and PI (3.0 and 1.5 Ω cm, respectively) due to their lower roughness. The 3 μm thick ITO-coated PET exhibited high transparency in the visible range, of ~ 85%, required for optoelectronic devices. They pointed out that annealing cannot improve conductivity on rough surfaces because high roughness impedes formation of homogenous films.

5.3 Results and discussion

The series of experiments aiming to develop conductive ITO ink following the steps as presented in the flowchart of Figure 2.1 did not provide promising results. The formulated ITO inks, printed on both glass and polymer substrates were not conductive even if they were heated to the maximum allowed annealing temperatures. The baked films on glass substrates at high temperatures (up to 600 ^{o}C) showed a lack of film continuity shown by cracks and voids (see Figure 5.1 as example) which in turn led to non-conductive products. This can be attributed to the evaporation of solvents and decomposition of partially hydrolyzed and condensed indium neodecanoate and tin neodecanoate in the films (Park and Mackenzie, 1995). In addition, post-printing UV irradiation did not help to improve opto-electrical properties of ITO films. These results are not presented in this work. Only the best achieved results are presented here and a description of the characterised samples can be found in chapter 2.

5.3.1 Morphology and quantitative analysis of ITO/glass systems

Figure 5.4 shows SEM micrographs of the surface of all samples investigated. White agglomerates on the surface are clear to see for all samples. However, the sample 0509 dip-coated at a rate of 5 mm/min [see Figure 5.4 (c)] exhibits bigger agglomerates compared with the rest of the samples. Moreover, the sample 0509 dip-coated at a rate of 10 mm/min [see Figure 5.4 (d)] exhibits craters in some places. These are probably left by white agglomerates, which were wiped off from the surface. Samples made from $In(ND)_3$ batch 1 (0309) exhibit slightly better surface quality than coatings made from $In(ND)_3$ batch 2 (0509). Despite white

agglomerates, all samples show good film continuity and smoothness. In addition, Figure 5.5 shows film surface profiles obtained by stylus profilometer. All samples exhibit smooth surfaces comparable with the glass substrate. However, a high peak is observed at the edge of the film for all samples investigated. This may be related to the dip-coating process for the ITO films.

Table 5.1 shows quantitative analysis conducted by SEM/energy diffraction X-ray (EDX) of indium content inside and outside the white agglomerates previously observed by SEM (see Figure 5.4). The content of indium (In) was found in both inside and outside agglomerates. In addition, the In content is almost the same throughout the analyzed sample. The presence of agglomerates in the film is due to the tendency of indium and tin precursors to segregation because of their different activities and solubilities (Veith et al., 2011). The different content of indium between samples may be due to different thickness and a different $In(ND)_3$ batches used for the wet-coating preparation. The measurements show that all the samples exhibit good homogeneity. In addition, quantitative analysis showed (see Table 5.2) that the tin/indium ratio in the 0309 samples is higher compared to the 0509 samples due to higher content of tin. The content of oxygen and indium is similar for all the samples investigated.

5.3.2 Structural investigation of ITO/glass systems

Figure 5.6 shows a wide angle XRD (WAXD) of dip-coated samples. Peaks at 30.6 2 theta (deg) indicate that the crystalline phase was formed with a characteristic for In_2O_3 (222) orientation (Kim et al., 1999c). This may suggest that ITO films are formed. The intensity of

the crystalline peak is very low and not sharp enough for further investigation. Glancing angle XRD (GAXD) was introduced to eliminate background noise originating from the substrate and to allow grain size calculation using Scherrer's formula [see equation (2.2)]. The GAXD spectra are presented in Figure 5.7, where the (222) peak for all samples investigated is clearly visible. Table 5.3 shows the grain size of dip-coated samples. The grain size equal to ~ 7.0 nm is very small and the same for all samples. Moreover, two different $In(ND)_3$ batches used for coating formation do not have an influence on the intensity of the crystalline phase peaks and hence the grain size. Similar grain size, of ~ 7.0 nm, to those of this work were found for ~ 250 nm thick SnO_2 films prepared via sol-gel for dip-coated glass substrates (Park and Mackenzie, 1995).

5.3.3 Opto-electrical properties of ITO-coated glass substrates

Table 5.4 shows the opto-electrical properties of dip-coated glass substrates with hydrolysed In/Sn(ND). The 0509 samples made from $In(ND)_3$ batch 2 exhibit better electrical properties and slightly lower transparency than the 0309 samples made from $In(ND)_3$ batch 1. The 0509 samples coated at the rate of 10 mm/min exhibit the lowest resistivity, of 1.85×10^{-2} Ω cm, and good optical transmittance in the visible spectrum (~ 80%). Moreover, it is clear to see that both optical and electrical properties depend on the layer thickness. For both batches investigated lower resistivity is observed for the thicker films. This is consistent with previous investigations (Sutapa Roy, 2001; Guillen and Herrero, 2008b), where it was pointed out that with increasing layer thickness, conductivity increases due to an increase of carrier concentration. The higher resistivity of the 0309 samples may also be related to the content of

tin in the films. The tin atoms may act as scattering centres for free electrons and reduce their mobility (Adurodija et al., 2002; Dekkers et al., 2006). It was found for ITO prepared via the so-gel route that a doping concentration exceeding the solubility limit of tin results in decreasing carrier mobility and concentration (Radhouane Bel Hadj et al., 1998). This takes place when Sn atoms can-not be substituted for In sites and act as donors. Instead, Sn(IV) atoms are changed to Sn(II) and act as acceptors (Kim et al., 1999c). The decrease of resistivity and transparency with thickness was also reported in (Hao et al., 2008).

5.4 Conclusions

A crystalline structure with a grain size of crystallites equal to ~ 7 nm was achieved for all samples investigated, regardless of the thickness of the films. The characteristic (222) orientation indicates that the sol-gel derived ITO film was formed.

The opto-electrical properties were found to be dependent on the thickness and the $In(ND)_3$ batch used. The lowest resistivity, of 1.8 x 10^{-2} Ω cm, for 175 nm thick ITO films, was achieved for $In(ND)_3$ batch 2 probably due to it having the lowest Sn/In ratio. The sample exhibited optical transmittance, of ~ 80%, in the visible range. The high resistivity is due to the low grain size of crystallites which increases grain boundary scattering; hence reduces carrier mobility and concentration. High resistivity could be also a result of incomplete formation of In – O – Sn networking in the film.

The original objectives of the SOLFLEX project of developing a low-temperature conductive ITO ink printable on polymer substrates were not achieved. In addition, the required conductive films with low sheet resistance between 10 – 100 Ω/□ and high optical transparency above 80% for end applications were not met even for ITO-coated glass substrates annealed at the temperature of 600 ^{o}C. Therefore, a pulsed-laser deposition system was employed to deposit ITO films on polymer substrates at low temperatures and meet the requirements for end applications. Pulsed-laser deposited ITO films on polymers enabled the investigation their electro-mechanical reliability which was not possible for the samples derived from the SOLFLEX project.

Table 5.1 SEM/energy diffraction x-ray (EDX) quantitative analysis of In content in the films.

Sample ; coating rate	Element	Weight %	
		Inside agglomerates	Outside agglomerates
0309 ; 10 mm/min	In	14.9	16.1
0309 ; 20 mm/min	In	19	18.4
0509 ; 5 mm/min	In	18.6	19.2
0509 ; 10 mm/min	In	26.6	26.7

Table 5.2 SEM/energy diffraction x-ray (EDX) quantitative analysis of O, In and Sn content in the films.

Element wt. %	Sample ; dposition rate			
	0509 ; 5 mm/min	0509 ; 10 mm/min	309 ; 10 mm/min	309 ; 20 mm/min
O	24.6	21.1	24.3	25
In	50	61.8	50.9	51.1
Sn	3.2	3.36	3.95	4.75
Sn/In ratio	**0.064**	**0.054**	**0.077**	**0.093**

Table 5.3 Grain size of dip-coated samples.

Sample ; deposition rate	Grain size D (nm)
0309 ; 10 mm/min	6.92 ± 0.059
0309 ; 20 mm/min	6.68 ± 0.234
0509 ; 5 mm/min	6.91 ± 0.130
0509 ; 10 mm/min	6.95 ± 0.247

Table 5.4 Optical and electrical properties of dip-coated glass substrates with hydrolysed In/Sn(ND).

Sample ; deposition rate	Thickness, h (nm)	Sheet resistance, R_s (Ω/□)	Resistivity, ρ (Ωcm)	Transparency, T (%)
0309 ; 10 mm/min	140	3,500	4.9×10^{-2}	86
0309 ; 20 mm/min	184	1,650	3.0×10^{-2}	85
0509 ; 5 mm/min	125	3,000	3.7×10^{-2}	83
0509 ; 10 mm/min	175	1,055	1.8×10^{-2}	80

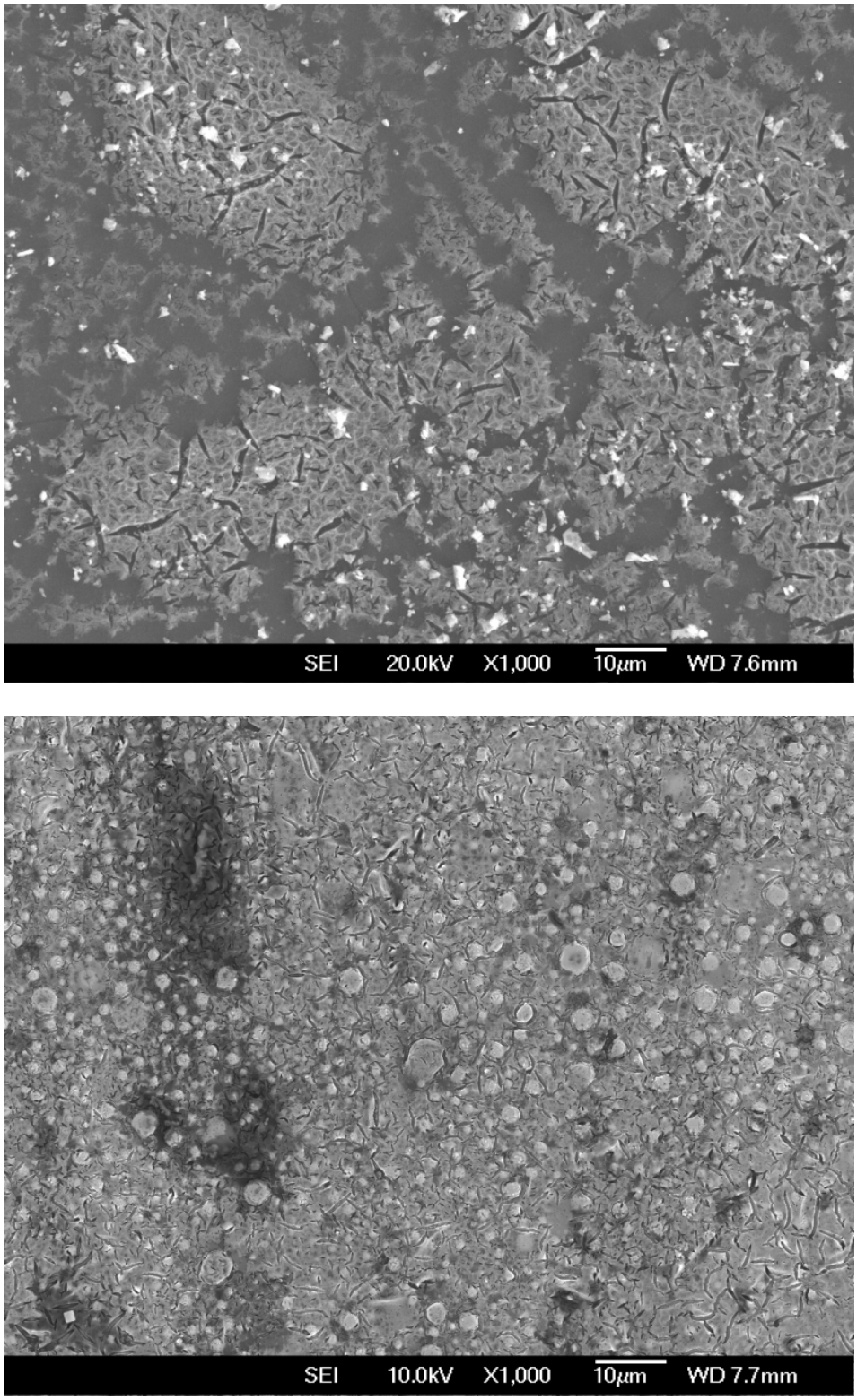

Figure 5.1 SEM micrographs showing morphology of sol-gel derived ITO films printed on glass substrates. The samples obtained from SOLFLEX project.

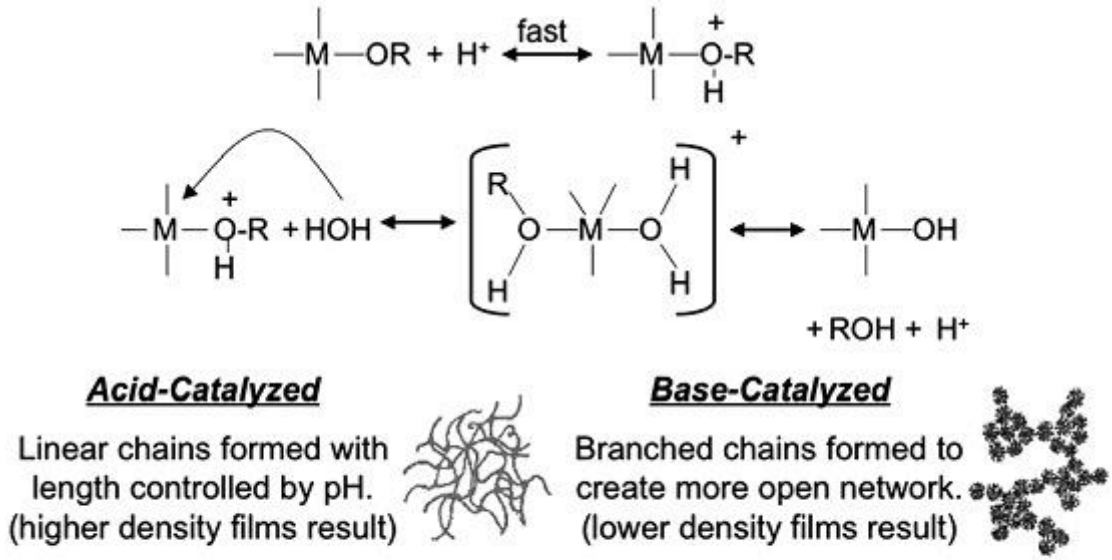

$$M_1 - OH + M_2 - OH \longrightarrow M_1 - O - M_2 + H_2O$$

Figure 5.2 The sol-gel reaction stages leading to metal oxide formation. M and R represent metal and alkyl group (e.g. $-CH_3$), respectively. Adapted from (Klein, 1988; Exarhos and Zhou, 2007).

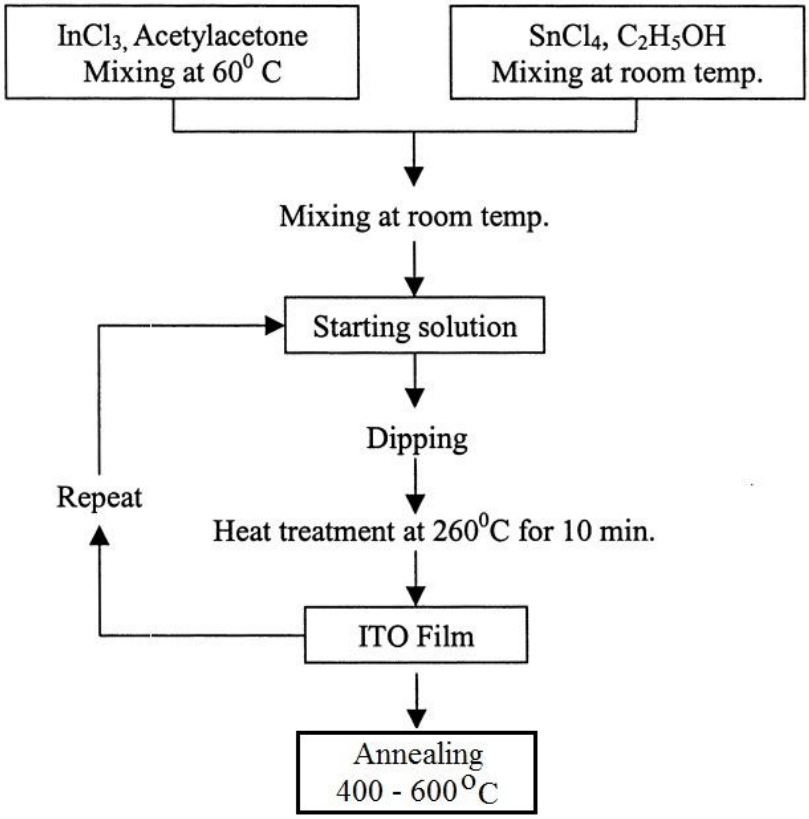

Figure 5.3 Preparation procedure of ITO films via sol-gel route based on dip coating deposition technique. Adapted from (Alam and Cameron, 2000).

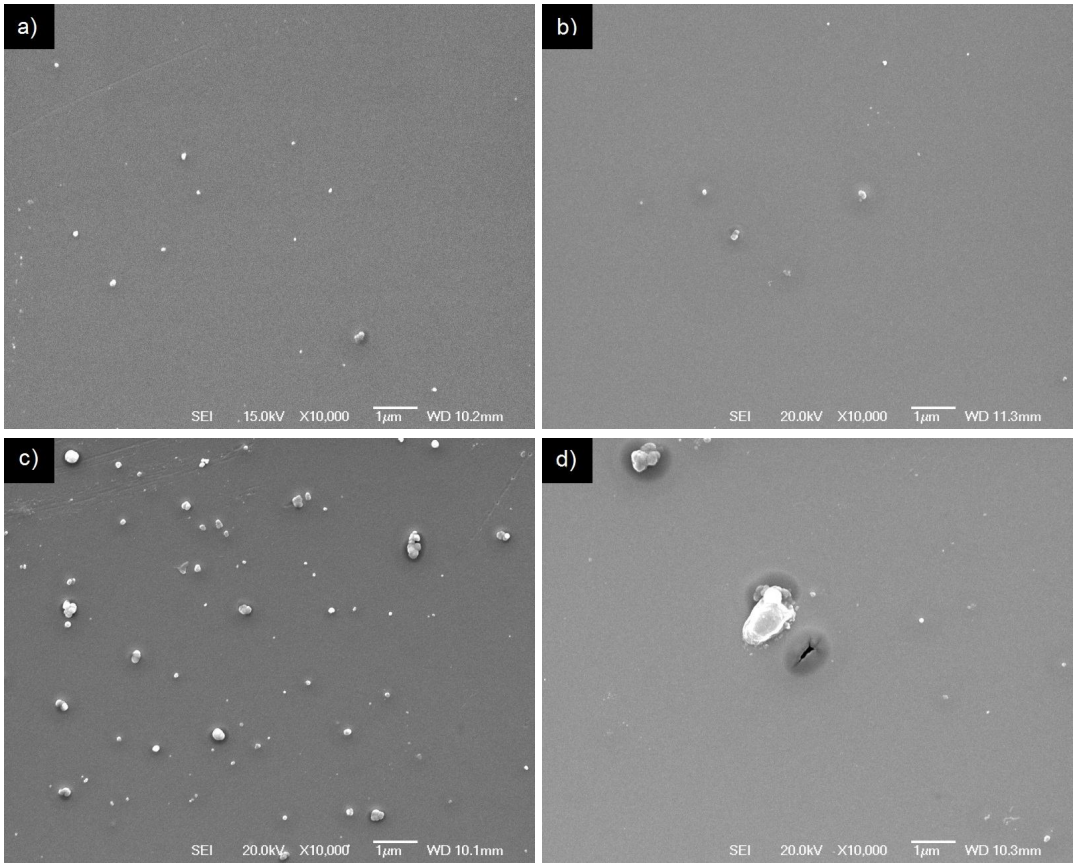

Figure 5.4 SEM micrographs showing surface quality of dip-coated glass substrates by hydrolysed In/Sn(ND). The 0309 samples coated at speed a) 10 mm/min and b) 20 mm/min. The 0509 samples coated at speed c) 5 mm/min and d) 10 mm/min.

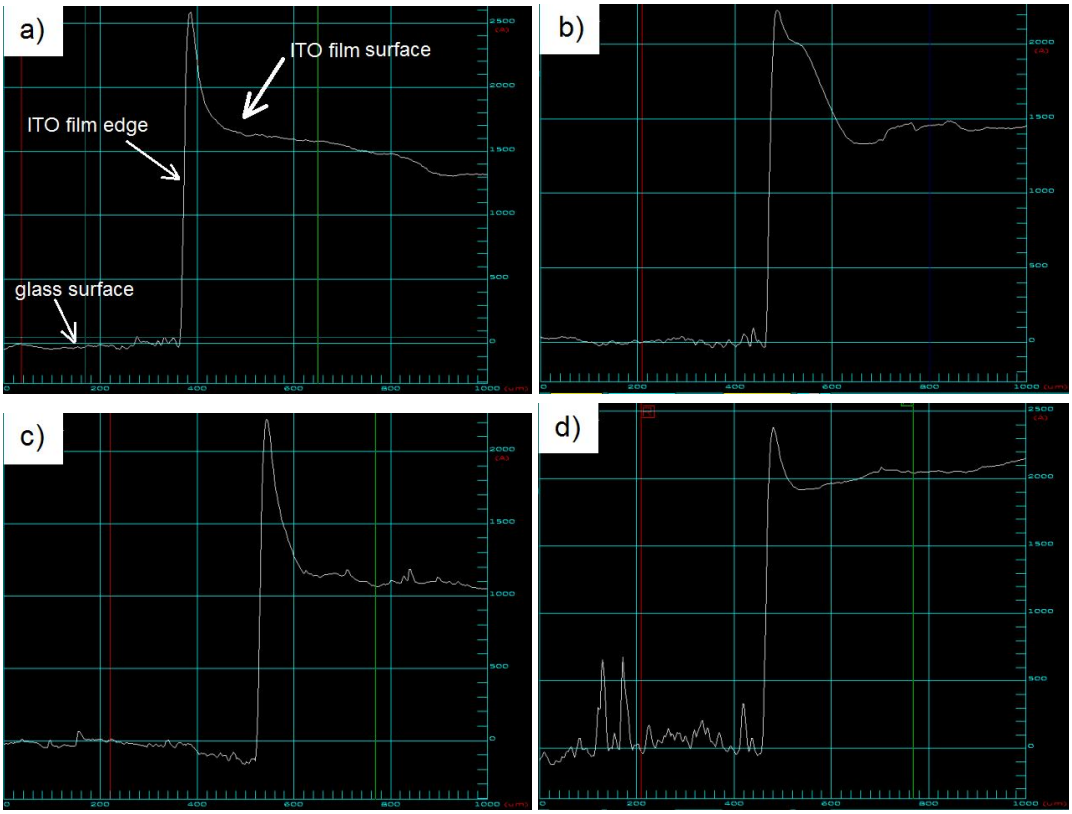

Figure 5.5 Stylus profilometer scans showing surface quality of dip-coated glass substrates by hydrolysed In/Sn(ND). The 0309 samples coated at speed a) 10 mm/min and b) 20 mm/min. The 0509 samples coated at speed c) 5 mm/min and d) 10 mm/min.

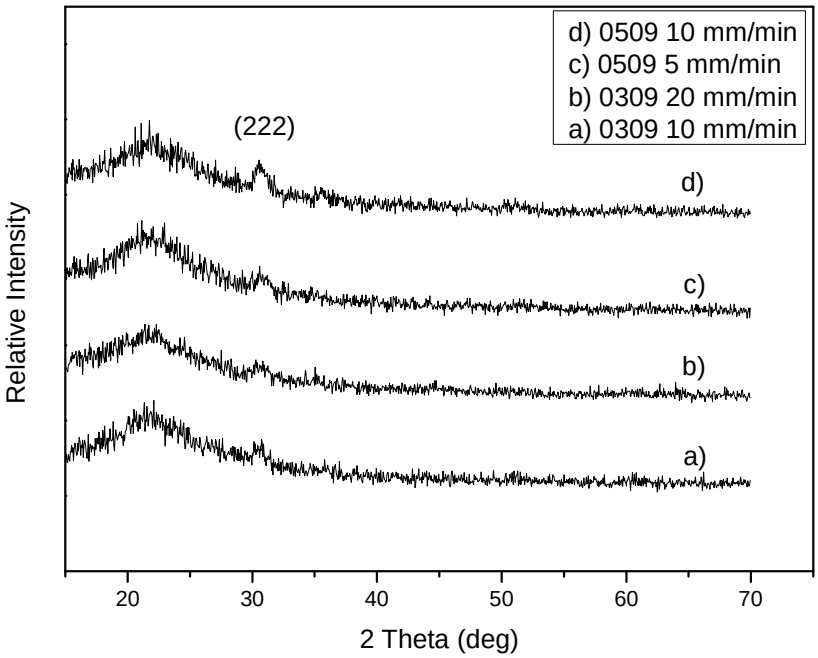

Figure 5.6 WAXD spectra of dip-coated glass substrates with hydrolysed In/Sn(ND) at different coating rates; a) 10 mm/min - 0309 sample, b) 20 mm/min - 0309 sample, c) 5 mm/min - 0509 sample and d) 10 mm/min - 0509 sample.

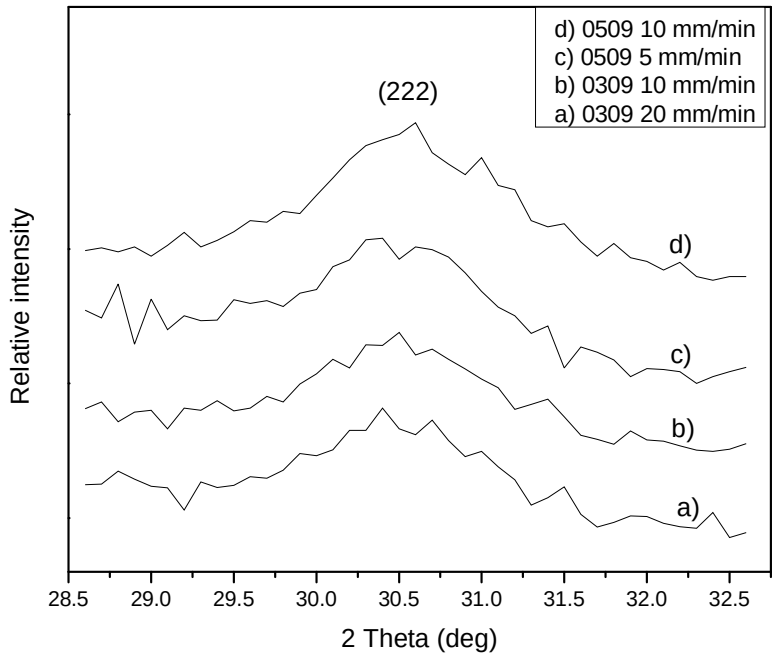

Figure 5.7 GAXD spectra of dip-coated glass substrates with hydrolysed In/Sn(ND) at different coating rates; a) 10 mm/min - 0309 sample, b) 20 mm/min - 0309 sample, c) 5 mm/min - 0509 sample and d) 10 mm/min - 0509 sample.

CHAPTER 6

6. MECHANICAL PROPERTIES OF ITO/POLYMER SYSTEMS

6.1 Introduction

Mechanical failure in a device is determined by the weakest component and certain devices such as flexible OLEDs require brittle inorganic films to be incorporated in them (Lewis, 2006). Therefore, one mechanical issue in these devices is the fracture of brittle, thin, conductive, oxide films deposited on flexible polymer substrates (Chen et al., 2002; Lewis, 2006). Understanding and improve their electro-mechanical limits under variety of stress conditions is of great importance as it provides essential information for display designers. Therefore the electro-mechanical behaviour of indium tin oxide (ITO) films deposited on poly(ethylene terephthalate) (PET), poly(ethylene naphthalate) (PEN) and polycarbonate (PC) polymer substrates by pulsed laser deposition (PLD) is discussed in this chapter. The work is focused on the failure of ITO/polymer systems under tensile and compressive strain, including a variety of mechanical test methods. Damage to the film including channelling cracks and buckling-driven delamination is characterised by atomic force microscopy (AFM) and scanning electron microscopy techniques (SEM). Furthermore, the influence of polymer substrates and ITO thickness on adhesion and critical onset strain of ITO/polymer systems is investigated and discussed. Buckling equipment was built to examine cracking and buckling resistance upon monotonic and repeated flexing of ITO films in tension and compression. The

uniaxial electro-fragmentation test with *in situ* ITO film monitoring was conducted to investigate crack evolution of ITO/polymer systems.

6.2 Film stress and substrate curvature

The deposition process of thin films on a substrate introduces residual stress into the film due to a misfit strain, ε_o (Ye et al., 1992). This misfit strain is biaxial and its magnitude depends on the differences in the coefficient of thermal expansion (CTE) of the film and the substrate. Following (Ye et al., 1992)

$$\varepsilon_0 = (b_f - b_s)\Delta T \tag{6.1}$$

where b_f and b_s are the coefficients of thermal expansion of the film and the substrate, respectively, and ΔT is the temperature drop. Therefore the residual stress is also biaxial and for a film much thinner than the substrate is equal to (Ye et al., 1992)

$$\sigma_0 = \varepsilon_0 E_f /(1-\nu_f) \tag{6.2}$$

where E_f is the Young's modulus of the film and ν_f is the Poisson's ratio of the film. Whether the residual stress is tensile or compressive depends on the CTE of both the film and the substrate. The residual stress is compressive when the CTE of the substrate is higher than that of the film (Ye et al., 1992) and is negative by convention (Leterrier et al., 2003). The stresses may turn from compressive to tensile when an annealing treatment is performed at

temperatures higher than those introduced during deposition (Bouten et al., 2005). Thin films in compressive residual stress are considered in this work.

During deposition of the thin film on the polymer substrate (for $CTE_s >> CTE_f$) the stress [equation (6.2)] is build-up due to bombardment of the highly energetic species which leads to an increase of temperature of the substrate and changes its dimensions (Leterrier et al., 2004). Next, after deposition when the sample cools down, the polymer substrate shrinks, simultaneously introducing compressive stress into the thin film. As a result bent samples are observed after deposition (Suo et al., 1999; Leterrier et al., 2004). The residual stress increases with thickness, since more time is needed to deposit thick films. Long deposition times increase thermal stress on the substrate hence increasing the residual stress (Lin et al., 2009). Figure 6.1 shows development of sample curvature with increasing annealing temperature. However, uniformity of the system can be achieved if the thickness of the substrate is large enough to prevent bending (Ambrico and Begley, 2002) or by careful control of deposition conditions. Stoney (1909) was the first who gave a relationship between the radius of curvature, r, of the bent film/substrate system and residual stress

$$\sigma_0 = \frac{\overline{E}_s t_s^2}{6rt_f} \tag{6.3}$$

where $\overline{E}_s, t_s$, and t_f are the biaxial elastic modulus of the substrate, the thickness of the substrate, and the thickness of the film, respectively.

When the Young's modulus of the film is much higher than that of the substrate ($\frac{E_f}{E_s} \rangle\rangle 1$) the above formula gives a good approximation only if $\frac{t_f}{t_s} \leq 0.001$ (Suo et al., 1999), which is the case in this study.

6.2.1 Consequences of residual stress in thin films

ITO films deposited on polymer substrates are continuously under compressive stress, which increases with film thickness (Leterrier et al., 2003). This residual stress may lead to undesirable consequences such as excessive deformation, fracture, delamination and microstructural changes in the materials (Freund and Suresh, 2003). Thin film/substrate systems play practical service functions in many electronic devices, e.g. flexible flat-panel displays. Hence it is important to determine the amount of residual stress in the film to characterise the resistance of film/substrate systems to failure. It was found that the residual compressive strain increases the net strain for tensile failure of the coating, which automatically leads to overestimation of failure strain (Leterrier et al., 2003).

6.3 Thin film cracking and delamination – mechanism of formation

The mechanical reliability of thin film/polymer systems during manufacture and service depends on numerous factors such as deposition-induced residual stress, thin film-substrate interfacial strength, roughness of the thin film and its polymer substrate (Sierros, 2006) and

mechanical compatibility between the components (Leterrier et al., 1997c). There are two possible failure modes of thin films: the film may fracture when subjected to tensile forces or delaminate (with or without film cracking) when subjected to compressive forces (Chen et al., 2002). Cohesive strength and adhesive strength are of great importance as they control fracture of the coating and delamination (Leterrier et al., 1997a; Chen et al., 2002; Jansson et al., 2006). The mechanics governing the failure modes of thin films is discussed in detail in (Hutchinson and Sou, 1992).

To evaluate mechanical compatibility between thin brittle films and flexible substrates the mechanical mismatch (or elastic mismatch) is introduced in terms of Dundurs' parameters α and β (Beuth Jr, 1992):

$$\alpha = \frac{E_f - E_s}{E_f + E_s}, \quad \beta = \frac{\mu_f(1-2\nu_s) - \mu_s(1-2\nu_f)}{2\mu_f(1-\nu_s) + 2\mu_s(1-\nu_f)} \tag{6.4}$$

where E is the Young's modulus, μ and ν are the material shear modulus and Poisson's ratio, respectively; the subscripts *f* and *s* indicate film and substrate, respectively. Parameter α is of more importance than parameter β, because it is used for more problems (Beuth Jr, 1992; Cotterell and Chen, 2000). Therefore α is also used in this work. For dissimilar materials bonded together the parameter α can vary from -1 to 1 (Beuth Jr, 1992). In the case of brittle ceramic films on compliant substrates α easily exceeds 0.9 ($\alpha \to 1$) (Ambrico and Begley, 2002; Bouten et al., 2005); for example ITO film on PET gives $\alpha = 0.95$ (Bouten et al., 2005).

A crack in thin film/substrate systems nucleates from a flaw in the film or at the edge and propagates towards the interface and laterally through the film creating a channelling crack (Ye et al., 1992). The channelling crack may terminate at the interface, penetrate into the substrate or bifurcate onto the interface (Ye et al., 1992), as Figure 6.2 visualises. Channelling cracks terminating at the interface and propagating with the interface debonding are considered in this work.

When the length of a channelling crack exceeds a few times the film thickness, (e.g. under uniform strain applied to brittle thin film/polymer systems), steady-state cracking may be present (Ye et al., 1992; Chen et al., 2001b). In this state, the crack length does not influence the level of strain and stress at the front of a propagating crack; hence the crack front shape and energy release-rate remain constant (Beuth Jr, 1992; Chen et al., 2001b). This means that the brittle coating will fail if this release of energy is equal to or grater than the energy required for the crack process (or crack-resistance energy) (Chen et al., 2001b; Freund and Suresh, 2003; Bouten et al., 2005). Under tensile strain the propagating channelling crack releases strain energy in the coating and the substrate adjacent to the crack. The strain energy release rate, G_{ten}, follows (Chen et al., 2001b)

$$\begin{aligned} G_{ten} &= G_o g(\alpha,\beta) \\ G_o &= \frac{1}{2}\bar{E}h\varepsilon^2 \end{aligned} \tag{6.5}$$

where G_o is the strain energy per unit width stored in the coating ahead of the crack process, h is the coating thickness and $g(\alpha,\beta)$ is a function of the two Dundurs parameters. The magnitude of $g(\alpha,\beta)$ depends on either the crack type (see Figure 6.2) and elastic mismatch

of film/substrate system (Bouten et al., 2005) and can be found elsewhere (Beuth Jr, 1992). The higher the Dundurs' parameter α the higher the energy release rate, which means that a compliant substrate attracts cracks more than a stiff substrate (Ye et al., 1992).

For brittle materials the cracking strain (or critical strain) depends on the crack resistance energy, G_c (G_{ten}^{cri}), and the flaw size (Chen et al., 2001b). Due to the difficulty of quantifying the largest possible flaw, especially for very thin films, one designs to avoid propagation rather than to avoid the initiation of a crack. In this case the coating thickness, h, is considered as the critical flaw which dictates the critical strain, ε_c (Chen et al., 2001b). The critical strain, is inversely proportional to the square root of coating thickness (Chen et al., 2001b)

$$\varepsilon_c = \alpha \frac{1}{\sqrt{h}} \tag{6.6}$$

where α is a proportionality constant dependent on all materials properties.

A thin film coated a substrate subjected to a compressive stress (either residual or external) may delaminate by a mechanism involving buckling (Thouless et al., 1992), as Figure 6.3 shows. During the buckling process elastic energy stored by the film/substrate system is released creating new free surface by peeling the coating from the substrate surface (Thouless et al., 1992; Bouten et al., 2005). A delaminate buckle can propagate from an edge or central flaw in the film (Cotterell and Chen, 2000).

Under compression the cracking of the film at the top of the buckle profile also occurs following its first buckling-driven delamination. Hence, the actual fracture mode of the coating is tensile (Chen et al., 2001b), as Figure 6.4 graphs. In compression the energy release rate, G_{com}, is based on the delamination area and hence the critical strain energy release rate is given by (Cotterell and Chen, 2000; Chen et al., 2001b)

$$G_{com}^{cri} = G_d + \frac{h}{2b} G_c \tag{6.7}$$

where G_d is delamination interfacial energy, $2b$ is the width of delamination and G_c is the crack resistance energy. The ratio of the crack resistance energy to the delamination toughness, $\frac{G_c}{G_d}$, determines whether the coating will fail first under tension or compression. When $G_d \langle G_c$, compressive failure may occur at a lower strain than under tension (Chen et al., 2001b; Chen et al., 2002). The effect of level of adhesion and loading mechanism (biaxial-compressive residual stress and uniaxial-compressive external stress) on buckling morphology of thin film coated polymer substrates was previously studied by several authors (e.g. Abdallah et al., 2006; Andersons et al., 2007a; Abdallah et al., 2011).

The durability of thin films on compliant substrates can be improved by increasing the adhesion strength between components and reducing the film thickness (Leterrier et al., 1997a; Chen et al., 2001b). However, in plastic electronics, there is a trade-off between using relatively thick conductive films to reduce the resistivity and thin conductive films that can withstand greater applied strains (Fortunato et al., 2002b). The durability can be further improved by placing the brittle film near the neutral axis, sandwiched between the substrate

and an encapsulation layer (Suo et al., 1999). When this system is bent the outer surface experiences tensile strain and the inner surface experiences compressive strain (the bending process will be described in section 6.5), but the thin brittle layer placed in the middle of the sample does not experience any uniaxial stress at all (Lewis, 2006). Therefore, the sandwiched layers can be curled to extremely low radii (Suo et al., 1999; Lewis, 2006); they can even be folded like a map (Suo et al., 1999). However, at the neutral axis the shear stress has its maximum value (Benham et al., 1996) and this affects adhesion between layers, especially when substrates with higher modulus are used (Lewis, 2006). The shear stress can be seen as effectively a frictional force applied tangential or parallel to a surface per unit area and is denoted by the symbol τ (Benham et al., 1996). Therefore, when sandwich structures are flexed, horizontal shear stresses must develop along a thin film placed between two components (Gere and Timoshenko, 1999), e.g. between substrates and encapsulation layers. These stresses can be present at the display edges or near the seal line for display cells where the curvature changes; hence adding to the loading itself and the residual stresses that are also present (Bouten et al., 2005). As one layer may affect the mechanical performance of another, it is important to understand the interactions between them that determine the failure modes in a multilayer stack device (Bouten et al., 2005; Lewis, 2006). Sandwich structures are complex and have many different failure modes (Shivakumar and Smith, 2004). One is for a crack to develop at the interface and propagate within a core (sandwiched layer), which is analysed by fracture toughness of the core (Shivakumar and Smith, 2004). Since an interface is the weakest fracture path in a composite body with dissimilar materials, an interface crack can stay in the interface even when shear stresses rise ahead of the crack tip due to load combinations (Suo and Hutchinson, 1989). In such cases interfacial fracture mechanics can be applied (Suo and Hutchinson, 1989). With the complexity of the layer structure in the

complete display, close attention to adhesion between layers should be paid in any work on flexible displays (Bouten et al., 2005). Adhesion and debonding of thin films in multi-layer stacks under flexing have been studied intensively (Dauskardt et al., 1998). Using the uniaxial fragmentation test, the adhesive strength between a thin film and substrate can be characterised by the interfacial shear strength (IFSS) (Leterrier et al., 1997a; Leterrier, 2003; Rochat et al., 2003a; Rochat et al., 2003b). After buckling-driven delamination of a thin film on a substrate, caused by compressive loading, both normal and shear stresses develop on the interface at the buckle front, which may encourage the unbonded area to grow like a crack (Gleskova et al., 1999). Shear stresses in adhesive layers used in device fabrication, e.g. OLEDs, should also be considered in investigating the mechanical effects of flexing (Lewis and Weaver, 2004a). In comparison with tensile and compressive stresses acting on conductive thin film/polymer structures, the data related to shear stresses acting along conductive layers used as an interlayer in sandwich structures is a far more limited, which opens a new area for further research. In this work tensile and compressive stresses acting on ITO layers are considered.

6.4 Tensile testing of uniaxially strained film/polymer systems

Besides many types of mechanical deformation geometries, the tensile test is one of those most commonly used to study film failure (Lewis, 2006). To evaluate fundamental properties of thin film/polymer systems crack onset strain (COS) is introduced. COS identifies the strain at which the thin film is subjected to irreversible damage (cracking) which affects the composite properties (e.g Young's modulus) (Leterrier et al., 1997c). In the case of

conductive layers COS is defined as the strain at which the increment of resistance $(\frac{\Delta R}{R_0})$, monitored *in situ* during the tensile test, is equal to 10% (Leterrier et al., 2003). This criterion corresponds well to the first crack spanning the whole sample width detected under optical microscopy (Bouten et al., 2005; Leterrier et al., 2009).

Mechanical properties of thin films on compliant substrates in tension have been studied in the past by many researchers (Beuth and Klingbeil, 1996; Leterrier et al., 1997a; Leterrier et al., 1997c; Leterrier and Manson, 1997; Yanaka et al., 1998; Rochat et al., 2003a; Rochat et al., 2003b).

Cairns *et al*. (2000a) were the first to study electrical conductivity changes of ITO films deposited on PET substrate as a function of applied uniaxial tensile strain. They observed that sharp increase in the resistance correlates well with the critical onset strain, estimated to lie between 2.0 and 2.5% strain. In addition, the COS depends on the ITO thickness; the thinner the film, the higher the COS. It was further observed that the ITO film exhibits finite resistance despite the fact that the cracks traverse the full sample width. This is attributed to a small amount of conductive material bridging the conductive ITO fragments, which was suggested to be a ductile layer at the interface of ITO/PET system (see Figure 6.5). To be more precise, for ITO fragment layer of length 1 μm and width 4.5 mm the thickness of conductive path equal to 1.6 nm was calculated.

Fortunato *et al*. (2002b, 2002a) also investigated the influence of applied uniaxial tensile strain on electro-mechanical behaviour of ZnO:Al films with different thicknesses coated on PET substrates. They observed that the critical strain decreases with increasing layer thickness

and reported a crack onset strain equal to 2.0% for the thinnest sample. Crack morphology investigation revealed intergranular fracture path at the grain boundary perpendicular to the applied strain, as Figure 6.6 shows. They also reported that the secondary cracks appear in the form of buckles due to Poisson's ratio compression effects at 8.0% applied strain. By observing the crack's morphology and resistance changes upon applied strain, they concluded that the resistance is not directly proportional to the number of cracks, but rather to the distance between neighbouring layer fragments, which depends also on the film thickness.

Kim *et al*. (2010b) investigated cracking and buckling-resistance under uniaxially strained ITO films deposited on PET substrates with chemically-modified surfaces by O_2 plasma treatment. ITO films with different thicknesses (50 - 150 nm) deposited on an untreated PET substrate show very low crack onset strain of between 1.0 and 2.0%. They observed that the plasma treatment on the PET substrate does not influence the crack onset strain of the ITO film as compared to ITO on untreated PET substrates. However, they showed that the plasma treatment significantly improved buckling onset strain due to improved adhesion between the ITO film and the polymer substrate. The buckling strain of ~ 4.0% is observed for ITO films on plasma-treated PET substrates independent of ITO thickness. They concluded that the O_2 plasma treatment can be used to improve interfacial strength between thin films and polymer substrates and hence improved buckling-resistance of the film.

Yang and Park (2010) investigated cracking and buckling resistance of low temperature ITO-deposited on PET substrate under uniaxial tensile strain incorporating silver (Ag) as an interlayer between the ITO and the PET. They observed that with an increase in interlayer thickness (from 5 to 15 nm) the cracking resistance increases significantly due to increase of

ITO crystallinity. A slight increase in buckling-resistance of ITO/Ag/PET samples is observed for Ag thickness ≥ 10 nm compared to that without an interlayer. Despite the improved mechanical resistance with increasing interlayer thickness, deterioration in transparency and conductivity is observed. Therefore, they pointed out that the optimum thickness should be found by designing devices incorporating interlayers.

Several alternative materials to ITO, such as conductive polymers are also evaluated to improve mechanical robustness (Lewis, 2006). The most commonly-used conductive polymer is polyethylenedioxythiophene doped with polystyrene sulphonate (PEDOT:PSS). Cairns *et al*. (2003) investigated the influence of temperature on electro-mechanical behaviour of ITO-coated PET and PEDOT:PSS-coated PET systems under uniaxial tensile strain. In case of the ITO/PET samples, they observed that with increasing temperature the crack onset strain also increases. For example at 90 ^{o}C the critical strain was observed to be equal to 5.5% which is much greater than 3.0% strain observed at 25 ^{o}C. They pointed out that this may be due to stress relaxation of stress in the substrate during the test or to enhanced interfacial strength between ITO and PET as a consequence of increased crystallinity in the PET substrate. It is concluded that the former is most likely to occur. In contrary, for the PEDOT:PSS/PET increased temperature deteriorates electrical conductivity. However, it should be noted that despite higher sheet resistance (> kΩ/□) and lower transmittance (< 90%), PEDOT:PSS can withstand strains of tens of percent larger in comparison to ITO.

6.4.1 Fragmentation test and crack density (CD)

The fragmentation test is a commonly-used mechanical technique to investigate interface performance in composite materials where the fragmented morphology, observed *in situ* by optical microscopy, reflects the interfacial stress field (Leterrier et al., 1997c). In case of conductive films, e.g. ITO-coated polymer substrates, the electrical resistance can be also monitored *in situ* as a function of applied tensile strain. The analysis of the results provides accurate determination of the influence of internal stresses and the layer thickness on the failure mechanism of thin film/substrate systems (Leterrier et al., 2003).

Characteristic stages related to the tensile fragmentation test of thin films on polymer substrates can be recognised with increasing applied strain :

1) Primary cracking of the film. At this stage the film cracks when critical stress is applied and the formed cracks are perpendicular to the applied tensile force;

2) Secondary cracking and delamination. At this stage cracks parallel to the applied strain may be formed due to lateral contraction resulting from the Poisson's ratio of polymer substrate (Leterrier et al., 1997c). Debonding of the film takes place along the secondary cracks as the film fragments tend to overlap due to the further extent of lateral contraction;

3) Tertiary cracking. At this stage parallel cracks to the primary cracks appear. However, they do not cross the full sample width as they are stopped by the secondary cracks and buckling zones of the film. The associated stress concentrated at the tertiary crack tip is relaxed when reaches debonded zone; therefore its growth terminates here (Leterrier et al., 1997c);

4) Crack saturation. At this stage the cracking process of the film is terminated, which means that new cracks perpendicular to the applied strain are not created. Saturation results from insufficient stress, that can be transferred to the film in order to promote the next crack, as most of the stress is absorbed by the polymer substrate at the base of existing cracks (Tsubone et al., 2007). Plotting crack density (CD) as a function of true strain allows one to evaluate accurately the crack onset saturation strain. Using this method instead of plotting CD as a function of nominal strain allows one to eliminate dissipative mechanisms, such us the plastic flow of the substrate, the cohesive failure and buckling of the film due to the Poisson effect and possible adhesive failure at the interface, that influence the linearity of the CD curve before reaching CD plateau (Leterrier et al., 1997c).

In some cases stages 2) and 3) may appear at the same applied tensile strain (see e.g. Leterrier et al., 1997c). Individual stages of fragmentation morphology of thin brittle films deposited on polymer substrates are shown in Figure 6.7. Numerical simulations (finite element) (Jansson et al., 2006) and analytical probabilistic models (Andersons et al., 2007b) of principal stages of the fragmentation process can be applied in order to identify the adhesive and cohesive fracture properties of brittle films on compliant substrates.

Leterrier *et al*. (1997a) investigated the influence of the thickness of silicon oxide (SiO_x) barrier film/PET systems on cohesive and adhesive strength in terms of the uniaxial fragmentation test. The cohesive strength and adhesive strength were characterised from the crack onset strain and crack density at saturation, respectively. The results show that the adhesion strength modelled using the Kelly-Tyson approach is independent of the layer

thickness in the range from 30 to 150 nm and equal to the substrate shear stress at saturation. They observed that the crack onset strain increases with decreasing coating thickness. In addition they pointed out that the cohesive strength and the crack onset strain are proportional and they can be predicted using fracture mechanics theories.

In addition Cairns *et al*. (2000a) incorporated cracking of the ITO film in a model to describe the observed increase in the resistance with increasing strain. They observed that the increase in resistance is not proportional to the number of cracks, and assumed that the resistance of individual cracks increases as a function of increasing strain. In addition it is assumed that the volume of conducting path is constant in each crack and undergo plastic deformation. They found good agreement between observed resistance change and modelling fit as Figure 6.8 shows. A different model assuming constant thickness of conductive paths was proposed by Leterrier *et al*. (2009). However, their model reproduced only experimental data from the first mature crack to the crack saturation point and above the saturation point the model underestimated the measured resistance. They results suggest that the model proposed by Cairns *et al*. (2000a) is more accurate above the crack saturation point than the model assuming constant thickness of conductive paths proposed by Leterrier *et al*. (2009).

Tsubone *et al*. (2007) investigated the influence of Young's modulus of the polymer substrates and adhesion effects on fracture properties of diamond-like carbon (DLC) films/polymer systems on uniaxial mechanical deformation. They found that the fracture mechanics of DLC film strongly depends on polymer substrates with different Young's modulus values. DLC-coated PET substrates showed the highest crack density compared with other DLC/polymer systems due to the Young's modulus of the PET substrate being the

highest. In addition, they reported that the buckling lines of the film on the PET substrate appeared at 10% strain and were parallel to the stretching direction. Interestingly, they observed that the crack density of DLC/polypropylene (PP) sample was lower than that of DLC/polyethylene (PE), despite the fact that the Young's modulus of PP is slightly higher than that of PE sample. Therefore, they pointed out that low adhesion of DLC/PP system, as compared with that of DLC/PE, overrode the influence of the small effect of the slightly higher Young's modulus of PP substrate.

6.5 Bending of conductive thin film /polymer systems

The bending process of a thin film/substrate can be simply described (Lewis, 2006); when the sample is bent the outer surface experiences tensile strain and inner compressive strain, as Figure 6.9 (a) and (b) show, respectively. If the film thickness is far lower than the substrate it can be assumed that the neutral plane, at which the sample does not experience any uniaxial stress at all, lies in the middle of the sample. Therefore, the strain acting on the film can be found using a relationship between strain and radius of curvature [see equation (2.16) in chapter 2]. With increasing curvature of the sample during bending the substrate changes its geometrical shape from circular to elliptical, as Figure 6.10 shows. Park *et al*. (2004) investigated position-dependent stress distribution of ITO-coated PC substrates during bending. They showed that when the sample (rectangular) takes an elliptical shape the highest stresses acting on the film are concentrated in the middle section and are lower towards the edges. This occurred with the higher crack density in the middle section of the sample resulting in conductive failure of ITO film.

Bending tests coupled with electrical probing enables accurate electrical resistance measurements of conductive film/polymer systems and correlates the mechanical failure of the film to the sharp increase of resistance (Leterrier et al., 2003). Figure 6.11 shows two commonly-used bending test methods to evaluate mechanical failure of thin film/polymer systems. Various bending test methods described in details can be found elsewhere (Chen et al., 2002; Gorkhali et al., 2004; Grego et al., 2007; Koniger and Munstedt, 2008b). The bending test method developed in this work is introduced in section 2.2.5 of chapter 2. Furthermore, fatigue tests are of great importance for flexible electronics, since more than 90% of all structural failures are caused by repeated loading force (Lukkassen and Meidell, 2003). Structures subjected to dynamic loads repeated for a large number of cycles fail at a lower stress than when the same loads are applied statically (Gere and Timoshenko, 1999). Flexible displays must withstand repeated bending loads, applied by the end user, for a large number of cycles. Therefore, brittle conductive layers coated on flexible substrates should be subjected to dynamic loading both in tension and compression to predict the life-time of flexible displays.

6.5.1 Monotonic bending on the tensile and compression side

Chen *et al*. (2001b) investigated cracking of 100 nm-thick ITO film on a PET substrate under controlled buckling in tension and compression with *in situ* resistance monitoring. They used loss of conductivity of ITO film as a marker for crack onset strain. The study showed that the bending on the tensile side is more critical than in compression. To be more precise the ITO film failed at applied strain equal to 1.1% and 1.7% under tension and compression,

respectively. Using the critical strain of the film obtained after flexing on the tensile and compression side they calculated the crack resistance energy and the delamination toughness equal to 65 and 32 J/m^2, respectively. It was postulated that the ratio of the crack resistance energy to the delamination toughness determines whether the coating will fail under tension or compression.

Leterrier *et al*. (2003) investigated the influence of ITO film thickness (in the range from 50 to 200 nm) on electro-mechanical properties under monotonic bending in tension. The ITO film was deposited on a high temperature aromatic polyester (ARY). They observed that a high residual stress, which increases with layer thickness, influences the measured strain to failure by means of its overestimation. The 50 nm thick ITO layer showed the highest critical strain equal to 1.8%, which corresponds to the minimum achievable radius of curvature of ~ 3 mm. Both 100 and 200 nm thick films showed a critical strain equal to ~ 1.5%, which corresponds to critical radius of curvature, of ~ 3.5 mm.

Sim *et al*. (2009) shown that electro-mechanical bending stability of ITO/PET systems can be enhanced by placing aluminium (Al) buffer layer (5 nm thick) between the two components with a slight deterioration in optical transmittance. They observed that for ITO/Al/PET systems normalised resistance starts to increase after severe bending to 1.25 mm radius of curvature due to ITO cracking. In contrast, for samples without the buffer layer the cracks were observed after bending to 9 mm radius of curvature. They concluded that enhanced electro-mechanical properties are accounted for by the fact that the elastic mismatch between ITO and PET can be alleviated with a buffer layer possessing intermediate elastic modulus; thus making crack propagation more difficult.

Sierros *et al.* (2009) investigated stress-corrosion cracking of ITO/PET systems under applied bending tensile strains by wrapping the samples around different diameter mandrels and immersing them in acrylic acid with different concentrations. They showed that ITO interacts with an acrylic-acid present in pressure sensitive adhesives (PSA) - used in flexible device stacks - in terms of a corrosion process. Deterioration in electrical properties was observed due to corrosion-induced cracking; the higher the acid concentration, the higher corrosion. In addition, when bending strain was applied, time to failure of ITO/PET systems in corrosive environment was significantly reduced as compared with the corroded systems without applied mechanical stress. Moreover, they observed that combination of stress and corrosion can promote ITO cracking at stresses less than a quarter of those needed without corrosion. It was pointed out that combined effect of applied stress and corrosion must be taken into account in order to properly predict a life-time of the device components. Finally, they concluded that the electrical failure of ITO is corrosion dominated with high contribution of externally applied stresses.

Chiba and Futagami (2008) investigated the influence of a carbon-nanotube (CNT) interlayer on bending electrical stability of ITO (20 nm thick with sheet resistance of 300 Ω/□) sputtered on PET substrates, in tension. The ITO/PET and ITO/CNT/PET systems were flexed on to a bar with diameter ranging from 1.5 to 6 mm and electro-mechanical behaviour was compared. When the CNT interlayer was placed between ITO and PET the sheet resistance increased from 300 to 400 Ω/□. However, enhanced bending stability of the ITO/CNT/PET system was observed in comparison with an ITO/PET system. For ITO-coated PET a sharp increase of resistance was observed at a radius of curvature of 2.5 mm, while for ITO/CNT/PET samples flexed to radius of 1.5 mm the resistance remained constant.

6.5.2 Cycling loading on the tensile and compression side

Gorkhali *et al*. (2004) investigated electro-mechanical failure mechanisms of ITO-coated PET and conductive polymer PEDOT:PSS-coated PET samples subjected to cycling loading in tension. The samples were flexed up to 100,000 times on mandrels with different diameters ranging from 8 to 24 mm and the resistance changes were monitored *in situ*. The closer examination of resistance changes during the test revealed that resistance increases linearly during loading and decreases exponentially during unloading. The exponential decrease is due to dimensional recovery of the substrate, which was strained during loading and its shape recovers over the time rather than spontaneously. They observed increase in resistance with increasing number of cycles of ITO-coated PET and selected three characteristic regimes (see Figure 6.12): I) initial (up to 100 cycles) increase in resistance due to changes in sample dimensions until the equilibrium point is reached, II) gradual increase in resistance probably due to cracking of the ITO layer and III) catastrophic conductive failure after 50,000 cycles due to severe cracking. In contrary, for PEDOT:PSS-coated PET the gradual increase in regime II) has not occurred due to higher mechanical stability of conductive polymer.

Lin *et al*. (2009) investigated the effect of repeated bending on mechanical and opto/electrical properties of ITO/PET systems in tension with ITO thickness vary from 100 to 250 nm. They measured resistivity and transparency every 10^{n+1} loading cycles. They observed that for ITO thickness higher than 100 nm resistivity starts to increase at 100 loaded cycles. For 100,000 cycles the transparency of 100 and 150 nm ITO remains unchanged. However, for 200 nm thick ITO film the transparency slightly decreases. It was pointed out that the deterioration of electrical and optical properties is related to adhesion level between ITO film and PET substrate which decreases with increasing ITO thickness. They claimed that the resistivity for

as deposited 100 nm thick ITO equal to 4.5 x 10^{-4} Ω cm did not change after 100,000 cycles. However, the applied bending radius or stresses acting on the ITO film during bending were not reported.

Koniger and Munstedt (2008b) investigated influence of radius of curvature and amplitude on electro-mechanical reliability of commercial, 100 nm thick ITO-coated PET substrate under oscillatory bending in tension. They observed that resistance starts to increase abruptly for radius of curvature smaller than 14 mm due to crack formation in the ITO film. They showed that for fixed radius of curvature the resistance increases with an increase of bending amplitude due to tensile stresses acting on a larger region of the film causing stronger crack formation. They reported a very high crack onset strain, of 12 %, in comparison to those frequently reported in the literature (1 – 3%) (Cairns et al., 2000a; Chen et al., 2001b; Leterrier et al., 2004; Bouten et al., 2005). They explained that this may be due to the buffer layer used to enhance the mechanical stability of ITO films.

Furthermore, Koniger and Munstedt (2008a) investigated the influence of oscillatory bending with alternating tensile and compression stress on electro-mechanical properties of ITO-nanoparticle coated PET (2 kΩ/□) and commercially available ITO-sputtered PET (60 Ω/□). They observed that an oscillating change in resistance occurs with increasing number of cycles, as Figure 6.13 shows. They explained that under tension the crack flanks are drawn apart causing an increase in resistance, whereas, under compression the crack flanks are pressed on to each other causing a slight decrease in resistance. The increase in resistance of ITO film under tension is stronger than the decrease of resistance under compression relative to the balanced state. Therefore the resistance in the balanced state increases with increasing

number of cycles and lies below the mean value of the oscillatory curve. In addition, for sputtered ITO films the sheet resistance strongly increased from 60 Ω/□ to 30 kΩ/□ after 100 cycles at 3 mm radius of curvature. ITO-nanoparticles coated PET showed much higher electro-mechanical reliability, where after 100 cycles the sheet resistance increased by only 10%, from 3 to 3.3 kΩ/□. They concluded that the difference in electro-mechanical behaviour is due to differences in crack formation. Sputtered ITO films are brittle and the cracks spanning the whole sample width increase resistance significantly. In contrast, ITO-nanoparticle films are less brittle due to a granular structure; hence smaller cracks with finite length are formed which allow the electrons to flow through the coating, as Figure 6.14 shows.

6.6 Results and discussion

6.6.1 Uniaxial fragmentation test

Uniaxial fragmentation tests were conducted by the miniature tensile machine (Minimat) at a constant crosshead speed set at 0.1 mm/min and an evolution of cracks of ITO 100 nm/polymer systems was observed *in situ* and recorded by a microscope camera. The samples after pulsed laser deposition were observed to be bent. Hence, prior to the tensile fragmentation testing, the residual stress, introduced into the ITO films during deposition, was evaluated in order to obtain intrinsic mechanical properties of the ITO films. The influence of the residual strain on the net crack onset strain (COS) value will be discussed.

Figure 6.15 shows optical micrographs of crack evolution of the ITO/PEN system, which were collected *in situ* during the uniaxial tensile test. The image (a) shows a surface defect (pin-hole) of the ITO film. This is a consequence of the impurities that are present on the polymer surface, as the SEM images show [Figure 3.19 (a) and (b)]. It is evident though, that the cracks start to form from these defects at a certain critical strain [Figure 6.15 (b)]. The sample exhibits a crack onset strain (corresponding to 10% increase in resistance) equal to 3.40 ± 0.053%, which is in good agreement with the collected micrographs showing the growth of the first cracks at that strain. Good correlation between the COS point and the first crack from fragmentation data was also observed previously (Leterrier et al., 2009). The cracks propagate and span through the whole sample width perpendicular to the applied tensile strain, as images (c) and (d) show in Figure 6.15. It is also clear to see, that with increasing strain the number of cracks increases creating an periodic array pattern of cracks. With a further increase of strain an adhesion-related failure occurs in terms of buckling of the ITO film. The tunnelling buckling is observed to form at a strain equal to ~ 8.0% and is parallel to applied tensile force, as image (e) in the same figure indicates. It is important to note that at the same strain secondary cracks appear along buckling profiles (see e.g. Figure 6.44). The secondary cracks and buckling of the film take place due to lateral contraction (Poisson's ratio) of the polymer substrate (Leterrier et al., 1997c; Tsubone et al., 2007). At ~ 8.2% tertiary cracks parallel to primary cracks start to form. However their growth is stopped by secondary cracks and buckling of ITO film. Figure 6.15 (f) shows the ITO film strained at 15% with a characteristic "bamboo forest-like" pattern clearly visible.

Figure 6.16 shows optical micrographs of crack evolution of the ITO/PET sample. The sample exhibits a COS equal to 2.80 ± 0.09% which corresponds to the first cracks spanning

through the whole sample width, as image (b) shows. The cracks originate from defects in the ITO film similar to that of the ITO/PEN sample. In contrast to the ITO/PEN sample, the ITO/PET sample exhibits lower COS and slightly lower strain, of ~7.5%, at which buckling of ITO film begins to form. Secondary cracks along the edge of the buckle profile are not observed to form (see Figure 6.38). Also at ~7.5% strain tertiary cracks are visible.

The ITO/PC sample shows the same crack evolution and buckling pattern to that of the ITO/PEN and ITO/PET samples, as Figure 6.17 shows. The COS equal to 3.26 ± 0.079% and the buckling onset strain equal to ~ 7.5% are similar to that of the ITO/PEN and ITO/PET samples, respectively. In addition, similar to ITO/PET sample and contrary to the ITO/PEN sample, secondary cracks are not observed (Figure 6.49). Moreover, also at ~7.5% strain tertiary cracks are observed to form.

Crack initiation in ITO films observed in this study is consistent with that observed previously by Leterrier *et al*. (2003; , 2004) who studied fragmentation morphology of ITO films on high temperature aromatic polyester. They pointed out that on loading the cracks originate from microdefects (pin-holes) remaining after deposition, and surface defects in the underlying polymer substrate. The periodic array pattern of progressive cracking of ITO film under applied tensile strain can be understood in terms of a stress relaxation process: at some distance from the crack the stress remains unrelaxed due to the constraint of the substrate. As a result new crack parallel to the previously formed can be created due to the tensile stress relieve (Freund and Suresh, 2003). Moreover, it is evident that for any samples investigated in this study tertiary cracks and debonding of the ITO film are observed to form simultaneously at the same applied tensile strain. Leterrier *et al*. (1997c) also reported that for SiO_x film

deposited on PET substrate these events occur simultaneously. However, they reported slightly higher applied strain (~ 10%) in comparison to this work.

The ITO film exhibits a different residual stress depending on the polymer substrate, as Table 6.2 shows. The residual stress originates from the differences in the coefficient of thermal expansion (CTE) between the ITO film and the polymer substrates (see Table 6.1) and was found to be compressive. Suo *et al.* (1999) also observed that compressive stress was introduced into the thin film transistors (TFTs) fabricated on polymer substrate when the CTE of the substrate was higher than the CTE of the TFTs. As a result, bent samples (with negative curvature) were observed after deposition. All samples investigated in this study show relatively high residual stress. The lowest residual stress shows the ITO/PEN sample, which is equal to ~ 600 MPa. In contrast, the highest residual stress equal to ~ 1000 MPa shows the ITO/PET sample. The ITO/PC sample shows an intermediate value of the residual stress equal to ~ 800 MPa. The differences in the ITO residual stress depend also on rigidity of the polymer substrates, as Table 3.5 shows. The PEN substrate shows the highest rigidity equal to 13.3 x 10^{-4} Nm and hence the lowest ability to distort. It explains the lowest residual stress of the ITO film on the PEN substrate. The PET and PC substrates show similar rigidity, 11.5 and 11.0 x 10^{-4} Nm, respectively. However, the residual stress of the ITO film on them is different. The explanation may lay in the difference in the glass transition temperature between the PET and PC substrates, which is 78 and 145 ^{o}C, respectively (Table 3.1 and Table 3.3). In addition, it was reported that PC can withstand high operating temperatures holding its rigidity and toughness up to 140 ^{o}C (Brydson, 1999). In contrast, MacDonald *et al.* (2007) showed, that the heat-stabilised PET film loses its rigidity significantly at around 110 ^{o}C. Furthermore, it can be concluded, that the PET substrate's surface temperature may

increase up to the softening point during deposition. In deed, Fan (1979) measured substrate temperature, of 80 ^{o}C, during ITO deposition on glass and polymer substrates by ion-beam sputtering. Moreover, Park *et al.* (2003) observed that when depositing ITO on PC with substrate heating temperature set at 100 ^{o}C, the temperature of the chamber rose up to ~ 130 ^{o}C due to the plasma process. Temperature of plasma as a function of target-to-substrate distance during deposition can be seen in Figure 6.18.

It is clear to see in Table 6.2 a beneficial effect of the residual stress on the net COS. The higher the residual stress, the higher the overestimation of the COS. The table shows intrinsic crack onset strain (COS*), which corresponds to intrinsic cohesive properties of the ITO film. Furthermore, the ITO/PEN sample exhibits the highest COS* equal to ~ 3.0%. The second highest COS* value is shown for the ITO/PC sample and the lowest for the ITO/PET sample, ~ 2.6 and ~ 2.0%, respectively. The beneficial effect of residual stress on ITO strain failure was also observed previously (Leterrier et al., 2004).

Figure 6.20 shows the crack density of the ITO film deposited on the PET Melinex ST 505, PEN Teonex Q65 FA and the PC Lexan 8010 MC substrates. It is clear to see, that the number of cracks increases immediately after the first crack is formed at the critical strain relative to the ITO/polymer systems. The fragmentation velocity decreases above 5% strain. With increasing strain the crack density of the ITO/polymer systems reaches a saturation point, above which further cracks are not formed. The strain, at which the cracks reach their saturation point depends on the polymer substrate and interfacial strength (adhesion). The crack density exhibits the saturation point at ~ 13% strain for both the ITO/PEN and the ITO/PET samples, and ~ 8.0% for the ITO/PC sample. In addition, the number of cracks also

depends on polymer substrate and shear forces transmitted through the interface (Leterrier et al., 1997c). It is evident, that the highest number of cracks belongs to the ITO/PEN system and is equal to ~ 105 mm^{-1}. The ITO/PET sample shows the second highest number of cracks equal to ~ 80 mm^{-1}. The lowest crack density of ~ 55 mm^{-1} falls to the ITO/PC sample. It should be noted, that this order is not accidental. Combining above results with the results obtained from the stress-strain data of the uncoated polymer substrates (Figure 3.15) it is clear to see that the crack density is strongly related to a strength of the polymer substrates. Indeed, it is assumed that the layer cracks at the constant critical stress (Tsubone et al., 2007); therefore as soon as the first crack appears at the critical stress, the next crack will be promoted when the polymer at the crack base deforms till it reaches the critical tensile stress. According to this mechanism, the critical stress to promote the next crack in the ITO film on stiffer polymers is obtained at a lower strain. Hence, the stiffer ITO/PEN and ITO/PET sample exhibits a larger number of cracks than ITO/PC sample as a result of the tensile stress relaxation. In contrast, for the less stiff ITO/PC sample, a higher strain is needed to achieve the critical stress that promotes further ITO cracking. As a result, a smaller number of cracks is observed. Figure 6.19 shows the above-mentioned cracking mechanism for ITO on PET and PC substrates as an example.

Moreover, it is interesting to note, that the buckling of the ITO film on the PEN, PET and PC substrates [Figure 6.15 (e), 6.16 (e) and 6.17 (e), respectively] starts to occur as the crack density reaches its saturation point (Figure 6.20). In the case of the ITO/PC sample the buckling of the ITO film takes place almost exactly at the saturation point (~ 8% strain). Similar observations were reported previously by Latella *et al*. (2007) for titania thin film on PC substrates. In addition, it is clear to see, e.g. in the Figure 6.17 (f), that the buckling of the

ITO film originates from the edges of the conductive ITO fragments and propagates toward the opposite edge. This is because the edge of the cracked film is a site of an abrupt change in geometrical shape; hence the stress is concentrated near its neighbourhood region (Freund and Suresh, 2003). In some cases, the buckles that originate from both edges, are aligned exactly opposite to each other, thus as they propagate they meet in the middle of the ITO fragments creating a "bow tie-like" pattern. This is due to the lateral compression of the polymer substrates that acts perpendicular to the applied strain; hence the ITO follows its shape caused by deformation. This is consistent with the study conducted by Cairns *et al*. (2001) who observed that the deformation of polymer substrate is mapped by the crack pattern in the ITO film. The width of the buckling zone becomes uniform with further elongation of the sample, as fig Figure 6.17 (e) shows.

6.6.2 Electro-mechanical properties of ITO/polymer systems under uniaxial tensile test

The uniaxial tensile test was conducted with an Instron tensile machine at a crosshead speed set at 0.05 and 0.5 mm/min. The ITO films with thickness of 100 nm were deposited by PLD on polymer substrates at a room temperature. A small prestrain was applied to the samples to assure their good alignment. The induced uncertainty in monitored value ranging from 0.2 to 0.4%. The tensile test with *in situ* resistance monitoring of ITO/polymer systems was performed in order to evaluate the critical onset strain (COS), at which ITO film started loosing its electrical properties and to observe the resistance behaviour above the critical point for the two different crosshead speeds. The rate of resistance change above the critical strain is referred to the slope of its linear behaviour.

Figure 6.21 shows electro-mechanical behaviour of the ITO/PEN sample strained at 0.5 mm/min crosshead speed. It is evident, that with increasing uniaxial tensile strain the normalised resistance stays constant until a certain strain – the critical onset strain (COS), which promotes the first cracks in the ITO layer and is equal to 2.70%. With further increase of strain the normalised resistance increases gradually due to cracking of the ITO layer, as the sequence of optical micrographs show in Figure 6.15. The linear increase in resistance of ITO film above COS is clear to see, which may suggest that the number of cracks is proportional to the applied strain. It can be true only for the applied strains up to crack saturation point (the strait line of the initial curves from crack onset strain to ~ 8% strain, Figure 6.20). It should be noted that a finite resistance, after the very first cracks spanned the whole sample width is observed. This is due to presence of conductive paths across the cracks' width connecting ITO film fragments (Cairns et al., 2000a). They resistive nature was confirmed recently by impedance spectroscopy measurements (Leterrier et al., 2009). These conductive bridges are suggested to be ductile layers at the interface between the ITO film and the plastic substrate (Cairns et al., 2000a).

It is believed that above the crack saturation point the resistance increases directly proportional to the extension of conductive bridges inside the cracks and buckling delamination till a catastrophic conductive failure occurs caused by plastic deformation of the polymer substrate. Indeed, Figure 6.22 shows, that above the crack saturation point the resistance increases with higher rate linearly with increasing strain till catastrophic conductive failure point, which takes place at ~ 12.5% strain. It should be noted that above 12.5% strain the resistance is still measurable. Leterrier *et al*. (2009) developed model to correlate the tensile damage of the ITO film to the increase of electrical resistance upon straining assuming

constant thickness of conductive paths rather than their constant volume proposed by Cairns *et al*. (2000a). However, the model based on constant thickness of conductive bridges reproduces only experimental data from the first mature crack to the crack saturation point. Above the saturation point the model underestimates the measured resistance. Therefore, based on our results it can be concluded that the model based on conduction paths with constant thickness applies till saturation point and then the conduction paths follow volume changes as the number of cracks stays constant. Hence good prediction of resistance changes may be achieved by finding a compromise between two modelling methods mentioned above.

The transition from progressive cracking to crack saturation point (at ~10.0% strain), evaluated from resistance changes above COS (see Figure 6.22), is in excellent agreement with the transition point (~ 10% strain) estimated by means of the crack density measurements (see Figure 6.20).

Similar electro-mechanical behaviour is observed for ITO film deposited on PET, as Figure 6.23 presents. However, slightly lower crack onset strain equal to ~ 2.50% is observed in comparison to that of ITO/PEN sample (~ 2.70%).

Interestingly, different electro-mechanical behaviour is observed for the ITO film on the PC substrate, as Figure 6.24 indicates. The sample shows the COS equal to ~ 2.50% which is the same to that of the ITO/PET sample, however it loses completely conductivity immediately above the COS point. The stress-strain curve, also visible on the graph, indicates high elasticity of the amorphous PC substrates. In addition, the ITO film on PC substrate exhibits the highest elastic mismatch equal to 0.98 in comparison with ITO/PEN and ITO/PET

systems (0.93 and 0.94, respectively), as Table 6.3 summarises. This suggests that the failure mechanism could be driven by high elasticity or local ductility of PC substrate. Also the fact, that the PC polymers are susceptible to crazing during a tensile test (Brydson, 1999), should be considered. It is said, that two mechanisms are responsible for crazing (Plummer et al., 1995): scission and disentanglement of a polymer chains. Scission crazing involves braking of the polymer chains and is driven by low temperatures and high deformation rates. The latter mechanism is favoured by low molecular weights, low deformation rates and the relatively high polymer chains mobility associated with elevated temperatures. The crazes were found to form at the tensile strains 0.75% or more, however it applies only for static loading (Brydson, 1999). The crazes in the sample can also be induced by solvents or even finger-grease, which act as plasticizers (Morgan and O'Neal, 1979). According to the work that has been done by Timóteo *et al*. (2008), the crazes or cracks were observed to form when the tensile loaded PC sample was simultaneously exposed to ethanol. However, no surface crazes or cracks were seen by them when the sample was exposed to ethanol before tensile testing. In this work special care was taken for substrates preparation before ITO deposition (see section 2.2.1 in chapter 2). Therefore, considering the tensile test conditions and the fact that the PC substrate was exposed to ethanol during surface cleaning before PLD process, the crazes or cracks were not observed by atomic force microscope (AFM).

Therefore the electro-mechanical failure of ITO/PC system can be explained by considering the existence of conductive paths across the cracks, relaxation dependence of the elastic modulus of the polymer substrate and also interfacial strength. As crazes were not observed, they are not considered as contributing to failure. Two possible reasons for conductive failure are suggested:

i) high elasticity or local ductility of the polymer substrates. Here, following the COS point conductive paths between ITO fragments can be created. However, high extensions of the polymer substrate at the crack base causes large crack opening displacements and disconnections between the conductive fragments of ITO film leading to infinite resistance, as Figure 6.25 (a) visualises.

ii) low interfacial strength due to poor adhesion between the two components. Here, delamination at the crack base of the ITO layer caused by slip or sliding of the polymer substrate, due to a low threshold for interfacial shearing (Leterrier et al., 1997b) under applied strain, may lead to conductive failure with infinite resistance. This assumes no existence of conductive paths at the crack base, as Figure 6.25 (b) visualises.

To help determine which mechanism is more likely to occur the adhesion level was measured. Figures 6.69, 6.70 and 6.71 show optical micrographs obtained after the adhesion test for ITO on PEN, PET and PC substrates, respectively. It is clear to see that the polymer substrates have an influence on interfacial strength. The ITO/PEN and ITO/PET systems show the highest level of adhesion equal to 5B (on a scale from 0B to 5B; ASTM D3359). In contrast, the ITO/PC system shows a poor adhesion level, of 2B, where the ITO coating cracked and flaked along the edges, as Figure 6.71 shows. Therefore, it is concluded that the conductive failure with infinite resistance following the COS of the ITO/PC system is due to poor adhesion between the two components without the presence of conductive paths, where a high elastic mismatch may accelerate the failure mechanism. Poor adhesion between the ITO film and PC substrate is a result of low wettability of the PC substrate and its very low roughness (RMS $\cong$ 0.77 nm, see AFM image in Figure 3.25) that may prevent any interlocking

mechanism between these two components. In addition, Figure 6.26 clearly shows that the sample lost conductivity at the very beginning of the ITO film cracking. This suggests that even the first mature crack spanning the whole sample width may be responsible for ITO conductive failure. The interfacial strength between the conductive ITO film and the polymer substrate may be a key parameter in understanding the mechanism of formation of conductive bridges connecting ITO fragments, but the details are still not clear.

Furthermore, it is clear to see from the stress-strain-resistance curve on Figure 6.21 and 6.23 for ITO/PEN and ITO/PET samples, respectively, that the COS of ITO film is related to the elongation at yield of the considered polymer substrates. It is evident though, that the conductive failure of the ITO film occurs at the beginning of the plastic deformation region of the substrate. This can be also clearly seen in Figure 1 in (Cairns et al., 2000a) for ITO/PET system. A different stress-train-resistance behaviour is observed for the ITO/PC sample, as Figure 6.24 shows. The conductive failure of ITO film takes place at ~ 2.50% strain, which is far before the elongation at yield of the PC substrate, reported to be between 6 and 7% (Brydson, 1999). It is due to a high elastic nature of the amorphous PC substrate, which elongates easily at the low stresses.

The strain-resistance behaviour of ITO/polymer systems tested at a crosshead speed of 0.5 mm/min is presented in Figure 6.27 for further comparison. Despite similar trends of resistance changes for both ITO/PET and ITO/PEN samples, it is clear to see, that their slopes differ significantly from each other. The critical strain of the ITO/PET sample is slightly lower than that of the ITO/PEN sample, however its resistance increases slower above the COS point. For example, at the 6% strain the increment of resistance is equal to ~ 31 and ~ 64

for ITO/PET and ITO/PEN samples, respectively, which is two times lower. Table 6.4 (column b) shows the slope values of resistance changes above the critical strain. It is important to note, that the standard deviation from the mean for the ITO/PET and ITO/PEN samples is very high in comparison to that of the ITO/PC sample. It introduces some ambiguity in the data interpretation. It also suggests that the resistance increase of each sample follows a different rate above the COS point. This behaviour is observed especially for the ITO/PET and ITO/PEN samples, which may be related to the surface quality (number of defects) of the ITO films. A number of defects and impurities in the ITO film plays a crucial role in the crack initiation [e.g. Figure 6.15 (b)], and hence may strongly influence the rate of resistance increase.

Figure 6.28 shows the samples strained at the crosshead speed set at 0.05 mm/min. It is clear to see, that the strain-resistance behaviour of the ITO/polymer systems is similar to that of the samples strained at the higher speed set at 0.5 mm/min (Figure 6.27). Table 6.4 summarises the results for the samples strained at different crosshead speed. It shows that the crosshead speed in the range from 0.05 to 0.5 mm/min does not influence the critical onset strain. In addition, the COS results for all the ITO/polymer samples are highly reproducible. Similar results, for both testing speeds, are observed for the resistance increase above COS point with one exception of the ITO/PET sample, where the rate of resistance increase is lower for the lower, 0.05 mm/min, crosshead speed.

6.6.3 Monotonic buckling

Monotonic buckling of the ITO/polymer systems was conducted using buckling device which was developed in this project (see section 2.2.5 in chapter 2). The test was performed in order to investigate the flexibility of pulsed–laser deposited ITO films on polymer substrates. The influence of polymer thickness is also discussed.

6.6.3.1 Monotonic buckling on the tensile side

Figure 6.29 shows increment of resistance as a function of radius of buckling curvature of the ITO-coated polymer substrates tested in tension. It is clear to see that with decreasing the radius of curvature resistance suddenly increases at the critical radius due to cracking of the ITO layer. The ITO films deposited on the PEN and PET substrates exhibit conductive failure in the vicinity of 3 mm radius of buckling curvature. With further decrease of the radius of curvature the resistance increases linearly.

In the case of the ITO/PC sample, conductive failure occurs in the vicinity of 4 mm radius of curvature (Figure 6.29), which is 1 mm larger than that of ITO/PEN and ITO/PET systems. Above the critical radius of curvature the resistance increases immediately due to poor adhesion between the ITO and PC substrate following the mechanism proposed in section 6.6.2. Despite the lower flexibility of ITO/PC systems, the ITO/PC samples show similar crack onset strain to ITO/PET and ITO/PEN samples, as Table 6.5 shows. It is evident though that the lower flexibility of ITO/PC systems in comparison with ITO/PET systems is due to the greater thickness of the PC substrate (see Table 3.5). This is consistent with equations (2.15) and (2.16) where the strain of the top ITO layer is directly proportional to the film and

substrate thicknesses. Therefore with increasing sample thickness a higher strain will be achieved at lower curvature. On the other hand, ITO films on thinner substrates show smaller stress corresponding to the same buckling curvature (Park et al., 2003).

In this study the ITO layer thickness is constant, therefore the results shows that by increasing polymer thickness by 0.05 mm the flexibility of ITO/polymer systems decreases by 25%.

6.6.3.2 Monotonic buckling on the compression side

Figure 6.30 shows increment of resistance as a function of the radius of buckling curvature of the ITO/polymer systems in compression. All samples investigated show very low critical radius of curvature in the vicinity of 1 mm. Above the critical radius the resistance increases immediately in the same manner for all samples. It is worth noting that with increasing curvature the resistance decreases, reaching a maximum decrease of ~ 20% just before the critical radius of curvature. This may be the result of the distance shortening between neighbouring atoms/grains in the ITO film, which leads to reduction of physical barriers for travelling electrons and increase of their mobility. The ITO films on polymer substrates flexed in compression exhibit much higher flexibility than those flexed in tension. This is due to the fact that the tensile properties of brittle materials are determined by defects such as surface flaws or submicroscopic cracks in both the film and polymer substrate (Nielsen, 1974a), which was also observed in this work during fragmentation test [see Figure 6.15 (b)]. When the sample is under compression the applied stresses tend to close these cracks rather than open them. Thus the compression test reflects the intrinsic properties of the materials while

the tensile test is characteristic of the defects in the materials (Nielsen, 1974a). The test shows that the bending in tension is critical for mechanical reliability of the ITO films, which is consistent with the results reported previously (Chen et al., 2001b).

Table 6.5 shows that the critical buckling onset strain, equal to ~ 7.0%, of the ITO/polymer samples flexed in the compression is almost three times higher than that of the samples flexed in tension. The highest critical buckling strain of ~ 8.0% is observed for the ITO/PC sample. The conductive failure under compression is adhesion-related due to buckling of the ITO film coupled with cracking. It is interesting to note that these critical strains of adhesion failure of the ITO film are almost equal to the strains at which buckling of the film was observed to occur in the tensile fragmentation test (see section 6.6.1). Such a high critical buckling onset strain of the ITO film subjected to flexing in compression has not previously been reported.

6.6.4 Cycling buckling test of ITO/polymer systems

The ITO/polymer systems were loaded repeatedly 100 times in both tension and compression with buckling speed set at 30 seconds/cycle using the same equipment as for monotonic bending. The resistance changes were recorded *in situ*. Using the data achieved from monotonic buckling tests conducted in tension a fixed radius of curvature equal to 4 mm was chosen. In the case of ITO/PEN and ITO/PET samples this gives strain, of ~ 1.80%, which is below the critical onset strain (~ 2.30%). For the ITO/PC sample the fixed radius of curvature is equal to the critical buckling radius due to the greater thickness of PC substrate in comparison with PEN and PET substrates. Fatigue tests were performed in order to

investigate the stability of the ITO/polymer systems after cycling loading at fixed curvature which is crucial for life-time prediction of flexible electronics.

6.6.4.1 Cycling buckling on the tensile side

Figure 6.31 shows variation of resistance as a function of applied number of cycles of the ITO/PEN sample. It is clear to see that after the few first cycles the resistance increases abruptly up to the certain level – an equilibrium point, which takes place in the vicinity of the ~ 7^{th} cycle. Then the resistance changes become more stable and increase gradually with further increase of the number of applied buckling cycles. During the unloading portion of the cycle a small resistance recovery of the tested ITO/PEN sample is observed, as the insert graph in Figure 6.31 shows.

The ITO film deposited on the PET and PC substrates shows similar electro-mechanical behaviour to that of the ITO/PEN sample with an equilibrium point also in the vicinity of the ~ 7^{th} cycle, as Figure 6.32 and 6.33 show. However, in the case of the ITO/PC sample enormous changes in the resistance are clear to see during loading and unloading of the sample. This is due to the applied strain, which is equal to the critical onset strain (~ 2.30%). Hence, such a variation in the resistance may be due to wide opening and closing microcracks in the ITO layer during the loading and unloading cycles. This is consistent with previous observations of ITO-cotaed PET under oscillatory bending (Koniger and Munstedt, 2008b).

Table 6.6 summarises the results of fatigue buckling tests in tension of the ITO/polymer system. It is evident that the highest increase of resistance (of ~ 72%) after 100 buckling cycles is observed for the ITO/PC sample. This result clearly demonstrates that an enormous increase of resistance is obtained when applied strain is equal to the critical onset strain. The ITO/PEN sample exhibits the lowest increase of resistance, ~ 8% for an applied buckling strain equal to 1.8%, which is lower than the critical onset strain (~ 2.30%). The ITO/PET sample shows ~ 16% increase of resistance, which is twice as high as that of the ITO/PEN sample at a similar applied strain. It should be noted that for a higher number of cycles a higher increase of resistance is expected due to material fatigue which finally leads to catastrophic conductive failure as described in detail in (Cairns, 2005).

Similar electro-mechanical behaviour to this work was reported previously by Cairns and Crawford (2005a) for the ITO film deposited on PET substrate. They suggested that the sudden increase in resistance observed at the beginning of the fatigue bending test is due to changes in dimensions of the polymer substrate. After each loading cycle the gauge width of the substrate decreases until an equilibrium point occurs between the applied strain and the recovery of the gauge width (Cairns and Crawford, 2005a). They also concluded that the gradual linear increase of the resistance above the equilibrium point is probably due to progressive cracking of the ITO layer; hence for a constant applied strain the resistance is directly proportional to the number of microcracks. This was also postulated by Koniger and Munstedt (2008b) who observed that the difference in resistance between unbent and bent state remains constant, whereas the overall resistance of the sample above the equilibrium point increases gradually with increasing number of cycles.

We also propose another possible scenario in which the number of microcracks may reach a saturation point at the initial stage of cycling under conditions where the applied stress is equal to the critical stress responsible for thin film cracking. Therefore, the observed equilibrium point is not only between the applied strain and the substrate dimension-recovery but may be also between the applied strain and the number of microcracks. Thus above the equilibrium point the variations in the resistance changes upon loading and unloading cycles may be due to opening and closing the finite number of microcracks. Each time a constant buckling strain is applied to the ITO film these microcracks can grow in length and depth due to material fatigue causing a gradual increase of resistance. This is consistent with the results showed in Figure 6.33 for ITO/PC samples, where with an increasing number of cycles the difference in resistance between unbuckled and buckled states increases gradually suggesting the growth in length and depth of a constant number of cracks. The electro-mechanical behaviour of the ITO/PC system suggests that our explanation may be correct for conditions where the applied repeated strain is equal to the crack onset strain of the ITO/polymer system because this implies that the microcracks are formed before the equilibrium point. However, further study based on fragmentation buckling tests coupled with *ex situ* SEM observation of the ITO surface after each buckling cycle (e.g. up to 20 applied cycles) are necessary to clarify this mechanism.

The lowest increase of the resistance after fatigue tests of ITO/PEN samples is attributed to the lowest mechanical mismatch between an ITO film and a PEN substrate as Dundurs parameter describes in Table 6.3.

6.6.4.2 Cycling buckling on the compression side

Figure 6.34 shows fatigue buckling in compression of the ITO film (100 nm) deposited on the PEN substrate. The electro-mechanical behaviour is similar to that observed for fatigue buckling in tension. However, the equilibrium point between the applied strain and the recovery of the gauge width takes place at a higher number of cycles, approximately at the 15^{th} cycle. Above the equilibrium point the resistance increases gradually with increasing number of cycles. It is interesting to note that after the fatigue test a significant resistance recovery is observed.

For the ITO/PET sample the equilibrium point takes place also in the vicinity of the 15^{th} cycle, as Figure 6.35 shows, which is twice as high compared with the fatigue test in tension. A significant resistance recovery is also observed after the cyclic loading test.

In the case of ITO/PC samples the equilibrium point is observed in the vicinity of the 20^{th} cycle, as Figure 6.36 shows. The resistance does not recover after the test.

The results show that the ITO-coated PC needs a greater number of cycles to reach the equilibrium point than the ITO/PEN or ITO/PET systems. This may be due to a higher applied strain (~ 2.30%) due to the higher thickness of the PC substrate and its higher elasticity (tendency to be deformed elastically when a force is applied to it) in comparison with the PEN and PET substrates. However, no differences between any of the samples were observed for the equilibrium point in a fatigue tests conducted in tension. Variations in the resistance changes during the loading and unloading cycles for the ITO/PC sample are much smaller in comparison with the fatigue test in tension (see Figure 6.33). This may be due to the fact that the applied strain is far less than the critical buckling strain (~ 8.0%) of the ITO

film found during the monotonic buckling test in compression (see section 6.6.3.2). It is interesting to note that after the test the resistance increase is similar for all samples investigated and lies in the range 25 - 29%, despite the higher applied strain for the ITO/PC sample. For the ITO/PC sample this increase in resistance is almost three times smaller than that observed after fatigue tests in tension. This result can be expected as the critical buckling onset strain for the ITO film in compression is higher than the crack onset strain in tension (see Table 6.5). The results of the fatigue buckling test in compression are shown in Table 6.7.

The electro-mechanical behaviour under compression can be explained by analogy with the mechanism proposed by Cairns and Crawford (2005a) for the fatigue test in tension. It is well known that failure of brittle films under compression is adhesion related (Chen et al., 2002; Jansson et al., 2006). Thus, above the equilibrium point, which probably occurs between the applied strain and recovery of the gauge width, the gradual linear increase of the resistance is related to the progressive microbuckling-driven delamination of the ITO layer (see SEM investigations after fatigue tests in section 6.6.7.2).

6.6.5 Ex situ SEM and AFM observation of crack profile and adhesion failure of ITO films after tensile testing

The 100 nm thick ITO films were investigated after uniaxial fragmentation testing using SEM and AFM techniques in order to reveal details of their failure that were not visible during *in situ* optical microscopy observations. This further insight into film failure is also necessary to understand its mechanism.

Figure 6.37 shows SEM micrographs of an ITO film deposited on a PEN substrate and strained up to ~ 11.0%. Cracking and buckling of the thin layer is clearly visible, as Figure 6.37 (a) shows. In addition, the fragments of the ITO film are peeled off from the substrate revealing its surface, as the red arrows indicate. Figure 6.37 (b) shows the buckling profile of the ITO film. The crack on the top of the buckle, parallel to the applied strain, is clear to see as shown by the red arrow.

Similar behaviour to that of the ITO/PEN sample is observed for the ITO-coated PC substrate. Cracking and buckling with cracks on the buckle top are observed, as Figure 6.39 shows.

In the case of the ITO/PET sample, strained up to ~ 11.0%, cracking on the buckle top is not observed. In addition the width of the buckle profile is larger than that of both the ITO/PEN and ITO/PC samples, as Figure 6.38 shows.

Figure 6.40 shows a 3D–AFM micrograph of a channelling crack of the ITO film deposited on the PEN substrate and strained up to ~ 11.0% strain. The cracks in ITO/PEN sample exhibit opened book–like morphology. In addition a cross–sectional view of the channelling crack reveals the “V” shape of the crack morphology (see Figure 6.41).

High resolution AFM images reveal the presence of micro-crack formation in the ITO film on a PEN substrate strained up to ~ 11.0% tensile strain, as Figure 6.42 (a) shows. It is clear to see that the cracks form along the grain boundaries of ITO layer, as the black arrows indicate. This suggests a typical intergranular, cohesive failure mechanism in which the neighbouring layer fragments separate from each other at their boundaries upon application of the applied tensile stress (Fortunato et al., 2002b; Sierros et al., 2010b). Figure 6.42 shows a cross–

sectional view of the ITO layer with micro-crack depth and width equal to ~ 35 and ~ 100 nm, respectively. It is believed, that these micro-cracks are tertiary cracks and were formed parallel to the primary cracks during tensile testing.

Figure 6.43 shows buckling profile of the ITO film on the PEN substrate. AFM analysis shows that besides the cracks on the buckle-top of the ITO layer other cracks exist. These cracks are formed at the edge of debonded zone and are aligned along its length, as the black arrow shows. The buckle and crack profile can be seen in cross–sectional view in Figure 6.44.

In the case of ITO/PET samples, similar "V" shape cracks are observed to that of the ITO/PEN sample as 3D–AFM and cross–sectional AFM micrographs show (Figure 6.45 and 6.46, respectively). Previous SEM observations did not reveal cracks on the buckle top. However, AFM analysis shows that they are present in some places. Figure 6.47 (a) and (b) show 2D-AFM images of the buckle with crack on the top and its cross–sectional view, respectively.

Similar crack and buckling morphology of the ITO film observed for the ITO/PEN and ITO/PET samples applies also to the ITO-coated PC substrates. Figure 6.48, 6.49, 6.50 and 6.51 show 3D view of the crack profile, cross–sectional view of the sample with channelling crack, 3D buckle profile and its cross–sectional analysis, respectively.

The pattern of buckling-driven delamination, especially the presence of the cracks at the edges of the debonded zone, observed for the ITO/PEN sample indicates good interfacial strength (Yang and Park, 2010). It can be explained as follows: as soon as the stress relaxes

within the buckled region a concentration of stress can be found at the edge of the buckled region. If the interfacial strength is sufficiently high such stress concentration can influence crack formation in the film. On the other hand, if the sample exhibits relatively low interfacial strength, the growth in size of a buckled region or a change in its shape may occur due to further coating delamination (Freund and Suresh, 2003). Indeed, e.g. the width of the buckle zone of ITO/PET strained up to ~11% strain is larger than that observed for ITO/PEN also strained up to 11% (see Figure 6.44 and 6.47, respectively). Thus, a slightly higher adhesion level in ITO/PEN systems is expected in comparison with ITO-coated PET and PC substrates.

It was previously assumed that the bottom of the channelling crack is a sharp crack lying on the interface (Ye et al., 1992), see Figure 6.2 (a). It should be noted that the AFM scanning technique has limitations to measure steep walls of relatively deep trenches. The steepest measurable angle using silicon nitride cantilevers is equal to ~ 65^{o}. The measured angle of the crack wall in Figure 6.49 is equal to ~ 65^{o}. This means, that in practice the walls of ITO fragments can be steeper or in some cases even vertical. The channelling crack morphology (see Figure 6.2) mostly depends on the relative fracture energies of the thin film, substrate and interface (Ye et al., 1992). Moreover, it is also more likely that the base of the crack is random or square shape rather than the “V” shape, for the cases where the polymer substrate undergoes plastic deformation due to large applied strains.

6.6.6 Ex situ SEM investigation after monotonic buckling test

Surface damage of the ITO films introduced by monotonic buckling test in tension and compression of the samples was investigated *ex situ* using scanning electron microscopy (SEM).

6.6.6.1 ITO surface investigation after monotonic buckling in tension

Figure 6.52 shows the surface of ITO film (100 nm) deposited on the PEN substrate after a monotonic buckling test. The sample was flexed in tension down to 2.5 mm radius of curvature, which is equivalent to an applied tensile strain of ~ 3.0%. Channelling cracks and delamination of the ITO film can clearly be seen. The cracks are parallel to each other and perpendicular to the buckling direction, which is consistent with the results obtained from the uniaxial tensile fragmentation test coupled with *in situ* optical microscopy observation (see, e.g. Figure 6.15). However, the cracks form in the middle of the sample curvature instead covering the full sample length. More aligned cracks with respect to each other and with finite length are observed for the ITO/PET sample flexed down to 2.4 mm radius of buckling curvature (Figure 6.53).

Figure 6.54 shows the surface of ITO film (100 nm) deposited on the PC substrate after monotonic buckling in tension at 3.0 mm radius of curvature, which is equivalent to an applied tensile strain of ~ 3.0%. Channelling cracks and surface delamination are also clear to see. In addition severe ITO film peeling is observed. In some places the ITO fragments are

completely removed revealing a surface of the substrate underneath. This suggests a poor adhesion level between ITO and PC, as will be discussed in section 6.6.9.1.

Cracking and delamination of the ITO film deposited on polymer substrates subjected to flexing in tension are responsible for conductive failure of the ITO layer, as Figure 6.29 shows.

6.6.6.2 ITO surface investigation after monotonic buckling in compression

Figure 6.55 shows an SEM micrograph of an ITO film (100 nm) deposited on a PEN substrate after monotonic buckling under compression at 0.9 mm radius of curvature, which is equivalent to an applied compressive strain of ~ 8.0%. Buckling delamination of the ITO layer is clear to see. The buckling zones are parallel to each other and perpendicular to the buckling direction. Moreover, cracks at the edges of the buckle profile aligned along its lengths are also evident. The same buckling pattern is observed for the ITO/PET and ITO/PC samples. In some places, the buckled ITO film is detached from the substrate creating a significant gap between the conductive ITO fragments, as in the case of the ITO/PET sample shown in Figure 6.56. Thus, an abrupt increase in the resistance is observed for all samples above the critical buckling radius, as shown in Figure 6.30. In addition, the buckling profile with cracks was observed previously by atomic force microscopy (AFM) investigation (e.g. Figure 6.43 and 6.44) for the ITO film coated on polymer samples submitted to the uniaxial tensile fragmentation test. Despite the fact that in the uniaxial fragmentation test the buckling

profiles are parallel to the applied force due to lateral contraction, in both cases the ITO film failure is adhesion-related and takes place almost at the same applied strain (~ 8.0%).

The morphology of cracks and buckles with top cracks observed in this study after flexing the samples in tension and compression, respectively, is consistent with that previously reported (Cairns et al., 2000b; Chen et al., 2001b). The fact that the damage of the ITO layer is observed in the middle region of the sample length, when it is subjected to the flexing in both tension and compression, means that the highest critical strains are created over that particular region. Therefore, it is evident that the curvature created during the sample flexing is not uniform through its entire length. These results are consistent with the study conducted by Park *et al*. (2004) who concluded that the stress introduced into the ITO layer during bending is position-dependent. They observed the highest crack density in the middle of the flexed sample due to the highest stress concentrated in that region.

6.6.7 Ex situ SEM investigation of ITO film after cycling buckling test

The SEM technique was employed to investigate the surface of the ITO layer (100 nm) deposited on polymer substrates and submitted to 100 repeated buckling cycles on the tensile and compression side at 4 mm radius of curvature. The influence of applied cycles on material fatigue was examined.

6.6.7.1 SEM investigation after cycling buckling on the tensile side

Figures 6.57 and 6.58 show SEM micrographs of the ITO/PEN and ITO/PET samples after fatigue test in tension. Despite exhaustive searches no cracks were found. However, some submicron cracks may be present in the ITO film, as the resistance during the test gradually increases with increasing number of cycles. The fact that cracks in the coating were not found is due to the strain recovery upon unloading of the sample which leads to closure of the microcracks (Leterrier et al., 1997c).

In the case of ITO film on a PC substrate, cracks perpendicular to the buckling direction are visible, as Figure 6.59 shows. Mature and growing cracks are present in the conductive layer due to the applied critical radius of buckling curvature (4 mm) during fatigue test. Thus an enormous variations in the resistance changes during loading and unloading cycles are observed, as was discussed in section 6.6.4.1.

6.6.7.2 SEM investigation after cycling buckling on the compression side

Figure 6.60 shows SEM micrographs of ITO/PEN samples after 100 cycles applied at 4 mm radius of curvature in compression. Vertical lines of buckling delamination perpendicular to buckling direction are clear to see [Figure 6.60 (a)]. In addition, in some places ITO layer fragments were completely removed from the substrate. Closer observation of the damage film revealed cracks along the buckling zones, as Figure 6.60 (b) shows. Similar adhesion failure was observed by AFM after uniaxial tensile testing (see Figure 6.43).

Figure 6.61 shows SEM micrographs of the ITO/PET system. The buckling width is higher than that of ITO/PEN samples. However, peeling of the ITO film is not so pronounced [Figure 6.61 (a)]. Cracks on the top of the buckle profile are clearly visible in Figure 6.61 (b). They are also visible on AFM micrographs taken after uniaxial tensile testing (see Figure 6.47)

The ITO/PC samples show similar buckling delamination pattern to that observed for ITO/PET systems, as Figure 6.62 presents.

It should be noted that the ITO/PEN systems exhibit the smallest area with ITO surface damage. On the other hand they show regions with ITO film fragments completely removed from the polymer substrate exposing its surface. In contrast, the ITO/PET and ITO/PC samples show more and longer buckling lines but with less pronounced peeling of the ITO film.

In addition, cycling buckling in compression is more critical than cycling buckling in tension. Therefore it is evident that the greater increase of resistance observed after cycling loading in compression is due to buckling-driven delamination of the ITO layer.

6.6.8 Influence of ITO thickness on residual stress and electro–mechanical behaviour

ITO films with three different thicknesses of 50, 100 and 150 nm were deposited on the PEN substrate. The PEN substrate was chosen, because the ITO film on PEN showed the best

electro-mechanical reliability in comparison with the ITO/PET and ITO/PC samples investigated in the previous sections. The series of mechanical tests were performed in order to investigate any influence of the conductive layer thickness on its electro–mechanical reliability.

6.6.8.1 Residual stress and critical onset strain

Figure 6.63 shows increment of resistance as a function of applied uniaxial tensile strain of 50, 100 and 150 nm thick ITO films deposited on PEN substrates. It is clear to see that the 50 nm thick ITO film exhibits the highest critical onset strain equal to 3.50%. A slightly lower critical strain of ~ 3.40% is observed for the 100 nm thick ITO film. The 150 nm thick ITO film shows the lowest critical strain equal to ~ 2.9%. The rate of resistance increase after the COS is similar for both the 100 and 150 nm ITO films. A much lower rate of resistance increase is shown for the 50 nm thick ITO film. In all cases a gradual linear increase of the resistance above the critical point is clear to see. This electro-mechanical behaviour was discussed previously in details in section 6.6.2.

Table 6.8 shows the residual compressive stress introduced into the ITO film during the deposition process. The residual compressive stress increases with ITO thickness. The residual compressive stress of a 50 nm thick ITO film on PEN was not measurable as the sample after deposition was flat. This means that the measured critical onset strain (COS) of the ITO film is equal to the intrinsic crack onset strain (COS*) and represents the intrinsic cohesive properties of the material. The 100 nm thick ITO film shows a relatively high

residual compressive stress of ~ 590 MPa. Interestingly, a slightly lower residual compressive stress equal to ~ 500 MPa is observed for the 150 nm ITO film. According to equation (2.14), it is clear to see that the residual compressive strain has a beneficial influence on the net critical onset strain, which leads to its overestimation, as Figure 6.64 shows. This was also observed where different polymer substrates were considered (see section 6.6.1). It is also evident that both the crack onset strain (COS) and the intrinsic crack onset strain (COS*) decrease with increasing ITO layer thickness. The decrease of intrinsic crack onset strain with increasing the layer thickness was previously found to follow scaling, where COS* is inversely proportional to the square root of coating thickness ($COS^* \alpha \frac{1}{\sqrt{h}}$) (Leterrier et al., 2004). The green line in Figure 6.64 represents this scaling fit to the COS* data. It is clear to see that the COS* points lie quite close to the fitted curve, however, a linear decrease is observed rather than an exponential decrease. The decrease of critical strain may be due to an increase of the number of nanosized defects in ITO film with increasing thickness (Sierros et al., 2010b). Also it may be due to the increase of ITO roughness with increasing thickness, since stress concentrations in valleys on rough surfaces causes crack initiation in brittle films (Yang and Park, 2010).

6.6.8.2 Fragmentation test and crack density

A uniaxial fragmentation test of the 50, 100 and 150 nm thick ITO film on PEN substrates was performed using the miniature tensile machine (Minimat) at a constant crosshead speed set at 0.1 mm/min. Crack evolution was observed in situ and recorded by a microscope camera. The resistance change was also monitored *in situ*.

The crack initiation of the ITO layer is governed by surface imperfections, such as pin holes or scratches, which act as stress centres independently of the layer thickness. The buckling of the 50 and 150 nm thick films starts to occur at the applied strain equal to ~ 8%. The same crack and buckling evolution was observed and discussed previously (see section 6.6.1) for the ITO 100 nm/PEN, PET and PC systems. Thus optical micrographs related to the 50 and 150 nm thick ITO films are not presented and discussed here.

Figure 6.65 shows crack density as a function of applied strain for different ITO layer thicknesses. It is clear to see that the crack density depends on the ITO layer thickness. From the critical strain up to 5% applied strain the rate of ITO film cracking is almost the same for all thicknesses. With a further increase of the strain, the 100 and 150 nm thick ITO films start to saturate reaching the saturation point in the vicinity of 13% strain. Moreover, both films exhibit the same crack density at the saturation point, of ~ 105 mm^{-1}. The crack density of 50 nm thick ITO film starts to saturate at the higher applied tensile strains, reaching the saturation point in the vicinity of 15% strain. In addition, the 50 nm thick ITO film shows the highest crack density at saturation, of ~ 150 mm^{-1}. The highest crack density for the thinnest film was also observed previously for a SiO_x barrier coating on PET substrate (Leterrier et al., 1997a). This is due to the higher coating strength which increases with decreasing thickness (Leterrier et al., 1997a).

6.6.8.3 Monotonic buckling on the tensile side

The monotonic buckling test on the tensile side was performed using buckling device which was developed in this project (see section 2.2.5 in chapter 2). The test was performed in order to investigate influence of the ITO layer thickness on its flexibility.

Figure 6.66 shows the increment of resistance as a function of the radius of buckling curvature for 50, 100 and 150 nm thick ITO films on PEN substrates. It is evident that with decreasing radius of curvature the normalised resistance starts to increase rapidly at the critical radius of buckling curvature. The increase of resistance is observed due to cracking of the conductive brittle ITO films, as it was discussed previously in section 6.6.2 and 6.6.3.1 where different types of polymer substrates were considered. It is clear to see that with increasing thickness of ITO film the critical radius of curvature also increases, as Figure 6.66 shows. The lowest critical buckling radius equal to ~ 2.60 mm is shown for the 50 nm thick ITO film, which is equivalent to a critical onset strain (COS), of 2.80%. The 100 and 150 nm thick ITO films exhibit higher critical radius of buckling curvature equal to ~ 3.0 mm, which is equivalent to the COS of ~ 2.40%. The results are summarised in Table 6.9.

6.6.8.4 Cycling buckling on the tensile side

The 50, 100 and 150 nm thick ITO films on the PEN substrates were loaded repeatedly 100 times in tension with buckling speed set at 30 seconds/cycle using the same equipment as for monotonic buckling tests. The resistance changes were recorded *in situ*. The samples were flexed at the fixed radius of curvature equal to 4 mm. This radius of curvature applies a tensile

strain to the top ITO layer equal to 1.80%, which is below the critical onset strain that has been found for the 50, 100 and 150 thick ITO films in monotonic buckling test (2.80, 2.35 and 2.38%, respectively).

Figure 6.67 shows increment of resistance as a function of applied number of cycles for the 50, 100 and 150 nm thick ITO film on PEN substrates. Similarly to the previous cycling loading tests for the ITO/PEN, ITO/PET and ITO/PC systems (see section 6.6.4.1) the resistance increases abruptly when the first cycles are applied. Then the samples reach an equilibrium above which the resistance increases gradually with increasing number of cycles. It is clear to see that the first applied cycles are crucial for electro-mechanical reliability of the ITO/PEN systems, as Figure 6.67 shows. It is evident that the ITO thickness influences electro-mechanical stability of the ITO/PEN systems. For the 50 and 100 nm thick ITO films the equilibrium point takes place in the vicinity of ~ 7^{th} cycle. However, the 50 nm thick ITO film shows the lowest increase of resistance, of ~ 3% after 100 cycles. The second lowest increase of resistance equal to 8% is shown by the 100 nm thick ITO film. In the case of 150 nm thick ITO film, a relatively high increase of resistance is observed between the first applied cycle and the equilibrium point, which takes place in the vicinity of 17^{th} cycle. The equilibrium point of the 150 nm thick ITO film takes place for a higher number of cycles than that of the 50 and 100 nm thick ITO films probably due to microcrack formation in the conductive layer. Furthermore, the 150 nm thick ITO film exhibits the highest increase of resistance, of ~ 27% after cycling loading. Table 6.10 summarises the results of fatigue tests for the different ITO layer thicknesses. It is important to point out that the 100 and 150 nm thick ITO films exhibit almost the same critical onset strain (~ 2.40%), independently of the layer thickness (as shown in previous section). However, both the ITO thicknesses react

differently to the cycling flexing test. Hence, despite having the same COS for both thicknesses of the ITO film, the 150 nm thick layer exhibits much lower resistance to material fatigue.

Figure 6.68 shows the increment of resistance after the cycling loading test as a function of ITO film thickness. It is evident that the ITO layer thickness has a significant influence on fatigue properties of the ITO/Polymer systems. An exponential increase of resistance increment can be expected after fatigue testing with increasing ITO layer thickness.

6.6.9 Adhesion measurements of ITO/polymer systems

In order to investigate influence of polymer substrates and the thickness of ITO film on interfacial strength, an adhesion test was performed by a tape test according to ASTM D3359 standard (2009e2). To investigate influence of polymer substrates on adhesion level 100 nm thick ITO film was deposited on PEN, PET, and PC substrates. To investigate the influence of ITO thickness on adhesion level 50, 100 and 150 nm thick films were deposited on a PEN substrate.

6.6.9.1 Influence of polymer substrate on adhesion level

Figure 6.69 and 6.70 show optical micrographs after adhesion tests of ITO film deposited on PEN and PET substrates, respectively. No peeling of ITO film is observed indicating a good adhesion level between two components.

In contrast, the ITO/PC system shows a poor adhesion level where ITO coating cracked and flaked along the edges of crosscut lines, as Figure 6.71 shows.

According to ASTM D3359 (2009e2) standard both ITO/PEN and ITO/PET systems exhibit the highest adhesion level, of 5B (on scale from 0B to 5B). A much lower adhesion level, of 2B, is shown by ITO/PC system due to the lower wettability of the PC substrate [see contact angle measurements for PET and PEN in (Sierros et al., 2010b) and PC in (Gururaj et al., 2011)]. In addition very low roughness of PC substrate in comparison to PEN and PET substrates (see Table 3.8) decreases the adhesion level as it prevents any interlocking mechanism (Pedrosa et al., 2010). The same, low adhesion level of 2B was observed recently for sol-gel derived hard coatings applied on PC (Gururaj et al., 2011)

6.6.9.2 Influence of ITO thickness on adhesion level

Figures 6.72, 6.69 and 6.73 show optical micrographs after adhesion tests of 50, 100 and 150 nm thick ITO films on PEN substrates. No peeling is observed for all samples investigated. All samples exhibit the highest adhesion level, of 5B. It is evident that ITO thickness in the range from 50 to 150 nm does not affect adhesion level. The results in this study differ from

that reported previously (Lin et al., 2009) where it has been shown that an increase of ITO film thickness increases shear stress between ITO film and PET substrate. This leads to a decrease of the adhesion level. The explanation may lie in the substrates preparation prior to deposition process, different deposition technique and different residual stress introduced to ITO layer during deposition process. Interestingly, similar results to that obtained in this work were reported for SiO_x films on PET substrates where the interfacial strength evaluated using Kelly-Tyson approach was found to be independent of the coating thickness in the rage from 30 to 150 nm (Leterrier et al., 1997a).

Table 6.11 summarises the results of adhesion level of ITO/polymer systems after the tape test.

6.7 CONCLUSIONS

It was shown in this work that ITO thickness and the type of polymer substrate strongly influence electro-mechanical stability of the ITO film. The PET, PEN and PC polymer substrates have an influence on residual stress, cracking mechanism and the adhesion level of ITO-deposited on them. Therefore, they should be carefully chosen as candidates for flexible electronics. The following conclusions provide necessary information to understand the failure mechanisms under variety of stress conditions which helps to design a robust, flexible displays.

The results reveal that the 100 nm thick ITO film-coated PEN substrates exhibit the lowest residual stress due to highest rigidity, and the highest intrinsic crack onset strain, evaluated by uniaxial tensile testing, equal to ~ 3% in comparison with ITO-coated PET and PC substrates. Considering the thickness of the film, such a high cracking-resistance was not reported previously.

For all samples investigated in this project buckling onset strain of the ITO film evaluated from uniaxial tensile fragmentation and monotonic buckling in compression tests, takes place at applied strain equal to ~ 8%. From a flexible displays point of view these components can be highly deformed in compression without coating failure.

The results shown that the crack density at saturation depends on the mechanical properties of the polymer substrates. ITO deposited on the stiffest PEN substrate exhibits the highest crack density.

The conductive failure with infinite resistance following the crack onset strain of the ITO/PC system was found to be due to poor adhesion between the two components without the presence of conductive paths, where a high elastic mismatch may accelerate the failure mechanism. PC substrates should be carefully considered as a candidate for flexible displays. Adhesion promotion coatings or plasma surface treatments should be applied for PC surface to improve its adhesion for ITO layer.

The mechanism of conductive path formation between ITO film fragments during progressive cracking of the ITO layer with applied strain is still not clear. Our study shown that the

interfacial strength between the conductive ITO film and the polymer substrate may be a key parameter in understanding this mechanism.

It was found that monotonic buckling in tension is more critical than that in compression. However, the cycling buckling test revealed that compression is more critical than the tension load. Buckling coupled with cracking of the film was found to be responsible for electro-mechanical failure. The results also shown that by increasing polymer thickness by 0.05 mm the flexibility of ITO/polymer systems decreases by 25%. This is a very important information for display designers as it provides the data for conditions that strongly influence a life-time of ITO/polymer systems.

It was found that ITO film deposited on PEN with thicknesses between 50 – 150 nm does not have influence on adhesion level. Moreover, 50 nm thick ITO film-coated PEN substrate shown the highest flexibility. The sample exhibits onset cracking at a very low radius of buckling curvature equal to 2.6 mm. In addition, the fatigue test in tension revealed that the sample exhibits high electro-mechanical reliability. The resistance increased only 3% after 100 cycles applied. This sample is strongly recommended as a candidate for flexible devices with a moderate degree of bending.

Table 6.1 Thermal mismatch - differences in coefficient of thermal expansion between ITO and polymer substrates.

Material	Coefficient of thermal expansion, CTE (ppm/^{o}C)
ITO	8.5[a]
PET	18-20[b]
PEN	20-25[b]
PC	70[c]

a: (Kim et al., 2001), b: (MacDonald et al., 2008) and c: (Siviour et al., 2005)

Table 6.2 Residual stress in ITO film after pulsed laser deposition and intrinsic crack onset strain of ITO/polymer systems strained at crosshead speed of 0.1 mm/min using a miniature tensile tester.

Sample	Residual stress σ (MPa)	COS % ($\Delta R/R_0$ = 10%)	COS* %
ITO/PET Melinex ST 505	962 ± 116	2.80 ± 0.0900	2.04 ± 0.183
ITO/PEN Teonex Q65 FA	587 ± 216	3.42 ± 0.0526	2.95 ± 0.225
ITO/PC Lexan 8010 MC	802 ± 92.0	3.26 ± 0.0790	2.62 ± 0.153

Table 6.3 Elastic mismatch for ITO/polymer systems.

Polymer substrate	Young's modulus, E (GPa)	Elastic mismatch*, α
PEN Teonex Q65 FA	3.37 ± 0.0378	0.93
PET Melinex ST 505	3.21 ± 0.0848	0.94
PC Lexan 8010 MC	1.22 ± 0.0737	0.98

* Elastic modulus of the ITO film equal to 100 GPa (Leterrier et al., 2004) was used for calculations

Table 6.4 Intrinsic crack onset strain of ITO films deposited on polymer substrates strained at crosshead speed set at 0.05 mm/min and 0.5 mm/min using Instron tensile machine.

Sample	COS* (%) [a]	COS* (%) [b]	Slope of resistance changes above COS*	
			a	b
ITO/PET Melinex ST505	2.46 ± 0.111	2.48 ± 0.0437	27.7 ± 35.4	67.3 ± 58.6
ITO/PEN Teonex Q65 FA	2.73 ± 0.147	2.70 ± 0.0328	98.1 ± 94.8	87.3 ± 95.5
ITO/PC Lexan 8010 MC	2.50 ± 0.0524	2.51 ± 0.0484	416 ± 122.8	401.5 ± 166

a: ITO/polymer samples strained with crosshead speed of 0.05 mm/min
b: ITO/polymer samples strained with crosshead speed of 0.5 mm/min

Table 6.5 Results of monotonic buckling tests in tension and compression for COS of ITO/polymer systems.

Sample	Buckling - tensile COS % ($\Delta R/R_0$ = 10%)	Buckling - compression COS % ($\Delta R/R_0$ = 10%)
ITO/PEN	2.35 ± 0.19	7.11 ± 0.20
ITO/PET	2.23 ± 0.22	7.18 ± 0.28
ITO/PC	2.38 ± 0.055	7.86 ± 0.28

Table 6.6 Results of cycling buckling tests on the tensile side of ITO 100 nm/polymer systems.

Sample	Number of cycles	Radius of buckling curvature, r (mm)	Applied strain during buckling, ε (%)	COS (%) ($\Delta R/R_0$ = 10%)	Increase of resistance (%)
ITO/PEN			1.8	2.35 ± 0.19	8.0
ITO/PET	100	4	1.7	2.23 ± 0.22	16.5
ITO/PC			2.3	2.38 ± 0.055	72.3

Table 6.7 Results of cycling buckling tests on the compression side of ITO 100 nm/polymer systems.

Sample	Number of cycles	Radius of buckling curvature, r (mm)	Applied strain during buckling test, ε (%)	COS % ($\Delta R/R_0$ = 10%)	Increase of resistance (%)
ITO/PEN			1.8	7.11 ± 0.20	28.6 ± 7.1
ITO/PET	100	4	1.7	7.18 ± 0.28	24.5 ± 5.5
ITO/PC			2.3	7.86 ± 0.28	24.5 ± 2.0

Table 6.8 Influence of ITO film thickness on residual stress, crack onset strain (COS) and intrinsic crack onset strain (COS*).

Sample	ITO thickness (nm)	Residual stress σ (MPa)	COS % ($\Delta R/R_0$ = 10%)	COS* % ($\Delta R/R_0$ = 10%)
ITO/PEN Teonex Q65 FA	50	-	3.50 ± 0.195	3.50 ± 0.195
	100	587 ± 216	3.42 ± 0.0526	2.95 ± 0.225
	150	496 ± 98	2.94 ± 0.113	2.54 ± 0.192

Table 6.9 Results of monotonic buckling on the tensile side for 50, 100 and 150 nm thick ITO films on PEN substrate.

Sample	ITO thickness (nm)	Critical radius of curvature, Cr (mm)	COS (%) ($\Delta R/R_0$ = 10%)
ITO/PEN Teonex Q65 FA	50	2.60 ± 0.12	2.80 ± 0.13
	100	3.10 ± 0.03	2.35 ± 0.19
	150	3.06 ± 0.11	2.38 ± 0.08

Table 6.10 Results of cycling buckling tests on the tensile side of 50, 100 and 150 nm thick ITO films on PEN substrate.

Sample	ITO thickness, (nm)	Number of cycles	Radius of curvature, r (mm)	Applied strain, ε (%)	COS (%) ($\Delta R/R_0$ = 10%)	Increase of resistance (%)
ITO/PEN Teonex Q65 FA	50	100	4	1.8	2.80 ± 0.13	2.85 ± 2.00
	100			1.8	2.35 ± 0.19	8.00 ± 1.22
	150			1.8	2.38 ± 0.08	26.7 ± 10.0

Table 6.11 Summary of results showing adhesion level of ITO/polymer systems after tape test.

Sample	Adhesion level*
ITO(100 nm)/PC	2B
ITO(100 nm)/PET	5B
ITO(150 nm)/PEN	5B
ITO(100 nm)/PEN	5B
ITO(50 nm)/PEN	5B

* In accordance with ASTM D3359 standard (2009e2)

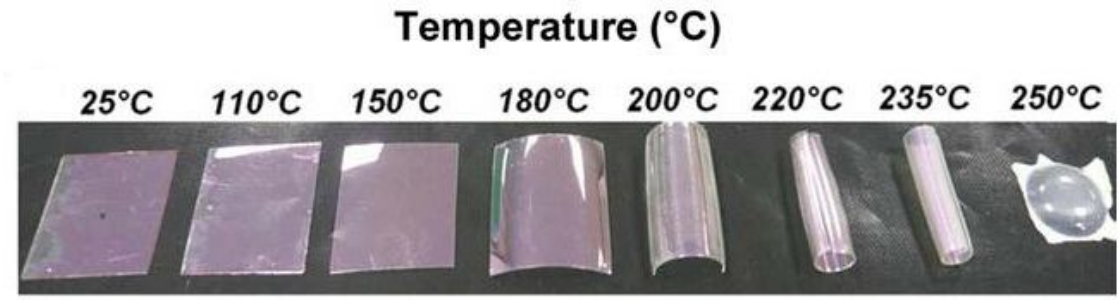

Figure 6.1 Curvature development of ITO-coated heat-stabilised H-S PET substrate with increasing annealing temperature.

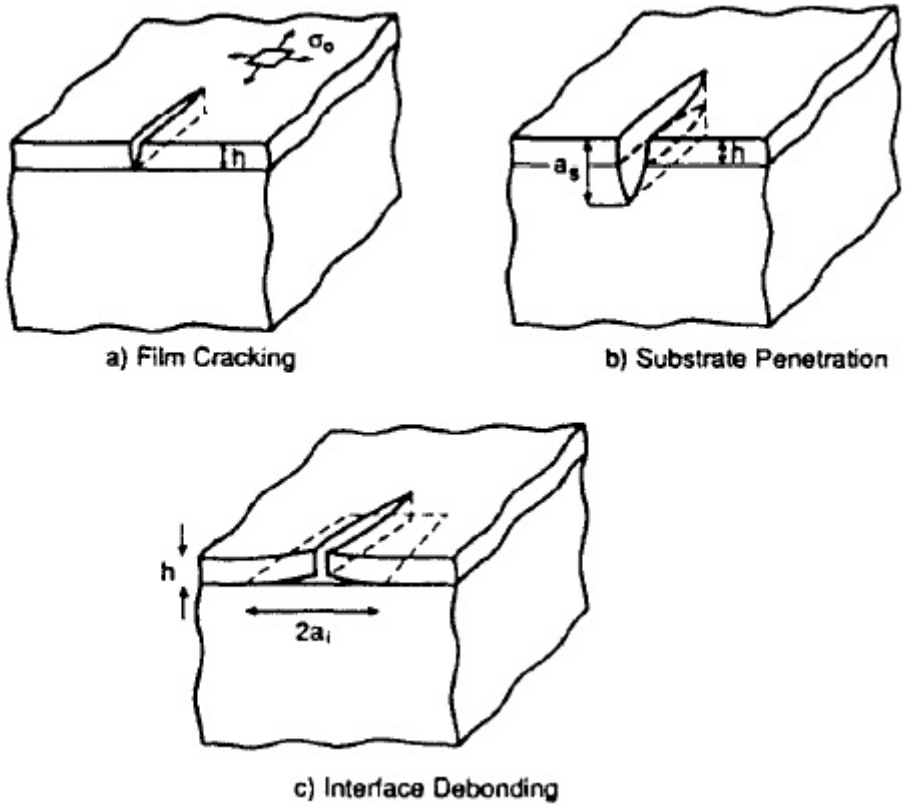

Figure 6.2 A channelling crack propagation a) within a thin film, b) penetrating into the substrate and c) with interface debonding. Adapted from (Ye et al., 1992).

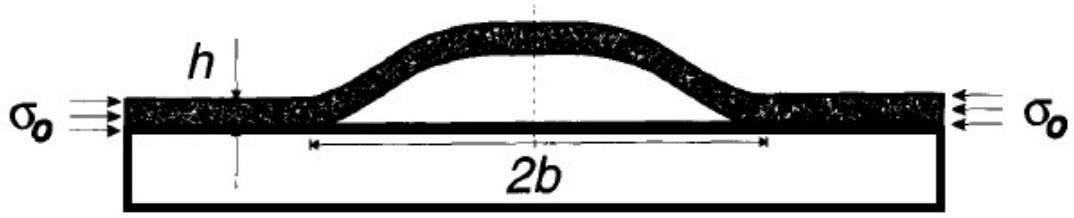

Figure 6.3 Buckling-driven delamination at the interface, adapted from (Thouless et al., 1992).

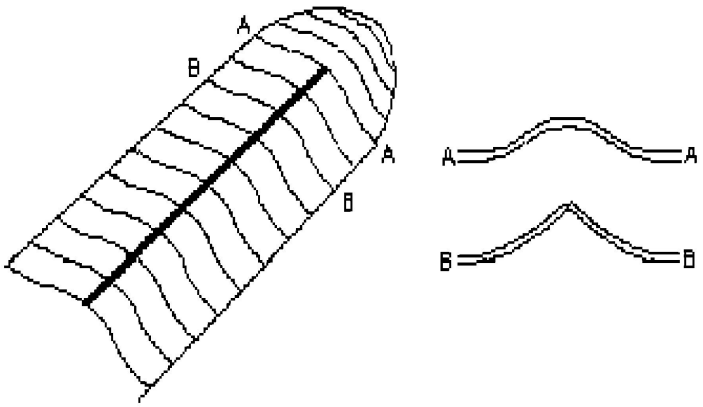

Figure 6.4 A tunnelling delamination-buckle crack. Adapted from (Chen et al., 2001b).

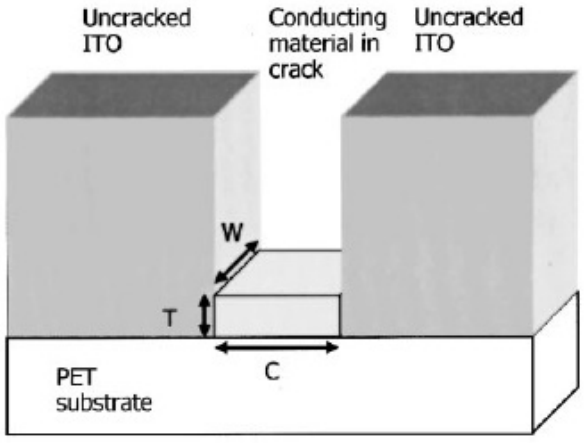

Figure 6.5 A schematic showing conductive path bridging ITO fragments, adapted from (Cairns et al., 2000a).

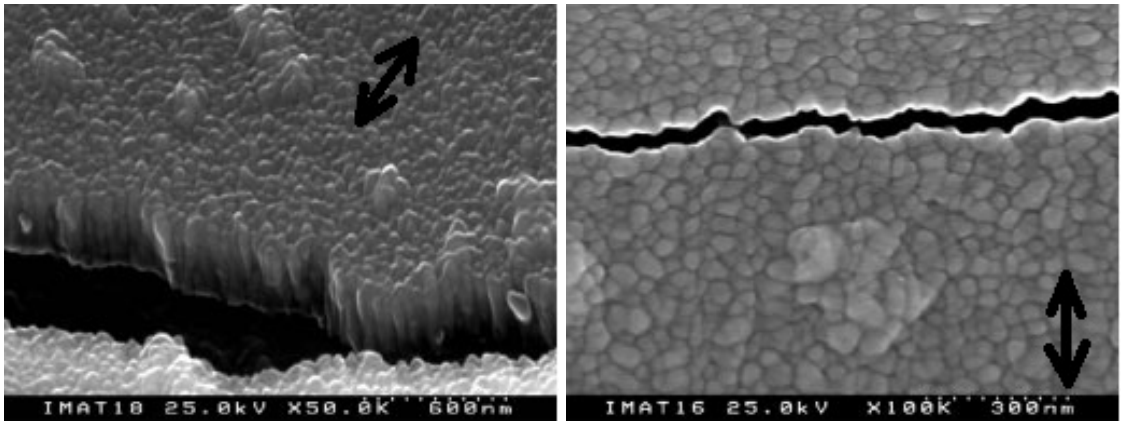

Figure 6.6 Intergranular crack path. Arrows indicate tensile strain direction. Adapted from (Fortunato et al., 2002b).

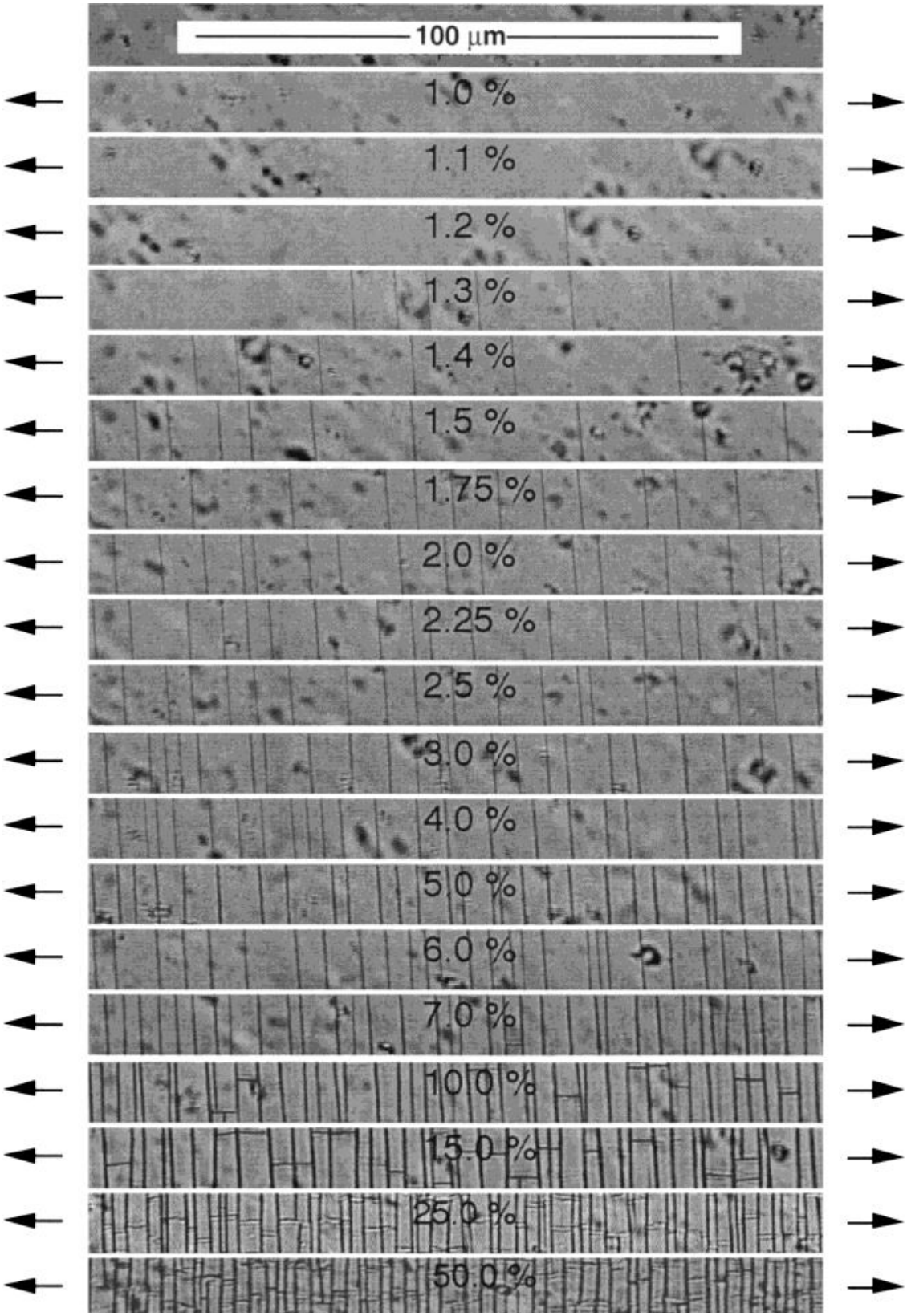

Figure 6.7 Morphology of fragmented SiO_x thin film on PET substrate, adapted from (Leterrier et al., 1997c).

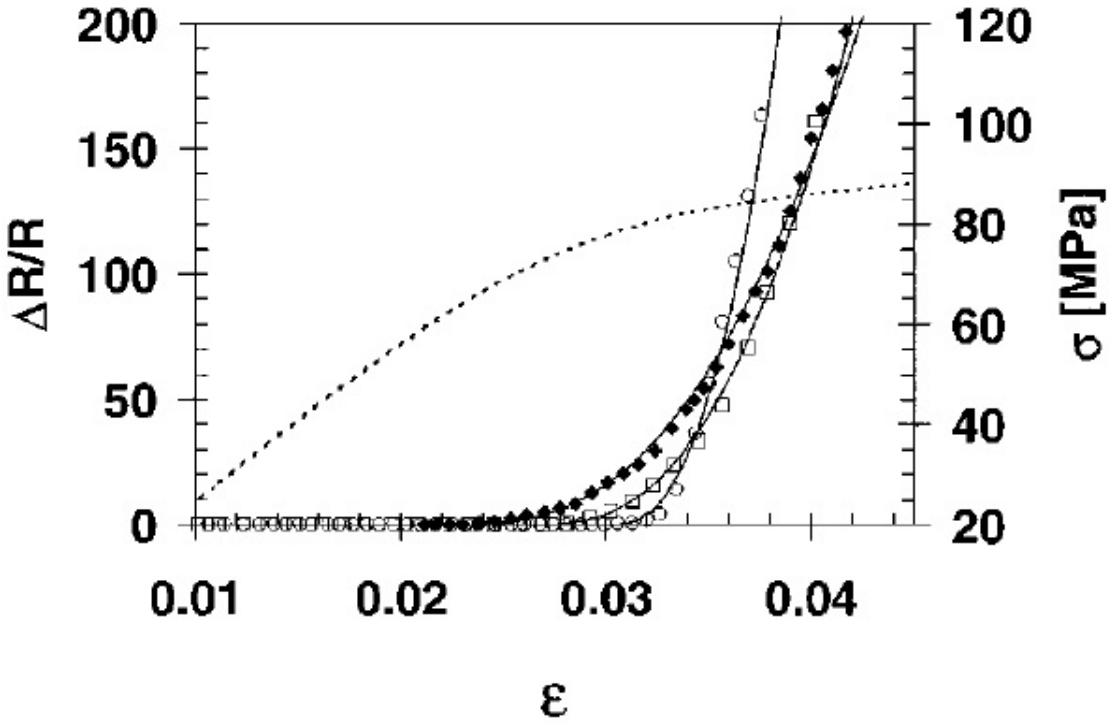

Figure 6.8 Increment of resistance (left axis) as a function of strain of ITO/PET systems. Experimental data are shown as points for (◆) 105, (□) 42 and (○) 16.8 nm thick ITO and modelled fits with solid lines. Stress-strain curve of ITO/PET system is shown as a dotted line Adapted from (Cairns et al., 2000a).

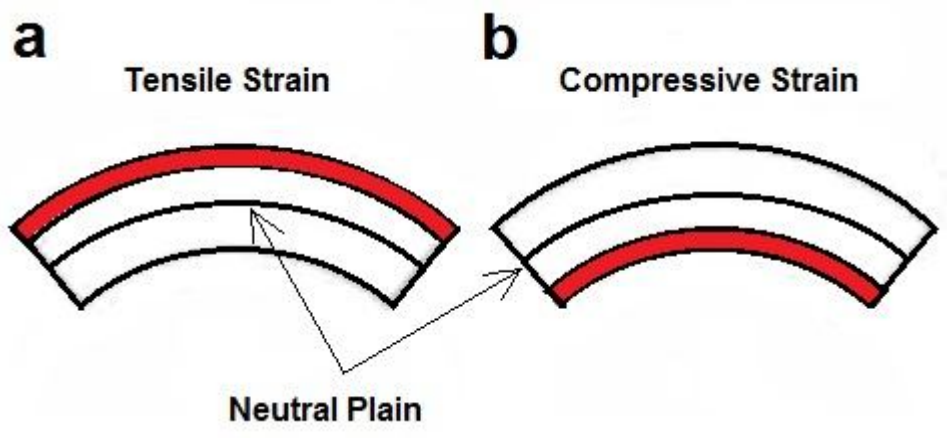

Figure 6.9 Bending - film under tension and compression.

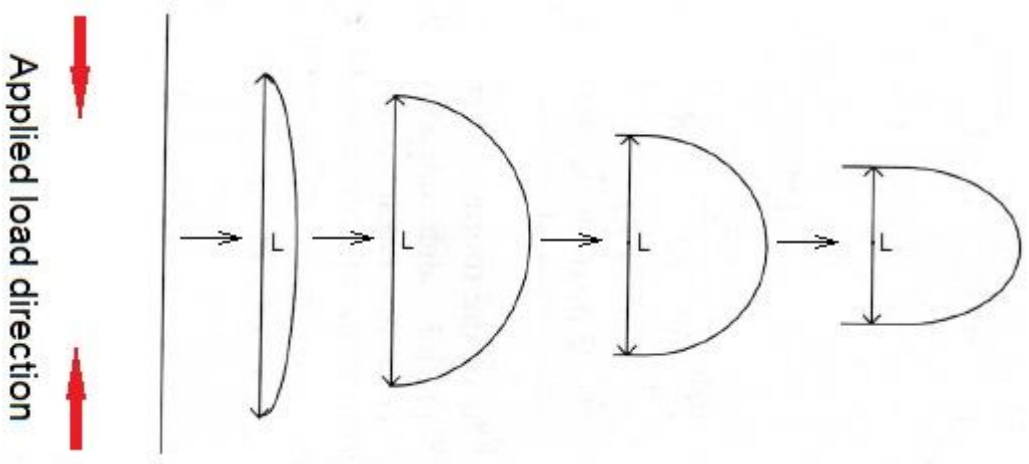

Figure 6.10 Geometrical changes of the polymer substrate during bending process; reproduced from (Park et al., 2004).

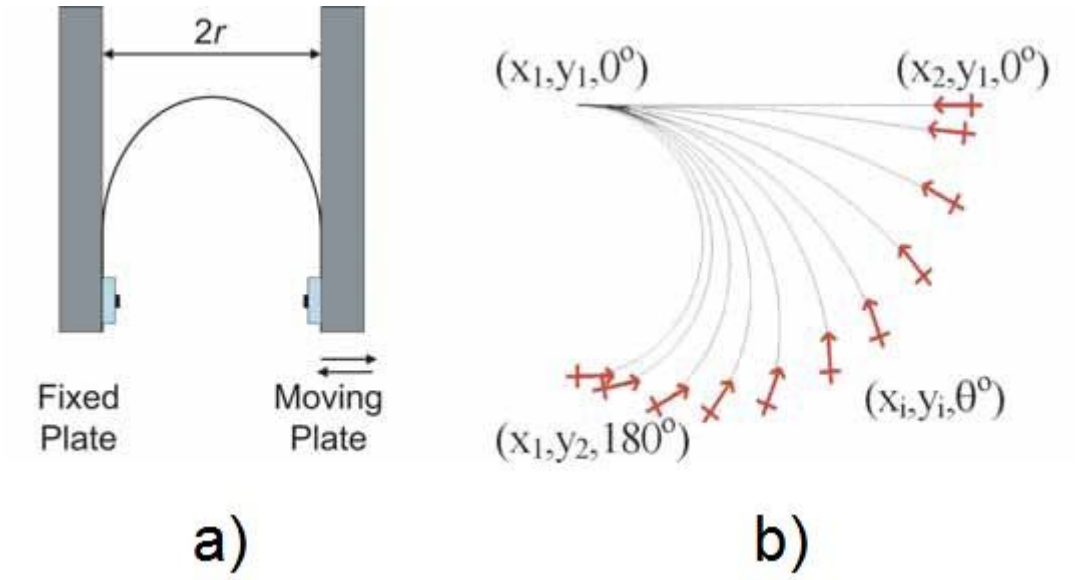

Figure 6.11 Two common bend test methods to investigate cracking-resistance of thin film/polymer systems: a) the collapsing radius test and b) the X-Y-θ test. Adapted from (Lewis, 2006).

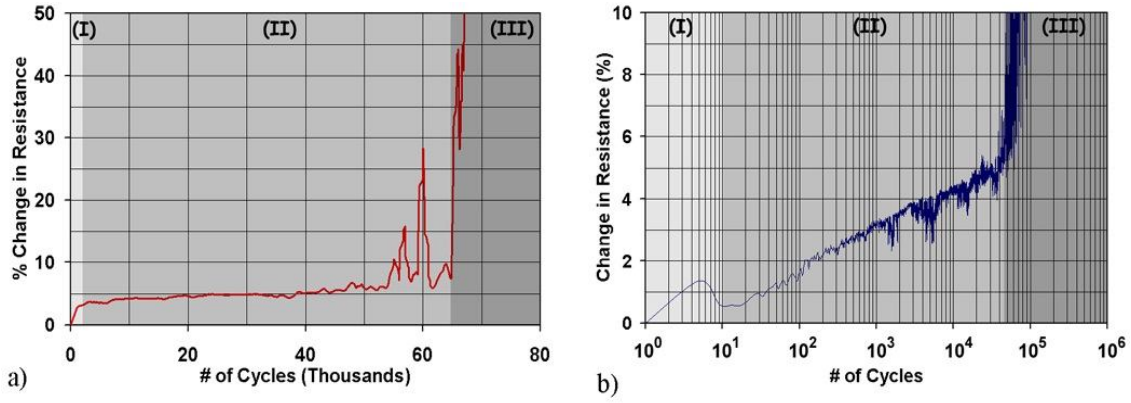

Figure 6.12 Cycling bending of ITO/PET system in tension (a - linear scale and b - logarythmic scale). Adapted from (Gorkhali et al., 2004)**.**

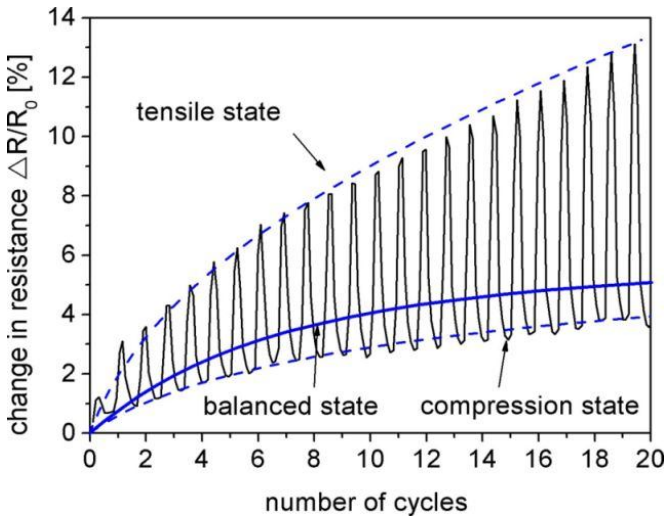

Figure 6.13 Change in resistance of ITO-nanoparticles coated PET under cycling bending with alternating tensile and compression stresses. Adapted from (Koniger and Munstedt, 2008a).

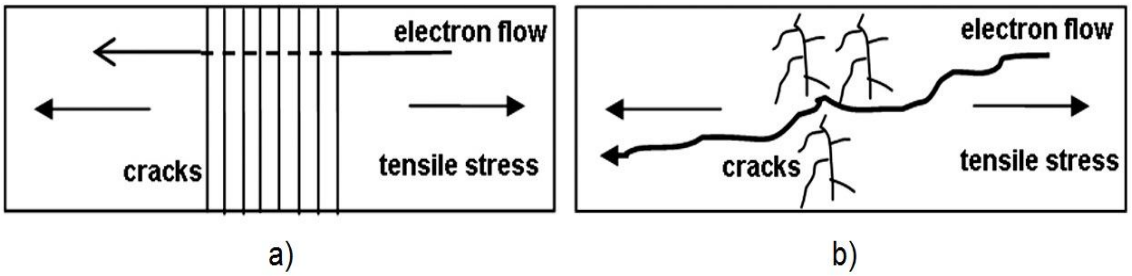

Figure 6.14 Comparison of crack formation in a) sputtered ITO-coated PET and b) ITO-nanoparticles coated PET. Adapted from (Koniger and Munstedt, 2008a).

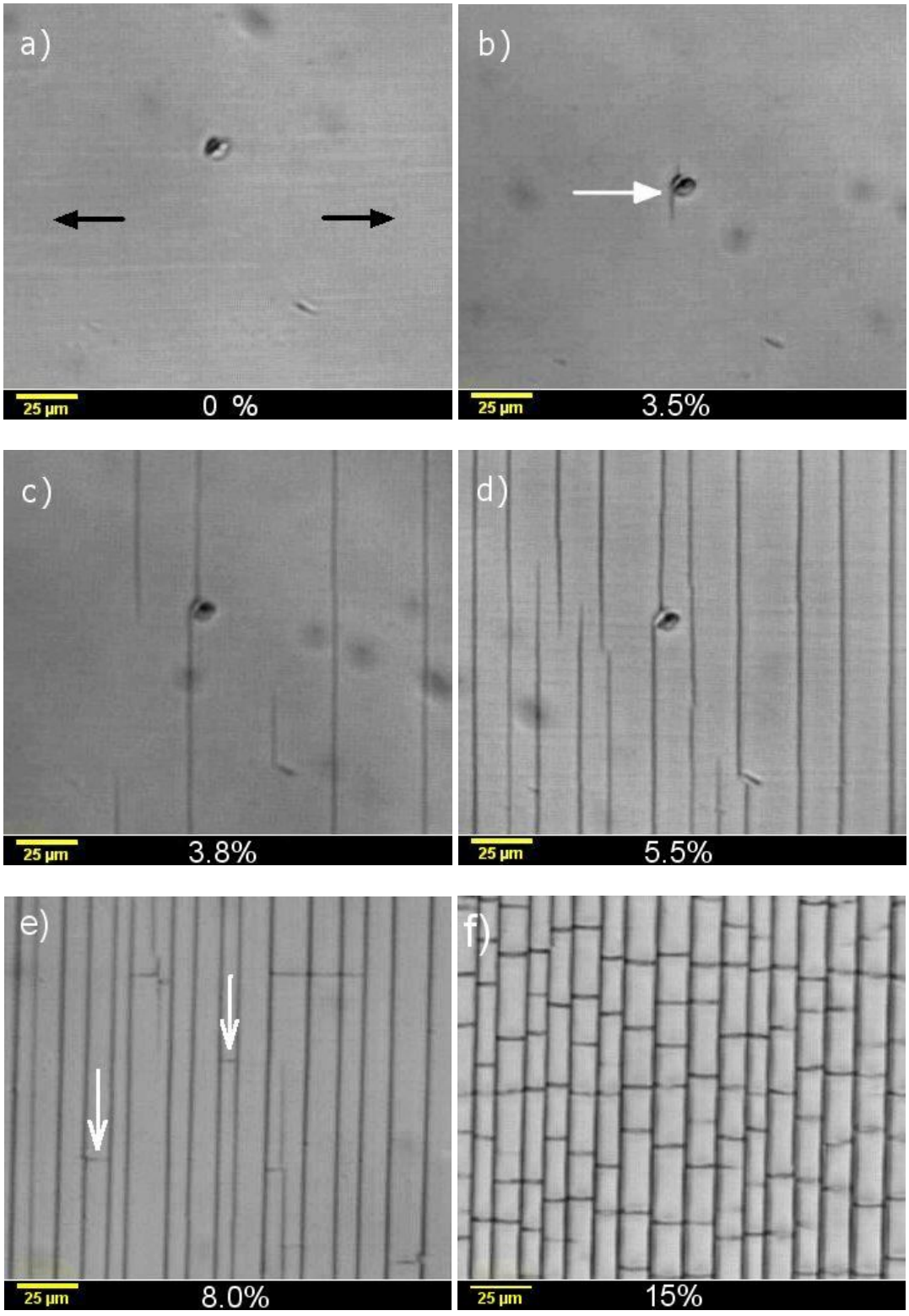

Figure 6.15 In situ optical micrographs presenting crack evolution of ITO (100 nm)/PEN Teonex Q65 FA sample tensile strained at: a) 0%, b) 3.5%, c) 3.8%, d) 5.5%, e) 8.0% and f) 15%. Black arrows on the image a) indicates the tensile strain direction.

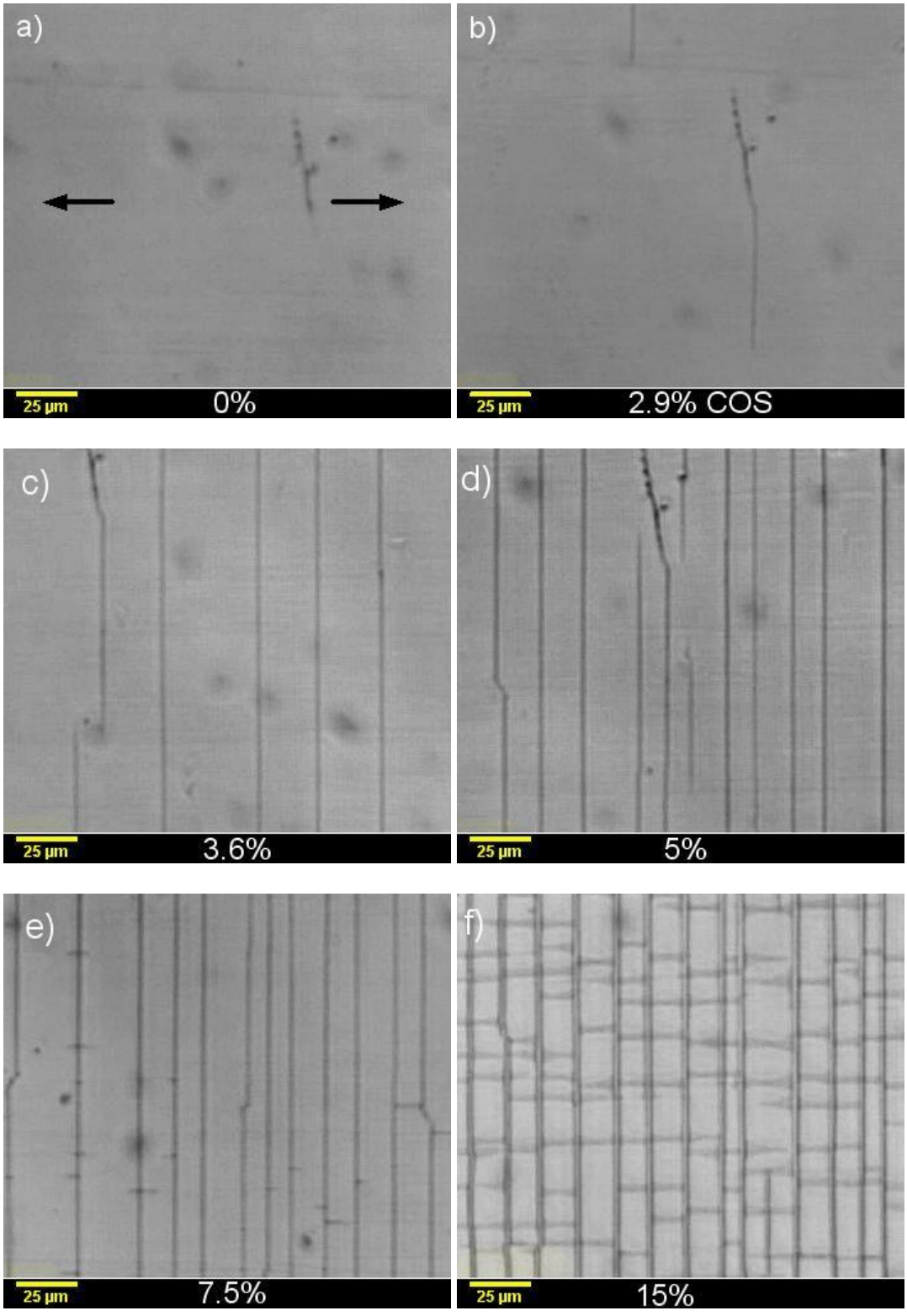

Figure 6.16 In situ optical micrographs presenting crack evolution of ITO (100 nm)/PET Melinex ST 505 sample tensile strained at: a) 0%, b) 2.9%, c) 3.6%, d) 5%, e) 7.5% and f) 15%. Black arrows on the image a) indicates the tensile strain direction.

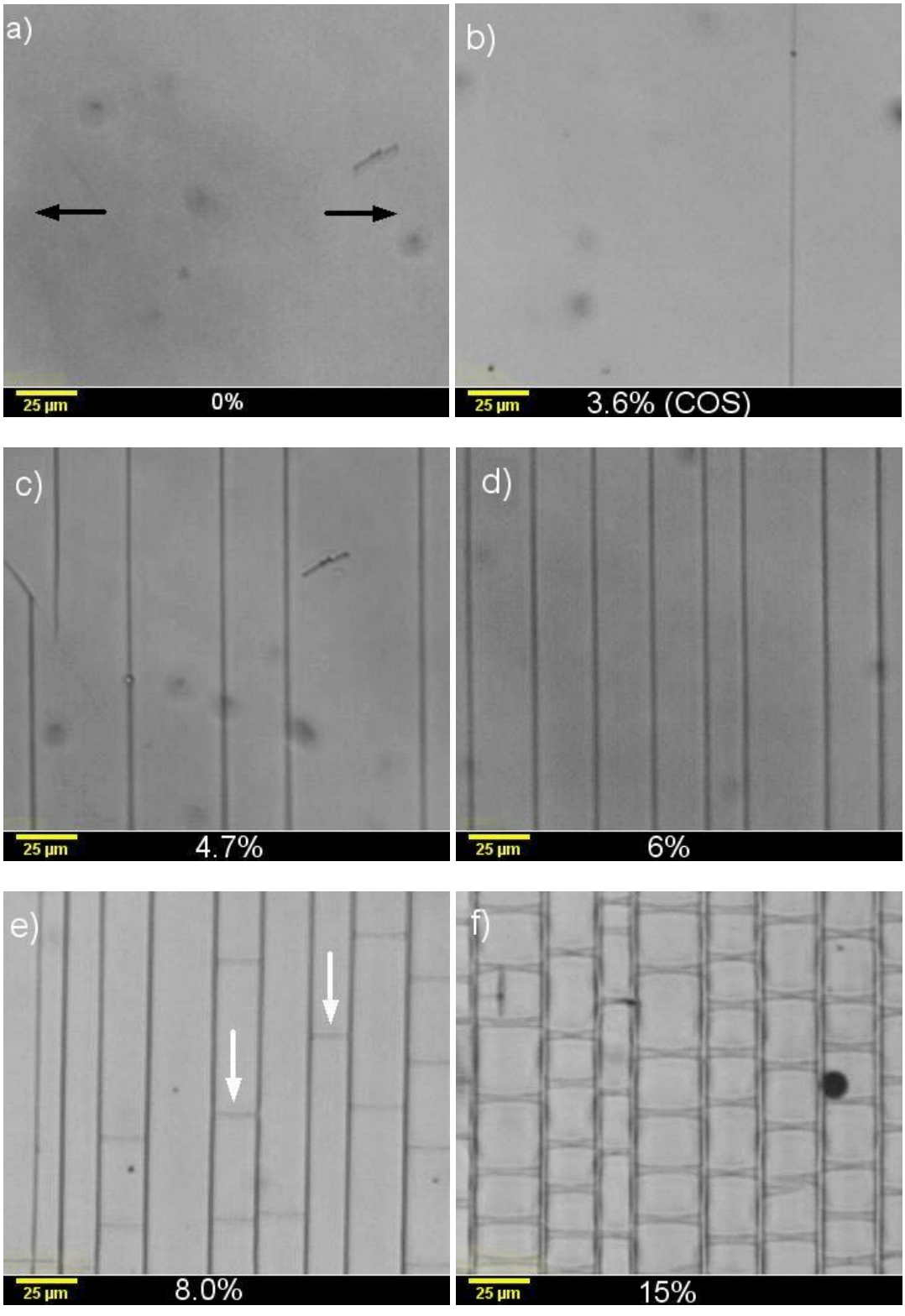

Figure 6.17 In situ optical micrographs presenting crack evolution of ITO (100 nm)/PC Lexan 8010 MC sample tensile strained at: a) 0%, b) 3.6%, c) 4.7%, d) 6%, e) 8.0% and f) 15%. Black arrows on the image a) indicates the tensile strain direction.

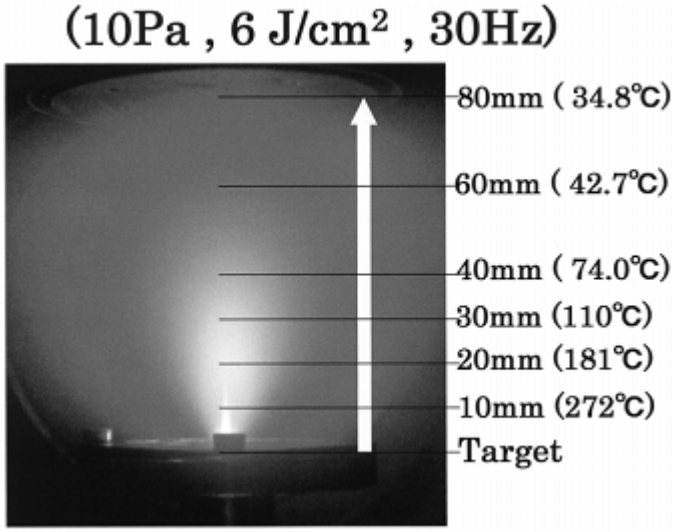

Figure 6.18 Temperature of plasma as a function of target-to-substrate distance. Adapted from (Suzuki et al., 2002).

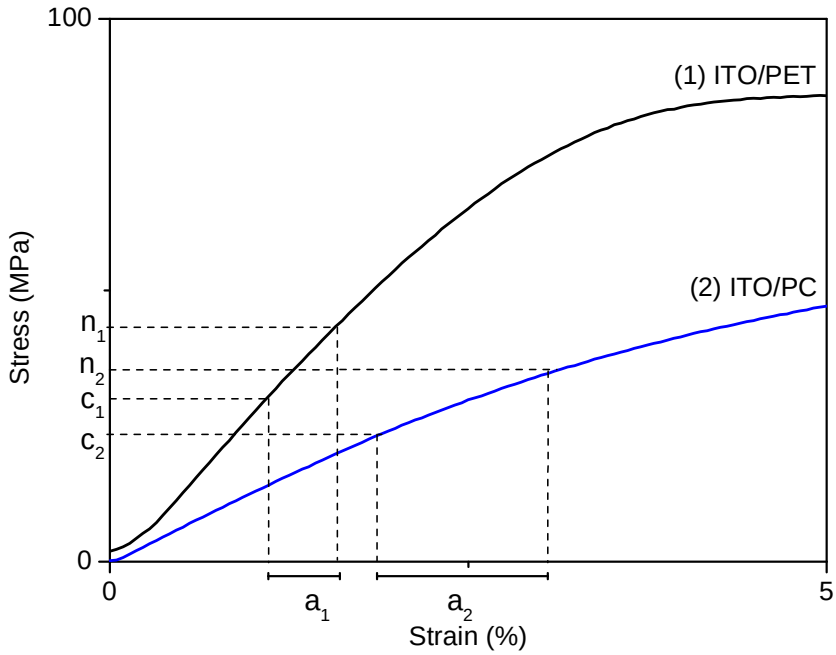

Figure 6.19 Cracking mechanism of ITO on PET and PC with different stiffness. The letters c, n and a stand for the critical stress to promote the first crack, the next crack in the layer and the strain necessary to promote the next crack, respectively. The subscripts 1 and 2 indicate ITO on stiff PET and ITO on less stiff PC, respectively.

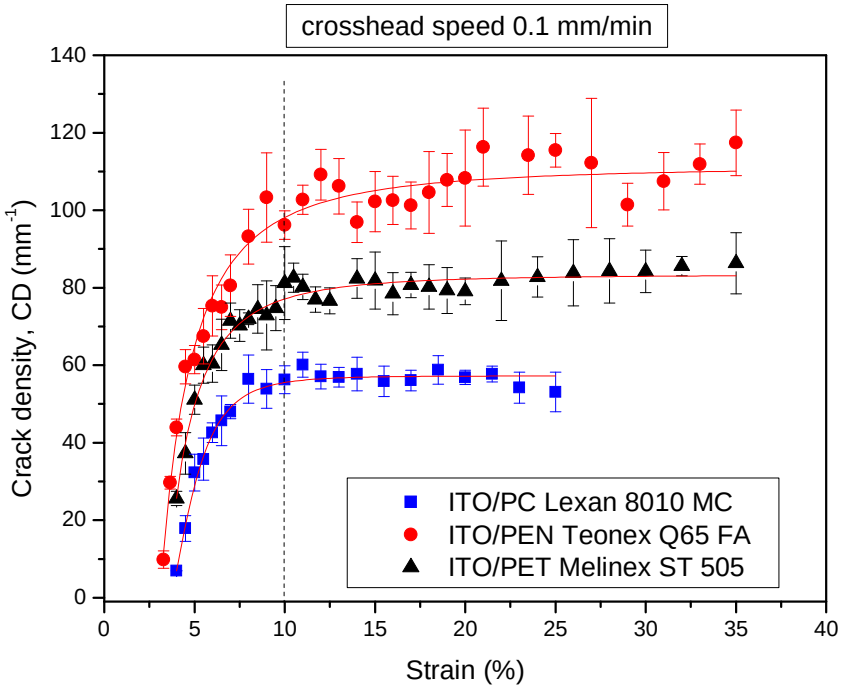

Figure 6.20 Crack density of ITO (100 nm)/polymer systems as a function of applied strain. Guidelines are provided for a better visualisation of the measured points.

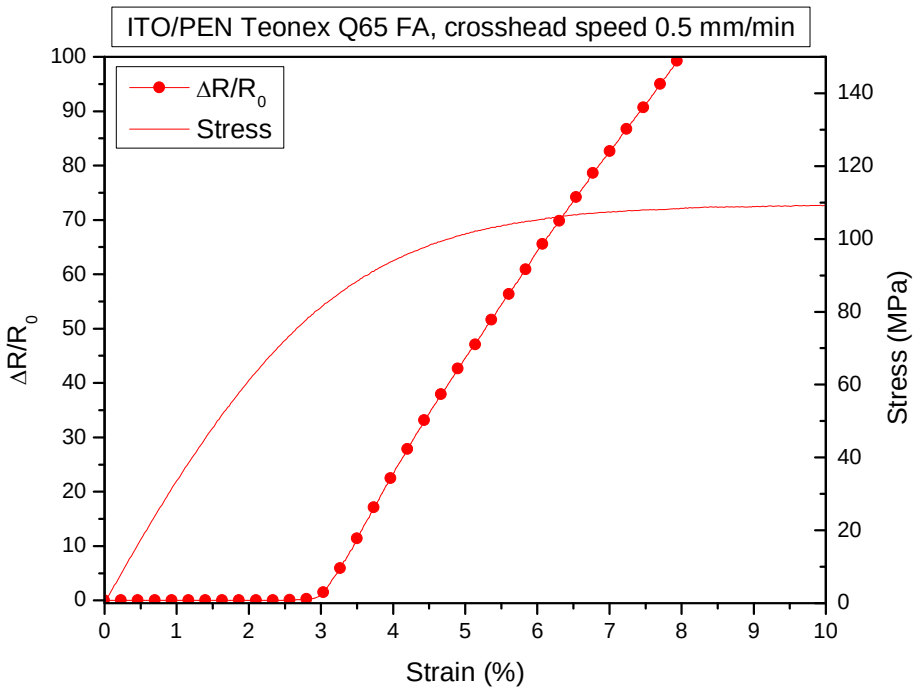

Figure 6.21 Resistance changes as a function of applied strain of ITO/PEN Teonex Q65 FA sample.

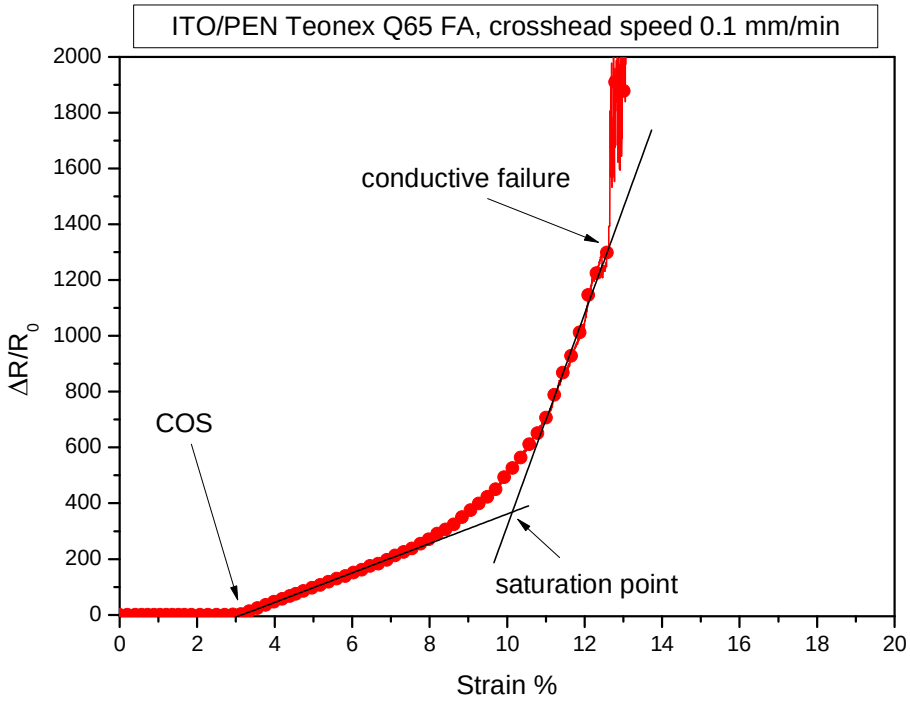

Figure 6.22 Electro-mechanical behaviour of ITO (100 nm)/PEN at high strains.

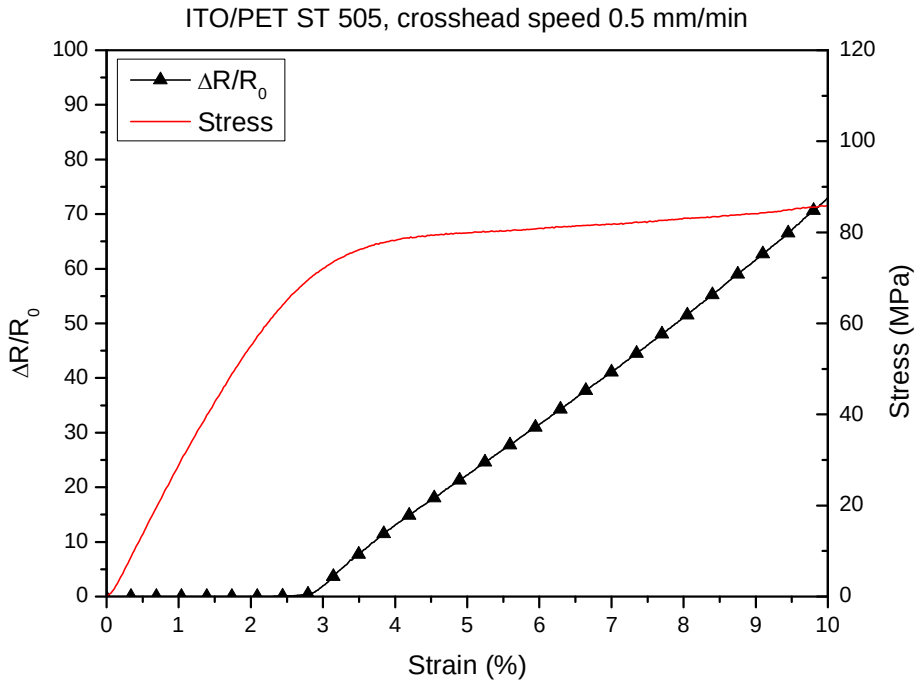

Figure 6.23 Resistance changes as a function of applied strain of ITO/PET Melinex ST 505 sample.

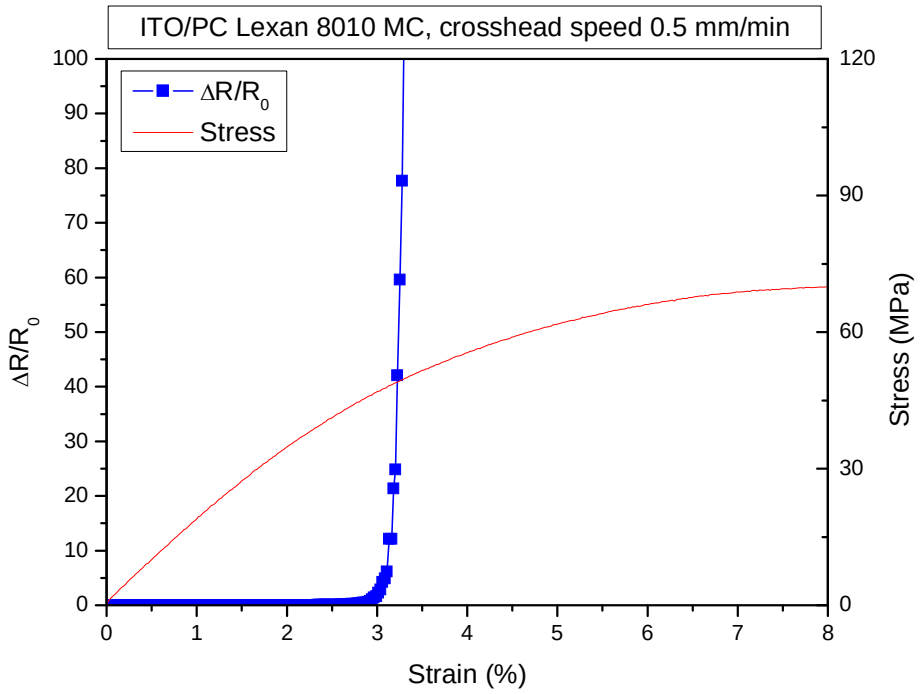

Figure 6.24 Resistance changes as a function of applied strain of ITO/PC Lexan 8010 MC sample.

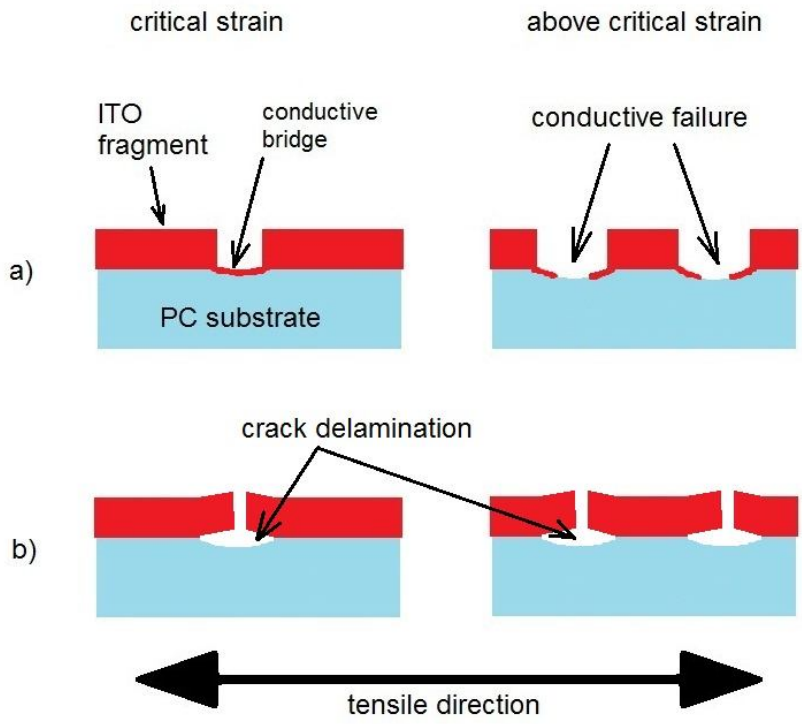

Figure 6.25 Visualisation of conductive failure mechanism above COS of ITO film deposited on highly elastic PC substrate; a) electro-mechanical failure mechanism based on the presence of conductive paths and b) electro-mechanical failure mechanism based on poor interfacial strength.

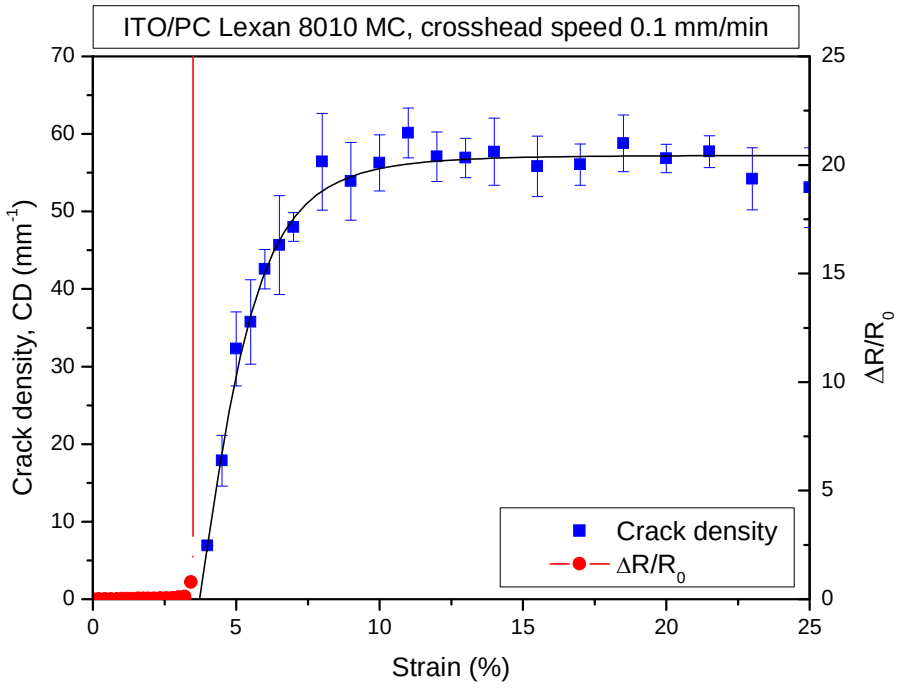

Figure 6.26 Crack density and increment of resistance as a function of applied strain. Note that black line is used as a guidance line.

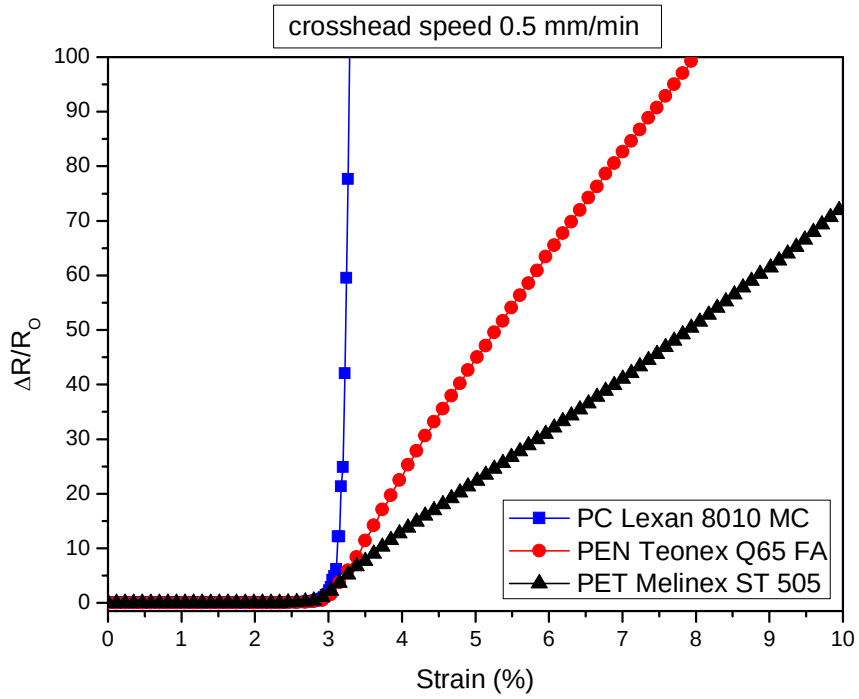

Figure 6.27 Comparison of resistance changes as a function of applied strain of ITO/polymer samples strained at crosshead speed of 0.5 mm/min.

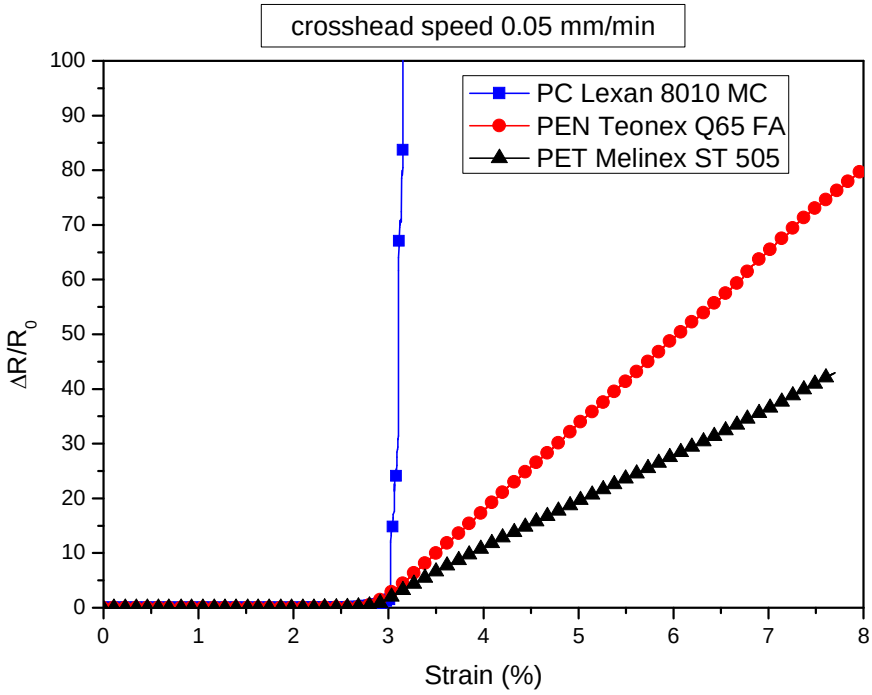

Figure 6.28 Comparison of resistance changes as a function of applied strain of ITO/polymer samples strained at crosshead speed of 0.05 mm/mi.

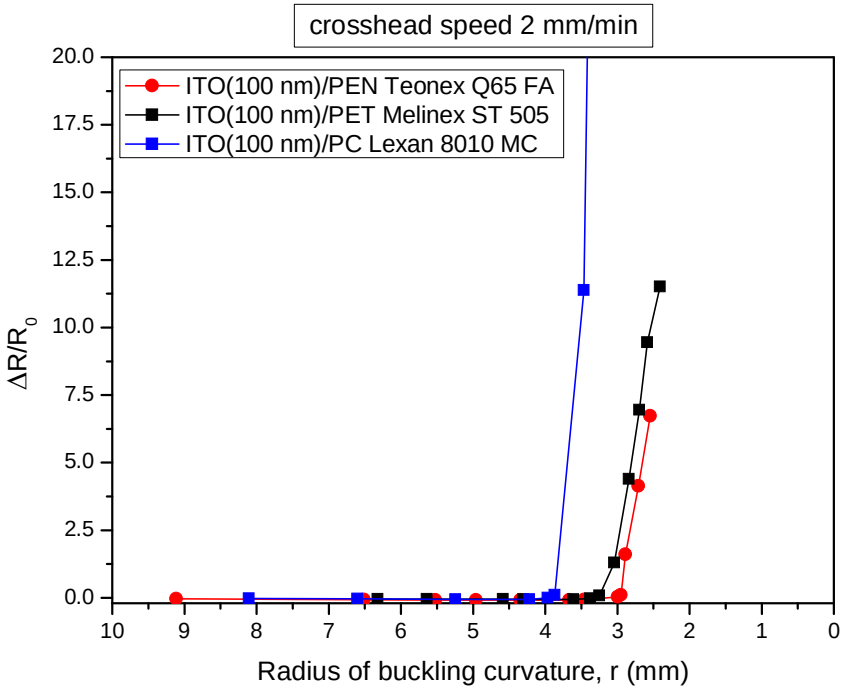

Figure 6.29 Increment of resistance as a function of radius of buckling curvature of ITO/polymer systems on the tensile side.

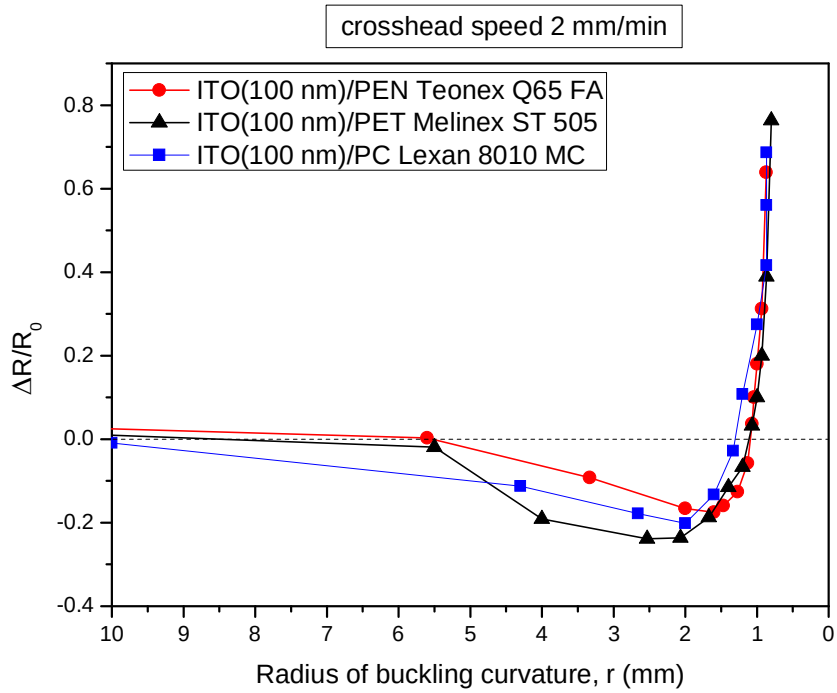

Figure 6.30 Increment of resistance as a function of radius of buckling curvature of ITO/polymer systems on the compression side.

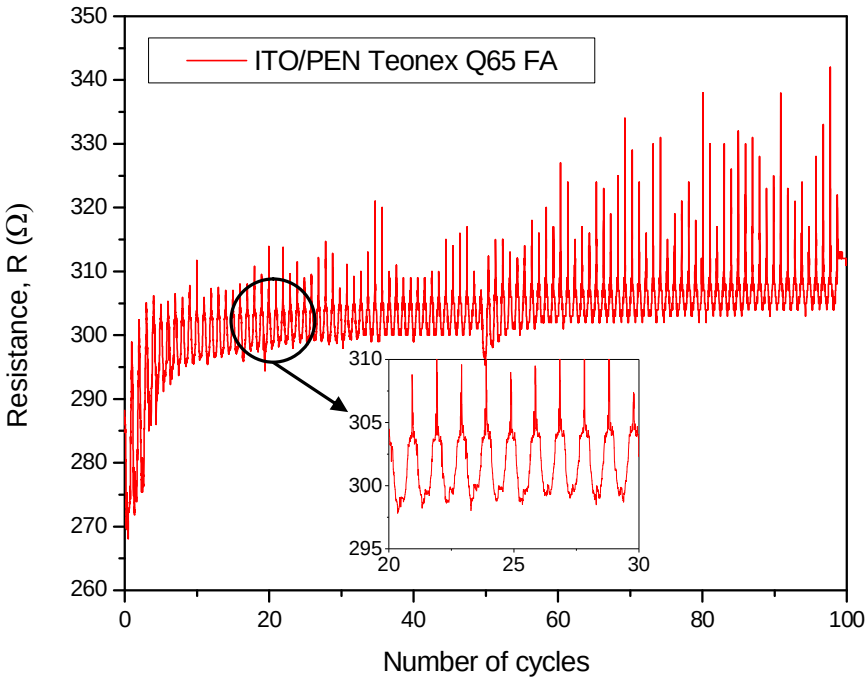

Figure 6.31 Variation of resistance as a function of applied number of cycles during cycling buckling test on the tensile side at 4 mm radius of curvature of ITO (100 nm)/PEN sample.

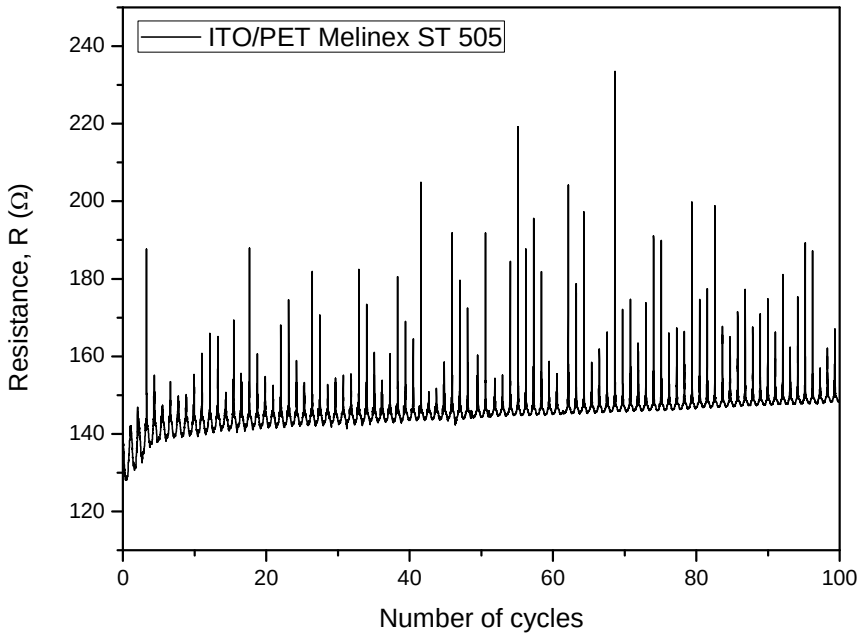

Figure 6.32 Variation of resistance as a function of applied number of cycles during cycling buckling test on the tensile side at 4 mm radius of curvature of ITO (100 nm)/PET sample.

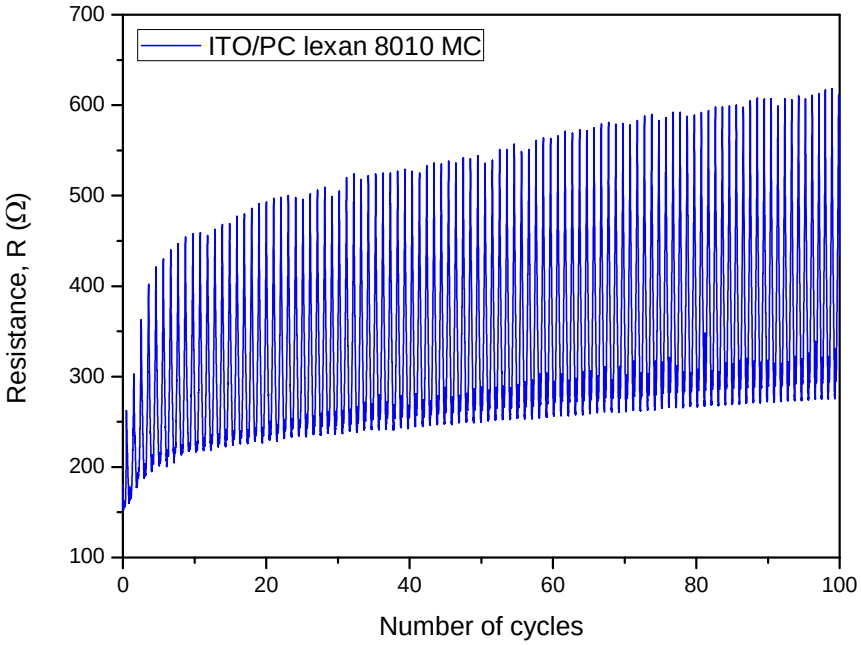

Figure 6.33 Variation of resistance as a function of applied number of cycles during cycling buckling test on the tensile side at 4 mm radius of curvature of ITO (100 nm)/PC sample.

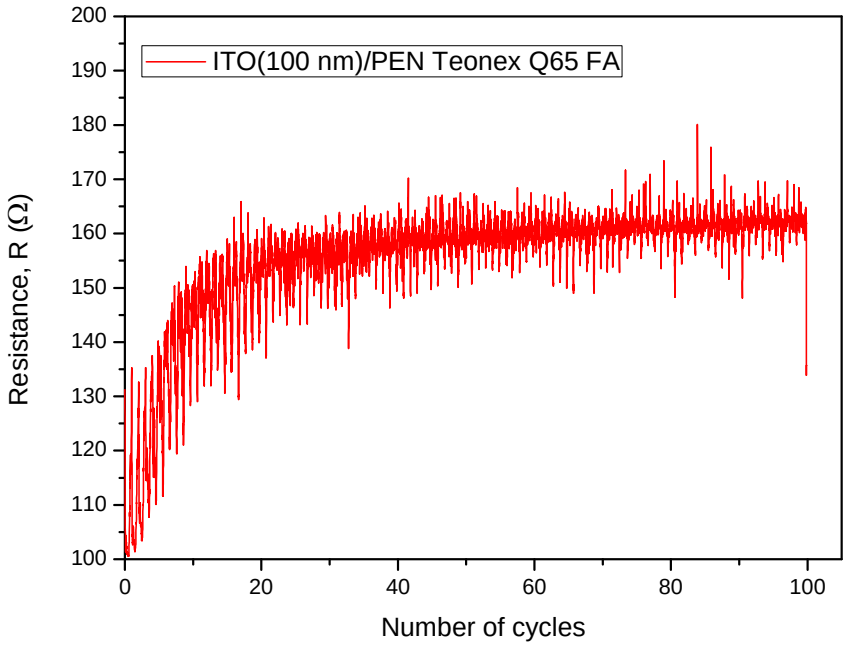

Figure 6.34 Variation of resistance as a function of applied number of cycles during cycling buckling test on the compression side at 4 mm radius of curvature of ITO (100 nm)/PEN sample.

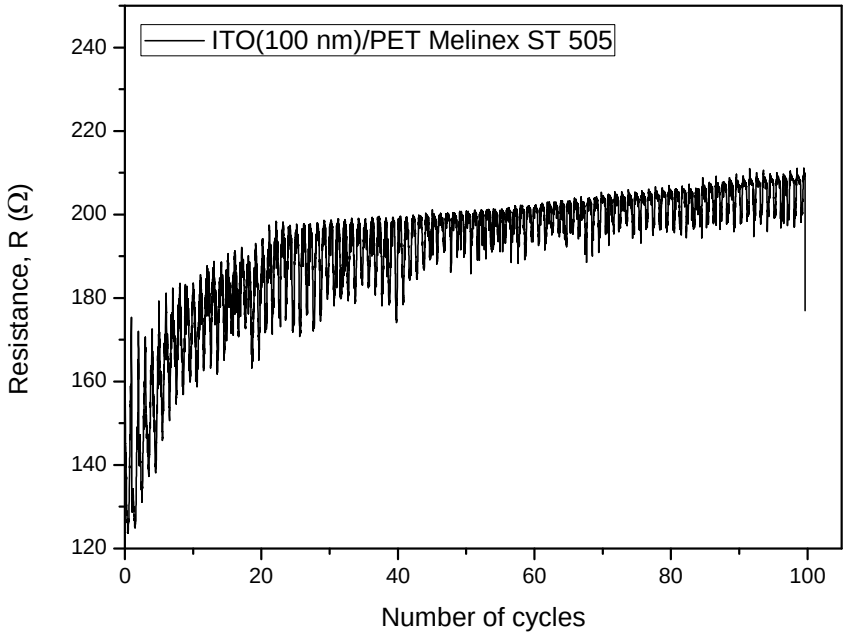

Figure 6.35 Variation of resistance as a function of applied number of cycles during cycling buckling test on the compression side at 4 mm radius of curvature of ITO (100 nm)/PET sample.

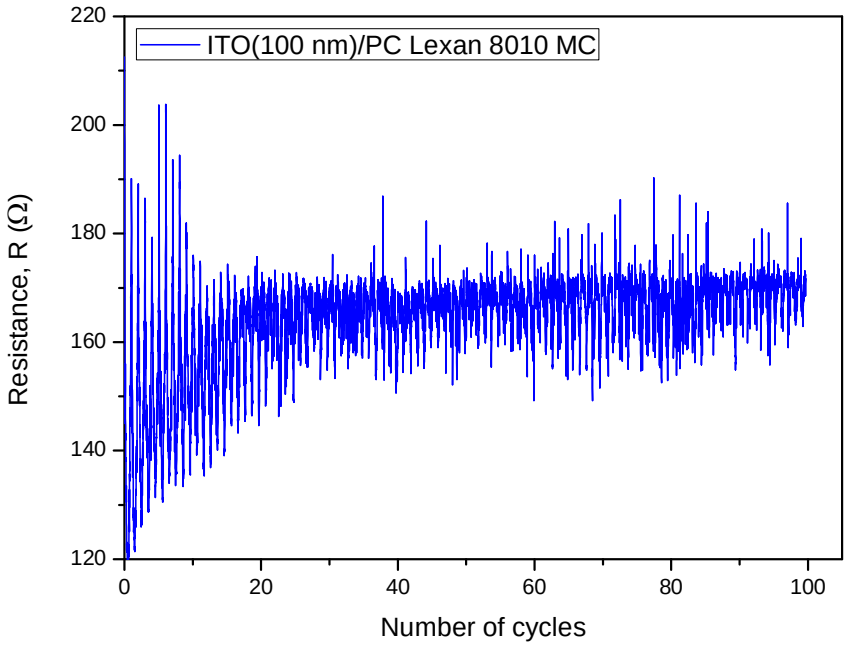

Figure 6.36 Variation of resistance as a function of applied number of cycles during cycling buckling test on the compression side at 4 mm radius of curvature of ITO (100 nm)/PC sample.

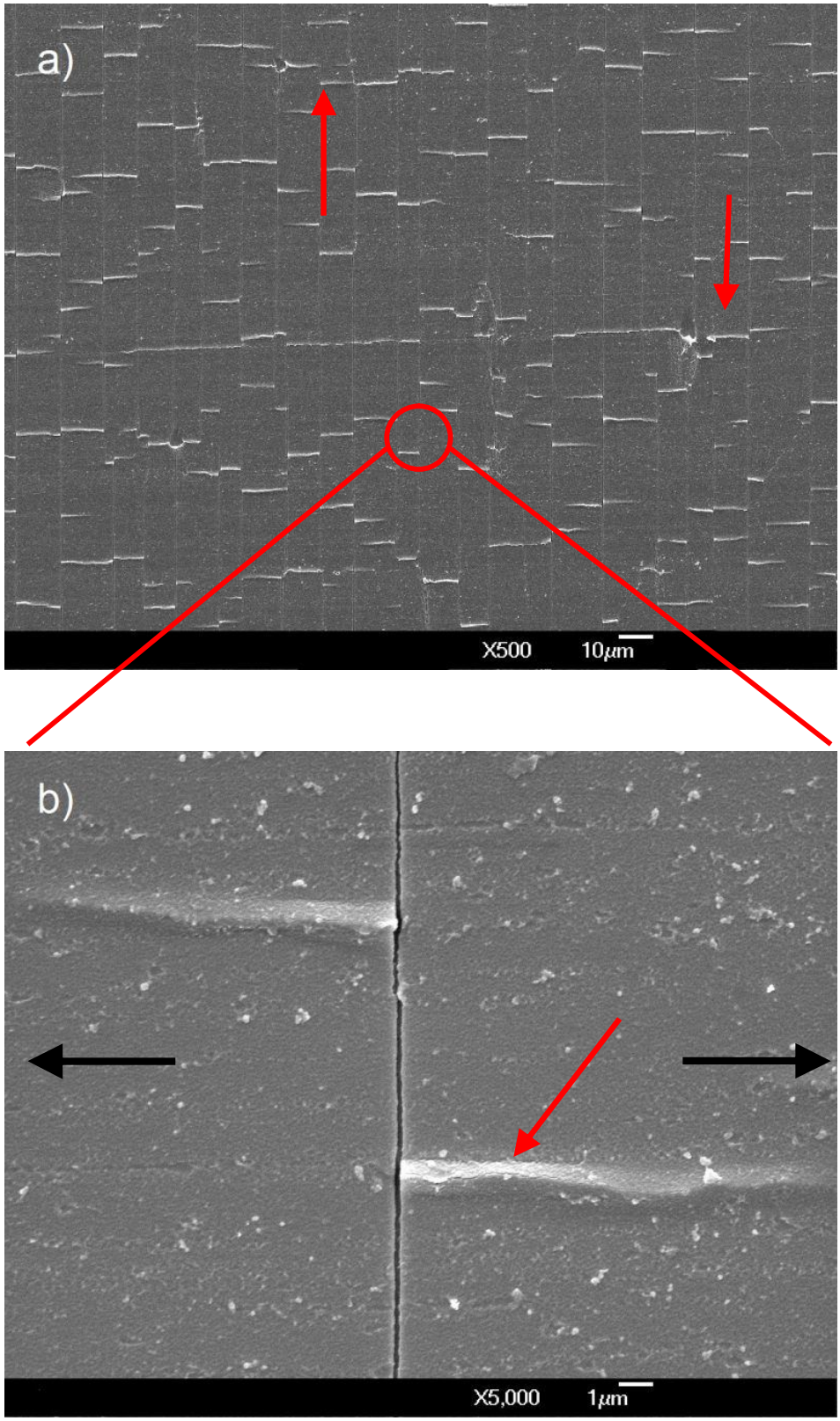

Figure 6.37 SEM micrographs of ITO/PEN Teonex Q65 FA sample strained at 11.2%. Black arrows indicate tensile direction.

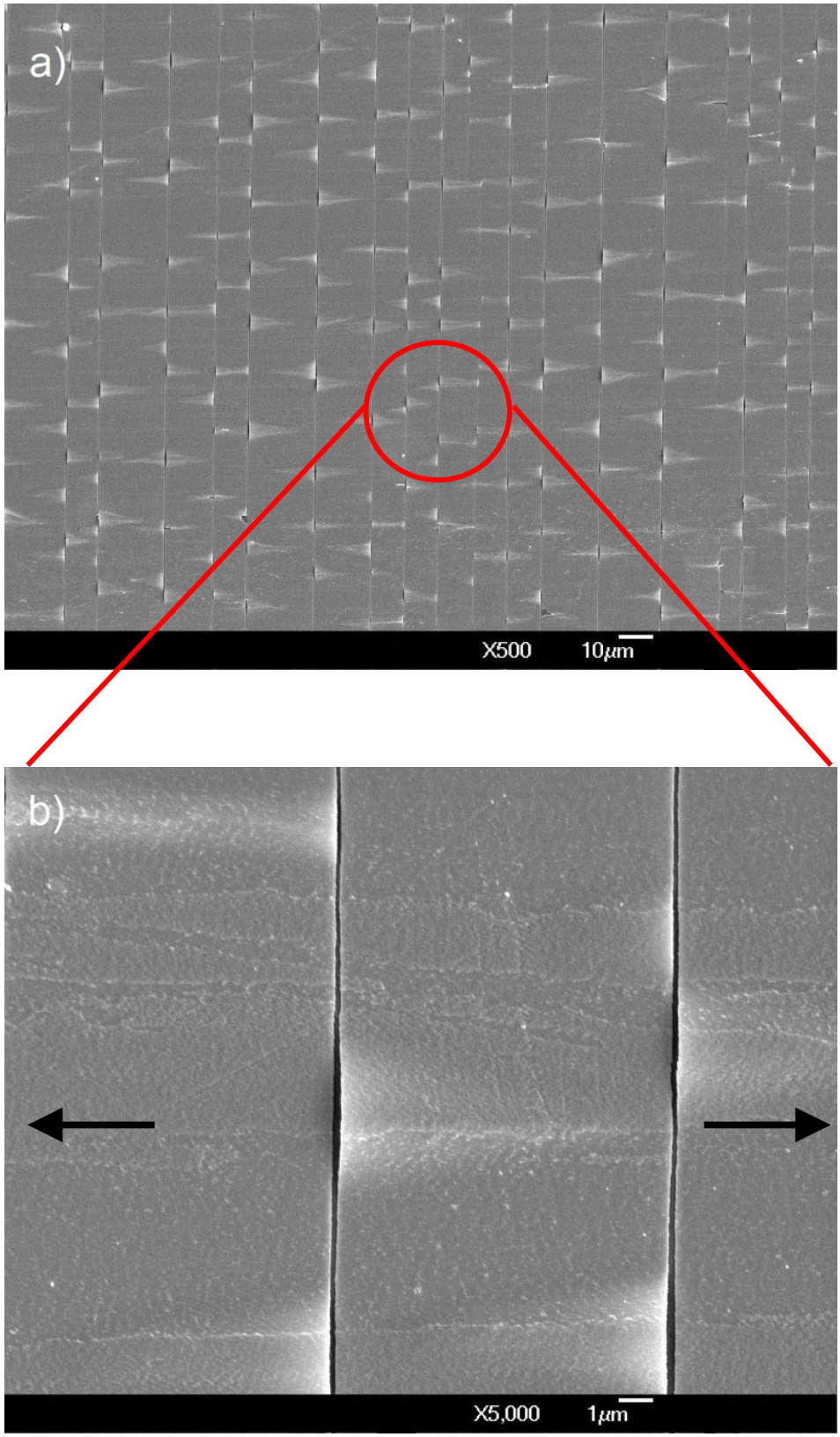

Figure 6.38 SEM micrographs of ITO/PET Melinex ST 505 sample strained at 11.3%. Black arrows indicate tensile direction.

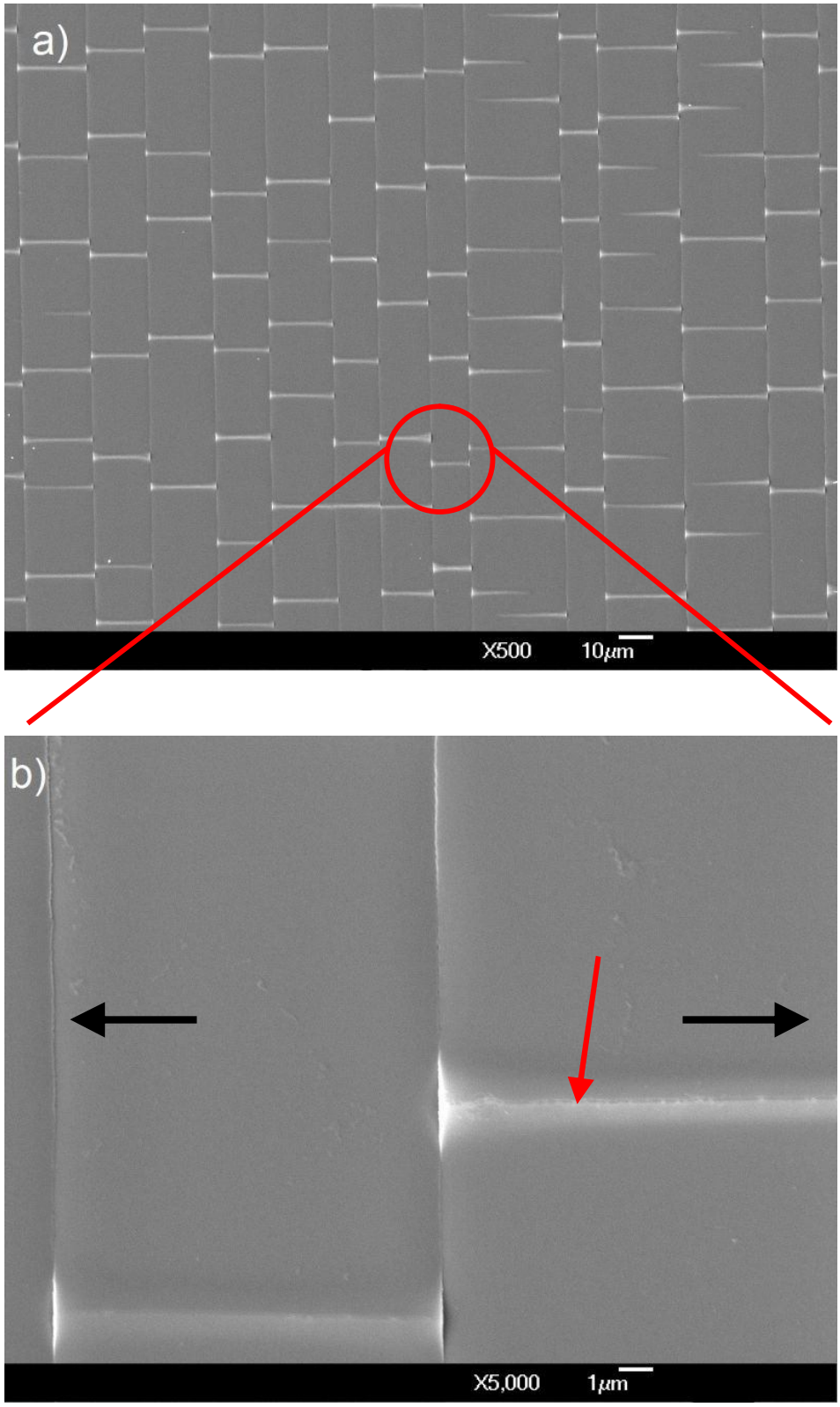

Figure 6.39 SEM micrographs of ITO/PC Lexan 8010 MC sample strained at 9.80%. Black arrows indicates tensile direction.

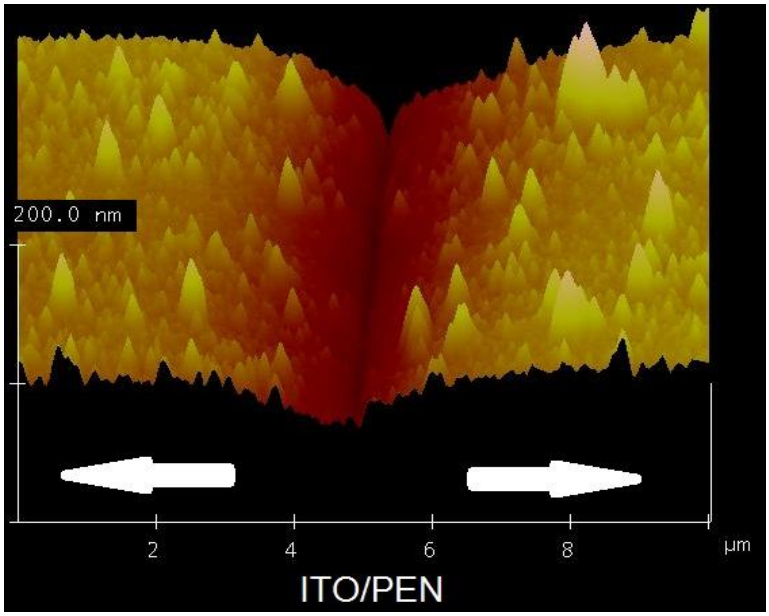

Figure 6.40 3D - AFM micrograph of channelling crack of 100 nm – thick ITO film on PEN substrate strained at 11.2%. Note that white arrows indicate tensile direction.

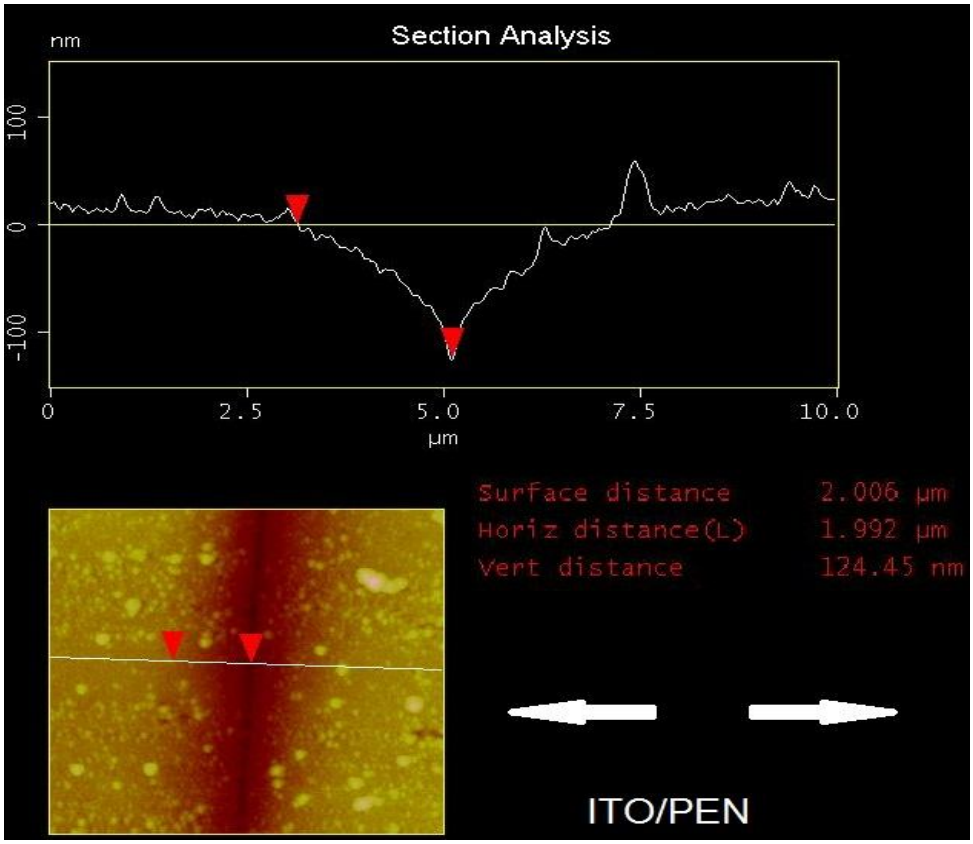

Figure 6.41 AFM cross – sectional view of channelling crack of 100 nm - thick ITO film on PEN substrate strained at 11.2 %. Note that white arrows indicate tensile direction.

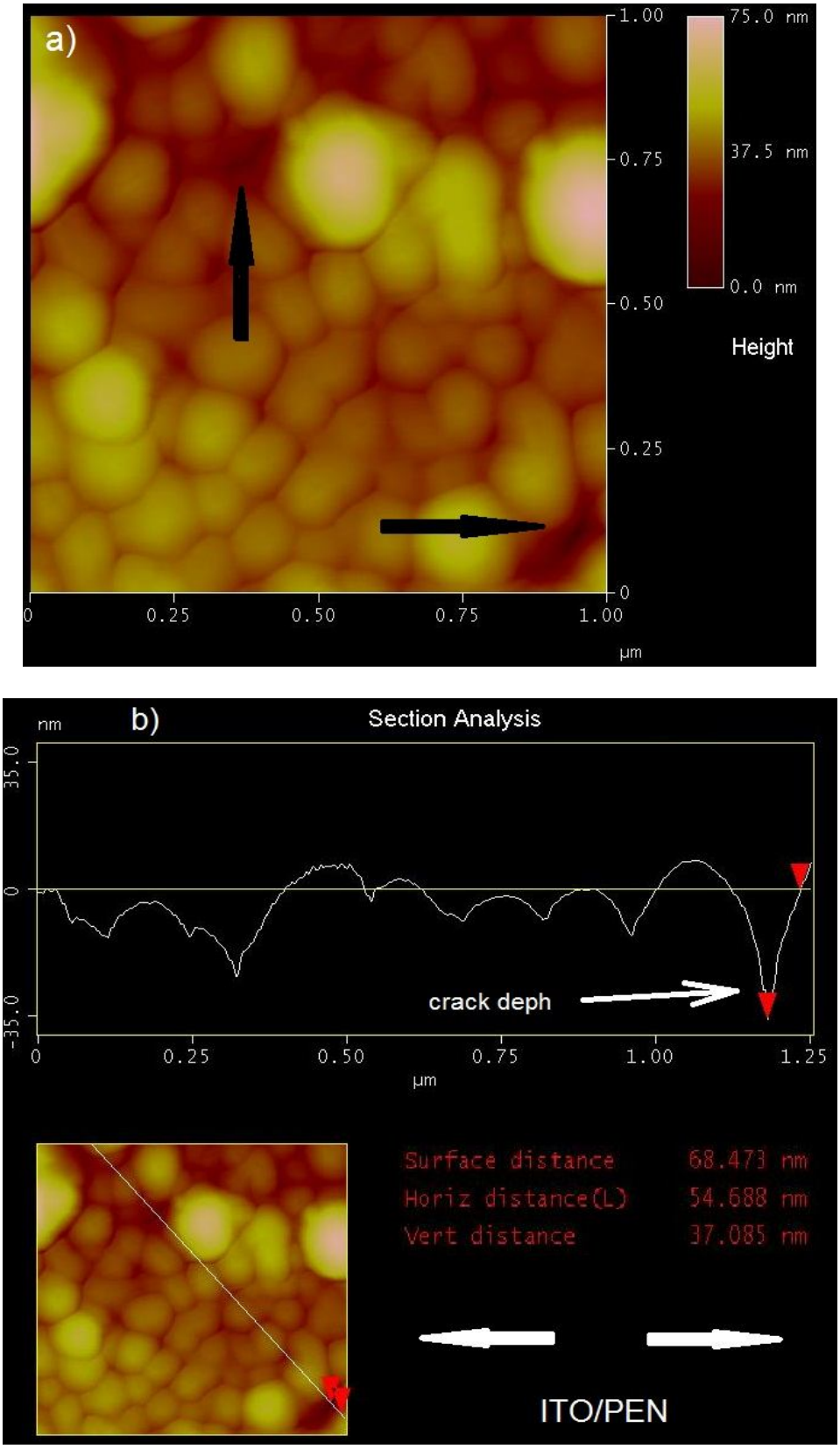

Figure 6.42 2D - high resolution AFM micrographs of crack propagation in 100 nm - thick ITO film deposited on PEN substrate and strained at 11.2%. Note that white arrows below sectional view indicate tensile direction.

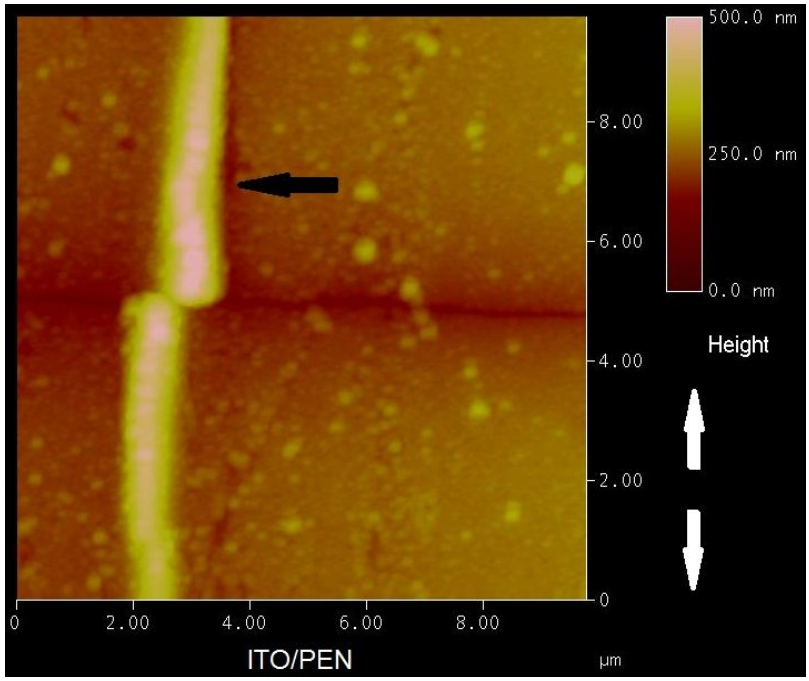

Figure 6.43 2D – AFM micrograph of buckling profile of 100 nm - thick ITO film deposited on PEN substrate strained up to 11.2%. Note that white arrows indicate tensile direction.

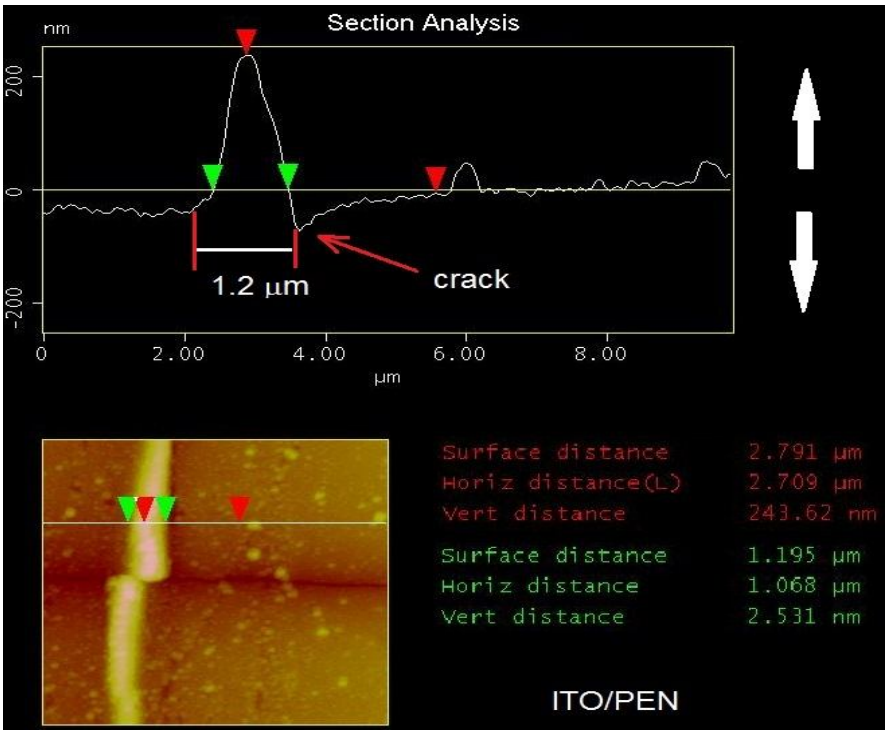

Figure 6.44 AFM cross – sectional view of buckling profile of 100 nm - thick ITO film deposited on PEN substrate. Sample strained up to 11.2% strain. Note that white arrows indicate tensile direction.

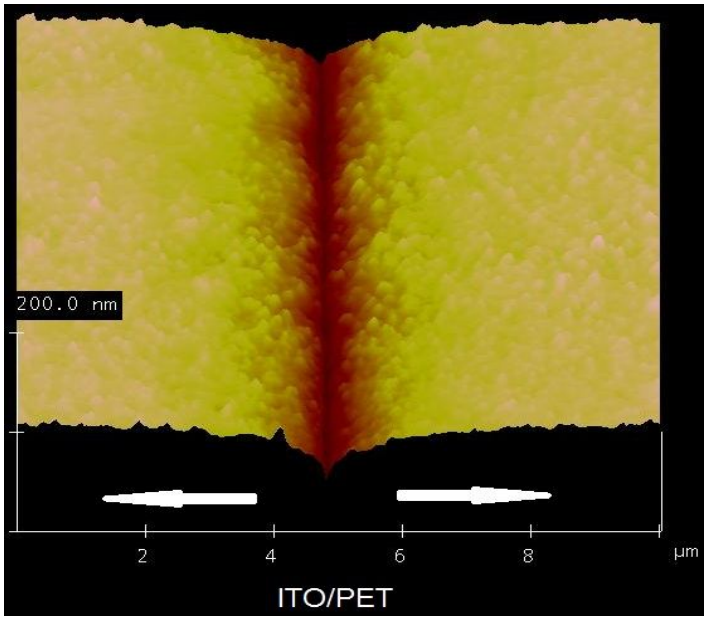

Figure 6.45 3D – AFM micrograph of channelling crack of 100 nm – thick ITO film on PET substrate strained at 11.3%. Note that white arrows indicate tensile direction.

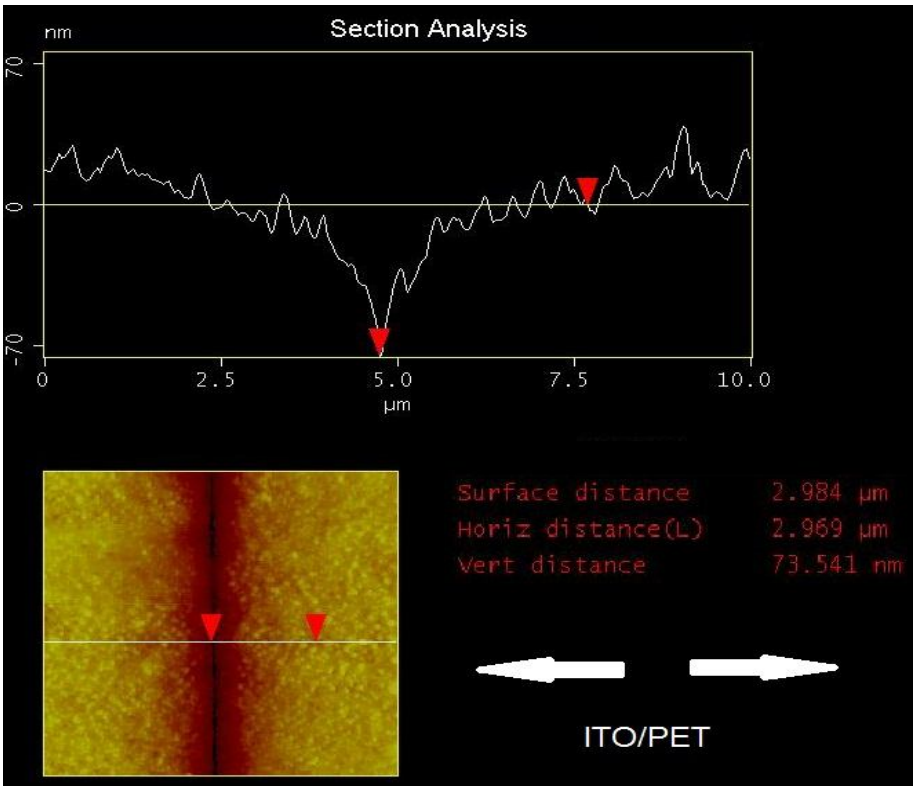

Figure 6.46 AFM cross – sectional view of channelling crack of 100 nm - thick ITO film on PET substrate strained at 11.3 %. Note that white arrows indicate tensile direction.

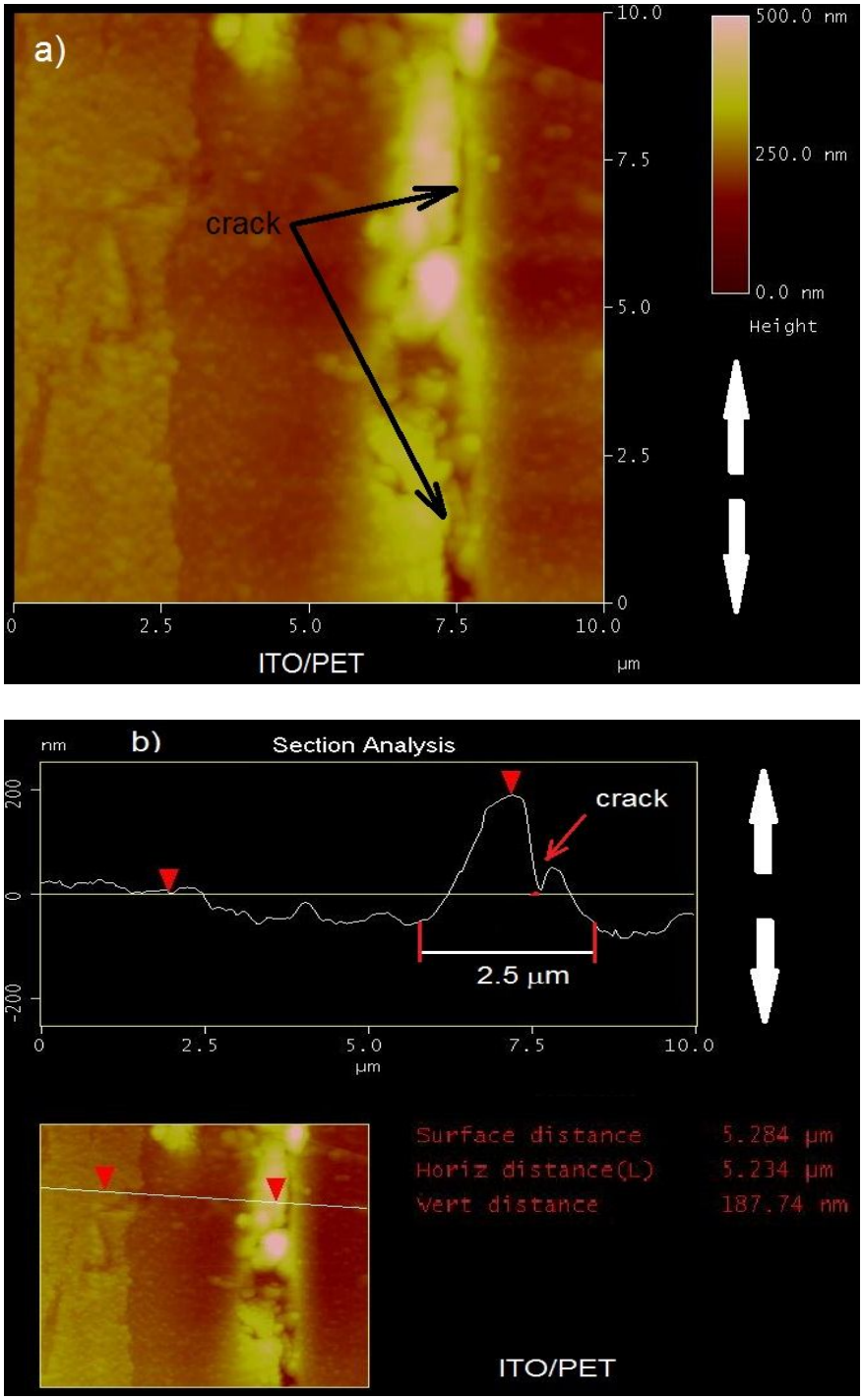

Figure 6.47 2D – AFM micrographs of buckling profile with cross - sectional view of 100 nm - thick ITO film deposited ob PET substrate strained up to 11.3%. Note that white arrows indicate tensile direction.

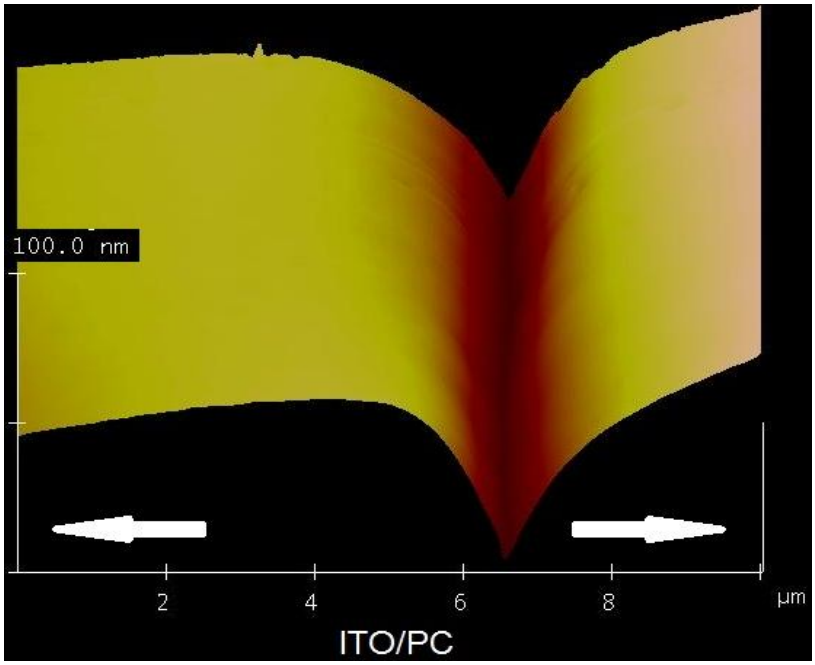

Figure 6.48 3D – AFM micrograph of channelling crack of 100 nm – thick ITO film on PC substrate strained at 9.80%. Note that white arrows indicate tensile direction.

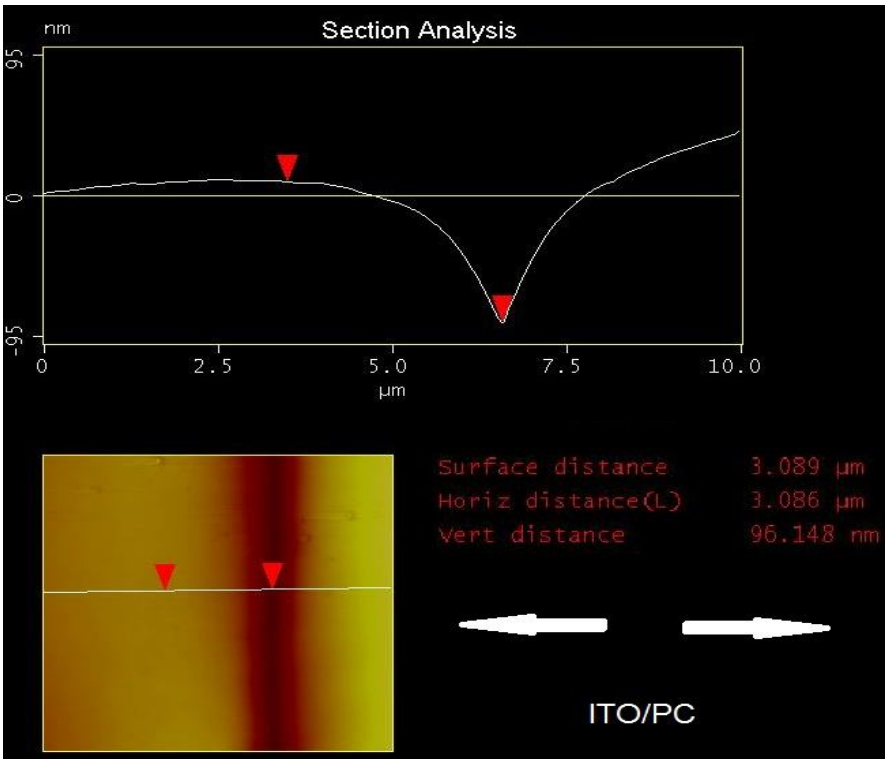

Figure 6.49 AFM cross – sectional view of channelling crack of 100 nm - thick ITO film on PC substrate strained at 9.80%. Note that white arrows indicate tensile direction.

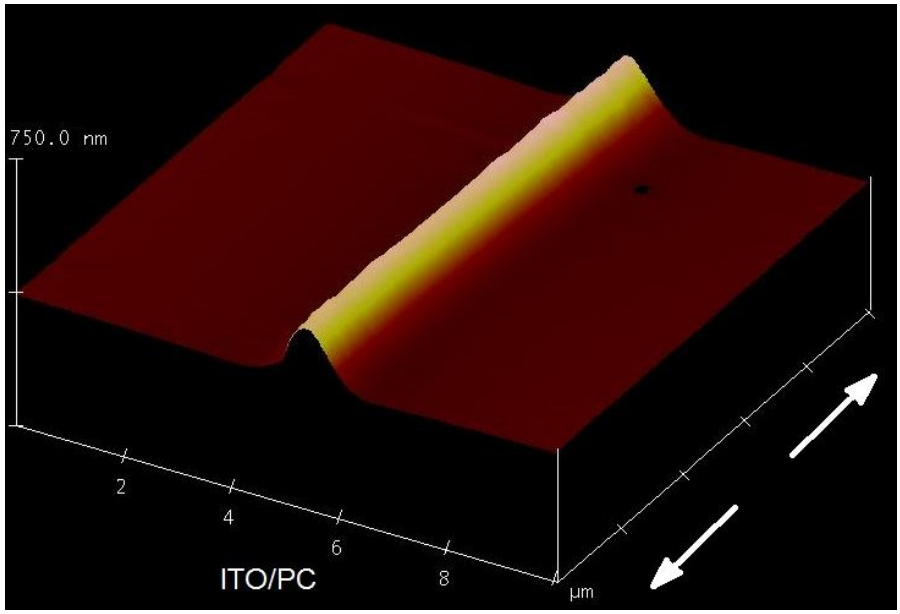

Figure 6.50 2D – AFM micrograph of buckling profile of 100 nm - thick ITO film deposited on PC substrate strained up to 9.80%. Note that white arrows indicate tensile direction.

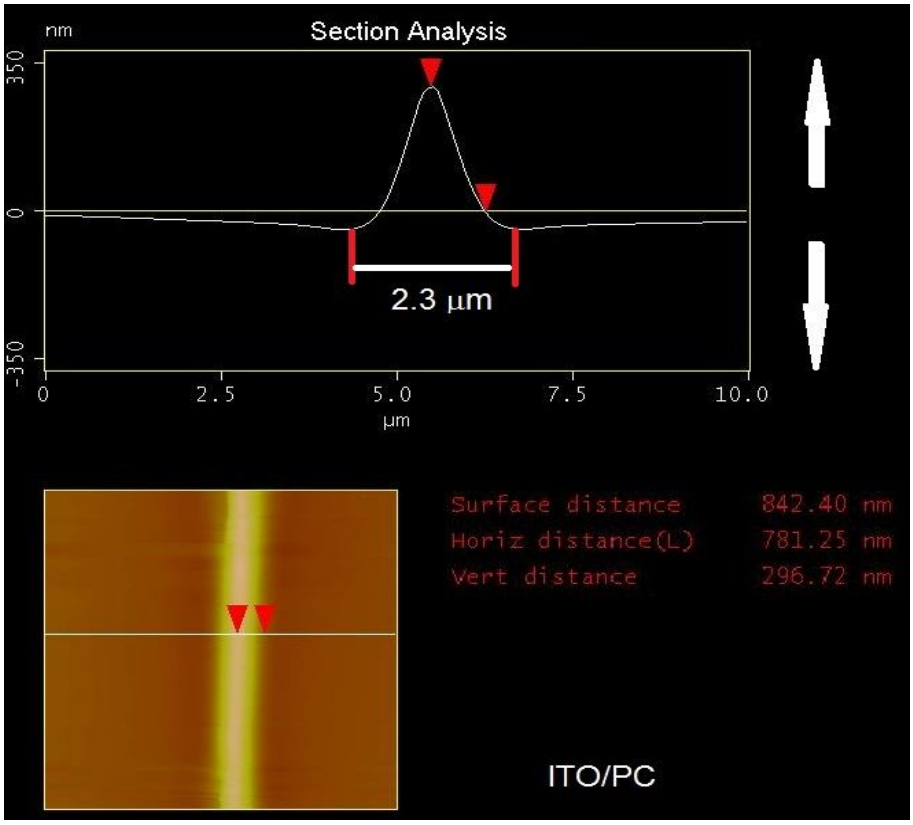

Figure 6.51 AFM cross – sectional view of buckling profile of 100 nm - thick ITO film deposited on PC substrate. Sample strained up to 9.80% strain. Note that white arrows indicate tensile direction.

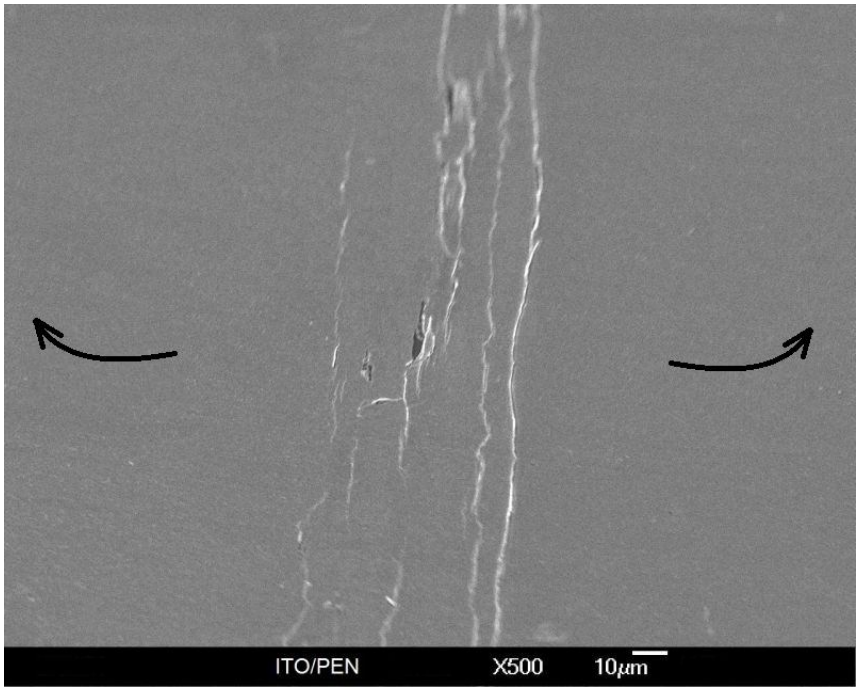

Figure 6.52 SEM micrograph showing cracking and delamination of ITO film deposited on PEN substrate and flexed monotonically at 2.5 mm radius of curvature on the tensile side. Note that black arrows show buckling direction.

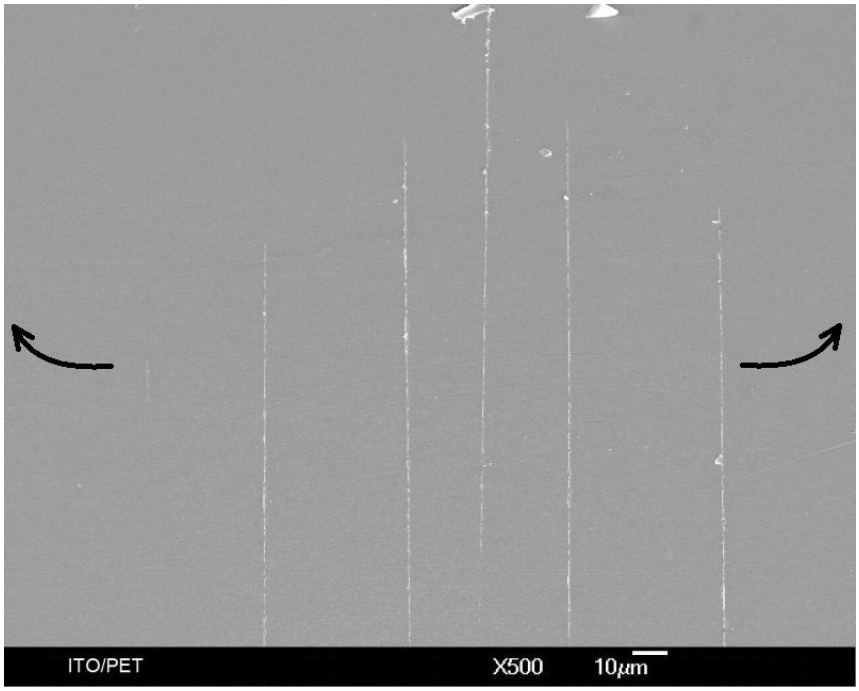

Figure 6.53 SEM micrograph showing cracks of ITO film deposited on PET substrate after monotonic buckling up to 2.4 mm radius of curvature on the tensile side. Note that black arrows indicate buckling direction.

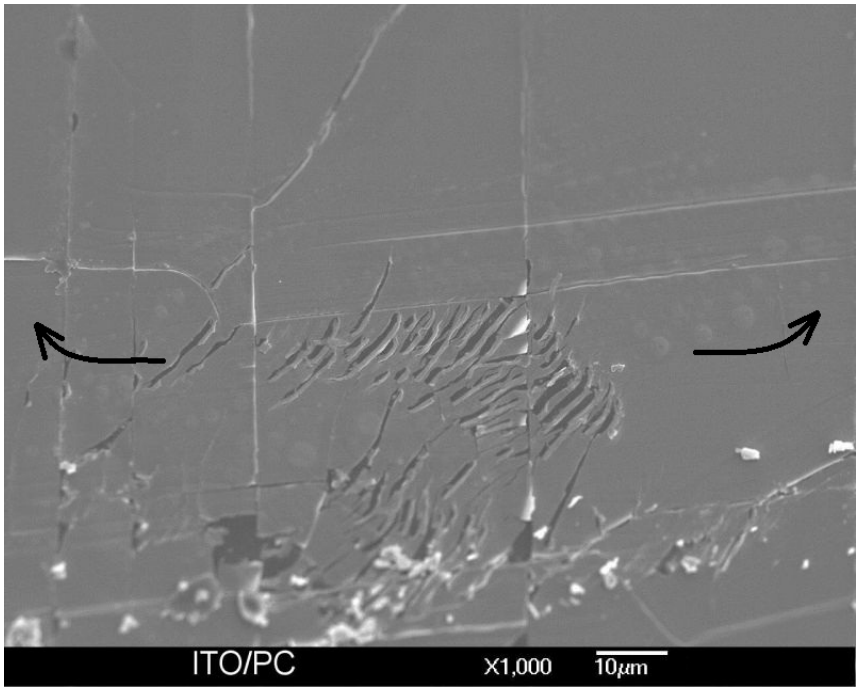

Figure 6.54 SEM micrograph showing cracking and delamination of ITO film deposited on PC substrate and flexed monotonically at 3.0 mm radius of curvature on the tensile side. Note that black arrows show buckling direction.

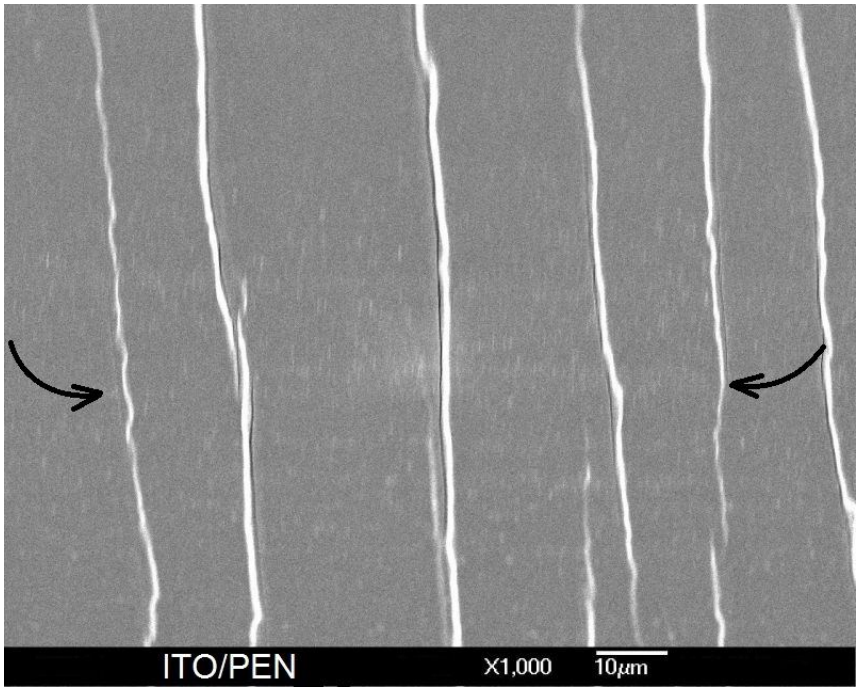

Figure 6.55 SEM micrograph showing cracking and delamination of ITO film deposited on PEN substrate and flexed monotonically at 0.9 mm radius of curvature on the compression side. Note that black arrows show buckling direction.

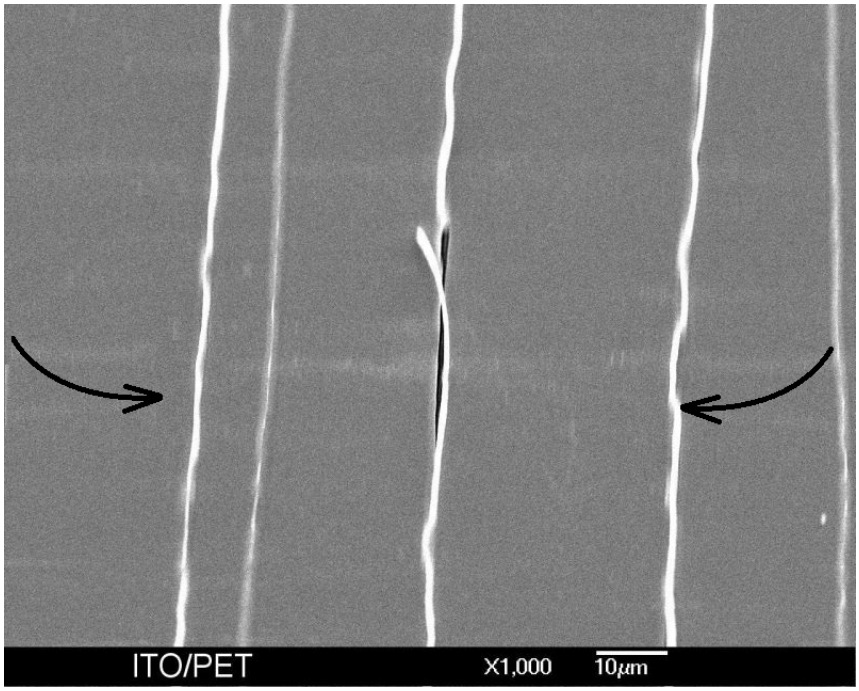

Figure 6.56 SEM micrograph showing cracking and delamination of ITO film deposited on PET substrate and flexed monotonically at 0.8 mm radius of curvature on the compression side. Note that black arrows show buckling direction.

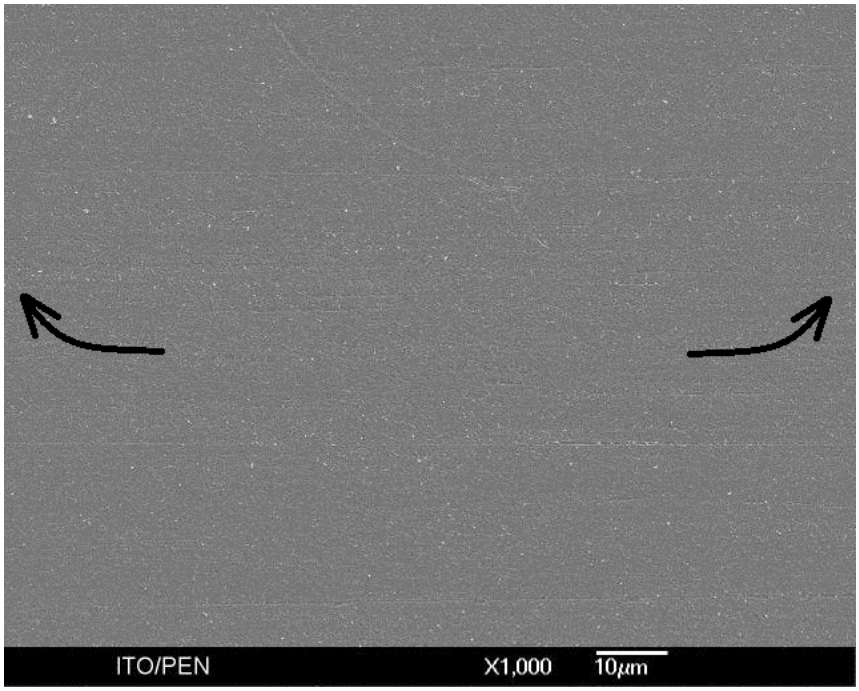

Figure 6.57 SEM micrograph showing surface of ITO film (100 nm) deposited on PEN substrate after 100 buckling cycles at 4 mm radius of curvature on the tensile side. Note that black arrows indicate buckling direction.

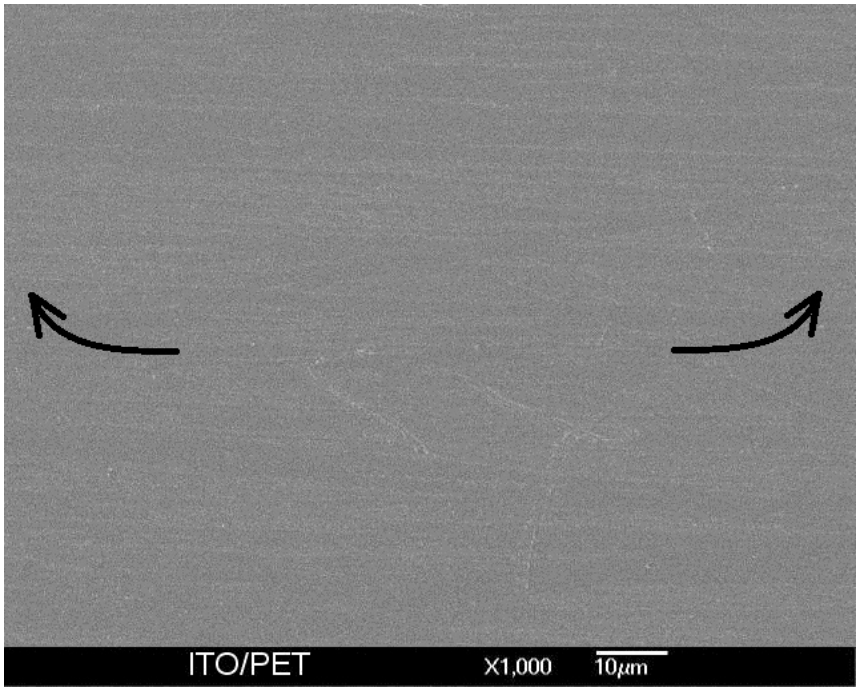

Figure 6.58 SEM micrograph showing surface of ITO film (100 nm) deposited on PET substrate after 100 buckling cycles at 4 mm radius of curvature on the tensile side. Note that black arrows indicate buckling direction.

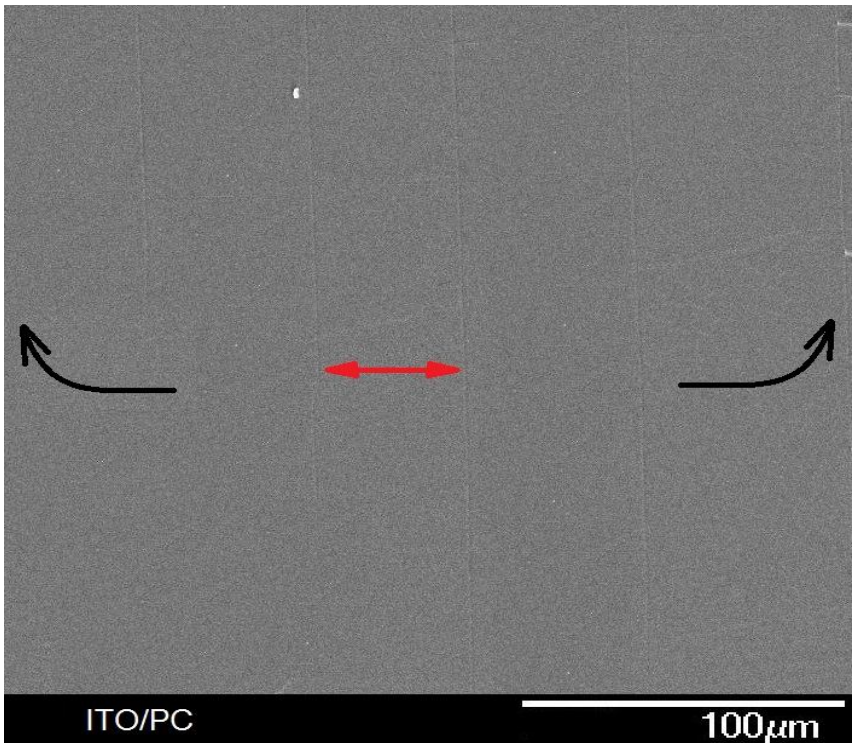

Figure 6.59 SEM micrograph showing cracks in ITO film (100 nm) deposited on PC substrate after 100 buckling cycles at 4 mm radius of curvature on the tensile side. Note that black arrows indicate buckling direction.

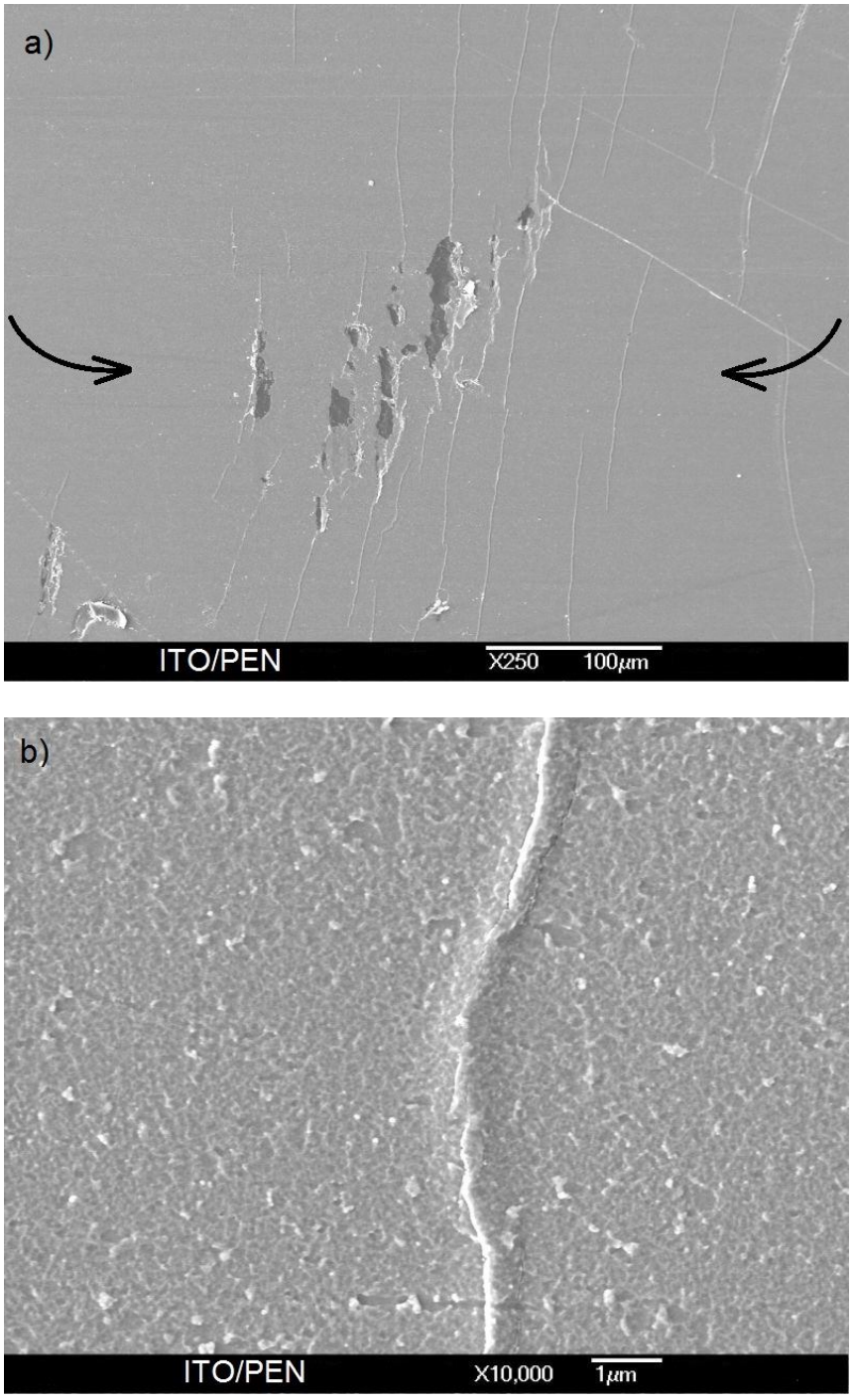

Figure 6.60 SEM micrographs showing buckling delamination of ITO (100 nm) film deposited on PEN substrate after 100 buckling cycles at 4 mm radius of curvature on the compression side; a) buckling delamination pattern and b) buckling profile with cracks.

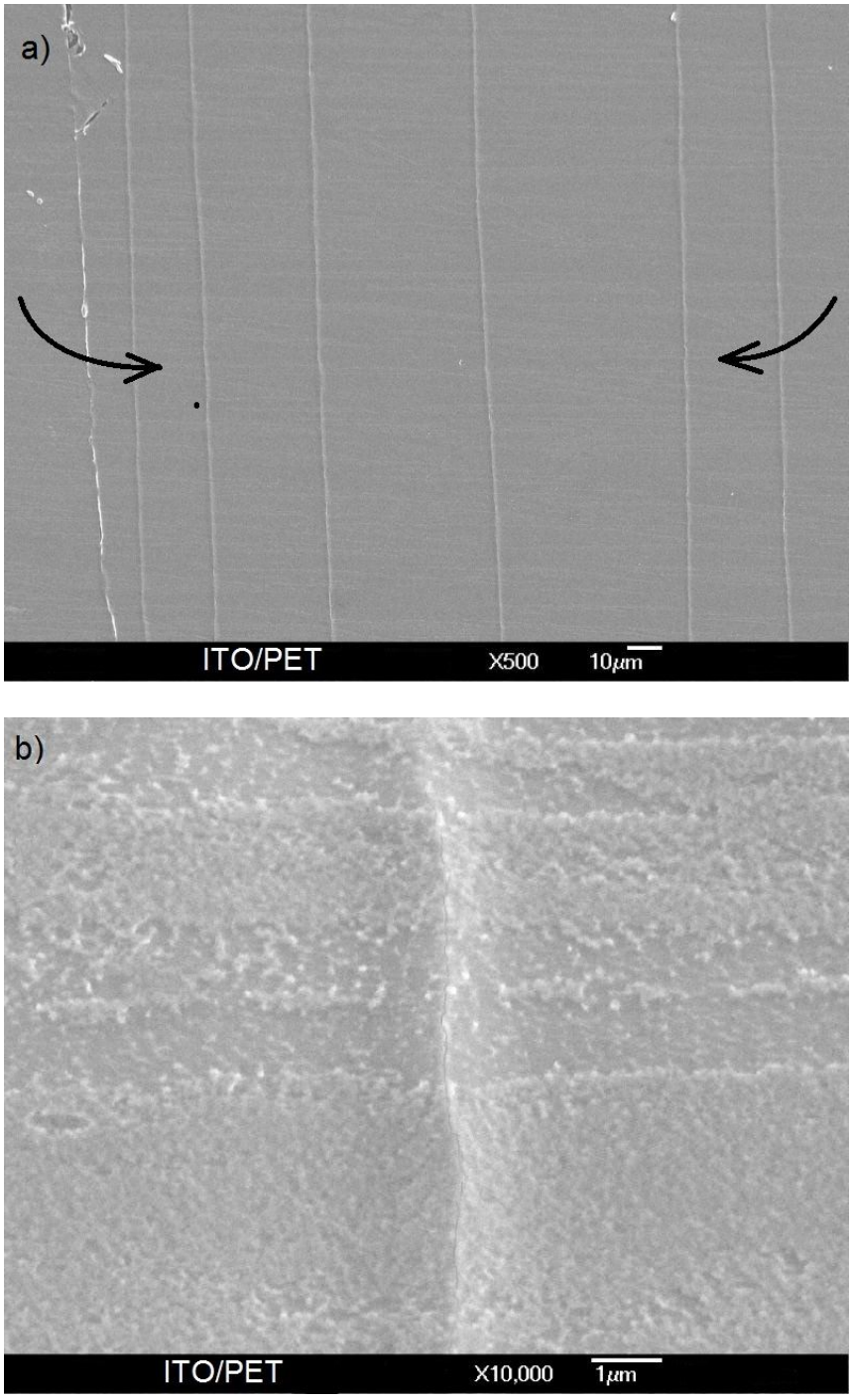

Figure 6.61 SEM micrographs showing buckling delamination of ITO (100 nm) film deposited on PET substrate after 100 buckling cycles at 4 mm radius of curvature on the compression side; a) buckling delamination pattern and b) buckling profile with crack on the top.

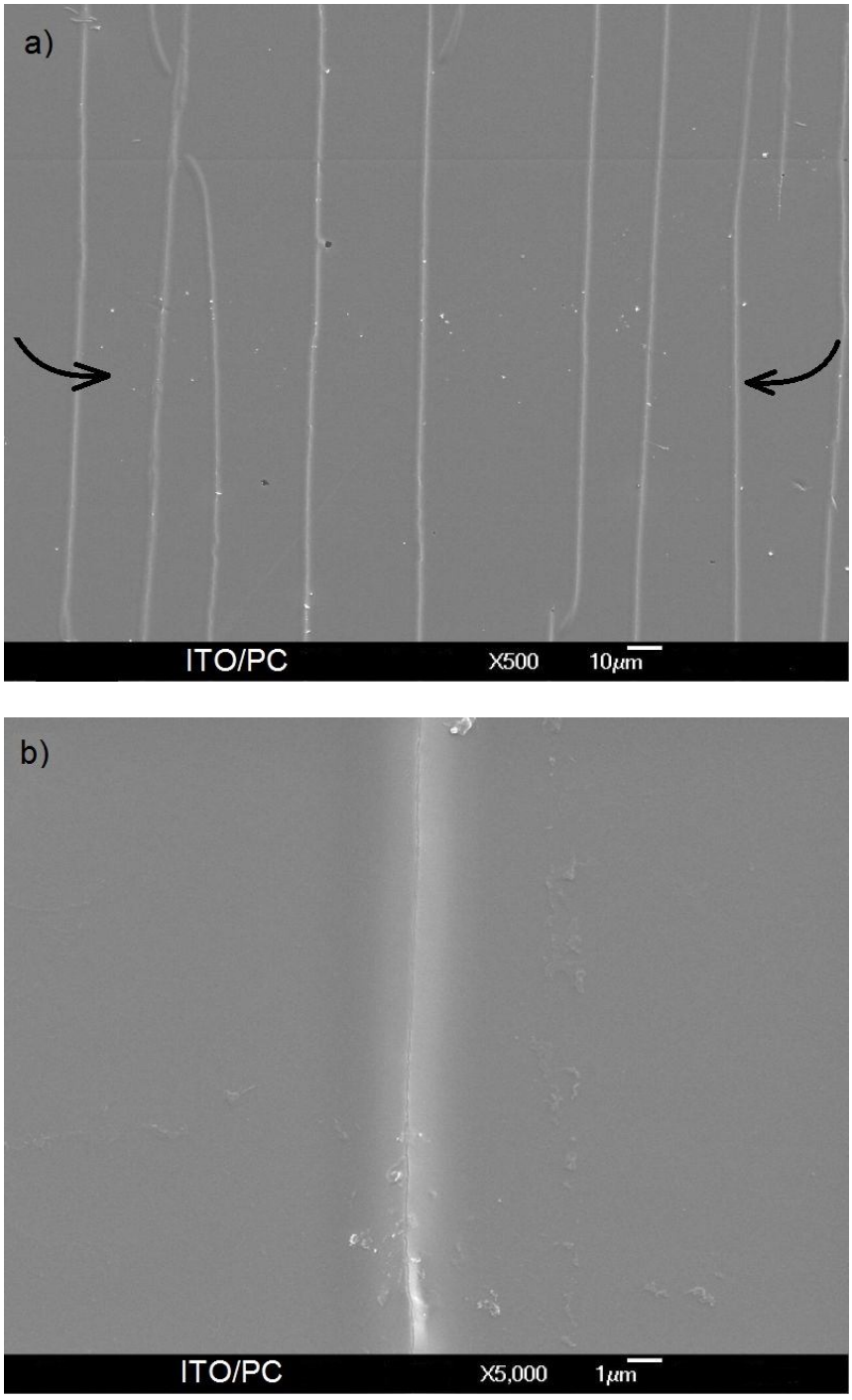

Figure 6.62 SEM micrographs showing buckling delamination of ITO (100 nm) film deposited on PC substrate after 100 buckling cycles at 4 mm radius of curvature on the compression side; a) buckling delamination pattern and b) buckling profile with crack on the top.

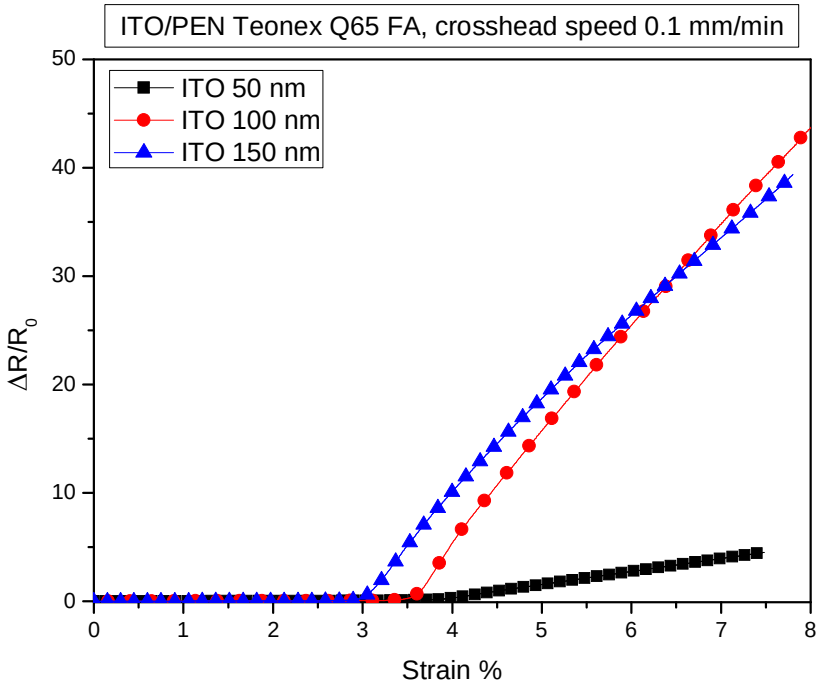

Figure 6.63 Increment of resistance as a function of strain of 50, 100 and 150 nm thick ITO film deposited on PEN substrate.

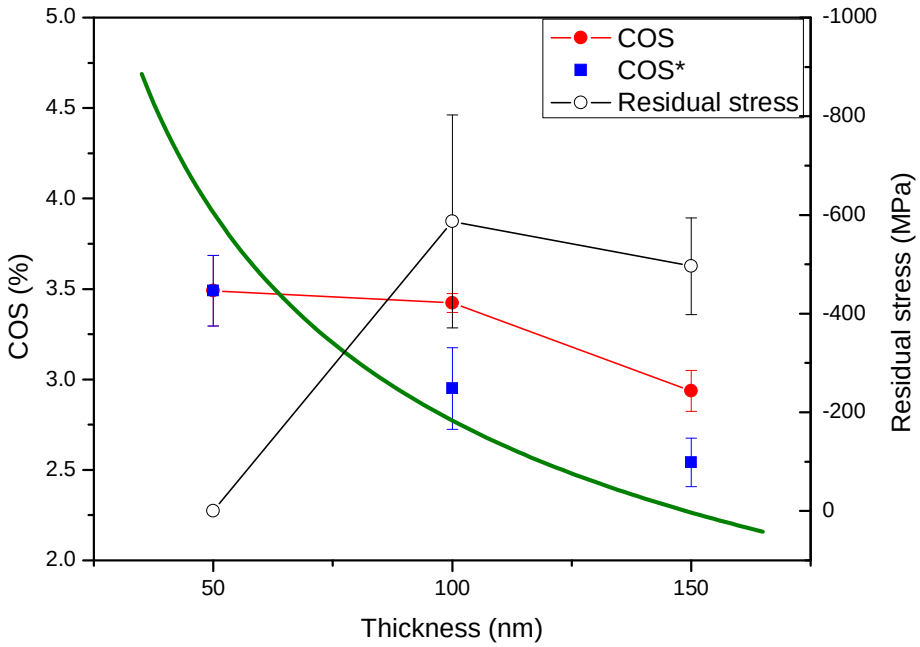

Figure 6.64 Graph showing influence of ITO thickness on residual stress, crack onset strain (COS) and intrinsic crack onset strain (COS*). The green line represents scaling fit ($COS^* \alpha \frac{1}{\sqrt{h}}$) to the COS* data.

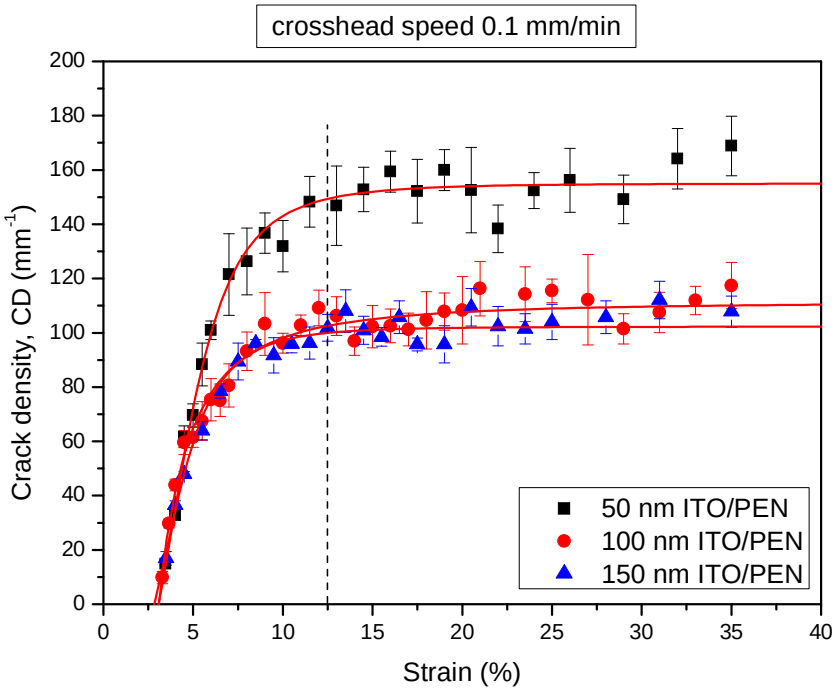

Figure 6.65 Crack density as a function of applied strain for 50, 100 and 150 nm thick ITO films deposited on PEN substrate. Red guidelines are provided for a better visualisation of the measured points.

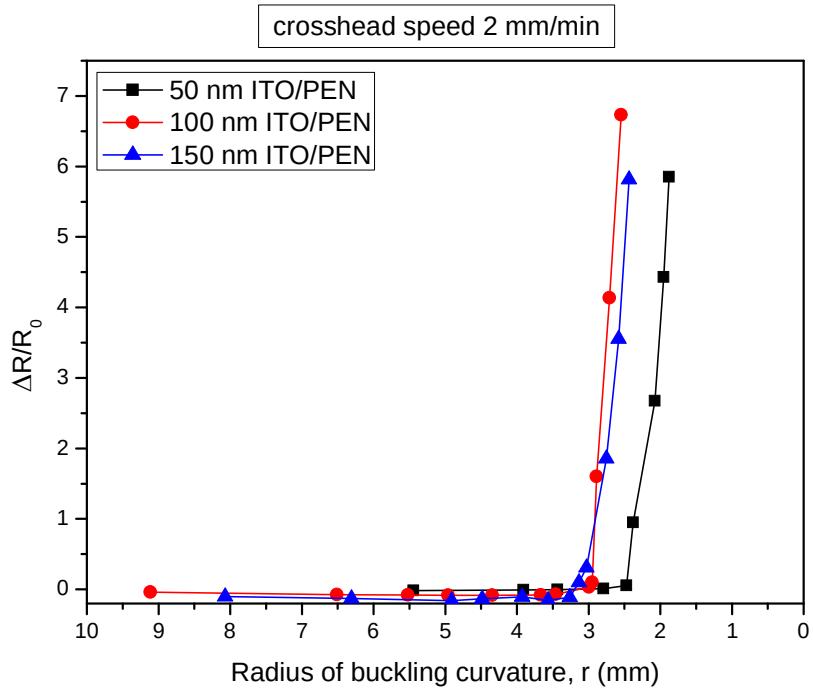

Figure 6.66 Increment of resistance as a function of radius of buckling curvature for 50, 100 and 150 nm thick ITO films deposited on PEN substrate. Samples flexed monotonically on the tensile side.

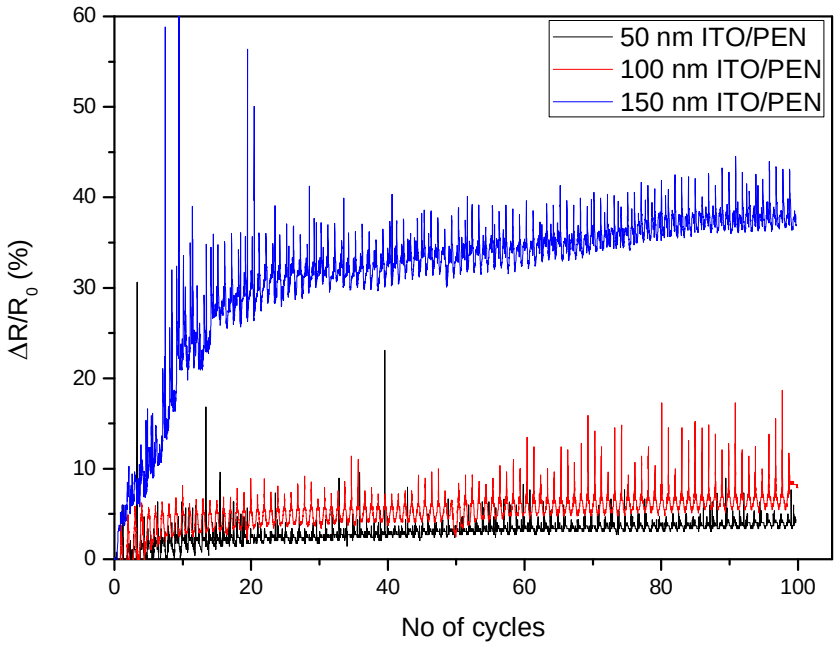

Figure 6.67 Increment of resistance versus number of cycles for 50, 100 and 150 nm thick ITO films deposited on PEN substrate and flexed in tension at 4 mm radius of curvature.

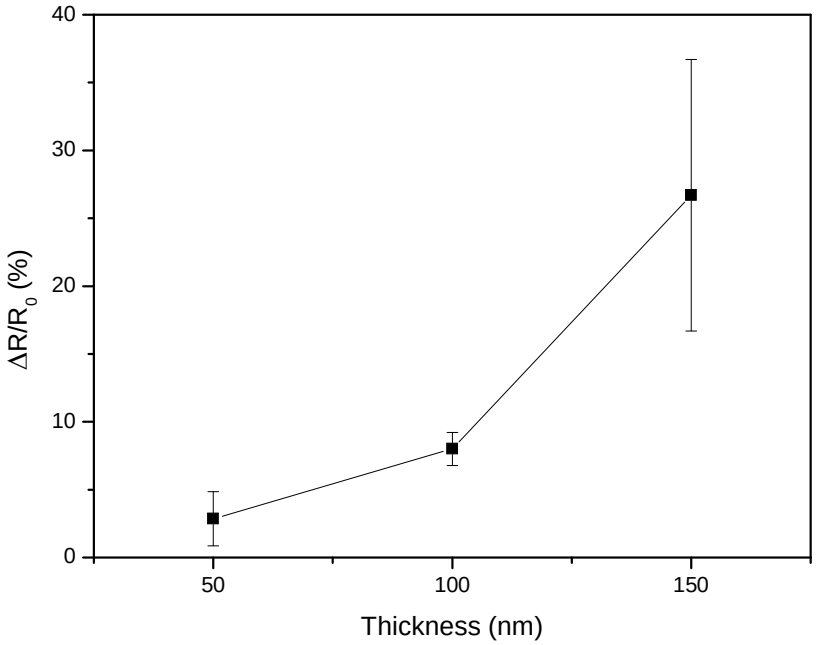

Figure 6.68 Increment of resistance as a function of ITO film thickness after 100 bending cycles in tension at 4 mm radius of curvature. ITO film was deposited on PEN polymer substrates.

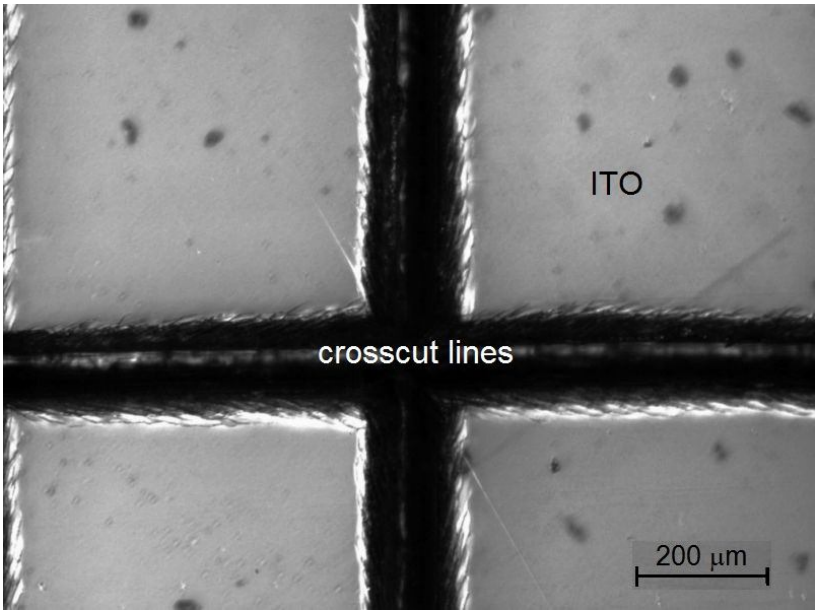

Figure 6.69 Optical microscopy micrograph showing effect on 100 nm thick ITO film adhesion of PEN polymer substrate.

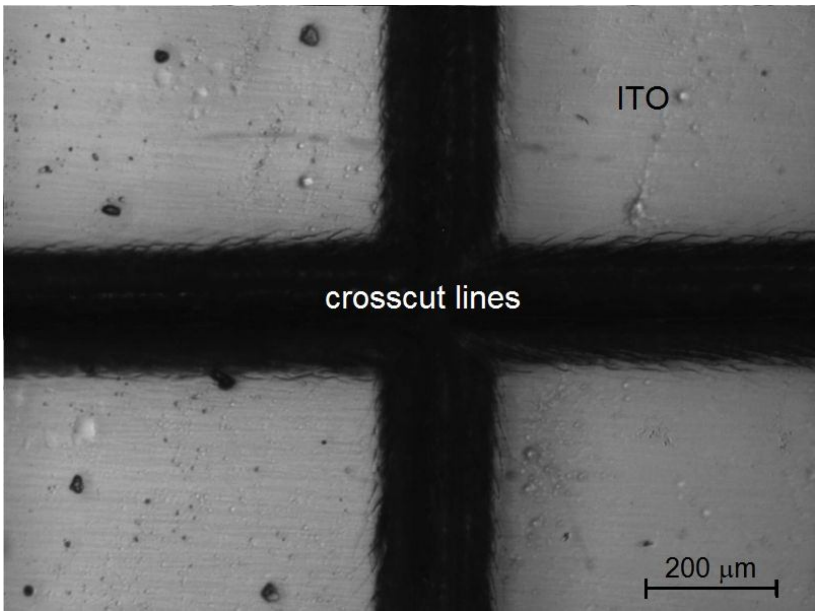

Figure 6.70 Optical microscopy micrograph showing effect on 100 nm thick ITO film adhesion of PET polymer substrate.

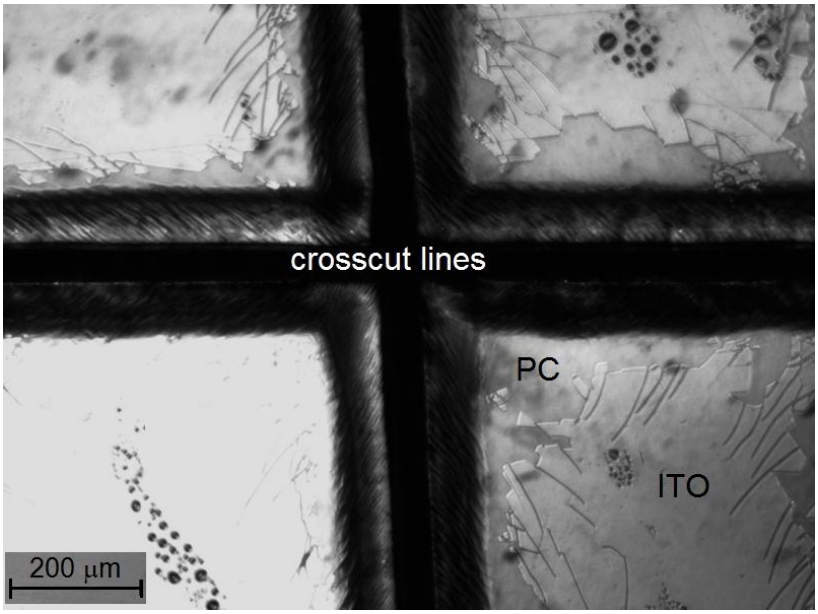

Figure 6.71 Optical microscopy micrograph showing effect on 100 nm thick ITO film adhesion of PC polymer substrate.

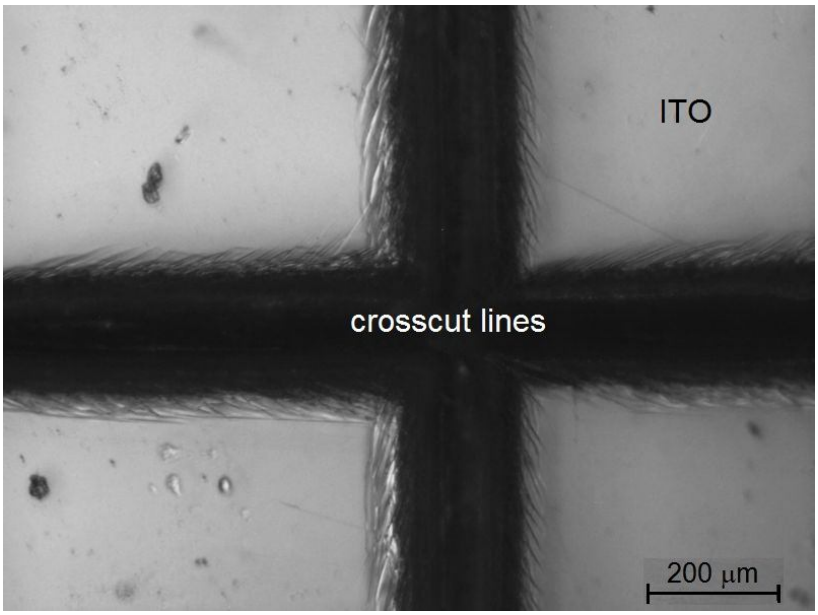

Figure 6.72 Optical micrograph showing influence of 50 nm thick ITO film on adhesion level for ITO/PEN system.

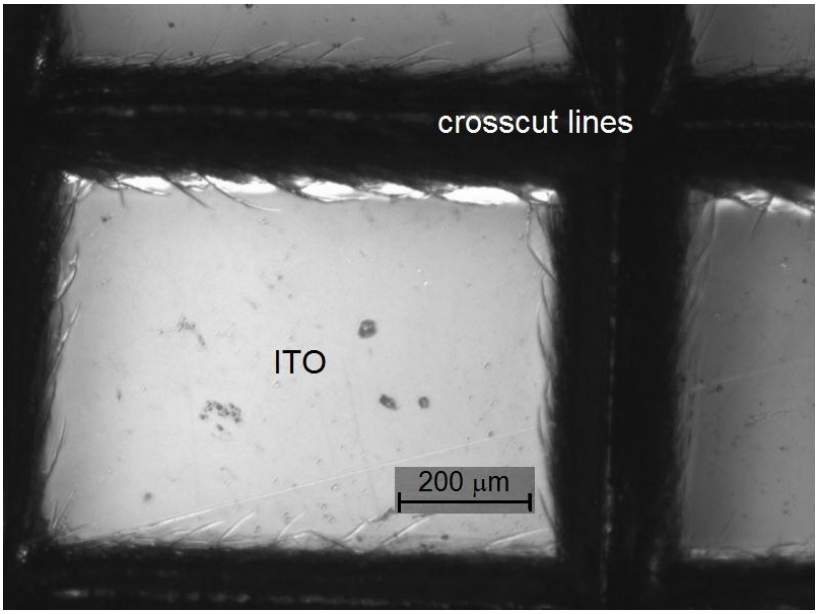

Figure 6.73 Optical micrograph showing influence of 150 nm thick ITO film on adhesion level for ITO/PEN system.

CHAPTER 7

7. OVERALL CONCLUSIONS AND RECOMMENDATIONS FOR FUTURE WORK

7.1 Summary of thesis

PET, PEN and PC polymer substrates were chosen as candidates for plastic electronics and characterised. The transparency, surface morphology, degree of crystallinity and mechanical properties were characterised using a spectrophotometer, AFM and SEM, DSC, and a Instron tensile machine, respectively. The results showed that all substrates exhibit high transmittance, of ~90%, in the visible range. However, PEN substrates exhibit the highest Young's modulus equal to 3.4 GPa.

The PLD process of ITO film growth on glass substrates was optimised by varying deposition conditions, such as oxygen pressure, target to substrate distance, number of pulses and temperature, systematically. The influence of deposition conditions on structural, morphological, and opto-electrical properties was studied. The optimised conditions were used to deposit ITO films on polymer substrates. Both ITO/glass and ITO/polymer samples were characterised using AFM, SEM, XRD, a four-point probe, profilometer and spectrophotometer. The results showed that all deposition conditions significantly influence opto-electrical and structural properties. High quality amorphous 100 nm thick ITO films with low resistivity, of 3.0×10^{-4} Ω cm, and high transparency, of 85%, were successfully

deposited on glass substrates at a temperature of 150 ^{o}C. A low resistivity, of ~ 5.0 x 10^{-4} Ω cm, and high transparency, of 80% in the visible spectrum was achieved for ITO-coated polymer substrates at room temperature.

The influence of layer thickness and indium batch type on structural, morphological and opto-electrical properties of sol-gel derived ITO films dip-coated on glass substrates was investigated. Devices, such as XRD, SEM, profilometer, four-point probe and spectrophotometer were involved in characterisation process. The opto-electrical properties were found to be dependent on the thickness and the kind of $In(ND)_3$ batch used. The lowest resistivity, of 1.8 x 10^{-2} Ω cm, for 175 nm thick ITO films and optical transmittance, of ~80%, in the visible range were achieved.

The influence of polymer substrate and ITO layer thickness on electro-mechanical reliability of ITO/polymer systems was investigated. The samples were subjected to variety of stress conditions. Uniaxial tensile electro-fragmentation tests with *in situ* observation of crack evolution and monitoring of resistance changes were conducted with a Minimat tensile machine. The monotonic and cycling buckling tests in both tension and compression were conducted with a bending device developed in this project. After the test the samples were characterised by SEM and AFM techniques. The samples were also characterised in terms of adhesion tests (the tape test was used). The results revealed that the 100 nm thick ITO-coated PEN substrates exhibit the lowest residual stress in comparison with ITO/PET and ITO/PC substrates due to their highest rigidity. Also the highest intrinsic crack onset strain, evaluated by uniaxial tensile testing, equal to 3.5%, was observed for ITO/PEN systems. Moreover, 50 nm thick ITO film-coated PEN substrate show the highest flexibility. The sample exhibits

onset cracking at a very low radius of buckling curvature equal to 2.6 mm. In addition, the fatigue test in tension revealed that the sample exhibits high electro-mechanical reliability. The resistance increased only 3% after 100 cycles applied.

7.2 Major conclusions

All pulsed laser deposition parameters showed a strong influence on opto-electrical properties of ITO films. The results also showed that by optimising the deposition parameters it is possible to achieve very thin films that still maintain a low resistivity and a high transparency. This result is important for flexible display designers, where low thickness of the film is necessary to increase flexibility whilst simultaneously maintaining a low resistivity and a high transparency for high device efficiency.

The original objectives of the SOLFLEX project of developing a low-temperature sol-gel derived conductive ITO ink printable on polymer substrates were not achieved. In addition, the required conductive films with low sheet resistance, between 10 – 100 Ω/□, and high optical transparency, above 80%, for end applications were not met even for ITO-coated glass substrates annealed at the temperature of 600 ^{o}C. The sol-gel process still needs to be developed to improve electrical conductivity at low curing temperatures to allow coatings to be applied on polymer substrates.

The results showed that electro-mechanical properties of ITO films are strongly dependent on their thickness, polymer substrates and stress conditions. The conductive failure with infinite

resistance immediately following the crack onset strain of ITO/PC systems was found to be due to poor adhesion at the interface, which in turn led to crack delamination with no conductive path formation between ITO film fragments. This experiment has also shown that the adhesion level between the ITO film and polymer substrate may be the crucial parameter in understanding the mechanism of conductive path formation. It is also concluded that by increasing polymer thickness by 0.050 mm the flexibility of ITO/polymer systems decreases by 25%. Therefore, the right choice of polymer substrate and the film thickness can significantly increase a life-time of the flexible devices. In this study ITO-coated PEN showed the best electro-mechanical reliability (the sample can be flexed in tension down to 3 mm radius of curvature without cracking). This sample should be chosen as a candidate for flexible devices with a moderate degree of bending.

7.3 Overall conclusions

It is believed that this work provides a solid background to help understand the electro-mechanical behaviour of transparent, conductive ITO thin-films on compliant substrates used for plastic electronic devices. A variety of stress conditions that may be present in a flexible devices during exploitation by the end user, were applied using standard and developed techniques. The results were presented and discussed in detail. According to the literature, in general, an electro-mechanical properties of ITO/polymer system are limited to 2% applied uniaxial strain. This work showed that the electro-mechanical properties of ITO-coated polymer substrates can be improved (up to 3.5%) by a careful control of the thickness of ITO film during its growth by pulsed laser deposition and a proper selection of the polymer

substrate. Moreover, this work can be used as a guidance for newly-developed conductive samples for flexible electronics, such as conductive polymers, metallic nanowire arrays or carbon nanotubes fabricated on polymer substrates, where electro-mechanical reliability tests are crucial before their commercialisation.

7.4 Future work

1. The pulsed-laser deposited ITO films on glass substrates, studied in chapter 4, showed that it is possible to achieve crystalline films at low temperature by increasing the layer thickness. However, crystalline films on polymer substrates studied in this work were not achieved. Further work is recommended in order to achieve crystalline ITO films on polymer substrates. Different polymer substrates with a higher glass transition temperature (T_g) should be used to increase the deposition temperature and allow ITO film crystallise. Polyethersulfone (PES), which exhibits a T_g = 210 ^oC and no dimensional changes up to 200 ^oC, or high-temperature polycarbonate (PC) with a Tg of 215 ^oC and a Young's modulus of 2.80 GPa at a temperature of 180 ^oC can be used. Once the crystalline c-ITO films are achieved on polymer substrates the electro-mechanical tests can be performed and achieved results compared with a performance of amorphous a-ITO-coated polymer substrates. Finally, it would be very valuable to perform electro-mechanical tests of acid-trited a-ITO and c-ITO/polymers for comparison.

I hypothesise that increase of deposition temperature during growth of ITO film on polymer substrates with a high glass transition temperature will result in crystalline film.

2. As a continuous study for PLD of ITO on polymers it could be also interesting to deposit buffer layers, e.g. aluminium oxide (Al_2O_3) with varying thicknesses, in order to investigate their influence on electro-mechanical properties. It was previously found (see literature review in chapter 4) that the buffer layers influence electro-mechanical stability of ITO/buffer layer/polymer systems as they possess intermediate elastic moduli.

I hypothesise that the presence of a buffer layer between the polymer substrate and ITO film will improve electro-mechanical stability of the ITO/polymer system.

3. A zinc oxide (ZnO) target can be used as an alternative transparent conductive oxide to ITO. The optimisation process for ZnO/polymers will be necessary in order to achieve highly conductive and transparent films at low temperatures. And again, once it is done, electro-mechanical tests can be performed and compared, e.g. with ITO/polymer systems.

I hypothesise that careful control of deposition conditions during growth of ZnO films on polymer substrates will result in high-quality films competitive with ITO.

4. As conductive samples, based on conductive polymers [e.g. poly(3,4-ethylenedioxythiophene) doped with polystyrene sulfonic acid (PEDOT:PSS)] or metallic nanowire arrays are promising candidates to replace brittle ITO films for flexible displays, they can be used for future projects. Cycling thermal treatments at different temperatures can be performed to simulate conditions of the device manufacturing. Then the influence of the thermal treatment on opto-electrical and electro-mechanical properties can be investigated. Corrosion tests can be also considered.

The hypothesis is that PEDOT:PSS serves better as a conductive component for flexible opto-electronic devices than ITO.

5. Interesting projects can be conducted based on wet deposition methods. Namely, carbon nanotubes (CNTs) or already crystalline ITO powders can be dispersed in alcoholic solutions and spin-coated on polymer substrates (with high T_g, as mentioned above, to allow baking and annealing). An influence of the solution concentration and the thickness of the films on opto-electrical properties can be investigated. Furthermore, these systems can be investigated in terms of electro-mechanical tests under variety of applied stresses (e.g. monotonic or dynamic bending in tension and compression).

The hypotheses are:

a) Replacing ITO by carbon nanotubes for conductive samples in flexible opto-electronics will improve electro-mechanical stability

b) Wet deposition method of ITO powder will improve cracking-resistance.

References

ASTM Standard D3359 (2009e2) **Standard Test Methods for Measuring Adhesion by Tape Test**. West Conshohocken, PA: ASTM International. Available from: www.astm.org

ABDALLAH, A. A., KOZODAEV, D., BOUTEN, P. C. P., DEN TOONDER, J. M. J., SCHUBERT, U. S. & DE WITH, G. (2006) Buckle morphology of compressed inorganic thin layers on a polymer substrate. **Thin Solid Films**, 503 (1-2): 167-176

ABDALLAH, A. A., BOUTEN, P. C. P., DEN TOONDER, J. M. J. & DE WITH, G. (2011) Buckle initiation and delamination of patterned ITO layers on a polymer substrate. **Surface and Coatings Technology**, 205 (8-9): 3103-3111

ADURODIJA, F., SEMPLE, L. & BRUNING, R. (2006) Crystallization process and electro-optical properties of In_2O_3 and ITO thin films. **Journal of Materials Science**, 41 (21): 7096-7102

ADURODIJA, F. O., IZUMI, H., ISHIHARA, T., YOSHIOKA, H., YAMADA, K., MATSUI, H. & MOTOYAMA, M. (1999) Highly conducting indium tin oxide (ITO) thin films deposited by pulsed laser ablation. **Thin Solid Films**, 350 (1-2): 79-84

ADURODIJA, F. O., IZUMI, H., ISHIHARA, T., YOSHIOKA, H. & MOTOYAMA, M. (2002) The electro-optical properties of amorphous indium tin oxide films prepared at room temperature by pulsed laser deposition. **Solar Energy Materials and Solar Cells**, 71 (1): 1-8

AL-DAHOUDI, N. & AEGERTER, M. A. (2003) Wet Coating Deposition of ITO Coatings on Plastic Substrates. **Journal of Sol-Gel Science and Technology**, 26 (1): 693-697

ALAM, M. J. & CAMERON, D. C. (2000) Optical and electrical properties of transparent conductive ITO thin films deposited by sol-gel process. **Thin Solid Films**, 377-378 455-459

ALAM, M. J. & CAMERON, D. C. (2001) Characterization of transparent conductive ITO thin films deposited on titanium dioxide film by a sol-gel process. **Surface and Coatings Technology**, 142-144 (0): 776-780

AMBRICO, J. M. & BEGLEY, M. R. (2002) The role of initial flaw size, elastic compliance and plasticity in channel cracking of thin films. **Thin Solid Films**, 419 (1-2): 144-153

ANDERSONS, J., TARASOVS, S. & LETERRIER, Y. (2007a) Analysis of thin film cracking and buckling on compliant substrate by fragmentation test. **Key Engineering Materials**, 348-349 329-332

ANDERSONS, J., LETERRIER, Y., TORNARE, G., DUMONT, P. & MANSON, J. A. E. (2007b) Evaluation of interfacial stress transfer efficiency by coating fragmentation test. **Mechanics of Materials**, 39 (9): 834-844

ANTONY, A., NISHA, M., MANOJ, R. & JAYARAJ, M. K. (2004) Influence of target to substrate spacing on the properties of ITO thin films. **Applied Surface Science**, 225 (1-4): 294-301

ARRESE-IGOR, S., MITXELENA, O., ARBE, A., ALEGRÍA, A., COLMENERO, J. & FRICK, B. (2006) Molecular motions in glassy polycarbonate below its glass transition temperature. **Journal of Non-Crystalline Solids**, 352 (42-49): 5072-5075

ASAKUMA, N., FUKUI, T., TOKI, M. & IMAI, H. (2003) Low-Temperature Synthesis of ITO Thin Films Using an Ultraviolet Laser for Conductive Coating on Organic Polymer Substrates. **Journal of Sol-Gel Science and Technology**, 27 (1): 91-95

BAÍA, I., FERNANDES, B., NUNES, P., QUINTELA, M. & MARTINS, R. (2001) Influence of the process parameters on structural and electrical properties of r.f. magnetron sputtering ITO films. **Thin Solid Films**, 383 (1-2): 244-247

BAUER, C. W. (1997) Effects of degree of stretching on the properties of heat set biaxially stretched naphthalate-containing polyester films. **Journal of Plastic Film and Sheeting**, 13 (4): 336-347

BEAKE, B. D., LEGGETT, G. J. & SHIPWAY, P. H. (2001) Tapping mode and phase imaging of biaxially oriented polyester films. **Surface and Interface Analysis**, 31 (1): 39-45

BENHAM, P. P., CRAWFORD, R. J. & ARMSTRONG, C. G. (1996) **Mechanics of engineering materials**. 2nd ed. Harlow: Longman.

BEUTH, J. L. & KLINGBEIL, N. W. (1996) Cracking of thin films bonded to elastic-plastic substrates. **Journal of the Mechanics and Physics of Solids**, 44 (9): 1411-1428

BEUTH JR, J. L. (1992) Cracking of thin bonded films in residual tension. **International Journal of Solids and Structures**, 29 (13): 1657-1675

BIRKHOLZ, M. (2006) **Thin Film Analysis by X-Ray Scattering**. Weinheim: Wiley-Vch Verlag GmbH & Co. KGaA.

BIRLEY, A. W., HAWORTH, B. & BATCHELOR, J. (1991) **Physics of Plastics: Processing and Materials Engineering**. Munich ; New York: Hanser Publishers : Oxford University Press (distributor).

BOUTEN, P. C. P., SLIKKERVEER, P. J. & LETERRIER, Y. (2005) "Mechanics of ITO on Plastic Substrates for Flexible Displays ". In CRAWFORD, G. P. (Ed.) **Flexible Flat Panel Displays**. Chichester: John Wiley & Sons, Ltd. pp. 99-120.

BOWER, D. I. (2002) **An Introduction to Polymer Physics**. New York: Cambridge University Press.

BRAUN, D., CHERDRON, H., REHAHN, M., RITTER, H. & VOIT, B. (2005) **Polymer Synthesis: Theory and Practice**. 4th ed. Berlin: Springer - Verlag.

BROWN, M. E. (Ed.) (1998) **Handbook of Thermal Analysis and Calorimetry. Vol. 1, Principles and Practice**. Amsterdam: Elsevier Science B.V.

BRYDSON, J. A. (1999) **Plastics Materials**. 7th ed. Oxford: Butterworth Heinemann.

BUCHNER, S., WISWE, D. & ZACHMANN, H. G. (1989) Kinetics of crystallization and melting behaviour of poly(ethylene naphthalene-2,6-dicarboxylate). **Polymer**, 30 (3): 480-488

BURROWS, P. E., GRAFF, G. L., GROSS, M. E., MARTIN, P. M., SHI, M. K., HALL, M., MAST, E., BONHAM, C., BENNETT, W. & SULLIVAN, M. B. (2001) Ultra barrier flexible substrates for flat panel displays. **Displays**, 22 (2): 65-69

CAIRNS, D. R., WITTE II, R. P., SPARACIN, D. K., SACHSMAN, S. M., PAINE, D. C., CRAWFORD, G. P. & NEWTON, R. R. (2000a) Strain-dependent electrical resistance of tin-doped indium oxide on polymer substrates. **Applied physics letters**, 76 (11): 1425-1427

CAIRNS, D. R., SPARACIN, D. K., PAINE, D. C. & CRAWFORD, G. P. (2000b) Electrical Studies of Mechanically Deformed Indium Tin Oxide Coated Polymer Substrates. **SID Symposium Digest of Technical Papers**, 31 (1): 274-277

CAIRNS, D. R., PAINE, D. C. & CRAWFORD, G. P. (2001) The mechanical reliability of sputter-coated indium tin oxide polyester substrates for flexible display and touchscreen applications. In **Transport and Microstructural Phenomena in Oxide Electronics. Symposium (Materials Research Society Symposium Proceedings Vol.666)**. Warrendale, PA, USA. pp. 3-24

CAIRNS, D. R., GORKHALI, S. P., ESMAILZADEH, S., VEDRINE, J. & CRAWFORD, G. P. (2003) Conformable displays based on polymer-dispersed liquid-crystal materials on flexible substrates. **Journal of the Society for Information Display**, 11 (2): 289-295

CAIRNS, D. R. & CRAWFORD, G. P. (2005a) Electrochemical properties of transparent conducting substrates for flexible electronic displays. **Proceedings of the IEEE**, 93 (8): 1451-1458

CAIRNS, D. R. (2005) "Mechanical Reliability of Conductive Polymers for Rollable Display Applications ". In CRAWFORD, G. P. (Ed.) **Flexible Flat Panel Displays**. Chichester: John Wiley & Sons, Ltd. pp. 163-177.

CAIRNS, D. R. & CRAWFORD, G. P. (2005b) Electromechanical properties of transparent conducting substrates for flexible electronic displays. **Proceedings of the IEEE**, 93 (8): 1451-1458

CHAN, J. (1994) Four - Point Probe Manual [online]. Available from: http://microlab.berkeley.edu/ee143/Four-Point_Probe/ [Accessed Spring 1994]

CHARSHA, K. S. S. (2006) **Principles of Physical Vapour Deposition Process of Thin Films** [online]. Elsevier Ltd. Available from: http://www.sciencedirect.com/science/book/9780080446998

CHEN, Z., COTTERELL, B., WANG, W., GUENTHER, E. & CHUA, S. J. (2001a) A mechanical assessment of flexible optoelectronic devices. **Thin Solid Films**, 394 (1-2): 202-206

CHEN, Z., COTTERELL, B., WANG, W., GUENTHER, E. & CHUA, S.-J. (2001b) A mechanical assessment of flexible optoelectronic devices. **Thin Solid Films**, 394 (1-2): 201-205

CHEN, Z., COTTERELL, B. & WANG, W. (2002) The fracture of brittle thin films on compliant substrates in flexible displays. **Engineering Fracture Mechanics**, 69 (5): 597-603

CHEOL, J., KUKJOO, K. & KYUNG CHEOL, C. (2012) Toward Flexible Transparent Plasma Display: Optical Characteristics of Low-Temperature Fabricated Organic-Based Display Structure. **Electron Device Letters, IEEE**, 33 (1): 74-76

CHEREMISINOFF, N. P. (1996) **Polymer Characterization: Laboratory Techniques and Analysis** Westwood, New Jersey: Noyes Publications.

CHIBA, K. & FUTAGAMI, A. (2008) Enhanced bending stability of carbon-nanotube-reinforced indium tin oxide films on flexible plastic substrates. **Applied physics letters**, 93 013114

CHOI, M.-C., KIM, Y. & HA, C.-S. (2008) Polymers for flexible displays: From material selection to device applications. **Progress in Polymer Science**, 33 (6): 581-630

CHWANG, A. B., HACK, M. & BROWN, J. J. (2005) Flexible OLED display development: Strategy and Status. **Journal of the SID**, 13 (6): 481-486

COTTERELL, B. & CHEN, Z. (2000) Buckling and cracking of thin films on compliant substrates under compression. **International Journal of Fracture**, 104 (2): 169-179

CULLITY, B. D. (1978) **Elements of X-Ray Diffraction**. 2nd ed. ed. London: Addison - Wesley

DAUSKARDT, R. H., LANE, M., MA, Q. & KRISHNA, N. (1998) Adhesion and debonding of multi-layer thin film structures. **Engineering Fracture Mechanics**, 61 (1): 141-162

DEKKERS, J. M., RIJNDERS, G. & BLANK, D. H. A. (2006) Role of Sn doping in In2O3 thin films on polymer substrates by pulsed-laser deposition at room temperature. **Applied physics letters**, 88 (15): 3

DELTA TECHNOLOGY LIMITED [online]. Available from: http://www.delta-technologies.com/products.asp?C=1

DEOKATE, R. J., SALUNKHE, S. V., AGAWANE, G. L., PAWAR, B. S., PAWAR, S. M., RAJPURE, K. Y., MOHOLKAR, A. V. & KIM, J. H. (2010) Structural, optical and electrical properties of chemically sprayed nanosized gallium doped CdO thin films. **Journal of Alloys and Compounds**, 496 (1-2): 357-363

DINELLI, F., ASSENDER, H. E., KIROV, K. & KOLOSOV, O. V. (2000) Surface morphology and crystallinity of biaxially stretched PET films on the nanoscale. **Polymer**, 41 (11): 4285-4289

DINIZ, A. S. A. C. (2011) The effects of various annealing regimes on the microstructure and physical properties of ITO (In2O3:Sn) thin films deposited by electron beam evaporation for solar energy applications. **Renewable Energy**, 36 (4): 1153-1165

DOUGLAS M, M. (1991) Sol-gel derived, air-baked indium and tin oxide films. **Thin Solid Films**, 204 (1): 25-32

DOUILLARD, A., HARDY, L., STEVENSON, I., BOITEUX, G., SEYTRE, G., KAZMIERCZAK, T. & GALESKI, A. (2003) Texture and morphology of biaxially stretched poly(ethylene naphthalene-2,6-dicarboxylate). **Journal of Applied Polymer Science**, 89 (8): 2224-2232

EASON, R. (Ed.) (2007) **Pulsed Laser Deposition of Thin Films: Application - Led Growth of Functional Materials**. Hoboken, New Jersey: John Wiley and Sons, Inc.

EXARHOS, G. J. & ZHOU, X.-D. (2007) Discovery-based design of transparent conducting oxide films. **Thin Solid Films**, 515 (18): 7025-7052

FAN, J. C. C. (1979) Preparation of Sn-doped In2O3 (ITO) films at low deposition temperatures by ion-beam sputtering. **Applied Physic Letters**, 34 (8): 515-517

FISCHER, T. (2009) **Materials Science for Engineering Students**. Canada: Academic Press (inprint of Elsevier).

FORTUNATO, E., NUNES, P., MARQUES, A., COSTA, D., ÁGUAS, H., FERREIRA, I., COSTA, M. E. V., GODINHO, M. H., ALMEIDA, P. L., BORGES, J. P. & MARTINS, R. (2002a) Transparent, conductive ZnO:Al thin film deposited on polymer substrates by RF magnetron sputtering. **Surface and Coatings Technology**, 151-152 247-251

FORTUNATO, E., NUNES, P., MARQUES, A., COSTA, D., ÁGUAS, H., FERREIRA, I., COSTA, M. E. V., GODINHO, M. H., ALMEIDA, P. L., BORGES, J. P. & MARTINS, R. (2002b) Influence of the Strain on the Electrical Resistance of Zinc Oxide Doped Thin Film Deposited on Polymer Substrates. **Advanced Engineering Materials**, 4 (8): 610-612

FREUND, L. B. & SURESH, S. (2003) **Thin film materials : stress, defect formation and surface evolution**. Cambridge: Cambridge University Press.

GEORGE, J. & MENON, C. S. (2000) Electrical and optical properties of electron beam evaporated ITO thin films. **Surface and Coatings Technology**, 132 (1): 45-48

GERE, J. M. & TIMOSHENKO, S. P. (1999) **Mechanics of materials**. 4th ed. Cheltenham: Stanley Thornes.

GLESKOVA, H., WAGNER, S. & SUO, Z. (1999) Failure resistance of amorphous silicon transistors under extreme in-plane strain. **Applied physics letters**, 75 (19): 3011-3013

GODEHARDT, R. (2008) "Scanning Electron Microscopy". In MICHLER, G. H. (Ed.) **Electron Microscopy of Polymers**. Hidelberg: Springer pp. 87-120.

GOEBBERT, C., GASPARRO, G., SCHULER, T., KRAJEWSKI, T. & AEGERTER, M. A. (2000) Influence of the Layer Morphology on the Electrical Properties of Sol Gel Transparent Conducting Oxide Coatings. **Journal of Sol-Gel Science and Technology**, 19 (1): 435-439

GORKHALI, S. P., CAIRNS, D. R. & CRAWFORD, G. P. (2004) Reliability of transparent conducting substrates for rollable displays: A cyclic loading investigation. **Journal of the Society for Information Display**, 12 (1): 45-49

GREENER, J., NG, K. C., VAETH, K. M. & SMITH, T. M. (2007) Moisture permeability through multilayered barrier films as applied to flexible OLED display. **Journal of Applied Polymer Science**, 106 (5): 3534-3542

GREGO, S., LEWIS, J., VICK, E. & TEMPLE, D. (2007) A method to evaluate mechanical performance of thin transparent films for flexible displays. **Thin Solid Films**, 515 (11): 4745-4752

GUILLEN, C. & HERRERO, J. (2005) Comparison study of ITO thin films deposited by sputtering at room temperature onto polymer and glass substrates. **Thin Solid Films**, 480-481 (0): 129-132

GUILLEN, C. & HERRERO, J. (2008a) Structural, optical and electrical characteristics of ITO thin films deposited by sputtering on different polyester substrates. **Materials Chemistry and Physics**, 112 (2): 641-644

GUILLEN, C. & HERRERO, J. (2008b) Influence of the film thickness on the structure, optical and electrical properties of ITO coatings deposited by sputtering at room temperature on glass and plastic substrates. **Semiconductor Science and Technology**, 23 (7): 5

GUILLEN, C. & HERRERO, J. (2011) TCO/metal/TCO structures for energy and flexible electronics. **Thin Solid Films**, 520 (1): 1-17

GURURAJ, T., SUBASRI, R., RAJU, K. R. C. S. & PADMANABHAM, G. (2011) Effect of plasma pretreatment on adhesion and mechanical properties of UV-curable coatings on plastics. **Applied Surface Science**, 257 (9): 4360-4364

HAN, H., ADAMS, D., MAYER, J. W. & ALFORD, T. L. (2005) Characterization of the physical and electrical properties of Indium tin oxide on polyethylene napthalate. **Journal of Applied Physics**, 98 (8): 083705-083708

HAN, J.-I. (2005) "Stability of Externally Deformed ITO Films". In CRAWFORD, G. P. (Ed.) **Flexible Flat Panel Displays**. Chichester: John Wiley & Sons, Ltd. pp. 121-133

HANADA, T., NEGISHI, T., SHIROISHI, I. & SHIRO, T. (2010) Plastic substrate with gas barrier layer and transparent conductive oxide thin film for flexible displays. **Thin Solid Films**, 518 (11): 3089-3092

HAO, L., DIAO, X., XU, H., GU, B. & WANG, T. (2008) Thickness dependence of structural, electrical and optical properties of indium tin oxide (ITO) films deposited on PET substrates. **Applied Surface Science**, 254 (11): 3504-3508

HARDY, L., STEVENSON, I., BOITEUX, G., SEYTRE, G. & SCHÖNHALS, A. (2001) Dielectric and dynamic mechanical relaxation behaviour of poly(ethylene 2,6 naphthalene dicarboxylate). I. Amorphous films. **Polymer**, 42 (13): 5679-5687

HARDY, L., STEVENSON, I., FRITZ, A., BOITEUX, G., SEYTRE, G. & SCHÖNHALS, A. (2003) Dielectric and dynamic mechanical relaxation behaviour of poly(ethylene 2,6-naphthalene dicarboxylate). II. Semicrystalline oriented films. **Polymer**, 44 (15): 4311-4323

HARPER, C. A. (2002) **Handbook of Plastics, Elastomers & Composites**. 4th ed. USA: McGraw-Hill Companies, Inc.

HEYA, A., MINAMIKAWA, T., NIKI, T., MINAMI, S., MASUDA, A., UMEMOTO, H., MATSUO, N. & MATSUMURA, H. (2008) Cat-CVD SiN passivation films for OLEDs and packaging. **Thin Solid Films**, 516 (5): 553-557

HOSONO, H. (2007) Recent progress in transparent oxide semiconductors: Materials and device application. **Thin Solid Films**, 515 (15): 6000-6014

HU, Y. S., ROGUNOVA, M., SCHIRALDI, D. A., HILTNER, A. & BAER, E. (2002) Crystallization kinetics and crystalline morphology of poly(ethylene naphthalate) and poly(ethylene terephthalate-co-bibenzoate). **Journal of Applied Polymer Science**, 86 (1): 98-115

HUTCHINSON, J. W. & SOU, Z. (1992) "Mixed Mode Cracking in Layered Materials". In HUTCHINSON, J. W. & WU, T. Y. (Eds.) **Advances in Applied Mechanics**. 29 vol., San Diego: Academic Press. pp. 63-191.

IZUMI, H., ADURODIJA, F. O., KANEYOSHI, T., ISHIHARA, T., YOSHIOKA, H. & MOTOYAMA, M. (2002a) Electrical and structural properties of indium tin oxide films prepared by pulsed laser deposition. **Journal of Applied Physics**, 91 (3): 1213-1218

IZUMI, H., ISHIHARA, T., YOSHIOKA, H. & MOTOYAMA, M. (2002b) Electrical properties of crystalline ITO films prepared at room temperature by pulsed laser deposition on plastic substrates. In pp. 32-35

JANOCHA, W. S., HOPPER, M. J. & MACKENZIE, K. J. (1988) "Polyesters, Films". In **Encyclopedia of Polymer Science & Engineering** 2nd ed, New York: Wiley. pp. 193-216.

JANOWITZ, C. & ET AL. (2011) Experimental electronic structure of In_2O_3 and Ga_2O_3. **New Journal of Physics**, 13 (8): 085014

JANSSON, N. E., LETERRIER, Y., MEDICO, L. & MANSON, J. A. E. (2006) Calculation of adhesive and cohesive fracture toughness of a thin brittle coating on a polymer substrate. **Thin Solid Films**, 515 (4): 2097-2105

KHODOROV, A., PIECHOWIAK, A. & GOMES, M. J. M. (2007) Structural, electrical and optical properties of indium-tin-oxide thin films prepared by pulsed laser deposition. **Thin Solid Films**, 515 (20-21): 7829-7833

KIM, D.-H., KIM, W.-J., PARK, S. J., CHOI, H. W. & KIM, K.-H. (2010a) Electrical and optical properties of In-Zn-Sn-O thin film deposited on polymer substrates through facing targets co-sputtering system. **Surface and Coatings Technology**, 205 (Supplement 1): S324-S327

KIM, E.-H., YANG, C.-W. & PARK, J.-W. (2010b) Improving the delamination resistance of indium tin oxide (ITO) coatings on polymeric substrates by O2 plasma surface treatment. **Current Applied Physics**, 10 (3, Supplement 1): S510-S514

KIM, H., GILMORE, C. M., PIQUE, A., HORWITZ, J. S., MATTOUSSI, H., MURATA, H., KAFAFI, Z. H. & CHRISEY, D. B. (1999a) Electrical, optical, and structural properties of indium-tin-oxide thin films for organic light-emitting devices. **Journal of Applied Physics**, 86 (11): 6451-6461

KIM, H., PIQUE, A., HORWITZ, J. S., MATTOUSSI, H., MURATA, H., KAFAFI, Z. H. & CHRISEY, D. B. (1999b) Indium tin oxide thin films for organic light-emitting devices. **Applied physics letters**, 74 (23): 3444-3446

KIM, H., HORWITZ, J. S., PIQUE, A., KUSHTO, G., KAFAFI, H., GILMORE, C. M. & CHRISEY, D. B. (2000) Effect of film thickness on the properties of indium tin oxide

thin film grown by pulsed laser deposition for organic light-emitting diodes. In Bellingham, WA, USA. pp. 140-149

KIM, H., HORWITZ, J. S., KUSHTO, G. P., KAFAFI, Z. H. & CHRISEY, D. B. (2001) Indium tin oxide thin films grown on flexible plastic substrates by pulsed-laser deposition for organic light-emitting diodes. **Applied physics letters**, 79 (3): 284-286

KIM, H. (2007) "Transparent Conducting Oxide Films". In EASON, R. (Ed.) **Pulsed Laser Deposition of Thin Films: Applications-Led Growth of Functional Materials**. Hoboken, New Jersey: Wiley & Sons, Inc. pp. 239 - 260.

KIM, J. C., CAKMAK, M. & ZHOU, X. (1998) Effect of composition on orientation, optical and mechanical properties of bi-axially drawn PEN and PEN/PEI blend films. **Polymer**, 39 (18): 4225-4234

KIM, J. H., JEON, K. A., KIM, G. H. & LEE, S. Y. (2006) Electrical, structural, and optical properties of ITO thin films prepared at room temperature by pulsed laser deposition. **Applied Surface Science**, 252 (13 SPEC ISS): 4834-4837

KIM, K. H., PARK, N. M., KIM, T. Y., CHO, K. S., LEE, J. I., CHU, H. Y. & SUNG, G. Y. (2005a) Indium tin oxide thin films grown on polyethersulphone (PES) substrates by pulsed-laser deposition for use in organic light-emitting diodes. **Etri Journal**, 27 (4): 405-410

KIM, S.-S., CHOI, S.-Y., PARK, C.-G. & JIN, H.-W. (1999c) Transparent conductive ITO thin films through the sol-gel process using metal salts. **Thin Solid Films**, 347 (1-2): 155-160

KIM, S. H., PARK, N.-M., KIM, T. & SUNG, G. (2005b) Electrical and optical characteristics of ITO films by pulsed laser deposition using a 10 wt.% SnO2-doped In2O3 ceramic target. **Thin Solid Films**, 475 (1-2 SPEC ISS): 262-266

KLEIN, L. C. (1988) Sol-Gel Technology for Thin Films, Fibers, Preforms, Electronics and Specialty Shapes. William Andrew Publishing/Noyes.

KONG, Y. & HAY, J. N. (2002) The measurement of the crystallinity of polymers by DSC. **Polymer**, 43 (14): 3873-3878

KONG, Y. (2002) **Structure and Property Relationships in PET blends**. PhD Thesis, University of Birmingham

KONIGER, T. & MUNSTEDT, H. (2008a) Coatings of indium tin oxide nanoparticles on various flexible polymer substrates: Influence of surface topography and oscillatory bending on electrical properties. **Journal of the Society for Information Display**, 16 (4): 559-568

KONIGER, T. & MUNSTEDT, H. (2008b) Advanced device for testing the electrical behavior of conductive coatings on flexible polymer substrates under oscillatory bending: Comparison of coatings of sputtered indium-tin oxide and poly3,4ethylenedioxythiophene. **Measurement Science and Technology**, 19 (5): 055709

KRUTPHUN, P. & SUPAPHOL, P. (2005) Thermal and crystallization characteristics of poly(trimethylene terephthalate)/poly(ethylene naphthalate) blends. **European Polymer Journal**, 41 (7): 1561-1568

KUMAR, C. V. R. V. & MANSINGH, A. (1989) Effect of target-substrate distance on the growth and properties of rf-sputtered indium tin oxide films. 65 1270-1280

LASER_FOCUS_WORLD (2004) Flexible displays open new windows of opportunity. In **Laser Focus World** [online]. Available from: http://www.laserfocusworld.com/articles/print/volume-40/issue-

3/features/optoelectronic-applications-novel-displays/flexible-displays-open-new-windows-of-opportunity.html
LASKARAKIS, A. & LOGOTHETIDIS, S. (2006) Investigation of the optical anisotropy of PET and PEN films by VIS-FUV to IR spectroscopic ellipsometry. **Applied Surface Science**, 253 (1 SPEC. ISS.): 52-56
LATELLA, B. A., TRIANI, G., ZHANG, Z., SHORT, K. T., BARTLETT, J. R. & IGNAT, M. (2007) Enhanced adhesion of atomic layer deposited titania on polycarbonate substrates. **Thin Solid Films**, 515 (5): 3138-3145
LAWTON, E. L. & RINGWALD, E. L. (1989) "Physical Constants of Poly(oxyethylene-oxyterephthaloyl) (Poly(ethylene terephthalate))". In BRANDRUP, J. & IMMERGUT, E. H. (Eds.) **Polymer Handbook**. New York, Chichester, Brisbane, Toronto, Singapore: John Willey & Sons. pp. V/101-105.
LEE, J.-H., LIU, D. N. & WU, S.-T. (2008) **Introduction to Flat Panel Displays**. West Sussex: John Willey & Sons Ltd. pp. 210
LEONID, R. S., HARI SINGH, N., M.SC & PH.D.A2 - HARI SINGH NALWA, M. S. P. D. (2002) "Chapter 13 - Pulsed laser deposition of thin films: Expectations and reality". In **Handbook of Thin Films**. Burlington: Academic Press. pp. 627-673. Available from: http://www.sciencedirect.com/science/article/pii/B9780125129084500163
LETERRIER, Y. & MANSON, J. A. E. (1997) Work of fragmentation of a thin oxide coating on a polymer film. **Journal of Materials Science Letters**, 16 (2): 120-121
LETERRIER, Y., ANDERSONS, J., PITTON, Y. & MANSON, J. A. E. (1997a) Adhesion of silicon oxide layers on poly(ethylene terephthalate). II: Effect of coating thickness on adhesive and cohesive strengths. **Journal of Polymer Science, Part B: Polymer Physics**, 35 (9): 1463-1472
LETERRIER, Y., BOOGH, L., ANDERSONS, J. & MANSON, J. A. E. (1997b) Adhesion of silicon oxide layers on poly(ethylene terephthalate). I: Effect of substrate properties on coating's fragmentation process. **Journal of Polymer Science, Part B: Polymer Physics**, 35 (9): 1449-1461
LETERRIER, Y., BOOGH, L., ANDERSONS, J. & MÅNSON, J. A. E. (1997c) Adhesion of silicon oxide layers on poly(ethylene terephthalate). I: Effect of substrate properties on coating's fragmentation process. **Journal of Polymer Science, Part B: Polymer Physics**, 35 (9): 1449-1461
LETERRIER, Y., FISCHER, C., MEDICO, L., DEMARCO, F., MANSON, J.-A. E., BOUTEN, P., DEGOEDE, J. & NAIRN, J. A. (2003) Mechanical Properties of Transparent Functional Thin Films for Flexible Displays. In **46th Annual Technical Conference Proceedings of the Society of Vacuum Coaters**. pp. 1-6
LETERRIER, Y. (2003) Durability of nanosized oxygen-barrier coatings on polymers. **Progress in Materials Science**, 48 (1):
LETERRIER, Y., MEDICO, L., DEMARCO, F., MANSON, J. A. E., BETZ, U., ESCOLA, M. F., OLSSON, M. K. & ATAMNY, F. (2004) Mechanical integrity of transparent conductive oxide films for flexible polymer-based displays. **Thin Solid Films**, 460 (1-2): 156-166
LETERRIER, Y., PINYOL, A., ROUGIER, L., WALLER, J. H. & MANSON, J.-A. E. (2009) Electrofragmentation modeling of conductive coatings on polymer substrates. **Journal of Applied Physics**, 106 (11): 113508-113505
LEWIS, J. (2006) Material challenge for flexible organic devices. **Materials Today**, 9 (4): 38-45

LEWIS, J. S. & WEAVER, M. S. (2004a) Thin-film permeation-barrier technology for flexible organic light-emitting devices. **Selected Topics in Quantum Electronics, IEEE Journal of**, 10 (1): 45-57

LEWIS, J. S. & WEAVER, M. S. (2004b) Thin-film permeation-barrier technology for flexible organic light-emitting devices. **IEEE Journal on Selected Topics in Quantum Electronics**, 10 (1): 45-57

LI, Y., ZHAO, G., REN, Y. & CHEN, D. (2011) Microstructure analysis of sol-gel-derived nanocrystalline ITO thin films. **Surface and Interface Analysis**, 43 (9): 1199-1202

LIN, Y. C., SHI, W. Q. & CHEN, Z. Z. (2009) Effect of deflection on the mechanical and optoelectronic properties of indium tin oxide films deposited on polyethylene terephthalate substrates by pulse magnetron sputtering. **Thin Solid Films**, 517 (5): 1701-1705

LOGOTHETIDIS, S. (2008) Flexible organic electronic devices: Materials, process and applications. **Materials Science and Engineering: B**, 152 (1-3): 96-104

LUKKASSEN, D. & MEIDELL, A. (2003) **Advanced Materials and Structures and their Fabrication Processes** [online]. Narvik University College, HiN. Available from: http://ebook4everything.com/

LUKKASSEN, D. & MEIDELL, A. (2007) **Advanced Materials and Structures and their Fabrication Processes** [online]. Narvik University College, HiN. Available from: http://www.scribd.com/doc/24165910/Advanced-Materials

MA, T. & BHUSHAN, B. (2003) Mechanical, hygroscopic, and thermal properties of ultrathin polymeric substrates for magnetic tapes. **Journal of Applied Polymer Science**, 89 (11): 3052-3080

MACDONALD, B. A., ROLLINS, K., EVESON, R., RAKOS, K., RUSTIN, B. A. & HANDA, M. (2003a) New Developments In Polyester Film for Flexible Electronics. In **Materials Research Society Symposium - Proceedings**. San Francisco, CA, United states. pp. 283-290

MACDONALD, B. A., ROLLINS, K., MACCERON, D., RACOS, K., EVESON, R., HASHIMOTO, K. & RUSTIN, B. (2005) "Engineered Films for Display Technologies". In CRAWFORD, G. P. (Ed.) **Flexible Flat Panel displays**. Chichester: Jon Wiley & Sons, Ltd. pp. 11-12.

MACDONALD, W. A., MACE, J. M. & POLACK, N. P. (2002) New Developments in Polyester Films for Display Applications. In **45th Annual Technical Conference Proceedings of the Society of Vacuum Coaters**. pp. 482-486

MACDONALD, W. A., ROLLINS, K., EVESON, R., RUSTIN, R. A. & HANDA, M. (2003b) P-17: Plastic Displays - New Developments in Polyester Film for Plastic Electronics. **SID Symposium Digest of Technical Papers**, 34 (1): 264-267

MACDONALD, W. A., ROLLINS, K., MACKERRON, D., EVESON, R., RUSTIN, R. A., RAKOS, K. & HANDA, M. (2004) P-46: Plastic Displays --- Latest Developments in Polyester Film for Plastic Electronics. **SID Symposium Digest of Technical Papers**, 35 (1): 420-423

MACDONALD, W. A. (2006) "Advanced Flexible Polymeric Substrates". In KLAUK, H. (Ed.) **Organic Electronics: Materials, Manufacturing and Applications.**, Weinheim: Wiley-VCH Verlag GmbH & Co. pp. 162-178.

MACDONALD, W. A., LOONEY, M. K., MACKERRON, D., EVESON, R., ADAM, R., HASHIMOTO, K. & RAKOS, K. (2007) Latest advances in substrates for flexible electronics. **Journal of the Society for Information Display**, 15 (12): 1075-1083

MACDONALD, W. A., LOONEY, M. K., MACKERRON, D., EVESON, R. & RAKOS, K. (2008) Designing and manufacturing substrates for flexible electronics. **Plastics, Rubber and Composites**, 37 (2-4): 41-45

MALPASS, D. B. (2010) **Introduction to Industrial Polyethylene - Properties, Catalysts, and Processes** [online]. Wiley - Scrivener. Available from: http://www.knovel.com/web/portal/browse/display?_EXT_KNOVEL_DISPLAY_bookid=4099

MANAVIZADEH, N., BOROUMAND, F. A., ASL-SOLEIMANI, E., RAISSI, F., BAGHERZADEH, S., KHODAYARI, A. & RASOULI, M. A. (2009) Influence of substrates on the structural and morphological properties of RF sputtered ITO thin films for photovoltaic application. **Thin Solid Films**, 517 (7): 2324-2327

MARTINEZ-VEGA, J. J., ZOUZOU, N., BOUDOU, L. & GUASTAVINO, J. (2001) Molecular mobility in amorphous and partially crystalline PEN after isothermal crystallization. **Ieee Transactions on Dielectrics and Electrical Insulation**, 8 (5): 776-784

MCCLURE, D. J. (2007) Polyester (PET) Films as a Substrate: a Tutorial. In **50th Annual Technical Conference Proceedings of the Society of Vacuum Coaters**. pp. 692-699

MCGRAW-HILL_CONCISE_ENCYCLOPEDIA_OF_PHYSICS (2004) **McGraw-Hill Concise Encyclopedia of Physics**. McGraw-Hill Professional.

MELNICK, J. (2011) Sorting hype from reality in flexible displays. **Solid State Technology**, 54 (10): 10-10

MENG, L.-J. & DOS SANTOS, M. P. (1997) Properties of indium tin oxide (ITO) films prepared by r.f. reactive magnetron sputtering at different pressures. **Thin Solid Films**, 303 (1-2): 151-155

MORENT, R., GEYTER, N. D., AXISA, F., SMET, N. D., GENGEMBRE, L., LEERSNYDER, E. D., LEYS, C., VANFLETEREN, J., RYMARCZYK-MACHAL, M., SCHACHT, E. & PAYEN, E. (2007) Adhesion enhancement by a dielectric barrier discharge of PDMS used for flexible and stretchable electronics. **Journal of Physics D: Applied Physics**, 40 (23): 7392

MORGAN, R. J. & O'NEAL, J. E. (1979) Modes of deformation and failure of polycarbonate. **Polymer**, 20 (3): 375-387

MORIGA, T., OKAMOTO, T., HIRUTA, K., FUJIWARA, A., NAKABAYASHI, I. & TOMINAGA, K. (2000) Structures and Physical Properties of Films Deposited by Simultaneous DC Sputtering of ZnO and In2O3 or ITO Targets. **Journal of Solid State Chemistry**, 155 (2): 312-319

NAKAMAE, K., NISHINO, T., TADA, K., KANAMOTO, T. & ITO, M. (1993) ELASTIC-MODULUS OF THE CRYSTALLINE REGIONS OF POLY(ETHYLENE-2,6-NAPHTHALATE). **Polymer**, 34 (15): 3322-3324

NAKAMAE, K., NISHINO, T. & GOTOH, Y. (1995) STUDIES ON THE TEMPERATURE-DEPENDENCE OF THE ELASTIC-MODULUS OF THE CRYSTALLINE REGIONS OF POLYMERS .15. TEMPERATURE-DEPENDENCE OF THE ELASTIC-MODULUS OF THE CRYSTALLINE REGIONS OF POLY(ETHYLENE 2,6-NAPHTHALATE). **Polymer**, 36 (7): 1401-1405

NAM, E., KANG, Y.-H., SON, D.-J., JUNG, D., HONG, S.-J. & KIM, Y. S. (2010) Electrical and surface properties of indium tin oxide (ITO) films by pulsed DC magnetron sputtering for organic light emitting diode as anode material. **Surface and Coatings Technology**, 205 (Supplement 1): S129-S132

NIELSEN, L. E. (1974a) **Mechanical Properties of Polymers and Composites**. Vol. 2, New York: Dekker.
NIELSEN, L. E. (1974b) **Mechanical Properties of Polymers and Composites**. Vol. 1, New York: Dekker.
NISATO, G., KUILDER, M., BOUTEN, P., MORO, L., PHILIPS, O. & RUTHERFORD, N. (2003) P-88: Thin Film Encapsulation for OLEDs: Evaluation of Multi-layer Barriers using the Ca Test. **SID Symposium Digest of Technical Papers**, 34 (1): 550-553
NORTON, D. P. (2007) "Pulsed Laser Deposition of Complex Materials: Progress Towards Applications". In EASON, R. (Ed.) **Pulsed Laser Deposition of Thin Films: Application - Led Growth of Functional Materials**. Hoboken, New Jersey: John Wiley and Sons, Inc. pp. 3 - 21.
OHRING, M. (1992) **The Materials Science of Thin Films**. London: Academic Press Ltd.
OUERFELLI, J., DJOBO, S. O., BERNÈDE, J. C., CATTIN, L., MORSLI, M. & BERREDJEM, Y. (2008) Organic light emitting diodes using fluorine doped tin oxide thin films, deposited by chemical spray pyrolysis, as anode. **Materials Chemistry and Physics**, 112 (1): 198-201
OWEN, T. (2000) **Fundamentals of Modern UV - visible Spectroscopy** [online]. Germany: Agilent Technologies. Available from: http://www.google.co.uk/url?sa=t&source=web&cd=1&sqi=2&ved=0CBsQFjAA&url=http%3A%2F%2Fwww.aue.auc.dk%2F~sp%2FAnalyt_Chem_K4_09%2FManual_de_Espectroscopia.pdf&rct=j&q=Fundamentals%20of%20Modern%20UV%20-%20visible%20Spectroscopy&ei=7hsvTZyHGcKJhQeLsrDmCg&usg=AFQjCNGlfYNtoRkIny8lecZuHxP7tHfMqw&cad=rja
PAENG, S.-H., PARK, M.-W. & SUNG, Y.-M. (2010) Transparent conductive characteristics of Ti:ITO films deposited by RF magnetron sputtering at low substrate temperature. **Surface and Coatings Technology**, 205 (Supplement 1): S210-S215
PAINE, D. C., YEOM, H.-Y. & YAGLIOGLU, B. (2005) "Transparent Conducting Oxide Materials and Technology". In CRAWFORD, G. P. (Ed.) **Flexible Flat Panel Displays**. Chichester: Wiley & Sons, Ltd. pp. 79 - 98.
PARK, J.-B., HWANG, J.-Y., SEO, D.-S., PARK, S.-K., MOON, D.-G. & HAN, J.-I. (2004) Position Dependent Stress Distribution of Indium-Tin-Oxide on Polymer Substrate by Applying External Bending Force. **Japanese Journal of Applied Physics**, 43 (5A): 2677-2680
PARK, S.-S. & MACKENZIE, J. D. (1995) Sol-gel-derived tin oxide thin films. **Thin Solid Films**, 258 (1-2): 268-273
PARK, S. K., HAN, J. I., MOON, D. G. & KIM, W. K. (2003) Mechanical stability of externally deformed indium-tin-oxide films on polymer substrates. **Japanese Journal of Applied Physics, Part 1: Regular Papers and Short Notes and Review Papers**, 42 (2 A): 623-629
PEDROSA, P., CHAPPÉ, J.-M., FONSECA, C., MACHADO, A. V., NÓBREGA, J. M. & VAZ, F. (2010) Plasma Surface Modification of Polycarbonate and Poly(propylene) Substrates for Biomedical Electrodes. **Plasma Processes and Polymers**, 7 (8): 676-686
PLUMMER, C. J. G., SOLES, C. L., XIAO, C., WU, J., KAUSCH, H. H. & YEE, A. F. (1995) Effect of Limiting Chain Mobility on the Yielding and Crazing Behavior of Bisphenol-A Polycarbonate Derivatives. **Macromolecules**, 28 (21): 7157-7164
PUSZYNSKI, A. & PIELICHOWSKI, J. (2003) **Technologia tworzyw sztucznych**. Warszawa: Wydawnictwo Naukowo-Techniczne. pp. 183

QIAO, Z., LATZ, R. & MERGEL, D. (2004) Thickness dependence of In2O3:Sn film growth. **Thin Solid Films**, 466 (1-2): 250-258

RADHOUANE BEL HADJ, T., TAKAYUKI, B., YUTAKA, O. & YASUTAKA, T. (1998) **Electronic transport in tin-doped indium oxide thin films prepared by sol-gel technique**. Vol. 83, AIP.

RAUMANN, G. & SAUNDERS, D. W. (1961) Anisotropy of Youngs Modulus in Drawn Polyethylene **Proceedings of the Physical Society of London**, 77 (497): 1028

ROCHAT, G., DELACHAUX, A., LETERRIER, Y., MANSON, J. A. E. & FAYET, P. (2003a) Influence of substrate morphology on the cohesion and adhesion of thin PECVD oxide films on semi-crystalline polymers. **Surface and Interface Analysis**, 35 (12): 948-952

ROCHAT, G., LETERRIER, Y., FAYET, P. & MANSON, J. A. E. (2003b) Mechanical analysis of ultrathin oxide coatings on polymer substrates in situ in a scanning electron microscope. **Thin Solid Films**, 437 (1-2): 204-210

RUDDER, J. D., N.ROSENQUIST, B.SAPP & P.SYBERT (2006) "Polycarbonates". In MARGOLIS, J. M. (Ed.) **Engineering Plastics Handbook**. McGraw-Hill. pp. 327-376. Available from: http://www.scribd.com/doc/47480426/Engineering-Plastics-Handbook

RUNYAN, W. R. & SHAFFNER, T. J. (1997) **Semiconductor measurements and instrumentation**. 2nd ed. New York ; London: McGraw-Hill.

SAUER, B., KAMPERT, W., MCLEAN, R. & CARCIA, P. (2000) TMDSC and Atomic Force Microscopy Studies of Morphology and Recrystallization in Polyesters Including Oriented Films. **Journal of Thermal Analysis and Calorimetry**, 59 (1): 227-243

SCHOUKENS, G., SAMYN, P., MADDENS, S. & VAN AUDENAERDE, T. (2003) Shrinkage behavior after the heat setting of biaxially stretched poly(ethylene 2,6-naphthalate) films and bottles. **Journal of Applied Polymer Science**, 87 (9): 1462-1473

SCHRODER, D. K. (1990) **Semiconductor material and device characterization**. New York ; Chichester: Wiley.

SHIN, J. H., SHIN, S. H., PARK, J. I. & KIM, H. H. (2001) Properties of dc magnetron sputtered indium tin oxide films on polymeric substrates at room temperature. **Journal of Applied Physics**, 89 (9): 5199-5203

SHIN, S. H., SHIN, J. H., PARK, K. J., ISHIDA, T., TABATA, O. & KIM, H. H. (1999) Low resistivity indium tin oxide films deposited by unbalanced DC magnetron sputtering. **Thin Solid Films**, 341 (1-2): 225-229

SHIVAKUMAR, K. N. & SMITH, S. A. (2004) In situ fracture toughness testing of core materials in sandwich panels. **Journal of Composite Materials**, 38 (8): 655-668

SIERROS, K. A. (2006) **Mechanical Properties and Characterisation of Substrates for Flexible Displays**. PhD thesis, University of Birmingham

SIERROS, K. A. & KUKUREKA, S. N. (2007) Tribological investigation of thin polyester substrates for displays. **Wear**, 263 (7-12): 992-999

SIERROS, K. A., MORRIS, N. J., RAMJI, K. & CAIRNS, D. R. (2009) Stress-corrosion cracking of indium tin oxide coated polyethylene terephthalate for flexible optoelectronic devices. **Thin Solid Films**, 517 (8): 2590-2595

SIERROS, K. A., CAIRNS, D. R., ABELL, J. S. & KUKUREKA, S. N. (2010a) Pulsed laser deposition of indium tin oxide films on flexible polyethylene naphthalate display substrates at room temperature. **Thin Solid Films**, 518 (10): 2623-2627

SIERROS, K. A., BANERJEE, D. A., MORRIS, N. J., CAIRNS, D. R., KORTIDIS, I. & KIRIAKIDIS, G. (2010b) Mechanical properties of ZnO thin films deposited on polyester substrates used in flexible device applications. **Thin Solid Films**, 519 (1): 325-330

SIM, B., KIM, E.-H., PARK, J. & LEE, M. (2009) Highly enhanced mechanical stability of indium tin oxide film with a thin Al buffer layer deposited on plastic substrate. **Surface and Coatings Technology**, 204 (3): 309-312

SITTINGER, V., RUSKE, F., WERNER, W., JACOBS, C., SZYSZKA, B. & CHRISTIE, D. J. (2008) High power pulsed magnetron sputtering of transparent conducting oxides. **Thin Solid Films**, 516 (17): 5847-5859

SIVIOUR, C. R., WALLEY, S. M., PROUD, W. G. & FIELD, J. E. (2005) The high strain rate compressive behaviour of polycarbonate and polyvinylidene difluoride. **Polymer**, 46 (26): 12546-12555

STONEY, G. G. (1909) The Tension of Metallic Films Deposited by Electrolysis. **Proceedings of the Royal Society of London. Series A, Containing Papers of a Mathematical and Physical Character**, 82 (553): 172-175

STROBL, G. (2007) **The Physics of Polymers: Concepts for Understanding Their Structures and Behavior**. 3rd ed. Berlin, Heidenberg, New York: Springer-Verlag.

SU, C., SHEU, T. K., CHANG, Y. T., WAN, M. A., FENG, M. C. & HUNG, W. C. (2005) Preparation of ITO Thin Films by Sol-Gel Process and Their Characterizations. **Synthetic Metals**, 153 (1-3): 9-12

SUO, Z. & HUTCHINSON, J. W. (1989) Sandwich test specimens for measuring interface crack toughness. **Materials Science and Engineering: A**, 107 (0): 135-143

SUO, Z., MA, E. Y., GLESKOVA, H. & WAGNER, S. (1999) **Mechanics of rollable and foldable film-on-foil electronics**. Vol. 74, AIP.

SUTAPA ROY, R. (2001) Dip coated ITO thin-films through sol-gel process using metal salts. **Thin Solid Films**, 389 (1-2): 207-212

SUZUKI, A., MATSUSHITA, T., AOKI, T., MORI, A. & OKUDA, M. (2002) Highly conducting transparent indium tin oxide films prepared by pulsed laser deposition. **Thin Solid Films**, 411 (1): 23-27

TAHAR, R. B. H., BAN, T., OHYA, Y. & TAKAHASHI, Y. (1998) Tin doped indium oxide thin films: electrical properties. **Journal of Applied Physics**, 83 (5): 2631

TERZINI, E., THILAKAN, P. & MINARINI, C. (2000) Properties of ITO thin films deposited by RF magnetron sputtering at elevated substrate temperature. **Materials Science and Engineering B**, 77 (1): 110-114

THESTRUP, B. & SCHOU, J. (1999) Transparent conducting AZO and ITO films produced by pulsed laser ablation at 355 nm. **Applied Physics A: Materials Science & Processing**, 69 (0): S807-S810

THOULESS, M. D., HUTCHINSON, J. W. & LINIGER, E. G. (1992) Plane-strain, buckling-driven delamination of thin films: Model experiments and mode-II fracture. **Acta Metallurgica et Materialia**, 40 (10): 2639-2649

TIAN, L. (2009) **Study of Indium Tin Oxide and Its Microwave Applications**. PhD Thesis, University of Birmingham

TIMÓTEO, G. A. V., FECHINE, G. J. M. & RABELLO, M. S. (2008) Stress cracking and photodegradation behavior of polycarbonate. The combination of two major causes of polymer failure. **Polymer Engineering & Science**, 48 (10): 2003-2010

TING, C.-C., CHENG, W.-L. & LIN, G.-C. (2011) Structural and opto-electrical properties of the tin-doped indium oxide thin films fabricated by the wet chemical method with different indium starting materials. **Thin Solid Films**, 519 (13): 4286-4292

TSENG, A. A. (2010) A comparison study of scratch and wear properties using atomic force microscopy. **Applied Surface Science**, 256 4246-4252

TSUBONE, D., HASEBE, T., KAMIJO, A. & HOTTA, A. (2007) Fracture mechanics of diamond-like carbon (DLC) films coated on flexible polymer substrates. **Surface and Coatings Technology**, 201 (14): 6423-6430

VASANT KUMAR, C. & MANSINGH, A. (1989) Effect of target-substrate distance on the growth and properties of rf-sputtered indium tin oxide films. **Journal of Applied Physics**, 65 (3): 1270

VEITH, M., BUBEL, C. & ZIMMER, M. (2011) A novel precursor system and its application to produce tin doped indium oxide. **Dalton Transactions**, 40 (22): 6028-6032

VIESPE, C., NICOLAE, I., SIMA, C., GRIGORIU, C. & MEDIANU, R. (2007) ITO thin films deposited by advanced pulsed laser deposition. **Thin Solid Films**, 515 (24 SPEC ISS): 8771-8775

WASA, K., KITABATAKE, M. & ADACHI, H. (2004) **Thin Film Materials Technology**. Norwich: William Andrew, Inc.

WONG, F. L., FUNG, M. K., TONG, S. W., LEE, C. S. & LEE, S. T. (2004) Flexible organic light-emitting device based on magnetron sputtered indium-tin-oxide on plastic substrate. **Thin Solid Films**, 466 (1-2): 225-230

YAN, M., KIM, T. W., ERLAT, A. G., PELLOW, M., FOUST, D. F., LIU, J., SCHAEPKENS, M., HELLER, C. M., MCCONNELEE, P. A., FEIST, T. P. & DUGGAL, A. R. (2005) A Transparent, High Barrier, and High Heat Substrate for Organic Electronics. **Proceedings of the IEEE**, 93 (8): 1468-1477

YANAKA, M., TSUKAHARA, Y., NAKASO, N. & TAKEDA, N. (1998) Cracking phenomena of brittle films in nanostructure composites analysed by a modified shear lag model with residual strain</b&gt. **Journal of Materials Science**, 33 (8): 2111-2119

YANG, C.-W. & PARK, J.-W. (2010) The cohesive crack and buckle delamination resistances of indium tin oxide (ITO) films on polymeric substrates with ductile metal interlayers. **Surface and Coatings Technology**, 204 (16-17): 2761-2766

YE, T., SUO, Z. & EVANS, A. G. (1992) Thin film cracking and the roles of substrate and interface. **International Journal of Solids and Structures**, 29 (21): 2639-2648

YEOM, H. Y., POPOVICH, N., CHASON, E. & PAINE, D. C. (2002) A study of the effect of process oxygen on stress evolution in d.c. magnetron-deposited tin-doped indium oxide. **Thin Solid Films**, 411 (1): 17-22

YONG, T. K., TOU, T. Y. & TEO, B. S. (2005) Pulsed laser deposition of tin-doped indium oxide (ITO) on polycarbonate. **Applied Surface Science**, 248 (1-4): 388-391

YOSHIOKA, H., ADURODIJA, F. O., IZUMI, H., ISHIHARA, T. & MOTOYAMA, M. (2000) Chemical state analysis on tin-doped indium oxide films prepared by pulsed laser deposition. **Electrochemical and Solid-State Letters**, 3 (12): 540-542

ZHANG, X., WU, W., TIAN, T., MAN, Y. & WANG, J. (2008) Deposition of transparent conductive mesoporous indium tin oxide thin films by a dip coating process. **Materials Research Bulletin**, 43 (4): 1016-1022

ZHENG, J. & KWOK, H. (1993) Low resistivity indium tin oxide films by pulsed laser deposition. **Applied physics letters**, 63 (1): 1

ZUMAILAN, A., DENIS, G., DARGENT, E., SAITER, J. & GRENET, J. (2002) The Influence of Drawing in Hot Water on The Morphological Properties of Pet Films as Measured by DSC and Modulated DSC. **Journal of Thermal Analysis and Calorimetry**, 68 (1): 5-13

Appendix A: SOLFLEX project

The author, for two years, was taking a part in a consortium project called SOLFLEX funded by the Technology Strategy Board (TSB). The project included partners from both academia and the industry and was led by the company TWI. The partners of the project are listed below.

The overall objective of the SOLFLEX project was to develop sol-gel conductive ITO ink and deposition procedures to print patterned coating on polymer substrates at low curing temperatures for roll-to-roll production. The end application required a conductive transparent so-gel derived ITO film with sheet resistance and transparency of 10 – 100 Ω/□ and ~ 90%, respectively to compete with sputtered ITO. In addition, good mechanical (flexure, adhesion) performance was required in order to utilised ITO/polymer system for flexible electronic applications.

The sol-gel development process and the samples used in this work are described in section 2.1.3 of chapter 2.

The author's role in the project was to provide crucial characterisation and assessment of the samples through the whole development process to establish a basic understanding of the microstructure-property relationships of the ITO thin-films.

SOLFLEX project partners:

TWI Limited,
Granta Park,
Great Abington,
Cambridge, CB21 6AL, UK
www.twi.co.uk

SAFC Hitech,
Power Road,
Bromborough,
Wirral, CH62 3QF, UK
www.safcglobal.com

Gwent Electronic Materials Limited,
Monmouth House,
Pontypool,
Gwent,
Wales, N94 0HZ, UK
www.gwent.org

Micro Circuit Engineering,
351 Exning Road,
Newmarket,
Suffolk, CB8 0AU, UK
www.microcircuit.com

Cadillac Plastic Limited,
Rivermead Drive,
Swindon, SN5 7EX, UK
www.cadillacplastic.co.uk

University of Wales Swansea,
Singleton Park,
Swansea,
Wales, SA2 8PP, UK
www.swan.ac.uk

University of Birmingham,
School of Metallurgy and Materials,
Edgbaston,
Birmingham, B15 2TT, UK
www.bham.ac.uk

Appendix B: Substrates and samples suppliers

Cadillac Plastic Limited,
Rivermead Drive,
Swindon, SN5 7EX, UK
www.cadillacplastic.co.uk

Delta Technologies Limited,
1110 N. Boise Avenue,
Loveland, CO 80537-5059, USA
www.delta-technologies.com

PI-KEM Limited,
Unit 20, Tame Valley Buisness Centre
Magnus,
Tamworth,
Staffordshire, B77 5BY, UK
www.pi-kem.co.uk

Appendix C: Publications

1. *G.A Potoczny, T.S. Bejitual, J.S. Abell, K.A. Sierros, D.R. Cairns, S.N. Kukureka, "Flexibility and Electrical Stability of polyester-based electrodes under monotonic and cycling buckling conditions"*. (submitted for XXXIX International Conference on Metallurgical Coatings and Thin Films, 23-27.04. 2012/San Diego, CA, USA)

2. *G.A. Potoczny, J.S. Abell, S.N. Kukureka, „Mechanically-induced catastrophic electrical deterioration of indium tin oxide film on polycarbonate substrates used for plastic electronics"*. (submitted to Thin Solid Films)

3. *G.A. Potoczny, J.S. Abell, S.N. Kukureka, „Electro-mechanical durability of indium tin oxide thin films pulsed-laser deposited on polycarbonate substrates for flexible electronic devices"*. (presented at conference; XXXI International Display Research Conference - Eurodisplay 2011, 19-22.09.2011/ France)